VNIVERSITAT DE VALÈNCIA

Neutrino physics from cosmological observables and oscillation experiments

Tesi Doctoral
Programa de Doctorat en Física

Pablo Fernández de Salas

IFIC - (CSIC / Universitat de València)
Departament de Física Teòrica

Director: Sergio Pastor Carpi

València, juliol 2018

Pablo Fernández de Salas
Neutrino physics from cosmological observables and oscillation experiments
Juliol, 2018
Director: Dr. Sergio Pastor Carpi

Universitat de València
Astroparticle and high energy physics group
Institut de Física Corpuscular (CSIC-UV)
Departament de Física Teòrica

Dr. Sergio Pastor Carpi,
científic titular del Consell Superior d'Investigacions Científiques (CSIC),

CERTIFICA:

Que la present memòria "Neutrino physics from cosmological observables and oscillation experiments" ha sigut realitzada sota la seua direcció a l'Institut de Física Corpuscular (centre mixt de la Universitat de València i el CSIC) per D. Pablo Fernández de Salas i constitueix la seua Tesi Doctoral per a optar al grau de Doctor en Física.

Y per a que conste, en compliment de la legislació vigent, presenta al Departament de Física Teòrica de la Universitat de València la referida Tesi Doctoral, i signa el present certificat.

Paterna (València), a 11 de juliol de 2018.

Dr. Sergio Pastor Carpi

A mis compañeros de piso Antonio y Laura, porque muchos matrimonios han durado menos que nuestra convivencia. Y a Juma por ese año con nosotros. ¿Quién nos verá darnos cabezazos contra la pared ahora?

Acknowledgements

This has been a long and exciting chapter of my life, full of people that made it possible. However, it's difficult to thank everyone who's been part of it, and even more difficult to give credit to someone in particular. The reason is that I might forget (not on purpose, I promise) some important name. I'm sure those I don't include, and feel they should have, would've actually deserved to be mentioned. So please, accept my apologies.

Of course, a great recognition go to my two families: the personal one, among which I count those who raised me (and that has become somewhat bigger along these years—I find Laura a bit guilty about it), and my scientific relatives, with whom I've spent many, many hours during the past five years. To all of them I'm very grateful and I wish our relationship doesn't stop at this point.

Even though family and work are two separated topics (or precisely because of that), I cannot do other than especially thank my parents, Isabel and Fernando (do not these names ring a bell to you? Well, even so, they did not get me interested in history), who've helped me grow up in confidence, and my brother, also Fernando, with whom I learnt there's more than fighting during childhood. Thanks a lot, really.

There is also a well deserved place here for all the friends I made during this journey, in particular those that have accompanied me during my studies in Sevilla (in and outside physics) and without whom physics itself wouldn't have been so interesting. This is the point where it's inevitable that I forget to mention people, but that's only because my brain doesn't work as it should time to time (did I say I studied physics already?), and this could be one of those moments. Since it wouldn't be fair, however, to pass without naming at least those with whom I spent more time, here they are: Carlos, Miguel (I know, I know. Which Carlos? Which Miguel? Something must be good about knowing people with the same name, don't you think? Just wait to see the list and you'll understand why I cannot distinguish among all of them!), Joaquín, Mario, Ana, Victoria, Laura, Rubén, Mercedes, Esaú, Luis, José, Inma, Maite, Juanlu, Alberto, Juan Antonio,

César, Elena, Lara, Kike, Caridad, Juan, Vicente, Javi, Manu... and many, many others that are unfortunately hiding from the fast scrutinise of memories inside my messy mind (I should seriously tidy this place up, I doubt I actually did call *iyo* to a professor... did I?).

Thanks also to those I was lucky to meet in Valencia, although the list is intentionally made shorter: Javi, Xavi, Elena, Victor, Antonio, Juanjo, Carlos, Miguel and Frodi; Ilenia, Andrea and Vittorio (these three were my first contact with Italian physicist, the first of another long list I'm happy to include, although split into small pieces); Luismi and Marina (I'll miss getting lost with you in the middle of nowhere—Wait. Am I sure about that?); and, in general, all postdocs and students from IFIC who, like me, are struggling against the dragon of bureaucracy in their attempt to reach the treasure of physics.

Of course, I'm also grateful to those that were already there even before I knew I wanted to become a scientist, especially to the "cockis" Alexandro, Inma and Nuria. I like our lunch and dinners, and I'm happy to know that I'll always have someone to call when I'm visiting el Valle. Thanks also to the Torrecera group (in which I'm certainly including Jon, our inseparable, *magic* friend), because without them I wouldn't have all the stories I'll be able to tell (maybe some day) to kids or students, like the hot day in Jerez with the amplifier, the trip back from Carranza's night or those green days of playing something we still insist in calling football.

I must express my special gratitude to the members of AHEP, both to those that are still in Valencia and also to those who already flown away: Roberto, Mariam, José, Martin, Eduardo, Thor (sorry, I meant Laslo), Urbano, Sofiane, David, Lucho, Ricardo, Christoph, Salva, Rario (ups, I don't know what happens to me today! Mario, his name is Mario), Tania, César, Massi, Stefano (both of them), Rahul, Masud, Kiko, Félix, Nicolás, Diego, Marco, Avelino, Valentina, Paulina, Carolina (am I imagining some pattern here? How many sigmas?) and, above all, Sergio, who knew how to guide me in order to achieve this goal. How can I miss my family with all the time I spend with you guys?

Of course I am also thankful to the people that made me feel comfortable during my two stays. To Julien and his group, for letting me be part of their routine during three rainy months in Aachen, and to Paolo and Massi for a similar reason: letting me feel like an Italian for some months in Ferrara. Thanks also to Massi and Martina for trying my "paella ferrarese". Among the people I've met I am particularly grateful to Thejs, Deanna, Cristian and Jan for so many unforgettable moments, and to Francesco, Linda, Valentina, Paolo, Adriano and many others I was lucky to meet in Italy.

And many, many thanks to all my collaborators as well, because without them this thesis wouldn't have been possible, in particular without the Napolitan crew, and especially without Ofelia, Gianpiero and Rino. I want to thank them twice for treating me as another member of their own families during the visits to such a hasty city.

Although I did not want to mention any teacher or professor (it wouldn't be fair for the majority not to appear here, since even the worst ones have taken me to this point, despite not having made the path easier or nicer), there's a couple of them who have gained a place in the acknowledgements. In chronological order, first I will refer to Jesús, with whom I've learnt that science can be fun. More than fun. Super fun! And secondly, I would especially remember someone whose lessons I followed during three out of the five years of bachelor. To you, Maria José (commonly known as "la Rubia"), because you were among the best professors I had. I particularly thank you for all you taught us. You might've made the trip difficult for some people, but no one can deny you made us get the most out of ourselves. I'm sorry for all the students who will not "suffer" during your lessons any more.

Continuing with teaching, I thank Pedro and Eduardo for the shared laboratory lessons of quantum physics, which I enjoyed much more than when I was the student. Who would've thought I'd be teaching in a lab? I'm sure not Rubén, Miguel or Carlos, my lab-mates during the bachelor.

I acknowledge the FPU contract as well, for paying me during these years, for supporting science at a difficult time for researchers, and for showing me that there is something more difficult and incomprehensible than physics: bureaucracy.

Of course I could not omit my flatmates: Nico, Juma, Antonio and Laura, especially the last two because of the extra years of coexistence. Only the five of us (and probably Esther, who I also thank for sharing all those moments with us. I hardly picture a board-game afternoon without her) know how absent-minded we can get after a tough day, and only us know how a sausage can appear in the cutlery drawer; a pasta be both cooked and raw at the same time; socks hang in a disturbingly flawless manner, and the air of the flat become unbreathable because of some spiders.

For all the lunches we had together, I'd like to mention Javi and Marija. Without them, lunch discussions are not the same. And speaking about lunch, many thanks to Miguel and Imma for feeding me with the needed energy to finish this task. Now I know what a Paella is!

Regarding this manuscript, I appreciate the effort made by Sergio, Mariam, Christoph, Stefano, Imma and Laura. Because of them there are surely less typos that might have gone unnoticed.

Finally, my deepest gratitude is for the person who's being there at any time I needed, either in the best moments or in the worst ones. This chapter is now closed and a new one opens up in my life, but this person has been the best I could've ever received in return for all these years. With love, to you, for your support, for your kindness and for making me smile through the days. Because physics is nothing more than just a bunch of mathematical expressions without you: thank you Laura.

List of scientific publications

This thesis is based on the following publications:

1. *Status of neutrino oscillations 2018: 3σ hint for normal mass ordering and improved CP sensitivity*
   P. F. de Salas, D. V. Forero, C. A. Ternes, M. Tórtola and J. W. F. Valle
   Physics Letters B **782**, 633 (2018) [arXiv:1708.01186]
   Chapter 1

2. *Relic neutrino decoupling with flavour oscillations revisited*
   P. F. de Salas and S. Pastor
   J. of Cosmology and Astroparticle Physics **07**, 051 (2016) [arXiv:1606.06986]
   Chapter 3

3. *Bounds on very low reheating scenarios after Planck*
   P. F. de Salas, M. Lattanzi, G. Mangano, G. Miele, S. Pastor and O. Pisanti
   Physical Review D **92**, 123534 (2015) [arXiv:1511.00672]
   Chapter 4

4. *Cosmological bounds on neutrino statistics*
   P. F. de Salas, S. Gariazzo, M. Laveder, S. Pastor, O. Pisanti and N. Truong
   J. of Cosmology and Astroparticle Physics **03**, 050 (2018) [arXiv:1802.04639]
   Chapter 5

5. *Calculation of the local density of relic neutrinos*
   P. F. de Salas, S. Gariazzo, J. Lesgourgues and S. Pastor
   J. of Cosmology and Astroparticle Physics **09**, 034 (2017) [arXiv:1706.09850]
   Chapter 6

6. *Neutrino propagation in the galactic dark matter halo*
   P. F. de Salas, R. A. Lineros and M. Tórtola
   Physical Review D **94**, 123001 (2016) [arXiv:1601.05798]
   Chapter 7

Other publications related to the topic of the thesis but which are not fully discussed:

7. *PArthENoPE reloaded*
   R. Consiglio, P. F. de Salas, G. Mangano, G. Miele, S. Pastor and O. Pisanti
   In press in Computer Physics Communications [arXiv:1712.04378]
   Section 2.2.3 (The `PArthENoPE` code is further used in chapters 4 and 5)

8. *Neutrino masses and their ordering: Global Data, Priors and Models*
   S. Gariazzo, M. Archidiacono, P. F. de Salas, O. Mena, C.A. Ternes and M. Tórtola
   J. of Cosmology and Astroparticle Physics **03**, 050 (2018) [arXiv:1801.04946]
   Section 1.4.3

9. *Neutrino Mass Ordering in 2018: Global Status*
   P. F. de Salas, S. Gariazzo, O. Mena, C. A. Ternes and M. Tórtola
   Invited review submitted to Frontiers in Physics [arXiv:1806.11051]
   Section 1.4.3

Contents

Introduction

"STARS EXPLODE, WORLDS COLLIDE,
THERE'S HARDLY ANYWHERE IN
THE UNIVERSE WHERE HUMANS
CAN LIVE WITHOUT BEING FROZEN
OR FRIED, AND YET YOU BELIEVE
THAT A...A BED IS A NORMAL THING.
IT IS THE MOST AMAZING TALENT."

– `Terry Pratchett`

Hogfather

(Capital letters are from the original)

This thesis is devoted to the phenomenology of neutrino physics. These elementary particles are relevant in studies related to particle physics, astrophysics and cosmology, being an important piece for their connection. In the particular case of the present manuscript, the emphasis is equally placed on the investigation of their flavour oscillations and on the role played by neutrinos in cosmology, especially during the early Universe.

Neutrinos are the outsiders of the standard model of particle physics. With practically null masses, whose exact value resists to be found experimentally, they present quantum properties rarely seen with such clarity. This is the case of their flavour oscillations. These neutral leptons only interact weakly, through the interchange of $W^{\pm}$ and Z gauge bosons, and only in their weak states as an electron, muon or tau neutrino, which are named after the accompanying charged lepton in a charged current interaction. These are the *flavour* neutrino eigenstates and it is well known that they do not coincide with the mass eigenstates (those that propagate freely in vacuum), as a consequence of which flavour oscillations occur.

Neutrino oscillations imply that one of these particles generated as a ν_α, where α could be any of the possible flavours, can be detected as a different flavour β at a given distance and with a given probability. It is this probability which presents an oscillatory behaviour, depending on the energy of the neutrino as well as on the distance between its origin and its detection locations. Moreover, the oscillation pattern is a function of certain parameters, which in the standard three-neutrino picture are: a) three mixing angles; b) one phase related to CP violation in the neutrino sector, and c) two differences of squared neutrino masses. One important result derived is that at least two of the three neutrinos are massive, as flavour oscillations are only possible if the squared mass differences are non-zero. The first part of this work is actually focused on the determination of such parameters from the global analysis of neutrino flavour oscillation experiments.

Beyond the phenomenon of oscillations, neutrinos are interesting from the point of view of cosmology. Given their tiny masses, neutrinos behaved as ultra-relativistic particles in the early Universe, contributing to the dominant radiation. Their share can be studied from $N_{\rm eff}$, a cosmological parameter known as the effective number of neutrinos. Similar to neutrinos, any other particle that does not interact electromagnetically and is ultra-relativistic at that epoch contributes to the energy density of the Universe. This type of radiation, that appears in some theoretical models and which is usually known as dark radiation, can be tested comparing the standard computation of $N_{\rm eff}$ with its experimental estimation. In the second part of the thesis we determine the standard value of the effective number of neutrinos, relaxing some approximations with respect to previous computations. Likewise, we study the effect of non-standard interactions between neutrinos and electrons.

One consequence of the feebleness of neutrino interactions is that their frequency was soon overcome by the expansion rate of the Universe. This leads to a process known as decoupling, from which relic neutrinos travelled through the Cosmos without interacting until today, keeping their frozen energy distribution close to a Fermi-Dirac. Neutrino influence in the primordial Universe must be accounted for when computing bounds from extensions of the standard model of cosmology. In particular, the deviations found in their frozen energy distributions have proven to be as important in some studies as the presence of flavour oscillations. We exploit this fact in a couple of chapters, where we set bounds both to the beginning of the last radiation-dominated epoch of the Universe and to the statistical properties of neutrinos.

In addition to make relic neutrinos decouple from the rest of the cosmic plasma, the continuous space-time expansion also induced a dilution of the en-

ergy of the decoupled particles, represented by a reduction of the characteristic temperature of their distribution. Since neutrinos are massive particles, they become non-relativistic at a certain time and contribute as matter to the energy density of the Universe. The exact moment of this transition, as well as the value of the neutrino masses, affects the evolution of the Cosmos, as for example large-structure formation. We have exploited the capability of these relics, non-relativistic nowadays, to feel large gravitational potentials, and we have studied their overdensity in the surroundings of the Solar System. This computation is especially relevant for future experiments aiming at relic neutrino detection.

Finally, in the last chapter of the thesis we assume a generic and non-universal interaction between neutrinos and dark matter particles. Our intention is to investigate to what extent this interaction can induce a possible deviation in the flavour of ultra-energetic neutrinos. The origin of these neutrinos is unknown, but some of them are likely to come from galactic sources. Therefore, in the same way as the oscillations are affected by baryonic matter, the presence of dark matter could modify the oscillatory pattern, provided that neutrinos and dark matter particles share a non-universal interaction. Moreover, we have taken into account the non-homogeneous distribution of dark matter in the Milky Way, which can also produce resonances that can further change the behaviour of oscillations.

Conventions

Throughout this document, the following conventions are used unless otherwise stated: we use natural units, in which $c = \hbar = k_{\mathrm{B}} = 1$; the accompanying uncertainties to experimental or theoretical determinations correspond to a standard deviation (1σ, about 68% assuming a normal distribution), and vectors $\vec{v}$ are denoted as $\mathbf{v}$ and their norm $|\vec{v}|$ as v.

Chapter 1

Neutrino oscillations

From a theoretical point of view, the concept of neutrino oscillations was first proposed by Bruno Pontecorvo [1,2] in 1957 regarding neutrino–antineutrino mixing. However, the idea of oscillations in terms of a difference between the interaction and propagation eigenstates was later conceived by Z. Maki, M. Nakagawa and S. Sakata [3] in 1962, and developed by Pontecorvo [4] in 1967. Experimentally there were hints that something was odd since the late 1960s, thanks to solar neutrino experiments. In particular, the *solar neutrino problem* was partially solved thanks to the results of SNO [5]. This experiment was able to show that the predicted flux produced in the Sun could be recovered when accounting for all flavours of the measured neutrinos, instead of summing only over the expected (produced) ν_e's. This result, together with that of the experiment KamLAND [6], definitively pointed towards neutrino flavour oscillations as the mechanism that shuffled their flavour.

The purpose of this chapter is twofold; on the one hand it serves as an introduction to neutrino flavour oscillations, that has an important role in most of the physics discussed in the present thesis, and on the other hand it also encloses one of the most relevant studies included in the thesis, namely a global fit of flavour neutrino oscillation parameters [7,8]. In this regard, a general view of the results extracted from the global fit is provided, with special emphasis given on the part in which the author has contributed. In particular, the focus is centred on the role of large-volume neutrino telescopes in measuring the oscillation parameters in the atmospheric sector (section 1.4.2).

1.1 Oscillations in vacuum

Neutrino oscillations arise as a consequence of the interaction eigenstates not being equal to the eigenstates of the propagation hamiltonian. We will denote the eigenstates of neutrino weak interactions, usually named flavour eigenstates, with a Greek subscript, $|\nu_\alpha\rangle$, where $\alpha = \{e, \mu, \tau\}$. On the other hand, the eigenstates of the evolution hamiltonian, or mass eigenstates, will be denoted with a Latin subscript, $|\nu_k\rangle$, where $k = \{1, 2, 3\}$. These states fulfil

$$\mathcal{H}_0 |\nu_k\rangle = E_k |\nu_k\rangle , \tag{1.1}$$

where $\mathcal{H}_0$ is the free hamiltonian and

$$E_k^2 = |\mathbf{p}|^2 + m_k^2, \tag{1.2}$$

being $\mathbf{p}$ the 3-momentum and m_k the mass of $|\nu_k\rangle$. We can link the eigenstates of both bases with a unitary transformation U. Therefore, the flavour eigenstates are a linear combination of the mass eigenstates,

$$|\nu_\alpha\rangle = \sum_k U_{\alpha k}^* |\nu_k\rangle , \tag{1.3}$$

where in the standard picture, when no sterile neutrino is considered, the sum in k extends up to three.

Solving the Schrödinger equation

$$i\partial_t |\nu_k(t)\rangle = \mathcal{H}_0 |\nu_k(t)\rangle , \tag{1.4}$$

the time evolution of a mass eigenstate $|\nu_k\rangle$ can be obtained,

$$|\nu_k(t)\rangle = \mathrm{e}^{-iE_k t} |\nu_k\rangle . \tag{1.5}$$

Using Eq. (1.3) we can also have the time evolution of a flavour eigenstate $|\nu_\alpha\rangle$,

$$|\nu_\alpha(t)\rangle = \sum_k U_{\alpha k}^* \mathrm{e}^{-iE_k t} |\nu_k\rangle . \tag{1.6}$$

However, precisely because flavour states are not eigenstates of the hamiltonian during propagation, we can also study the evolution of a neutrino produced as a

$|\nu_\alpha\rangle$ in terms of the different flavour states $|\nu_\beta\rangle$,

$$|\nu_\alpha(t)\rangle = \sum_\beta \left(\sum_k U^*_{\alpha k} \mathrm{e}^{-iE_k t} U_{\beta k} \right) |\nu_\beta\rangle \,. \tag{1.7}$$

From the coefficient proportional to $|\nu_\beta\rangle$ we get the probability amplitude

$$\mathcal{A}_{\nu_\alpha \to \nu_\beta}(t) = \langle \nu_\beta | \nu_\alpha(t) \rangle = \sum_k U^*_{\alpha k} U_{\beta k} \mathrm{e}^{-iE_k t}, \tag{1.8}$$

from which we obtain the probability of detecting a neutrino with flavour β at time t, when it was created with flavour α at $t = 0$,

$$P_{\nu_\alpha \to \nu_\beta}(t) = \left| \mathcal{A}_{\nu_\alpha \to \nu_\beta}(t) \right|^2 = \sum_{k,l} U^*_{\alpha k} U_{\beta k} U_{\alpha l} U^*_{\beta l} \, \mathrm{e}^{-i(E_k - E_l)t}. \tag{1.9}$$

Notice that flavour oscillations are a quantum effect arising from our incapability of distinguishing among the mass eigenstates (since we identify flavour eigenstates with the mass eigenstates of the charged leptons). If we had an experiment able to resolve the different neutrino masses, we would know for sure what neutrino had been produced, as a mass eigenstate, and we would refer to neutrino *flavour* as something affecting their interactions, similar to spin, rather than a label for the neutrinos themselves.

Actually, for neutrino flavour oscillations to be observable, the coherence of different mass eigenstates is not only necessary at detection, but also at production and during propagation. If this condition is not satisfied, flavour oscillations are washed out and only their average effect is noticeable. This is the case, for example, of non-relativistic neutrinos with non-degenerate masses [9]. Except for chapter 6, in which we treat relic neutrinos at present times, we will always deal with ultra-relativistic neutrinos along this manuscript.

Assuming that neutrinos are ultra-relativistic particles, i.e. that their energy is much larger than their mass, we can approximate

$$E_k = \sqrt{p^2 + m_k^2} \approx p + \frac{m_k^2}{2p} \approx p + \frac{m_k^2}{2E}, \tag{1.10}$$

where $E \approx p$ is the energy of the neutrino. Then, Eq. (1.9) can be rewritten as

$$P_{\nu_\alpha \to \nu_\beta}(t) = \sum_{k,l} U^*_{\alpha k} U_{\beta k} U_{\alpha l} U^*_{\beta l} \, \mathrm{e}^{-i \frac{\Delta m^2_{kl}}{2E} t}, \tag{1.11}$$

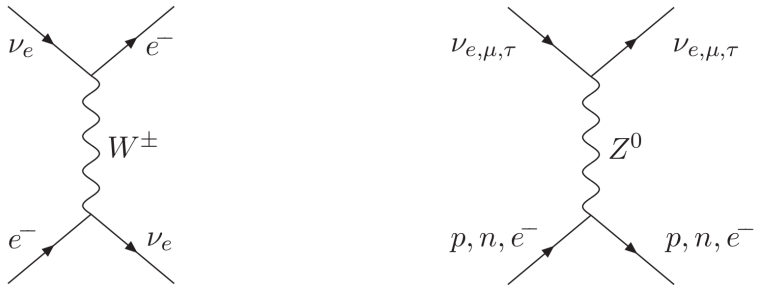

Figure 1.1: Feynman diagrams corresponding to neutrino scattering with other fermions.

where $\Delta m^2_{kl} = m^2_k - m^2_l$.

1.2 Oscillations in matter

When neutrinos propagate in a medium they can interact with its particles through the exchange of weak gauge bosons, either via charged current (CC, implying the exchange of a $W^\pm$) or via neutral current (NC, with the exchange of a neutral Z boson). In media such as the Sun or the Earth, only electrons, protons and neutrons are present in important amounts. Therefore, electron neutrinos interact via CC with their corresponding charged leptons while all flavour neutrinos do it with all weakly interacting particles through NC (see figure 1.1). Neutrino self interactions can also be relevant in some particular environments, but we neglect them in this section. Another assumption that we make is to treat the interactions shown in Fig. 1.1 under the four-fermion approximation, which holds in the cases discussed in this thesis, where $E^2_\nu \ll m^2_{W,Z}$, being $m_{W,Z}$ the mass of the W and Z gauge bosons.

The dominant contribution to neutrino scattering interactions comes from coherent forward elastic scatterings, which are proportional to G_F while harder interactions[1] scale as G^2_F, where $G_\mathrm{F} \simeq 1.166 \times 10^{-5}\,\mathrm{GeV}^{-2}$ [10] is the Fermi constant. The latter seldom occur in common media and they only play an important role in extremely dense media (such as the early Universe) or for extremely large neutrino energies. Coherent forward elastic scatterings leave the medium unchanged, and so the magnitude and direction of the neutrino momentum. However, being that neutrinos interact as flavour eigenstates but propagate

[1] With *harder* we mean those interactions involving particle-antiparticle annihilation or in which the energy or momentum of the scattered neutrino is not conserved.

as mass eigenstates, this type of interaction is important during neutrino propagation, again due to the difference between mass and flavour states, being able to change the probability of detecting a neutrino with one or another flavour.

In the following we calculate such effect, as an example, for the CC interactions between an electron neutrino and an isotropic and homogeneous medium of unpolarised electrons. The four-fermion weak hamiltonian for a $\nu_e - e^-$ CC interaction is

$$\mathcal{H}_{\text{eff}}^{\text{CC}}(x) = \frac{G_F}{\sqrt{2}} \left\{\bar{e}(x)\,\gamma^\mu\,(1-\gamma_5)\,\nu_e(x)\right\} \left\{\bar{\nu}_e(x)\,\gamma_\mu\,(1-\gamma_5)\,e(x)\right\} \tag{1.12}$$

$$= \frac{G_F}{\sqrt{2}} \left\{\bar{\nu}_e(x)\,\gamma^\mu\,(1-\gamma_5)\,\nu_e(x)\right\} \left\{\bar{e}(x)\,\gamma_\mu\,(1-\gamma_5)\,e(x)\right\}, \tag{1.13}$$

where the second line is obtained after applying a Fierz rearrangement to the Dirac fields of electrons $e(x)$ and neutrinos $\nu_e(x)$. This separation is needed in order to easily perform the average of the hamiltonian over the electron background. In the rest frame of a medium of electrons with number density n_e and a statistical distribution function[2] $f(E_e)$, where

$$\int \frac{\mathrm{d}^3\mathbf{p}_e}{(2\pi)^3} f(E_e) = n_e, \tag{1.14}$$

this average gives

$$\overline{\mathcal{H}_{\text{eff}}^{\text{CC}}}(x) = \frac{G_F}{\sqrt{2}} \left\{\bar{\nu}_e(x)\,\gamma^\mu\,(1-\gamma_5)\,\nu_e(x)\right\} \int \frac{\mathrm{d}^3\mathbf{p}_e}{(2\pi)^3\,2E_e} \Bigg\{ f(E_e) \times \frac{1}{2} \sum_{h_e=\pm1} \left\langle e^-\,(p_e,h_e)\right| \bar{e}(x)\,\gamma_\mu\,(1-\gamma_5)\,e(x) \left|e^-\,(p_e,h_e)\right\rangle \Bigg\}. \tag{1.15}$$

Notice that we are averaging over the two helicities of electrons, noted by h_e, while keeping their energy and momentum unchanged, as we have explained above. The average over helicities results in

$$\frac{1}{2} \sum_{h_e=\pm1} \left\langle e^-\,(p_e,h_e)\right| \bar{e}(x)\,\gamma_\mu\,(1-\gamma_5)\,e(x) \left|e^-\,(p_e,h_e)\right\rangle = 2p_{e\mu}, \tag{1.16}$$

[2] In this example we avoid any mention to the dependence with temperature T, since it only affects the specific value of the medium density and the course of our derivations is independent of this fact.

where $p_{e\mu}$ is the 4-momentum of the electron. If the background is isotropic

$$\int \frac{\mathrm{d}^3\mathbf{p}_e}{(2\pi)^3} f(E_e)\, \frac{\not{p}_e}{E_e} = n_e \gamma_0, \tag{1.17}$$

so in the end

$$\overline{\mathcal{H}^{\mathrm{CC}}_{\mathrm{eff}}}(x) = \sqrt{2}\, G_F\, n_e\, \bar{\nu}_{eL}(x)\, \gamma_0\, \nu_{eL}(x), \tag{1.18}$$

where the subscript L stands for left-chiral fields. This leads to an effective potential for electron neutrinos

$$V_{\mathrm{CC}} = \sqrt{2}\, G_F\, n_e. \tag{1.19}$$

Following the same approach we get the effective potential from NC interactions,

$$V_{\mathrm{NC}} = -\frac{1}{\sqrt{2}}\, G_F\, n_n. \tag{1.20}$$

The NC potential depends only on the number density of neutrons n_n because we have imposed charge neutrality of the background, which in environments such as the Sun and the Earth means that the number density of protons n_p is the same as that of electrons n_e, and their contributions are equal but opposite in sign. Similarly, if we consider an antineutrino instead of a neutrino, the sign of the potentials changes.

The effect of coherent forward elastic scattering on neutrino oscillations in a medium can be studied in a similar way as we did in section 1.1 for the case in vacuum. The total hamiltonian can be divided into a vacuum term $\mathcal{H}_0$ and an interaction term $\mathcal{H}_I$,

$$\mathcal{H} = \mathcal{H}_0 + \mathcal{H}_I, \tag{1.21}$$

where the mass states $|\nu_k\rangle$ follow Eq. (1.1), while the interaction term is diagonal in the flavour basis

$$\mathcal{H}_I\, |\nu_\alpha\rangle = V_\alpha\, |\nu_\alpha\rangle\,, \tag{1.22}$$

being

$$V_\alpha = V_{\mathrm{CC}}\delta_{\alpha e} + V_{\mathrm{NC}} = \sqrt{2}\, G_F \left(n_e \delta_{\alpha e} - \frac{n_n}{2} \right). \tag{1.23}$$

The sign of V_α in Eq. (1.23) holds for a Dirac or a Majorana left-helical neutrino, but its sign is opposite for a right-helical Majorana neutrino or a Dirac antineutrino.

The Schrödinger equation for a neutrino state initially produced with flavour α is

$$i\partial_t \left|\nu_\alpha(t)\right\rangle = \mathcal{H} \left|\nu_\alpha(t)\right\rangle , \tag{1.24}$$

from which we can get the time evolution of the transition amplitude $\mathcal{A}_{\nu_\alpha\to\nu_\beta}(t) = \langle\nu_\beta|\nu_\alpha(t)\rangle$,

$$i\partial_t \, \mathcal{A}_{\nu_\alpha\to\nu_\beta}(t) = \sum_\lambda \left(\sum_k U_{\beta k} E_k U^*_{\lambda k} + V_\beta \delta_{\lambda\beta} \right) \mathcal{A}_{\nu_\alpha\to\nu_\lambda}(t). \tag{1.25}$$

We now consider the approximation (1.10) for ultra-relativistic neutrinos and cancel the terms common to all flavours, since they are irrelevant for oscillation probabilities because they lead to a global phase that cancels when squaring the transition amplitudes

$$P_{\nu_\alpha\to\nu_\beta}(t) = \left| \mathcal{A}_{\nu_\alpha\to\nu_\beta}(t) \right|^2 . \tag{1.26}$$

In the standard picture with three active neutrinos, the equation for the evolution of the transition amplitudes takes the form

$$i\partial_t \, \mathcal{A}_{\nu_\alpha\to\nu_\beta}(t) = \sum_\lambda \left(\sum_k U_{\beta k} \frac{\Delta m^2_{k1}}{2E} U^*_{\lambda k} + V_{\mathrm{CC}} \delta_{\lambda\beta}\delta_{\beta e} \right) \mathcal{A}_{\nu_\alpha\to\nu_\lambda}(t). \tag{1.27}$$

In the second term, the one that accounts for the matter effects, V_{NC} does not appear because it is common to all flavours (see Eq. (1.23)). However, this term contributes when one ore more sterile neutrinos are included in the oscillations, since it only appears for active states. Solving Eq. (1.27) in vacuum we recover the same solution that we obtained in section 1.1, as can be easily checked if we input the transition amplitude (1.8) into it for $V_{\mathrm{CC}} = 0$.

Equation (1.27) can be expressed in matrix form as

$$i\partial_L \, \Psi_\alpha(L) = \mathsf{H}_{\mathrm{F}} \Psi_\alpha(L), \tag{1.28}$$

where we have also considered that for ultra-relativistic neutrinos $t = L$, being L the distance covered by the neutrino. In this expression, Ψ_α is a vector of the different transition amplitudes and H_{F} is the effective hamiltonian matrix in the flavour basis,

$$\mathsf{H}_{\mathrm{F}} = U \mathsf{H}_{\mathrm{M}} U^\dagger + \mathsf{V}, \tag{1.29}$$

where H_{M} is the free hamiltonian matrix in the mass basis, V the effective potential matrix, expressed in the flavour basis, and U the mixing matrix, which accounts for the unitary transformation between flavour and mass bases.

The mixing matrix for N neutrinos depends on $N(N-1)/2$ mixing angles, $(N-1)(N-2)/2$ Dirac phases and $N-1$ extra phases that are only present if neutrinos are Majorana particles. However, the Majorana phases cancel in the equations of flavour transition probability and they do not affect the pattern of oscillations. This has the implicit drawback of oscillations not being able to determine whether neutrinos are Dirac or Majorana particles.

1.3 Two-neutrino approximation

The role of the different parameters defining neutrino flavour oscillations is better understood if we assume that there are only two neutrinos. Because the two differences of squared masses differ in almost two orders of magnitude, this picture is actually very powerful, since the oscillation patterns coming from both mass differences can be treated independently at first order approximation, as we will illustrate in this section.

The mixing matrix in the two-neutrino approximation only depends on one mixing angle θ (which can get a value in the interval $[0, \pi/2]$ radians), taking the form

$$U = \begin{pmatrix} \cos\theta & \sin\theta \\ -\sin\theta & \cos\theta \end{pmatrix}. \tag{1.30}$$

Consequently, there are only two parameters controlling vacuum oscillations, θ and the difference of the squared masses Δm^2, which is defined to be positive given our chosen range for θ. Hence, the conversion probability (1.11) reads

$$P_{\nu_\alpha \to \nu_\beta}(L, E) = \sin^2(2\theta) \sin^2\left(\frac{\Delta m^2 L}{4E}\right) \tag{1.31}$$

for $\alpha \neq \beta$. Complementary, the survival probability is

$$P_{\nu_\alpha \to \nu_\alpha}(L, E) = 1 - \sin^2(2\theta) \sin^2\left(\frac{\Delta m^2 L}{4E}\right). \tag{1.32}$$

From equations (1.31) and (1.32) it is clear that θ controls the amplitude of the oscillations, whilst Δm^2 governs its frequency. This explains why the two-

neutrino approximation works well when the two squared mass differences are more than one order of magnitude away from each other.

Another subject that this approximation helps us to understand is the different aspects of matter effects. Despite its simplicity, the two-neutrino framework accounts for all important issues arising from matter effects, namely the presence of resonances and the well-known MSW effect, turning its plainness into an advantage. To study those points we use the matrix formalism, which allows us to compute the effective oscillation parameters for the flavour conversion (1.31) and survival (1.32) probabilities.

In this approximated scheme, the effective hamiltonian in the flavour basis (1.29), when a medium of electron background with constant density n_e is assumed, takes the form

$$\mathsf{H}_{\mathrm{F}} = \frac{1}{4E}\begin{pmatrix} -\Delta m^2\,\cos(2\theta) + A_{\mathrm{CC}} & \Delta m^2\,\sin(2\theta) \\ \Delta m^2\,\sin(2\theta) & \Delta m^2\,\cos(2\theta) - A_{\mathrm{CC}} \end{pmatrix}, \tag{1.33}$$

where we have defined

$$A_{\mathrm{CC}} = 2E\,V_{\mathrm{CC}}, \tag{1.34}$$

being V_{CC} that of Eq. (1.19). To express the hamiltonian (1.33) in this traceless form, a global phase $-\left(\Delta m^2 + A_{\mathrm{CC}}\right)/2$ was subtracted. We can diagonalise this matrix using an orthogonal transformation, that we will call for convenience

$$U_{\mathrm{eff}} = \begin{pmatrix} \cos\theta_{\mathrm{eff}} & \sin\theta_{\mathrm{eff}} \\ -\sin\theta_{\mathrm{eff}} & \cos\theta_{\mathrm{eff}} \end{pmatrix}. \tag{1.35}$$

Hence

$$U_{\mathrm{eff}}^T \mathsf{H}_{\mathrm{F}} U_{\mathrm{eff}} = \mathsf{H}_{\mathrm{M,eff}} = \frac{1}{4E}\mathrm{diag}\left(-\Delta m^2_{\mathrm{eff}}, \Delta m^2_{\mathrm{eff}}\right). \tag{1.36}$$

The effective parameters θ_{eff} and $\Delta m^2_{\mathrm{eff}}$ are related to those in vacuum as

$$\tan\left(2\theta_{\mathrm{eff}}\right) = \tan\left(2\theta\right)\left(1 - \frac{A_{\mathrm{CC}}}{\Delta m^2\,\cos\left(2\theta\right)}\right)^{-1}, \tag{1.37}$$

$$\Delta m^2_{\mathrm{eff}} = \sqrt{\left(\Delta m^2\,\cos\left(2\theta\right) - A_{\mathrm{CC}}\right)^2 + \left(\Delta m^2\,\sin\left(2\theta\right)\right)^2}. \tag{1.38}$$

As can be seen, both U_{eff} and $\mathsf{H}_{\mathrm{M,eff}}$ get the same dependence on θ_{eff} and $\Delta m^2_{\mathrm{eff}}$ as U and H_{M} on θ and Δm^2 in vacuum, after subtracting the global phase $-\Delta m^2/2$, irrelevant for oscillations. Therefore, the probability equations (1.31) and (1.32)

can be used, changing the oscillation parameters in vacuum with the effective ones.

A mixing angle of value $\theta = \pi/4$ is called *maximal* because, as appreciated e.g. in Eq. (1.31), the amplitude of the oscillations is maximal. This means that a neutrino with energy E, generated with flavour α, would have a 100% probability of being detected with flavour $\beta \neq \alpha$ at a certain distance $L = 2E(2n+1)\pi/\Delta m^2$. In this sense, the presence of matter can enhance oscillations up to maximal values, turning any non-zero mixing angle in vacuum θ, even a tiny one, into $\theta_{\text{eff}} = \pi/4$ when the number density of electrons fulfils the condition

$$n_{e,\text{res}} = \frac{\Delta m^2 \cos(2\theta)}{2\sqrt{2}EG_{\text{F}}}, \tag{1.39}$$

as can be obtained from Eq. (1.37). This resonant condition reflects in the difference of the squared masses (1.38) as well, which gets a minimal value a factor $\sin(2\theta)$ smaller than in vacuum, therefore maximising the oscillation length with respect to that when no matter is present. Figure 1.2 shows this resonant effect and the further suppression of flavour oscillations when the density of the medium is larger than the resonant density (1.39).

When the density is not constant, oscillations are affected in a different way. Similar to relation (1.3), when a neutrino evolves in a medium, the flavour eigenstates can be expressed as a linear combination of *instantaneous* mass eigenstates,

$$|\nu_\alpha\rangle = \sum_k U^*_{\alpha k,\text{eff}} \, |\nu_{k,\text{eff}}\rangle \,, \tag{1.40}$$

with the instantaneous effective masses of $|\nu_{k,\text{eff}}\rangle$ being those resulting from the diagonalisation of (1.29) without subtraction of global phases, for the given (instantaneous) potential associated to the corresponding density of the medium at that specific point. The effective (also instantaneous) mixing matrix is the unitary transformation that diagonalises the hamiltonian for that value of the potential,

$$U^\dagger_{\text{eff}} \mathsf{H}_{\text{F}} U_{\text{eff}} = \mathsf{H}_{\text{M,eff}}. \tag{1.41}$$

Defining $\Phi_\alpha(L)$ as the vector of the amplitudes $\langle \nu_k | \nu_\alpha(L) \rangle$, for a fixed flavour α and with elements running in the values of the mass states k, then

$$\Psi_\alpha(L) = U_{\text{eff}}(L) \Phi_\alpha(L), \tag{1.42}$$

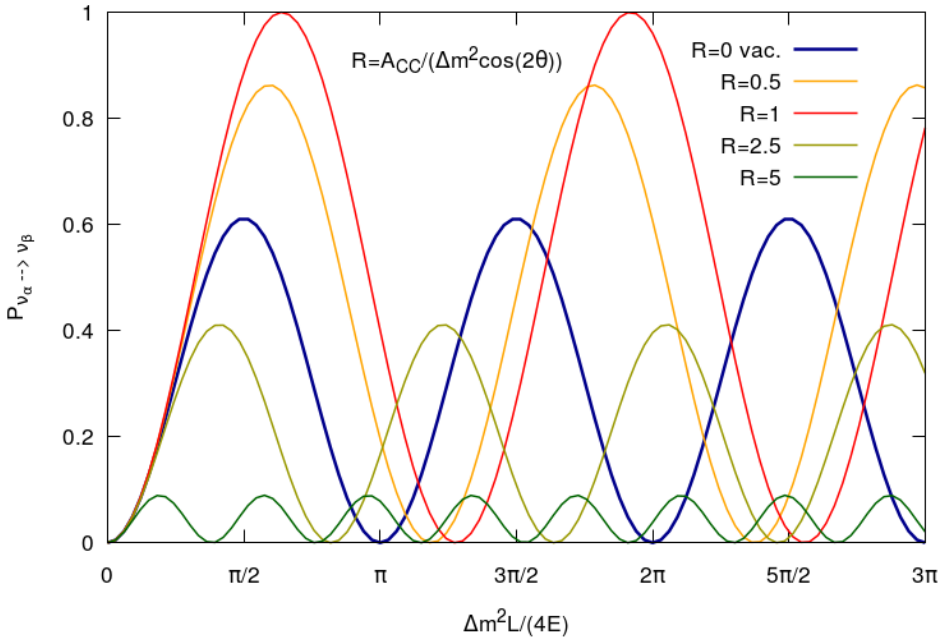

Figure 1.2: Conversion probability in the presence of a constant matter background of electrons, for different values of $A_{\rm CC}$. A two-neutrino picture with mixing angle $\theta = \pi/7$ in vacuum is assumed.

where the effective oscillation parameters depend on the neutrino position L for a varying density. This leads to

$$\partial_L \left(U_{\rm eff}(L)\Phi_\alpha(L) \right) = \dot{U}_{\rm eff}(L)\Phi_\alpha(L) + U_{\rm eff}(L)\dot{\Phi}_\alpha(L), \tag{1.43}$$

where the dot denotes the derivation with respect to L. Therefore, from Eq. (1.28) we have

$$i\dot{\Phi}_\alpha(L) = \left(\mathsf{H}_{\rm M,eff}(L) - iU^\dagger_{\rm eff}(L)\dot{U}_{\rm eff}(L) \right) \Phi_\alpha(L). \tag{1.44}$$

From expression (1.44) we understand why it was convenient to express the effective flavour hamiltonian (1.33) in a traceless way. Since the trace is conserved under a unitary transformation, the second term in the right-hand side of Eq. (1.44) only enters in the non-diagonal elements, being the only one affecting them. When the variation of the number density of the medium is large enough, the non-diagonal terms coming from $-iU^\dagger_{\rm eff}(L)\dot{U}_{\rm eff}(L)$ can not be neglected with

respect to those of the diagonal that comes from the traceless $\mathsf{H}_{\mathrm{M,eff}}(L)$. Hence, from the definition of $\Phi_\alpha(L)$ we notice that a varying medium allows a non-zero probability of transition from a mass state to another, as a result of the effective mass states not being eigenstates of the hamiltonian for a fast enough variation of the medium number density.

This transition probability between mass states can be ignored when the change of the medium is slow enough so neutrinos oscillate many times before the medium density effectively changes. This translates into neglecting the effect of the non-diagonal terms. In this scenario, the change in the medium can be interpreted, from the point of view of an effective mass eigenstate, as a smooth, adiabatic transition through different effective mass states that can be treated as eigenstates of the effective hamiltonian at the current density of the medium.

In order to check whether the propagation of a neutrino through a varying medium is adiabatic, we can define the adiabaticity parameter[3] [11]

$$\eta = \frac{\left\langle \left| U_{\mathrm{eff}}^\dagger \dot{U}_{\mathrm{eff}} \right| \right\rangle}{\left\langle \left| \mathsf{H}_{\mathrm{M,eff}} - \frac{\mathrm{Tr}\left(\mathsf{H}_{\mathrm{M,eff}}\right)}{n} \mathbb{I} \right| \right\rangle}, \tag{1.45}$$

where n is the dimension of the squared matrix $\mathsf{H}_{\mathrm{M,eff}}$ ($n = 3$ in the standard case), $\langle \cdots \rangle$ indicates the average over the matrix indices and $\mathbb{I}$ is the identity matrix. When $\eta \ll 1$ the medium changes slowly with respect to the frequency of flavour oscillations. In this case the propagation is adiabatic. On the contrary, when $\eta \geq 1$ the effective mass states are far from behaving as eigenstates of the hamiltonian and the propagation is non-adiabatic, which enables a mixing in the mass eigenstates as well as in the flavour eigenstates.

In the two-neutrino approximation

$$\eta = 4E \left| \frac{\dot{\theta}_{\mathrm{eff}}}{\Delta m^2_{\mathrm{eff}}} \right|. \tag{1.46}$$

Again, despite its simplicity, this approximation is useful to show that when $\eta \ll 1$ the frequency of oscillations, ruled by $\Delta m^2_{\mathrm{eff}}$, is much larger than the change of the medium, guided by $\dot{\theta}_{\mathrm{eff}}$.

[3] As far as we know, the adiabaticity parameter has always been defined in the two-neutrino scheme, although sometimes as $\gamma = \eta^{-1}$. The definition (1.45), here extended to a generic number of neutrinos, was first introduced in the appendix A of reference [11] for a three-neutrino scheme.

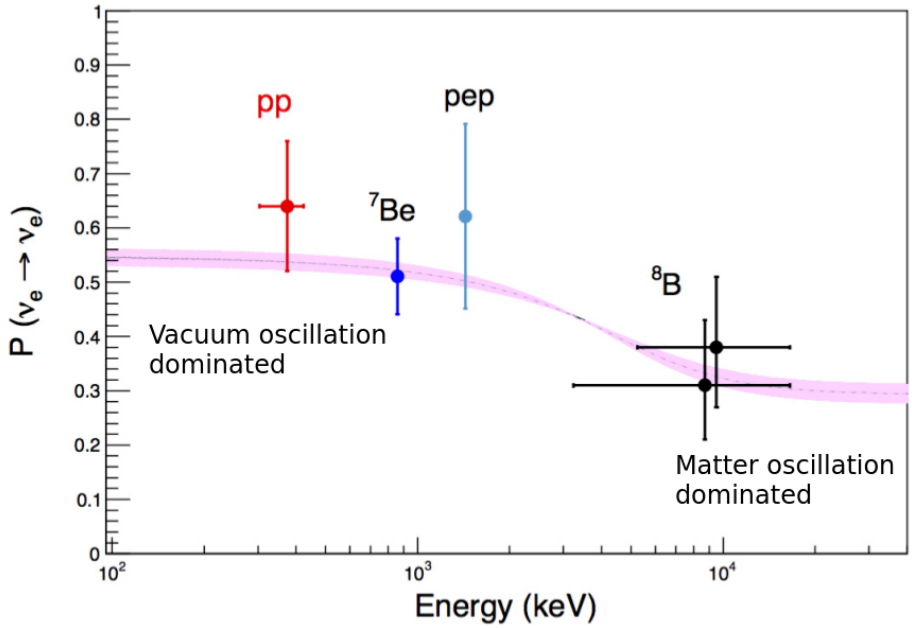

Figure 1.3: Solar electron neutrino survival probability at the Earth for different energies. Points are data from Borexino measurements. The MSW effect is observed in the region $E_\nu \gtrsim 2\,\text{MeV}$. Figure inspired from [12].

Contrary to what one could think, a varying medium can have an imprint in the oscillation pattern even when a neutrino propagates adiabatically, especially when it goes through a resonant region. In the two-neutrino scheme, for instance, electron neutrinos produced in the interior of the Sun are generated inside a medium with densities much higher than the resonant one (1.39) for the largest energies of their distribution. This high density leads to an effective angle $\theta_{\text{eff}} \approx 90°$, which implies that $\nu_e \approx \nu_2$ (see Eqs. (1.35) and (1.37)). Instead, since in vacuum $\theta_{12} \sim 35°$ [7], a ν_e is mostly generated as a ν_1. Because the propagation through the Sun at the energies in which solar neutrinos are produced (from $\sim 1\,\text{keV}$ to $\sim 10\,\text{MeV}$) is adiabatic, they leave the star in the same mass eigenstate that they were generated. Thus, when they reach the Earth, after propagating through the empty space[4], they are detected in a different flavour composition depending on their energy (see Fig. 1.3). This effect was originally studied by

[4]Although in a secondary way, Earth matter effects can also be measured in solar neutrinos through a day-night asymmetry. We explain this in more detail in section 1.4.1.1.

S. P. Mikheev, A. Yu. Smirnov and L. Wolfenstein [13–15], and it is known as the *MSW effect*. For $\Delta m^2 \sim 10^{-4}\,\mathrm{eV}^2$ and solar densities, the MSW resonance happens at a neutrino energy of $\sim 2\,\mathrm{MeV}$, giving rise to different probabilities below and above that energy.

The presence of matter can have further consequences, even less trivial than those discussed here, as the *parametric resonance*, for example (see e.g. Ref. [16] and references therein). However, their discussion is beyond the scope of this thesis. In what follows, we focus in the next section on the role of different experiments in the determination of the oscillation parameters.

1.4 Neutrino oscillation parameters

In the three-neutrino scenario, the free hamiltonian and effective potential matrices of Eq. (1.29) take the form

$$\mathsf{H}_{\mathrm{M}} = \frac{1}{2E}\begin{pmatrix} 0 & 0 & 0 \\ 0 & \Delta m^2_{21} & 0 \\ 0 & 0 & \Delta m^2_{31} \end{pmatrix}, \qquad \mathsf{V} = \begin{pmatrix} V_{\mathrm{CC}} & 0 & 0 \\ 0 & 0 & 0 \\ 0 & 0 & 0 \end{pmatrix}, \tag{1.47}$$

and the mixing matrix depends on three mixing angles θ_{ij} and a phase δ related to CP violation. It is commonly parameterised as

$$U = \begin{pmatrix} c_{12}c_{13} & s_{12}c_{13} & s_{13}\mathrm{e}^{-i\delta} \\ -s_{12}c_{23} - c_{12}s_{23}s_{13}\mathrm{e}^{i\delta} & c_{12}c_{23} - s_{12}s_{23}s_{13}\mathrm{e}^{i\delta} & s_{23}c_{13} \\ s_{12}s_{23} - c_{12}c_{23}s_{13}\mathrm{e}^{i\delta} & -c_{12}s_{23} - s_{12}c_{23}s_{13}\mathrm{e}^{i\delta} & c_{23}c_{13} \end{pmatrix}, \tag{1.48}$$

where $c_{ij} = \cos\theta_{ij}$ and $s_{ij} = \sin\theta_{ij}$, and it can also be expressed as a product of three rotations,

$$U = \begin{pmatrix} 1 & 0 & 0 \\ 0 & c_{23} & s_{23} \\ 0 & -s_{23} & c_{23} \end{pmatrix} \begin{pmatrix} c_{13} & 0 & s_{13}\mathrm{e}^{-i\delta} \\ 0 & 1 & 0 \\ -s_{13}\mathrm{e}^{i\delta} & 0 & c_{13} \end{pmatrix} \begin{pmatrix} c_{12} & s_{12} & 0 \\ -s_{12} & c_{12} & 0 \\ 0 & 0 & 1 \end{pmatrix}. \tag{1.49}$$

From these equations we see that neutrino oscillations in vacuum depend on six parameters: two differences of squared masses Δm^2_{21} and Δm^2_{31}; three mixing angles θ_{12}, θ_{23} and θ_{13}, and one CP-violating phase δ. None of them exists in the standard model (SM) of particle physics and have to be determined experimentally.

As we have already mentioned, it is found that the two differences of squared masses differ in almost two orders of magnitude, which makes the two-neutrino picture a good approximation. Therefore, from Eqs. (1.31) and (1.32) it is easy to see that experiments with diverse characteristics are sensitive to different oscillation parameters. In particular, the mixing angles θ_{23}, θ_{13} and θ_{12} appearing respectively in the first, second and third matrices of expression (1.49) are commonly known, also respectively, as *atmospheric*, *reactor* and *solar* angles. These parameters are named after the type of neutrino oscillation experiments in which they are the dominant accessible mixing angles.

The atmospheric angle θ_{23} mostly enters in oscillations involving a ν_μ, the most common neutrino flavour produced in the atmosphere and in long-baseline (LBL) accelerators. On the other hand, due to the specific energies of the electron antineutrinos released in nuclear reactors ($\mathcal{O}\,(\mathrm{MeV})$), detectors placed at close distances from a reactor are sensitive to oscillations weighted predominantly by θ_{13}. For both types of neutrino sources, the frequency of flavour oscillations is controlled by the squared mass difference $\Delta m^2_{32} \approx \Delta m^2_{31}$, almost two orders of magnitude larger than Δm^2_{21}. This fact is advantageous in experiments where the fraction L/E (where L is the distance covered by a neutrino with energy E) is small enough to be sensitive only to the fastest oscillations.

The third mixing angle, the so-called solar angle θ_{12}, is accessible in experiments that are sensitive to the oscillations driven by Δm^2_{21} and mostly related to electron-flavour neutrinos travelling long distances. This is the reason why solar neutrino experiments are good in measuring these two parameters. An exception worth mentioning is KamLAND, a reactor neutrino experiment whose average distance, two orders of magnitude larger than those in other reactor experiments, makes it sensitive to a fraction L/E more suited to study the "solar" parameters.

Finally, the CP-violating phase δ changes sign in the probability equations for neutrinos and antineutrinos. Therefore, in order to measure it, a good distinction between particles and antiparticles is needed. This is easily achieved in accelerator experiments, which can switch between neutrino and antineutrino modes. At present, the best constraint to δ comes from T2K, an experiment of this kind.

If neutrinos are Majorana particles, two other phases (let us call them α_1 and α_2) need to be considered and the mixing matrix in Eq. (1.49) should be modified as

$$U_{\text{Majorana}} = U \times \mathrm{diag}\left(1, \mathrm{e}^{-i\alpha_1}, \mathrm{e}^{-i\alpha_2}\right). \tag{1.50}$$

However, since both U and $U^\dagger$ enter in neutrino oscillations (Eq. (1.29)), the Majorana phases have no effect in the oscillatory patterns and we will not care about them along this thesis.

The current determination of the parameters is surprisingly accurate. However, there are still some important questions to answer. To be more specific, we do not know yet the order of neutrino masses, the octant of the mixing angle θ_{23} and whether the value of δ leads towards CP violation in the neutrino sector. The first point is particularly important since it affects the sum of the neutrino masses, a parameter to which the evolution of the Universe is sensitive. The ambiguity comes from the sign of Δm^2_{31}. By definition $\Delta m^2_{21} > 0$, and $|\Delta m^2_{31}| \gg \Delta m^2_{21}$; for this reason, the two possibilities for the order of neutrino masses are: a) $m_1 < m_2 < m_3$, which is known as the *normal ordering* (NO) of neutrino masses, and b) $m_3 < m_1 < m_2$, which receives the name of *inverted ordering* (IO). Regarding the second point, since θ_{23} mainly enters flavour oscillations through a term proportional to $\sin^2(2\theta_{23})$, it is difficult to establish experimentally whether its value, close to the maximal 45°, is actually smaller (first octant) or larger (second octant) than maximal. A discussion on the current status of these unknowns, from the particular point of view of the results presented in the global fit [7], is presented in section 1.4.3.

The rest of the section is devoted to review the role of the different type of neutrino oscillation experiments in the determination of flavour oscillation parameters. We list in table 1.1 all those that we use in our global fit. In subsection 1.4.1 we briefly describe solar, reactor and accelerator experiments, while in subsection 1.4.2 we focus on the part in which the author has a major contribution, namely the role of large-volume neutrino telescopes in the measurement of the parameters of the atmospheric sector.

1.4.1 Results from solar, reactor and accelerator experiments

In this section we describe the solar, reactor and accelerator experiments included in the global fit [7]. First we concentrate on those focused on the determination of the solar parameters θ_{12} and Δm^2_{21}; later we discuss the sensitivity to θ_{13} as well as Δm^2_{31} from reactor experiments, and finally we mention the results from LBL accelerator experiments, including the current status of the measurements of δ.

1.4.1.1 Solar experiments

Solar neutrinos are generated in the thermonuclear reactions produced in the inner shells of the Sun, and they are usually named after the source reaction leading to their different energy spectrum. There are two main nuclear chains in which neutrinos are produced: the proton-proton (*pp*) chain, to which the

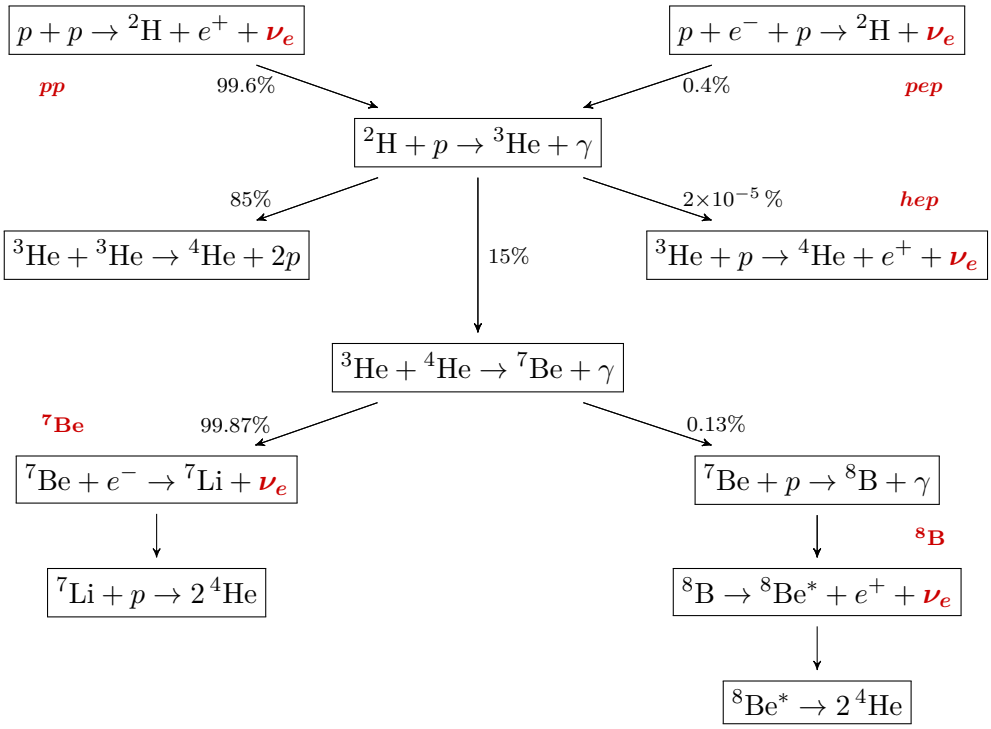

Figure 1.4: The proton-proton (*pp*) chain in the Sun.

processes *pp*, *pep*, *hep*, ^{7}Be and ^{8}B belong (see Fig. 1.4), and the CNO cycle, whose main processes producing neutrinos are those starting from a ^{13}N, ^{15}O and ^{17}F (see Fig. 1.5). The different fluxes are shown in figure 1.6. In summary, all processes lead to the fusion reaction of four protons into a ^{4}He nucleus,

$$4p \to {}^4\mathrm{He} + 2e^+ + 2\nu_e + \gamma, \tag{1.51}$$

with an energy released of $Q = 4m_p - m_{^4\mathrm{He}} - 2m_e \simeq 26\,\mathrm{MeV}$, most of which is radiated into photons and only a small part into neutrinos, $\langle E_{2\nu_e} \rangle = 0.59\,\mathrm{MeV}$ [17].

Solar experiments are well suited to determine the values of θ_{12} and Δm^2_{21}. The first experiments devoted to measuring solar neutrinos were based on specific neutrino capture reactions, for which they received the name of *radiochemical experiments*. These were counting detectors, which measured the number of certain isotopes produced by specific neutrino reactions after a certain exposure time. Therefore, they have the drawback of not being able to work on real-

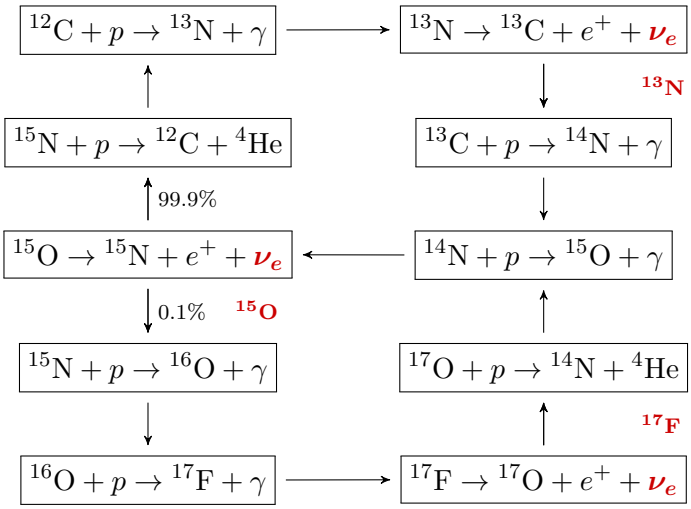

Figure 1.5: The CNO cycle in the Sun.

time. From this category we include data from the pioneering Homestake chlorine detector [20], which measured electron neutrinos through

$$\nu_e + {}^{37}\mathrm{Cl} \to {}^{37}\mathrm{Ar} + e^-; \tag{1.52}$$

from GALLEX/GNO [21], and finally from SAGE [22], both using the electron neutrino capture

$$\nu_e + {}^{71}\mathrm{Ga} \to {}^{71}\mathrm{Ge} + e^-. \tag{1.53}$$

Low-energy neutrinos from ^{7}Be measured in the real-time scintillator detector Borexino [23, 24] have also being included in the global fit. Signal events are produced in this experiment through neutrino elastic scattering with electrons,

$$\nu + e^- \to \nu + e^-. \tag{1.54}$$

In principle, all flavour eigenstates interact with electrons through elastic scattering, although the cross-section for $\nu_{\mu,\tau}$ is about 4.5 times lower than for ν_e at the working energies of Borexino [23].

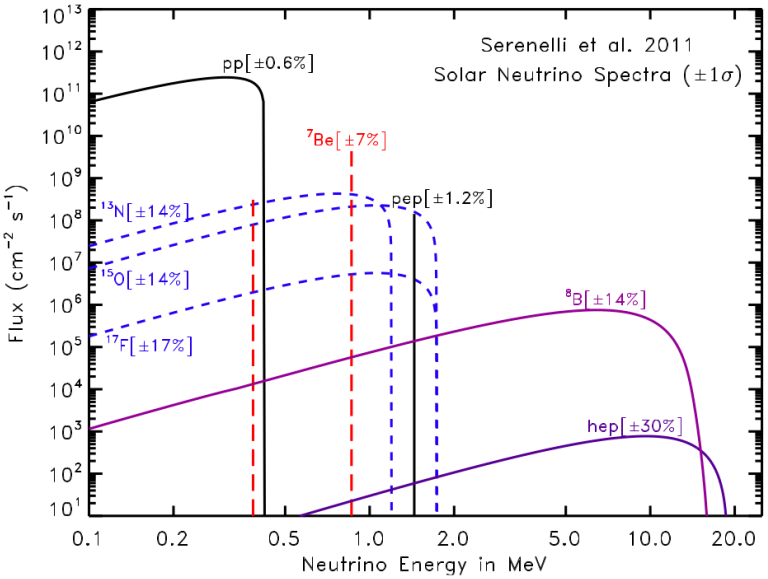

Figure 1.6: Solar neutrino fluxes from the solar model in Ref. [18]. Figure taken from [19].

The same reaction (1.54) is used to detect neutrinos in Super-Kamiokande (SK), which is still in operation, although this neutrino telescope[5] uses a different technique to see the passing of the weakly interacting particles; its walls are filled with photomultipliers (PMTs) that catch the Cherenkov light emitted when an accelerated charged lepton travels through the contained water at a larger speed than that of light inside the medium. Data from phases SK-I to SK-IV [25–29] are included in our analysis.

Another solar experiment whose detection technique was based on Cherenkov radiation was the Sudbury Neutrino Observatory (SNO). However, contrary to Super-Kamiokande, this experiment used heavy water (whose molecules contain deuterium instead of hydrogen) as a detection medium. This choice allowed the experiment to be sensitive to different channels when capturing solar neutrinos. Apart from elastic scattering with electrons (1.54), two other interactions were

[5]Whenever the word *telescope* is used in this document referring a neutrino detector, it means that it is a real-time detector with the ability to determine the event arrival direction. In the bibliography, however, the word *telescope* is usually reserved for large-volume neutrino detectors.

Solar		
Experiment	Detection method	Main source
Homestake	Radiochemical	^{8}B
GALLEX/GNO	Radiochemical	*pp*
SAGE	Radiochemical	*pp*
Super-Kamiokande	Cherenkov rad. (pure water)	^{8}B
SNO	Cherenkov rad. (heavy water)	^{8}B
Borexino	Scintillator	^{7}Be
Reactor		
Experiment	$\langle L \rangle$ near detectors	$\langle L \rangle$ far detectors
Daya Bay	$(350, 600)$ m	$(1500, 1950)$ m
RENO	294 m	1383 m
Double Chooz	400 m	1050 m
Long-baseline		
Experiment	$\langle E_\nu \rangle$	Baseline
K2K	1 GeV	250 km
MINOS	3 GeV	735 km
T2K	0.6 GeV	295 km
NOνA	2 GeV	810 km
Atmospheric		
Experiment	Energy range	Detection medium
Super-Kamiokande	Hundreds of MeV to tens of GeV	Pure water
ANTARES	$(20, 140)$ GeV	Sea water
IceCube DeepCore	$(6, 56)$ GeV	Polar ice

Table 1.1: List of experiments used in the global fit, with the most relevant characteristic for each type. For the solar experiment Borexino, we consider as main source the one used in the global fit, although it measures other fluxes. Moreover, Double Chooz has already taken data with the near detector, but we did not include them in the global analysis.

possible: a CC interaction of electron neutrino capture,

$$\nu_e + d \to p + p + e^-, \tag{1.55}$$

where d represents deuterium and p a proton, and a NC interaction where neutrinos of all flavours equally interact with deuterium nuclides, breaking them into

a neutron and a proton,

$$\nu + d \to n + p + \nu. \tag{1.56}$$

Thanks in particular to the NC reaction (1.56), SNO was able to solve the solar neutrino problem in favour of neutrino oscillations, showing that the solar neutrino flux for this particular channel agreed with theoretical expectations [30,31]. Data from this experiment are also included in the global fit.

As explained in section 1.2 and further commented in section 1.3, matter effects are important for solar neutrinos. The main impact comes from the Sun, as was shown in Fig. 1.3, but also the Earth affects oscillations. Solar neutrinos captured during nights have to traverse our planet to reach the detectors. This leads towards a day-night asymmetry

$$A_{\mathrm{D/N}} = 2\left(\frac{\phi_{\mathrm{D}} - \phi_{\mathrm{N}}}{\phi_{\mathrm{D}} + \phi_{\mathrm{N}}}\right), \tag{1.57}$$

where the difference between the day flux ϕ_{D} and the night one ϕ_{N} can only be seen with real-time telescopes, like Super-Kamiokande or SNO. Radiochemical experiments are based on a counting technique after some exposure time; therefore, they are blind to the day-night asymmetry. The measurement of $A_{\mathrm{D/N}}$ from SK-IV data leads to a value [32]

$$A_{\mathrm{D/N}} = (-3.6 \pm 1.6(\mathrm{stat.}) \pm 0.6(\mathrm{syst.}))\,\%. \tag{1.58}$$

From solar experiments alone, we obtain a combined measurement of solar parameters

$$\theta_{12} = \left(35.4^{+1.2}_{-1.0}\right)^{\circ}, \tag{1.59}$$

$$\Delta m^2_{21} = \left(5.04^{+1.17}_{-0.89}\right) \cdot 10^{-5}\,\mathrm{eV}^2. \tag{1.60}$$

These measurements are further improved when we include KamLAND results. However, since it is a reactor experiment, we will discuss it at the beginning of the next subsection.

1.4.1.2 Reactor experiments

A large amount of electron antineutrinos are released in the fission processes inside nuclear power reactors, that have being used since the first attempt to capture these elusive particles. Actually, the first detected neutrinos came from a reactor and left their signal in a detector developed by a team led by F. Reines and C.L. Cowen in 1956.

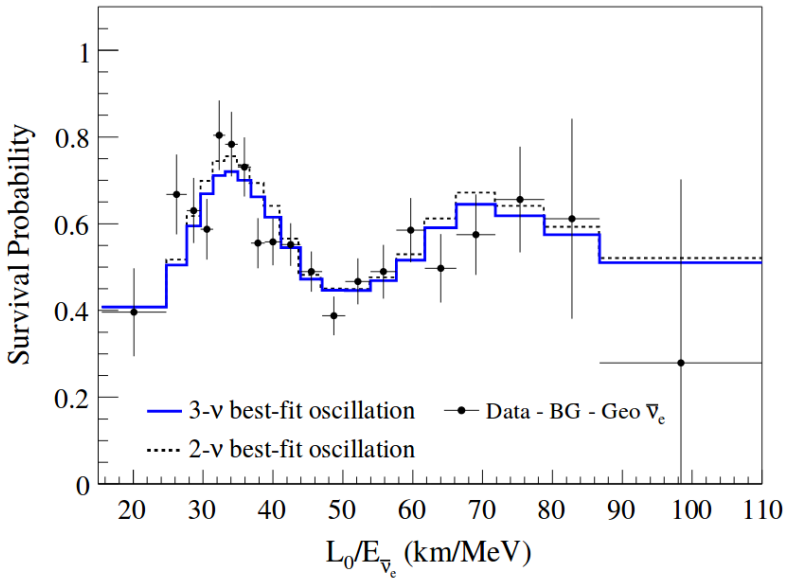

Figure 1.7: Survival probability $P_{\bar{\nu}_e \to \bar{\nu}_e}$ as a function of the neutrino energy $E_{\bar{\nu}_e}$ for the flux-weighted average distance $L_0 = 180\,\text{km}$. Data points, measured by KamLAND [33], correspond to the ratio of the observed antineutrino spectrum to the non-oscillated expectation, including background and geologically produced antineutrinos (geo-$\bar{\nu}_e$). Lines show the best fit for a three- and two-neutrino oscillation scheme. Figure taken from [33].

The first reactor experiment we are going to mention is rather peculiar. It is the case of KamLAND, which is the only reactor neutrino experiment devised to measure the solar neutrino oscillation parameters θ_{12} and Δm^2_{21} so far.[6] This goal was accomplished by placing a single detector at a flux-weighted average distance of 180 km from the 56 Japanese nuclear power reactors. The long distance, together with neutrino energies of the order of a few tenths of MeV, led to a clear picture of the low-frequency oscillatory pattern, as shown in Fig. 1.7. A two-neutrino oscillation fit is also present in the figure, from which we notice once more the utility of this approximated scheme. Thanks to KamLAND and the previous results from SNO, the picture of flavour oscillations was firmly consolidated.

[6] In the future, the Jiangmen Underground Neutrino Observatory (JUNO) will also be one of such experiments.

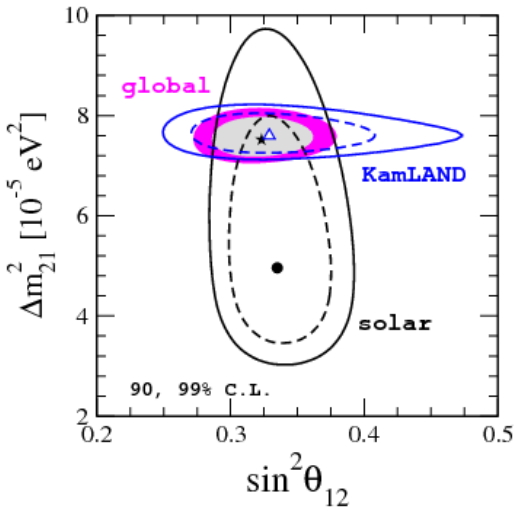

Figure 1.8: 90% and 99% CL regions for the solar neutrino oscillation parameters. Black lines correspond to the solar experiments, blue lines to the results of KamLAND and the coloured regions to the combined global-fit results [7]. The dot, triangle and star represent their best-fit values, respectively.

The last results from KamLAND [33] are used in our global fit, leading to a joint measurement with solar experiments of

$$\theta_{12} = \left(34.5^{+1.2}_{-1.0}\right)^\circ, \tag{1.61}$$

$$\Delta m^2_{21} = \left(7.55^{+0.20}_{-0.16}\right) \text{ eV}^2. \tag{1.62}$$

Some tension is currently present in the measurement of Δm^2_{21}, as exhibited in Fig. 1.8.

Other reactor experiments focus on the determination of the so-called reactor angle θ_{13}, as well as the squared mass difference Δm^2_{31}. In order to achieve this purpose and because of the larger frequency of these oscillations, they need to place the detectors much closer to the reactors than in KamLAND. Instead of having a single detector placed at almost 200 km away from the nuclear reactors, the other experiments of this type that we include in the global fit have two detector locations, a near one at around 0.3 km from the reactors, and a far location at a distance of about 1.4 km, with some variations in both sides depending on the

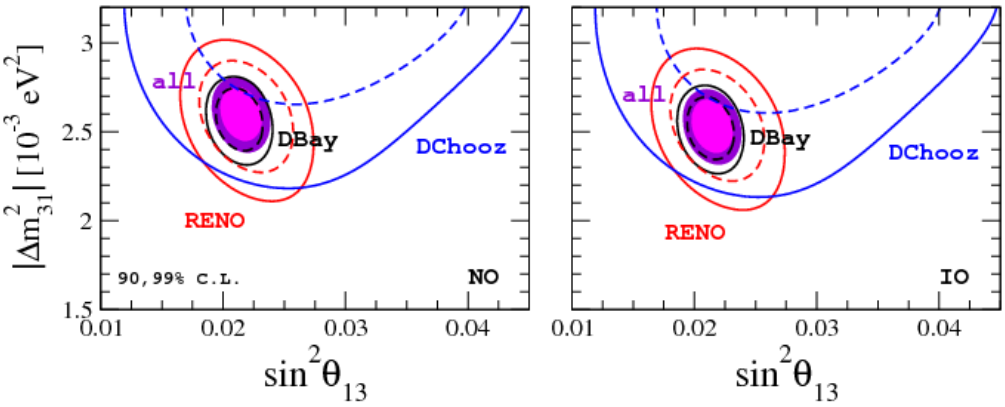

Figure 1.9: 90% and 99% CL regions for reactor neutrino oscillation parameters. Red, blue and black lines correspond to RENO, Double Chooz and Daya Bay experiments, respectively. Coloured regions show the combined global-fit results [7]. Results are presented for both normal (left panel) and inverted (right panel) mass orderings.

experiment (see Tab. 1.1). The number of detectors needed in those experiments is therefore at least two.

We consider the last available data from RENO [34–36], Daya Bay [37] and Double Chooz [38, 39]. We do not include data from older reactor experiments since they only give upper bounds on θ_{13}. Results from a joint analysis of reactor experiments are shown in Fig. 1.9, where we can appreciate that the measurement of reactor neutrino oscillation parameters is clearly dominated by Daya Bay.

1.4.1.3 Long-baseline accelerator experiments

Beams of neutrinos can be produced in accelerators by pion, kaon and muon decay whose parent particles are created by a proton beam hitting a target. The accelerators of all experiments included in the global fit [7] work as pion decay in flight neutrino accelerators, in which muon neutrinos and antineutrinos are produced in the decay of pions and kaons in a tunnel. A particle or antiparticle beam is chosen by changing the polarity of the magnetic horn that focalise the parent particles.

Apart from the possibility of choosing a neutrino or antineutrino beam, the use of an accelerator also guarantees a good treatment of how narrow the flux is wanted around the selected energy. In order to boost this characteristic into almost monochromatic beams, NOνA and T2K have placed the far detector off-

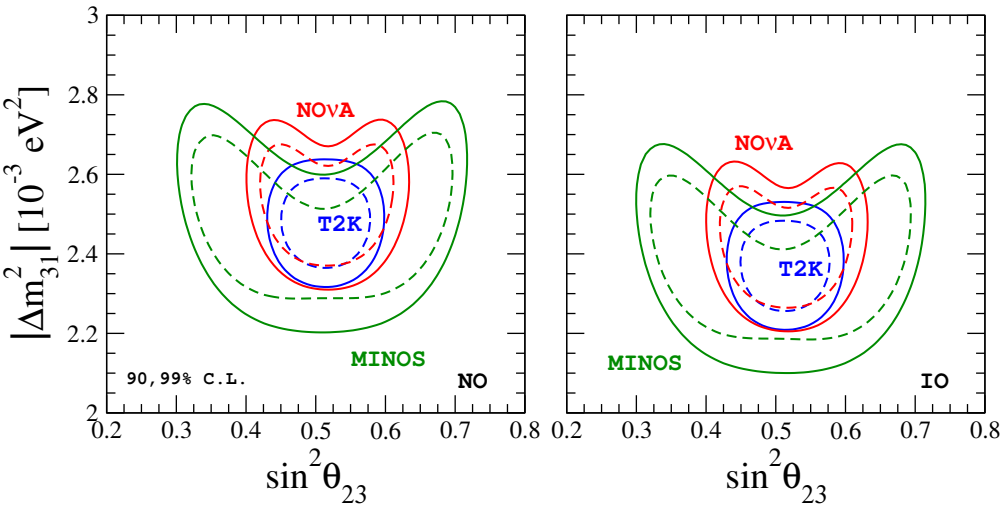

Figure 1.10: 90% and 99% CL regions in the $|\Delta m^2_{31}| - \sin^2\theta_{23}$ plane from long-baseline accelerator experiments. Red, blue and green lines correspond, respectively, to NOνA, T2K and MINOS accelerator experiments. Results are shown for both normal (left panel) and inverted (right panel) mass orderings.

axis, ensuring a narrower neutrino beam peaked at the desired energy. Near detectors are used in accelerator experiments, as in the case of reactor neutrino experiments, to control the properties of the neutrino beams and reduce systematics.

The long baseline, up to 810 km in the case of NOνA, is useful to gain some sensitivity in the neutrino mass ordering, though currently very small, thanks to Earth matter effects. Because neutrinos are mostly produced as muon-flavour particles in the accelerators, these experiments are sensitive to the atmospheric mixing angle θ_{23}, as well as to Δm^2_{31}. Thanks to the possibility of choosing a neutrino or an antineutrino mode, some bounds can also be put on the CP-violating phase δ. At present, the best constraint from a single experiment comes from T2K, which is able to reach alone more than 3σ exclusion for some values of δ in IO.

We include in the global fit the final data from K2K [40], and the latest data from T2K [41–43], NOνA [44–46] and MINOS [47–49]. Sensitivity plots to Δm^2_{31} and $\sin^2\theta_{23}$ for the most recent LBL neutrino accelerator experiments are shown in Fig. 1.10.

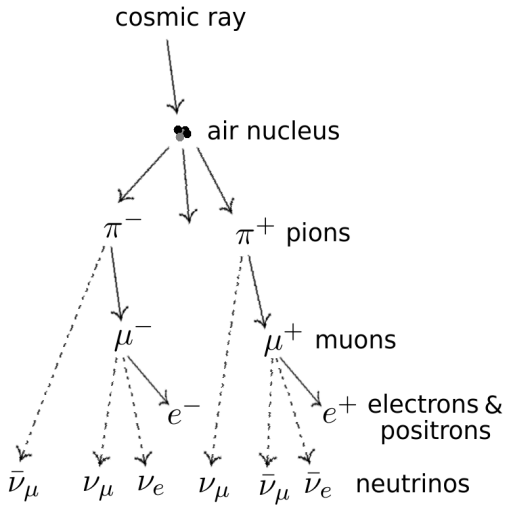

Figure 1.11: Schematic view of atmospheric neutrino production.

1.4.2 Atmospheric experiments and the role of large-volume neutrino telescopes

Atmospheric neutrinos are secondary particles resulting from the interaction of cosmic rays with the molecules in the atmosphere. This interaction generates cascades of particles with multiple charged pions and kaons, whose decay products give rise to muon and electron neutrinos (see Fig. 1.11). Because of its origin, the atmospheric neutrino spectrum is closely related to that of cosmic rays. At energies small enough for all parent particles to decay (E_ν smaller than several GeV), the neutrino spectrum is similar in power to the parent spectrum, turning into a steeper energy dependence at larger neutrino energies (see Fig. 1.12, left panel). Approximately twice as many ν_μ's are generated with respect to ν_e's, although this fraction increases with energy because muons reach the ground before decaying, while pions and especially kaons decay faster, still producing ν_μ's. The decay of parent particles is more prominent for vertical neutrinos, because the amount of atmosphere they can traverse is smaller before hitting the ground. All these details are depicted in the two panels of Fig. 1.12, where the energy and zenith angle dependence of atmospheric neutrino fluxes is represented. A deeper discussion about their properties and how to estimate atmospheric neutrino fluxes can be found, for instance, in [50].

Although most atmospheric neutrinos come from π and K decay, the tail of their energy distribution includes the contribution from the decay of heavy (in

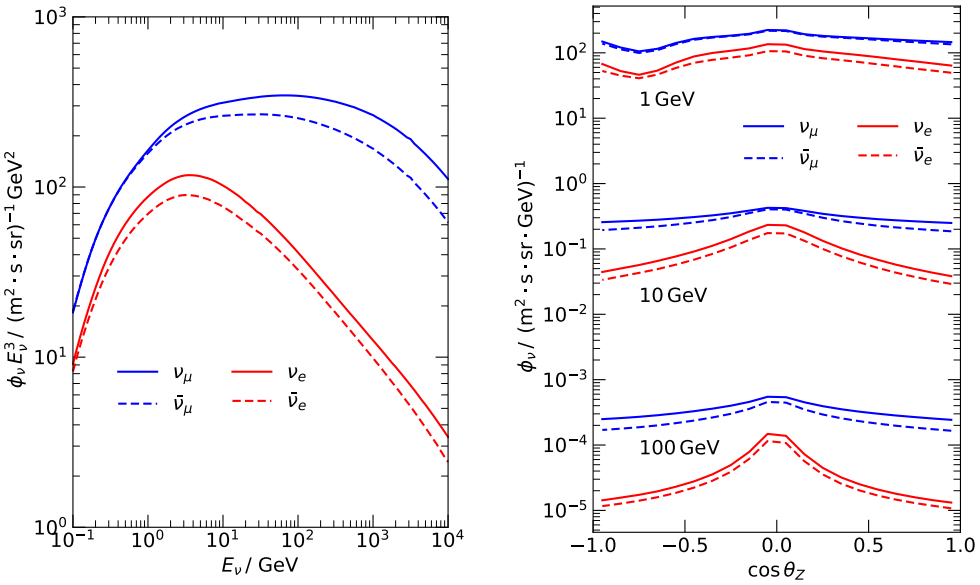

Figure 1.12: Atmospheric neutrino fluxes at the South Pole for minimum solar activity as obtained from the model in [51, 52]. Left: energy dependence of the zenith and azimuth angles averaged fluxes. Right: dependence on the cosine of the zenith angle of the azimuth angle averaged fluxes, for three chosen energies.

particular charmed) hadrons. Contrary to the *conventional* flux (from π and K decay), the *prompt* flux (from heavy hadrons decay) is predicted to dominate at very large energies, larger than a PeV. Only very large-volume neutrino telescopes (VLVNTs) have the ability to detect such energetic neutrinos and, at present, only IceCube is prepared to do so, although ARCA from KM3NeT and GVD (Gigaton Volume Detector) will join very soon. However, in spite of the few tens of high-energy neutrinos detected by IceCube [53], this prompt contribution to atmospheric neutrino fluxes has not been detected so far. The origin of the highest energetic events seen in IceCube is still under debate[7] and both galactic and extragalactic sources are studied. Although the two sources are expected to contribute to the high-energy neutrino flux, the extragalactic component is found to dominate over the galactic one [56, 57].

[7]Recently, blazars have been confirmed as one of the sources by the coincident location signal in high-energetic neutrinos, gamma rays and cosmic rays by IceCube, Fermi-LAT and MAGIC, respectively [54, 55], among other experiments.

From the point of view of studying neutrino oscillations, however, only energies below $\sim 100\,\text{GeV}$ are important, because more energetic neutrinos do not have time to oscillate since the frequency of flavour oscillations are proportional to E_ν^{-1}. In particular, future large-volume neutrino telescopes (LVNTs) are centred on the energy range covering the Earth matter resonant effects, at about $(4, 8)$ GeV, which helps these experiments to disentangle the problem of the neutrino mass ordering. For instance, ORCA, the telescope of the KM3NeT collaboration devoted to oscillation research, might have a 5σ determination in the most propitious scenario (NO and second octant for θ_{23}) in less than three years [58]. Since the sensitivity of the detector depends on the true value of θ_{23} and the true neutrino mass ordering, in less favourable conditions we might need to wait a bit longer for a 5σ resolution. This neutrino telescope, together with PINGU (a proposed update of IceCube [59]), reduces the energy threshold needed for a neutrino event identification by instrumenting the detection medium in which they are built with denser arrays of digital optical modules (DOM, the detection units in which the PMTs are placed).

Besides the possibility of studying the neutrino mass ordering, another aspect that makes neutrinos produced in the atmosphere worth studying is their varying long baseline, especially when there is a good directional resolution available. If this is achieved, a good sensitivity of atmospheric neutrino oscillation parameters can be accomplished even at energies above the resonance.

As we have mentioned above, atmospheric neutrinos are accompanied by lots of muons produced in the same cosmic-ray interactions. The large amount of atmospheric μ's constitutes the worst source of background for experiments trying to catch atmospheric neutrinos. However, since muons can not traverse the Earth, contrary to neutrinos, this background can be almost completely eliminated if only those events with reconstructed zenith angle $\theta_z > 90^\circ$ (i.e. up-going) are selected.

We include data from three neutrino telescopes in the global fit [7]: SK, ANTARES and IceCube. Among the three, SK is the smallest but denser in PMTs. This makes it sensitive to neutrinos from sub-GeV energies (hundreds of MeV) to several tens of GeV. However, its size is too small to accumulate enough statistics, and its detection technique, based on measuring the deposited energy through the light of Cherenkov rings in the detector walls, is not enough to make a good discrimination of the neutrino type at large energies. The analysis of Super-Kamiokande data is very complicated from the information publicly available; therefore, although we include the most recent results from SK (phases

I to IV) [29], we have not made the simulation ourselves, adding instead to the global fit the χ^2 tables provided by the collaboration.

In the following subsections we discuss the analysis of the atmospheric events measured in the LVNTs ANTARES [60] and IceCube DeepCore [61, 62], the two relevant analyses for the contribution to the global fit [7] during the development of the present thesis.

1.4.2.1 Analysis of atmospheric neutrinos from ANTARES

ANTARES is a large-volume neutrino telescope located in the Mediterranean sea. Its detection technique, as in SK, is based on capturing the light emitted by Cherenkov radiation when a charged particle travels through a medium at a larger speed than light in the same medium. The particles in question can not be the neutrinos themselves, since they are electrically neutral, but the associated charged leptons produced in their interaction with the nucleons of the medium's molecules. ANTARES uses the sea water as detection material and it consists of 12 lines with 75 digital optical modules each. At the same time, each DOM contains a big PMT able to catch the photons emitted by Cherenkov radiation. To avoid as much background from atmospheric muons as possible, the detector lines are anchored at the sea floor, covering a height of 350 m at a depth of 2.5 km. The separation between neighbouring lines is about 70 m, and its exact position, that can change depending on the sea currents, is regularly monitored with a LED-based calibration system.

Different neutrino interactions with sea water particles develop different topologies, which allows, to some extent, to distinguish between neutrino flavours. In particular, we will differentiate between *tracks* and *showers*. Such discrimination is better at larger energies, but it can also be applied to the energies detected by ANTARES. When a muon neutrino interacts through CC, a muon is produced, moving faster than light in the sea water. This long-lived lepton travels large distances inside the detector before losing all its energy, giving rise to an elongated signal in form of a track and, consequently, allowing a good angular resolution. At energies larger than the ones we are going to consider, muons may even leave the fiducial volume of the telescope before depositing all its energy, what makes impossible an accurate estimation of the original neutrino energy. However, this is not the case for the energies of the atmospheric events that are important when determining neutrino oscillation parameters, smaller than about $\sim 100\,\text{GeV}$.

On the other hand, for CC interactions of electron neutrinos, or for any NC interaction, independently of the neutrino flavour, electromagnetic and hadronic showers are produced and the neutrino energy is distributed among several par-

ticles that release it faster than in CC-ν_μ interactions. This topology features a worse angular resolution than tracks.

The distance between lines imposes a threshold in the detected neutrino energy of about 50 GeV. However, neutrino oscillations for atmospheric baselines are better seen at smaller energies. Since the distances between DOMs belonging to the same line are smaller than between lines, in order to reduce the energy threshold the analysis is divided in two samples: a single-line sample, constituted by vertical up-going events whose Cherenkov light is detected by a single line, and a multi-line sample, when more than one line detects light. In this way the energy threshold is reduced to 20 GeV.

The analysis is done following the procedure described in [60], including numerical three-neutrino oscillations with Earth matter effects. A χ^2 is computed, comparing experimental data with theoretical estimations for a 24-binned data count in terms of $E_{\nu,\mathrm{rec}}/\cos\theta_{z,\mathrm{rec}}$ (where $E_{\nu,\mathrm{rec}}$ is the reconstructed neutrino energy and $\cos\theta_{z,\mathrm{rec}}$ the reconstructed cosine of the zenith angle), in the range $[20, 140]$ GeV, plus an overflow bin including the events with $E_{\nu,\mathrm{rec}}/\cos\theta_{z,\mathrm{rec}} > 140$ GeV,

$$\chi^2 = \sum_i \left(\frac{N_i - (1-\epsilon)N^{\mathrm{1L}}_{\mathrm{MC},i} - (1-\eta)N^{\mathrm{ML}}_{\mathrm{MC},i}}{\sigma_i} \right)^2 + \left(\frac{\epsilon - \eta}{\sigma_R} \right)^2 . \tag{1.63}$$

In this construction, N_i is the data count for the i-th bin; $N^{\mathrm{1L}}_{\mathrm{MC},i}$ and $N^{\mathrm{ML}}_{\mathrm{MC},i}$ are the theoretical estimations for single and multiple line events, respectively; σ_i is the statistical uncertainty per bin, and finally ϵ and η are pull factors that take into account systematic uncertainties affecting the normalisation, and whose variation is restricted by σ_R.

The theoretical events are computed from a Monte Carlo (MC) sample of unoscillated neutrino events at detection level (including all needed detector information, such as effective volumes and resolutions), provided by the ANTARES collaboration[8]. Then, we weight the simulated fluxes, in an event-by-event basis, with the corresponding oscillation probabilities. In the simulations, the numerical integration in matter is performed using the Preliminary Reference Earth Model (PREM) [63].

Systematic effects are accounted for by ϵ and η, whose overall normalisations are left free, but we impose a constraint in $\epsilon - \eta$ (second term in the right-hand side of Eq. (1.63)). The shape of the $E_{\nu,\mathrm{rec}}/\cos\theta_{z,\mathrm{rec}}$ distribution can be affected

[8] Private communication.

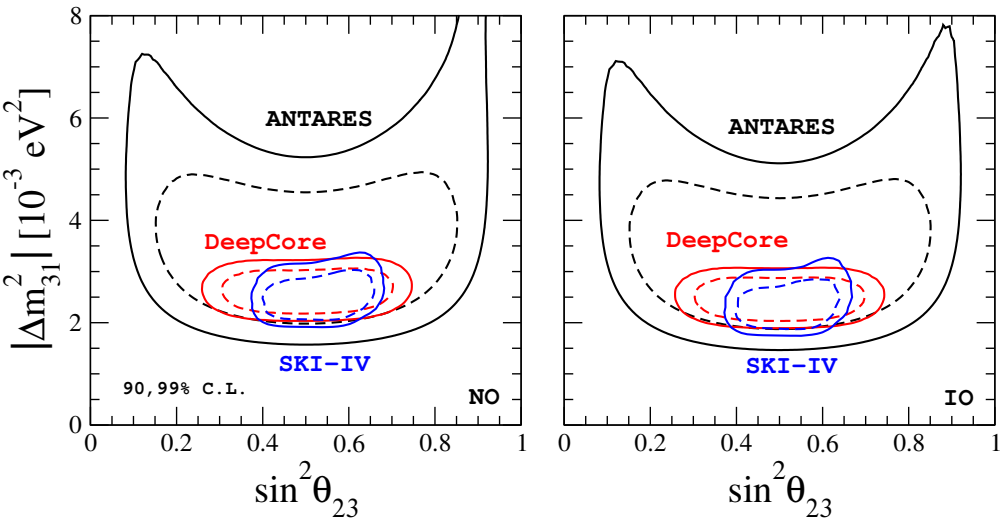

Figure 1.13: 90% and 99% CL regions in the $|\Delta m^2_{31}| - \sin^2\theta_{23}$ plane from atmospheric experiments. Black, red and blue lines correspond, respectively, to the neutrino telescopes ANTARES, IceCube DeepCore and Super-Kamiokande (phases I to IV). Results are shown for both normal (left panel) and inverted (right panel) mass orderings.

by a change in the ratio $N^{1L}_{MC,i}/N^{ML}_{MC,i}$; so we can translate this into

$$R(\epsilon,\eta) = \frac{N^{1L}_{MC,i}}{N^{ML}_{MC,i}}\frac{1+\epsilon}{1+\eta} \simeq \frac{N^{1L}_{MC,i}}{N^{ML}_{MC,i}}(1+\epsilon-\eta)\,, \tag{1.64}$$

where the last step is made assuming small ϵ and η. From this relation we get the second term in the right-hand side of Eq. (1.63). Finally, $\epsilon - \eta$ is constrained to vary with $\sigma_R = 0.05$, since the ANTARES collaboration found that, changing the relevant parameters in the Monte Carlo affecting the normalisations, the ratio (1.64) is stable within 5% of its original value [60].

In the end, from the analysis of the χ^2 in Eq. (1.63) we obtain the 90% and 99% confidence level (CL) regions shown in Fig. 1.13.

1.4.2.2 Analysis of atmospheric neutrinos from IceCube DeepCore

IceCube is the largest neutrino telescope ever built, covering an instrumented volume of 1 km^3 at the Amundsen-Scott South Pole Station. Following the same

detection technique as ANTARES, it exploits Cherenkov radiation to detect high-energy neutrinos, with the difference that it uses the ice of the South Pole as detection medium. It consists of a total of 86 strings set 125 m apart from their neighbours, each of them containing 60 DOMs with a vertical separation of 17 m and one PMT per DOM, and it is placed at a depth between 1450 m and 2450 m into the ice. The telescope was built to detect ultra-energetic neutrinos, which explains its energy threshold of about 100 GeV, too large to study neutrino oscillations. However, the analysis of neutrino oscillation parameters is performed thanks to a denser region inside IceCube, named DeepCore and with a horizontal and vertical spacing of about 70 m and 7 m, respectively, which comprises 8 of the total number of strings of IceCube. The energy range accessible for the analysis lies between 6.3 GeV and 56.2 GeV.

Even though IceCube has already taken more than 8 years of data with its full configuration, useful public information for neutrino oscillations is only given for the first three years of complete detector setup, with 86 strings [61, 62]. A new analysis has been performed by the collaboration, also for three years of data but shifted one year ahead [64]. However, there is no public information to reproduce this analysis, so we have not included these last results in the global fit. The analysis of the remaining years of operation has not been released by the collaboration yet.

The dataset that we analyse (corresponding to Refs. [61, 62]) is presented in a binned way, with a 8×8 grid in the reconstructed quantities $\log_{10}(E_{\rm rec}/1\,{\rm GeV})$ and $\cos\theta_{z,\rm rec}$, being $E_{\rm rec}$ the reconstructed energy and $\theta_{z,\rm rec}$ the reconstructed zenith angle of the neutrinos. Public information also provides tables with systematic detector uncertainties, including optical efficiencies that account for the uncertainties brought about during depletion of the DOMs, because of light scattering in the frozen water of the holes opened in the ice. Finally, effective areas including other detector properties and efficiencies, as well as neutrino cross sections and interactions when traversing the Earth, are also supplied [62].

We simulate the theoretical expectations varying the neutrino oscillation parameters θ_{23} and Δm^2_{31}, keeping the rest of parameters fixed to the best fit obtained from the other experiments. Among the systematics that we consider, those related to atmospheric neutrino fluxes are chosen to reproduce the uncertainties reported in [65]. Therefore, starting from unoscillated atmospheric fluxes [51, 52] $\phi_{\beta,0}$, with $\beta = \{e, \mu\}$, we compute neutrino fluxes at the detector as

$$\frac{{\rm d}^2\phi_\alpha}{{\rm d}\cos\theta_z {\rm d}E_\nu}(E_\nu, \cos\theta_z) = \mathcal{N}_\alpha \cdot \epsilon \cdot \left(\frac{E_\nu}{28\,{\rm GeV}}\right)^\gamma \sum_\beta P_{\nu_\beta \to \nu_\alpha} \frac{{\rm d}^2\phi_{\beta,0}}{{\rm d}\cos\theta_z {\rm d}E_\nu}, \quad (1.65)$$

where $\frac{\mathrm{d}^2\phi_{\beta,0}}{\mathrm{d}\cos\theta_z \mathrm{d}E_\nu}$, $P_{\nu_\beta\to\nu_\alpha}$ and ϵ also depend on the true values of neutrino energy E_ν and zenith angle θ_z. $\mathcal{N}_\alpha$ is a systematic accounting for the uncertainty on the flux normalisation, and

$$\epsilon\left(E_\nu, \cos\theta_z\right) = 1 + \delta_{\mathrm{uh}} \cdot \left(\cos\theta_z - \cos\theta_0\right)\left(1 + \frac{E_\nu - E_0}{E_1\left(1 + \mathrm{e}^{-\kappa(\cos\theta_z - \cos\theta_0)}\right)}\right) \quad (1.66)$$

regards the so-called up-horizon uncertainty, where $\cos\theta_0 = 0.4$, $E_0 = 360\,\mathrm{GeV}$, $E_1 = 11279\,\mathrm{GeV}$ and δ_{uh} is a parameter to be fit in the analysis, with a nominal value equal to zero. This systematic is included to account for energy and zenith variation effects in the atmosphere specially connected with its density. The functional form (1.66) is taken from [66]. We have also tested the effect on flux normalisations of systematics accounting for $\phi_{\nu_\alpha}/\phi_{\nu_\beta}$, with $\alpha \neq \beta$, and $\phi_{\nu_\alpha}/\phi_{\bar{\nu}_\alpha}$, and we found them to be negligible. Therefore, we only assume a single normalisation $\mathcal{N} = \mathcal{N}_e = \mathcal{N}_\mu = \mathcal{N}_\tau$.

We also include systematics provided by the collaboration regarding DOM efficiency and hole-ice photon scattering, that are given as polynomials of a parameter with coefficients depending on the bin of reconstructed variables. Absorbing them in the effective areas A_{eff}, the simulated number of events for a neutrino flavour α reads

$$\begin{aligned}\frac{\mathrm{d}^2 N_\alpha}{\mathrm{d}\cos\theta_{z,\mathrm{rec}}\,\mathrm{d}E_{\mathrm{rec}}} = 2\pi T \int_{-1}^{1} \mathrm{d}\cos\theta_z \int_0^\infty \mathrm{d}E_\nu \\ \times \sum_{p=\nu_\alpha,\bar{\nu}_\alpha} \frac{\mathrm{d}^2 A^p_{\mathrm{eff},\alpha}}{\mathrm{d}\cos\theta_{z,\mathrm{rec}}\,\mathrm{d}E_{\mathrm{rec}}} \frac{\mathrm{d}^2\phi^p_\alpha}{\mathrm{d}\cos\theta_z \mathrm{d}E_\nu},\end{aligned} \quad (1.67)$$

where the factor 2π comes from the integration in the azimuthal angle and T is the operational time. The sum in ν_α and $\bar{\nu}_\alpha$ is needed since IceCube is not able to distinguish the charge of the particle giving rise to Cherenkov radiation. The expression (1.67) implies a simulated number of events per reconstructed bin

$$N_{ij,\mathrm{th}} = \int_{\cos\theta_{z,\mathrm{rec},i}}^{\cos\theta_{z,\mathrm{rec},i+1}} \mathrm{d}\cos\theta_{z,\mathrm{rec}} \int_{E_{\mathrm{rec},j}}^{E_{\mathrm{rec},j+1}} \mathrm{d}E_{\mathrm{rec}} \sum_{\alpha=e,\mu,\tau} \frac{\mathrm{d}^2 N_\alpha}{\mathrm{d}\cos\theta_{z,\mathrm{rec}}\,\mathrm{d}E_{\mathrm{rec}}}. \quad (1.68)$$

Parameter	Best fit (NO)	Best fit (IO)	Nominal	Prior (μ, σ)
$\lvert\Delta m^2_{31}\rvert$ $[10^{-3}\,\mathrm{eV}^2]$	2.60	2.45	—	—
$\sin^2\theta_{23}$	0.56	0.54	—	—
DOM syst. par.	1.0	1.0	1.0	$(1.0, 0.1)$
hole ice syst. par.	0.02	0.02	0.02	$(0.02, 0.01)$
global norm. $\mathcal{N}$	0.96	0.96	1.0	—
spectral index γ	0.125	0.125	0.0	—
up-hor δ_{uh}	0.0	0.0	0.0	$(0.0, 0.1)$

Table 1.2: Parameters and systematics included in the fit of IceCube DeepCore data. The best fits for NO and IO of neutrino masses are shown. The expectation value μ and standard deviation σ when a prior is used are also shown.

From Eq. (1.68) a χ^2 is constructed,

$$\chi^2\left(\Delta m^2_{31}, \theta_{23}, \boldsymbol{\vartheta}\right) = \sum_{i,j}\left(\frac{N_{ij,\mathrm{exp}} - N_{ij,\mathrm{th}}\left(\Delta m^2_{31}, \theta_{23}, \boldsymbol{\vartheta}\right)}{\sqrt{N_{ij,\mathrm{exp}}}}\right)^2 + \sum_n\left(\frac{\vartheta_n - \mu_n}{\sigma_n}\right)^2, \tag{1.69}$$

where $\boldsymbol{\vartheta}$ is a vector of all systematic parameters and ϑ_n are those for which we include pull factors. Table 1.2 contains the best-fit values for all parameters, including systematics, for both normal and inverted ordering of neutrino masses. Although the value of several systematic parameters at the best fit coincides with its nominal value, their interplay with other parameters is important for the fit, and they are needed in order to properly obtain the confidence level intervals.

Figure 1.13 displays the 90% and 99% CL regions in the atmospheric plane of neutrino oscillation parameters for the analyses of both large-volume telescopes, ANTARES and IceCube DeepCore, together with the region obtained by SK. Although large-volume telescopes can not compete yet with other experiments, in particular with long-baseline accelerators when measuring neutrino oscillation parameters, future telescopes will improve substantially their present situation. That is the case, for example, of the ORCA neutrino telescope, whose lines are currently being deployed and which is part of KM3NeT [58], a big collaboration of neutrino telescopes in the Mediterranean sea.

1.4.3 Results from the global fit

Single experiments are sensitive to a selected number of neutrino oscillation parameters. However, when combining them in a global fit, a better determi-

nation is obtained. Here we summarise the main results in the particular case of the global fit presented in Ref. [7], which includes the data analyses from the experiments discussed throughout section 1.4. In particular, there are several unknowns related to neutrinos, such as their mass scale and ordering, their nature (whether they are Dirac or Majorana fermions), the existence or not of one or more sterile states or the presence of CP violation in the neutrino sector. We are going to address the conclusions regarding the three main unknowns that can be studied from neutrino oscillations in the three-neutrino paradigm; namely, the value of the CP-violating phase δ, the improvements on the determination of the atmospheric mixing angle θ_{23} octant, and the remarkable results on the neutrino mass ordering, where a sensitivity of more than 3σ is currently achieved from the combination of neutrino oscillation experiments. In the following discussion, the results derived for a specific neutrino mass ordering correspond to a comparison with respect to the best fit for that particular ordering.

Regarding the CP-violating phase, a value of $\delta = \pi/2$ is disfavoured at 4.8σ for NO and 6.1σ for IO, while the best fit is close to $\delta \sim 3\pi/2$ in both cases. Although the best constraint on this parameter from a single experiment comes from T2K, a LBL experiment, the combination with reactors is crucial in order to reach the final sensitivity. This combination is even more powerful when it comes to the neutrino mass ordering determination, as we are going to discuss soon. However, let us first comment on the results for the atmospheric mixing angle.

The last results from the combination of LBL experiments lead to a preference towards maximal mixing in the atmospheric sector. For both neutrino mass orderings a best-fit value $\sin^2\theta_{23} = 0.508$ is found. Including atmospheric experiments this value is slightly shifted into the second octant, with the best fit in normal and inverted orderings giving, respectively, $\sin^2\theta_{23} = 0.54$ and $\sin^2\theta_{23} = 0.53$. The incorporation of reactor experiments set the final value of $\sin^2\theta_{23} \simeq 0.55$ for both orderings. However, these results are still far from robust and values of $\sin^2\theta_{23} < 0.5$ are allowed at $\Delta\chi^2 \geq 1.6$ for NO and $\Delta\chi^2 \geq 3.2$ for IO.

Finally, the main result from the global fit [7] is the great improvement in the combined determination of the neutrino mass ordering. Since the impact of matter effects on neutrinos is different than on their antiparticles and changes with the two orderings, LBL accelerator experiments seem a good way of gaining sensitivity on this issue. However, the impact of matter effects is not enough for current baselines and T2K and NOνA lead to a preference for NO of only $\Delta\chi^2 \sim 1$. If we think about atmospheric experiments, in principle we would expect an improvement because of the varying, long baselines and the presence

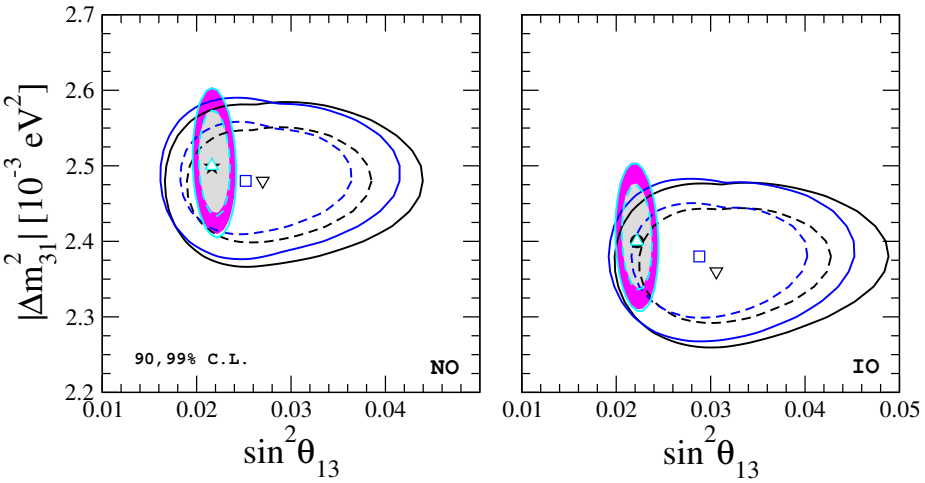

Figure 1.14: 90% and 99% CL regions and best-fit values in the $|\Delta m^2_{31}| - \sin^2\theta_{13}$ plane for NO (left) and IO (right). Black lines and down triangles correspond to LBL data only; blue lines and squares to LBL plus atmospheric data; cyan lines and up triangles to LBL plus reactor experiments, and the coloured regions show the results from the global combination, where the star is the global best fit and the dot indicates the local best fit for IO.

of a resonance at $(4, 8)$ GeV. Nevertheless, the distinction of neutrinos from antineutrinos is not possible in such experiments, and from the combination of LVNTs, which also have an energy threshold above the resonance, we only reach a preference for NO of $\Delta\chi^2 = 0.4$, coming mostly from IceCube DeepCore. On the other hand, Super-Kamiokande is sensitive to lower energies (affected by resonant matter effects) than current LVNTs, so it can achieve a preference of $\Delta\chi^2 = 3.5$ for NO. A simple, naive summation of the sensitivity of LBL experiments plus LVNTs is, however, not enough to reach the final preference, which is obtained thanks to the interplay between the different type of experiments.

In order to understand how the combination of experiments leads towards more than 3σ preference for NO, we depict in Fig. 1.14 the best fit together with the 90% and 99% contours for different cases. The main contribution in favour of NO with respect to IO comes from the combination of LBL accelerator experiments and reactor experiments. The reason is a mismatch on the preferred value of θ_{13}, more pronounced for IO. The global best-fit value of $\sin^2\theta_{13} \approx 0.022$ for both neutrino mass orderings mostly comes from reactor data, in particular from Daya Bay (see Fig. 1.9). While LBL experiments reach a value of $\sin^2\theta_{13} =$

0.026 for NO, a value of $\sin^2\theta_{13} = 0.031$ is instead obtained for IO, further from the reactor measurement. This mismatch in the value of θ_{13} for inverted ordering, together with a similar one in the value of Δm^2_{31}, increases the preference for NO up to $\Delta\chi^2 = 7.5$. The final inclusion of data from atmospheric neutrino experiments lead to the global-fit result of $\Delta\chi^2 = 11.7$ (3.4σ) in preference of normal neutrino mass ordering.

Apart from flavour-oscillation-devoted experiments, other experimental probes can be exploited in order to achieve a determination of the ordering of neutrino masses. For instance, neutrinoless double-beta ($0\nu\beta\beta$) decay experiments (provided that neutrinos are Majorana particles) constrain the effective Majorana mass $m_{\beta\beta}$, which at the same time depends on the neutrino masses as

$$m_{\beta\beta} = \left| \sum_{k=1}^{N} \mathrm{e}^{i\alpha_k} U_{ek}^2 m_k \right| , \tag{1.70}$$

where we notice the dependence on the Majorana phases α_k, contrary to oscillation experiments. Also cosmology can be sensitive to the mass ordering. Since the evolution of the Universe is affected by the sum of neutrino masses, a non-degenerate scenario differs for both NO and IO, and given the larger value of $\sum_k m_k$ in the inverted case and the precision of current cosmological observations, the next generation of probes could either determine the value of the sum of neutrino masses or point towards a normal ordering. We will discuss a bit more about this issue in the next chapter, after having set the basics of cosmology needed for the present thesis. However, before continuing let us make just a brief comment regarding the determination of the ordering of neutrino masses. Despite the different approaches available to access the true ordering, nowadays it is the global combination of flavour oscillation experiments that leads the quest. In fact, in Ref. [67] we combined data from oscillations, double-beta decay and cosmology, and we found that, for a proper choice of the needed priors in our Bayesian analysis, the addition of the last two probes barely improves the preference coming from flavour oscillation experiments. A dedicated discussion is however beyond the scope of the present thesis and we refer the interested reader to the original reference [67] and to a recent review [68], in both of which the author has participated.

Coming back to neutrino flavour oscillations, future experiments of this kind will exploit different techniques in the search for resolving the true ordering of neutrino masses. As examples, large-volume atmospheric experiments such as ORCA or PINGU will rely on large statistics and good angular resolution, while

parameter	best fit ± 1σ	2σ range	3σ range
Δm^2_{21} $[10^{-5}\text{eV}^2]$	$7.55^{+0.20}_{-0.16}$	7.20–7.94	7.05–8.14
$\lvert\Delta m^2_{31}\rvert$ $[10^{-3}\text{eV}^2]$ (NO)	2.50±0.03	2.44–2.57	2.41–2.60
$\lvert\Delta m^2_{31}\rvert$ $[10^{-3}\text{eV}^2]$ (IO)	$2.42^{+0.03}_{-0.04}$	2.34–2.47	2.31–2.51
$\sin^2\theta_{12}/10^{-1}$	$3.20^{+0.20}_{-0.16}$	2.89–3.59	2.73–3.79
$\theta_{12}/^\circ$	$34.5^{+1.2}_{-1.0}$	32.5–36.8	31.5–38.0
$\sin^2\theta_{23}/10^{-1}$ (NO)	$5.47^{+0.20}_{-0.30}$	4.67–5.83	4.45–5.99
$\theta_{23}/^\circ$	$47.7^{+1.2}_{-1.7}$	43.1–49.8	41.8–50.7
$\sin^2\theta_{23}/10^{-1}$ (IO)	$5.51^{+0.18}_{-0.30}$	4.91–5.84	4.53–5.98
$\theta_{23}/^\circ$	$47.9^{+1.0}_{-1.7}$	44.5–48.9	42.3–50.7
$\sin^2\theta_{13}/10^{-2}$ (NO)	$2.160^{+0.083}_{-0.069}$	2.03–2.34	1.96–2.41
$\theta_{13}/^\circ$	$8.45^{+0.16}_{-0.14}$	8.2–8.8	8.0–8.9
$\sin^2\theta_{13}/10^{-2}$ (IO)	$2.220^{+0.074}_{-0.076}$	2.07–2.36	1.99–2.44
$\theta_{13}/^\circ$	$8.53^{+0.14}_{-0.15}$	8.3–8.8	8.1–9.0
δ/π (NO)	$1.32^{+0.21}_{-0.15}$	1.01–1.75	0.87–1.94
$\delta/^\circ$	218^{+38}_{-27}	182–315	157–349
δ/π (IO)	$1.56^{+0.13}_{-0.15}$	1.27–1.82	1.12–1.94
$\delta/^\circ$	281^{+23}_{-27}	229–328	202–349

Table 1.3: Summary of neutrino oscillation parameters determined from the global analysis of neutrino oscillation data performed in [7]. The ranges for inverted ordering refer to the local minimum for this neutrino mass ordering.

the 50 kt magnetised iron calorimeter (ICAL) at the India-based Neutrino Observatory (INO) will exploit the ability of distinguishing between neutrinos and antineutrinos. In all these cases the determination of the neutrino mass ordering is achieved from the difference in matter effects in both scenarios. On the other hand, the proposed reactor experiment JUNO intends to differentiate between the two orderings with precision measurements, from the direct effect that the change in sign of Δm^2_{31} has on vacuum oscillations of reactor electron antineutrinos.

We close this section with a summary of the results from the global fit [7], presented in table 1.3. We also show a summary of the neutrino oscillation parameters in figures 1.15 and 1.16, where $\Delta\chi^2$ and confidence intervals can be seen.

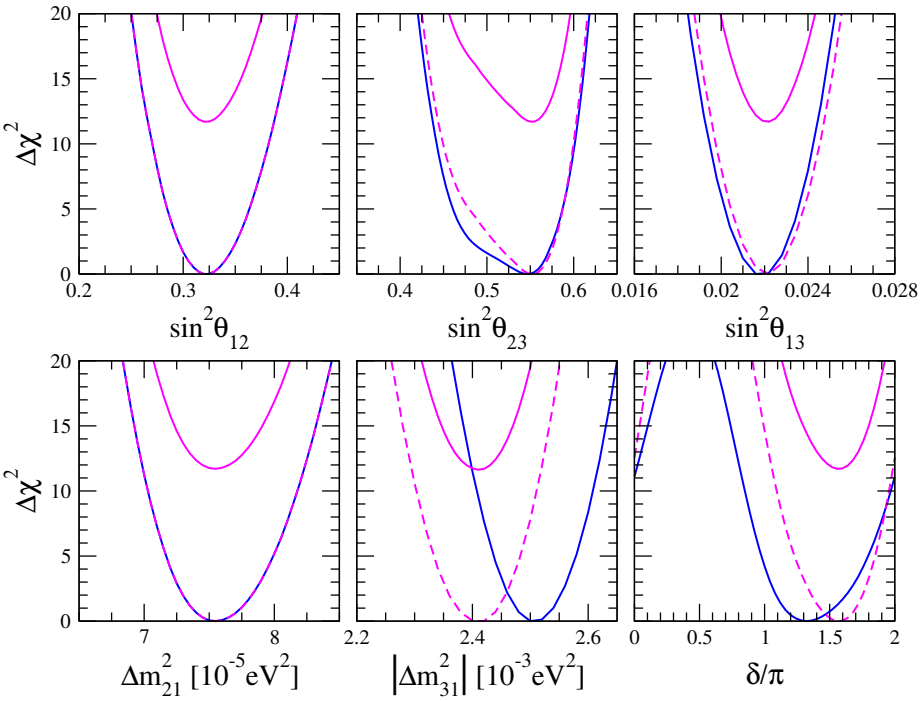

Figure 1.15: $\Delta\chi^2$ for the oscillation parameters from the combined analysis of Ref. [7]. Solid lines are drawn with respect to the global minimum and dashed lines with respect to the local minimum of IO. Blue lines are for NO and pink lines for IO.

1.5 Sterile neutrinos

Sterile neutrinos are those that do not feel weak interactions and therefore couple to the active ones only through the lagrangian mass term. They appear in a variety of scenarios beyond the SM of particle physics, with a wide range of masses. For example, they are common in models where a dark matter (DM) fermion is needed, in which case a mass larger or equal to order keV is usually required. However, there are also scenarios, motivated by the so-called short-baseline (SBL) neutrino oscillation anomalies, in which light sterile neutrinos (with $m_{\nu_s} \sim \mathcal{O}(1\,\text{eV})$) can be the solution.

From the point of view of the standard three-neutrino flavour oscillations, some SBL experimental data are difficult to explain. In particular, it seems challenging to accommodate the LSND [69, 70] data, the Gallium [71–75] anomaly

and the reactor [76] anomaly. Several experiments were built with the intention of testing these anomalies, like DANSS [77], regarding the reactor and Gallium measurements, and MiniBooNE [78], regarding the LSND data. The improvements from DANSS come from its ability of taking measurements at different distances (between 10.5 m and 12.5 m from the centre of the reactor), while MiniBooNE tests the same L/E ratio than LSND but with different values of both distance and neutrino energy. Beyond systematic uncertainties, a possible explanation for the anomalies would involve oscillations with a fourth neutrino mass eigenstate, mainly mixed with the new sterile flavour eigenstate and having a small mixing with the three active neutrino flavours (see references [17, 79–81]).

In principle, more than one sterile neutrino could be invoked. However, strong constraints coming from cosmology make it difficult to explain the existence of more than one (or even one) sterile neutrino species. This constraint is related to the measurement of a cosmological parameter called *effective number of neutrinos* (see section 2.3.4), which will be explained in detail in chapter 3. Anyway, among the possible scenarios including one or more sterile neutrinos, the most favoured is the 3+1, in which the sterile is heavier than the standard three states. Nevertheless and despite all the anomalies, the sterile neutrino hypothesis is currently under debate, since some tensions appear among the various experiments, which can not be explained at the same time with the same values of the mixing parameters. Therefore, it is very likely that something else is needed in order to explain all the anomalies, perhaps a better understanding of the systematics.

In any case, for the purposes of the present thesis, light sterile neutrinos are only mentioned when we discuss about relic neutrino clustering in chapter 6, and only as an example in a non-standard scenario in which a large enhancement of the local density of relic neutrinos could be possible.

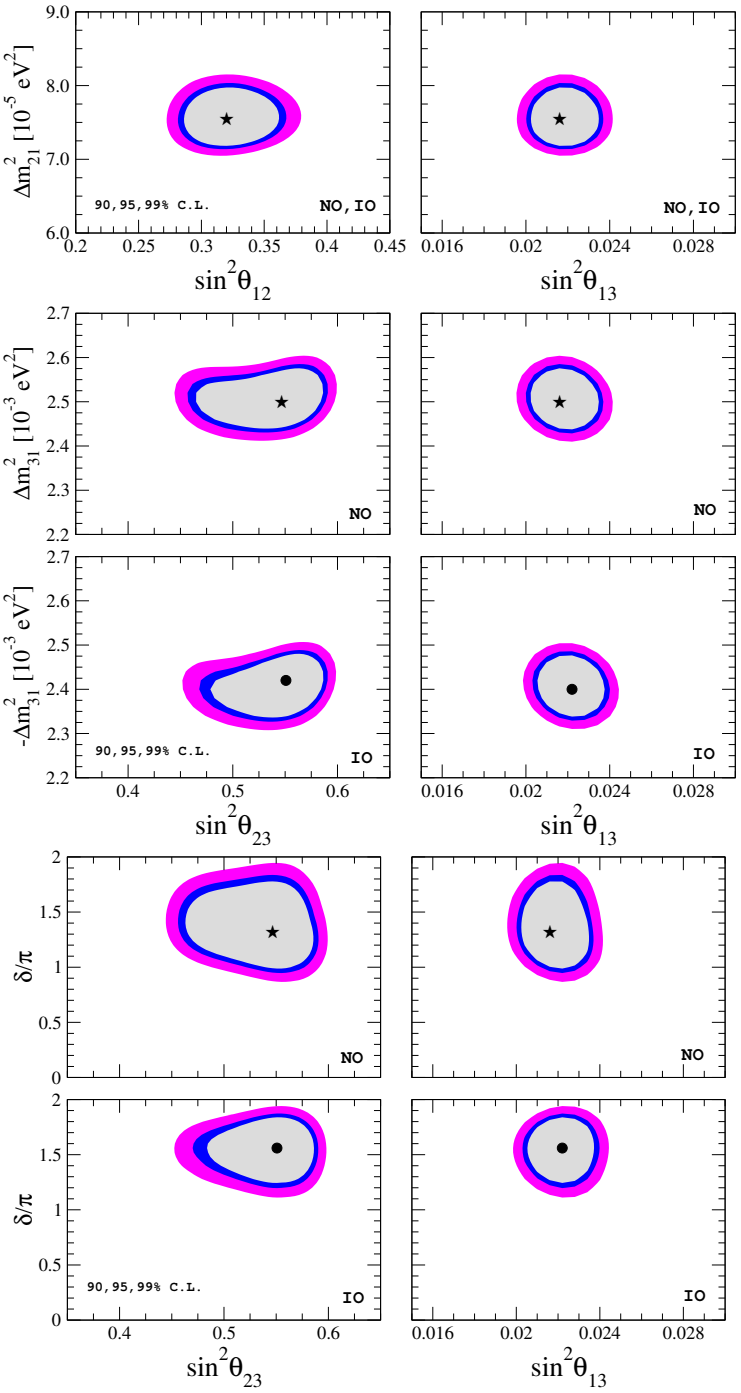

Figure 1.16: 90%, 95% and 99% CL (2 d.o.f.) regions for several planes of two neutrino oscillation parameters, as obtained in the global fit of Ref. [7]. Results for both neutrino mass orderings are shown. While the star refers to the global best fit, the black dot represents the best fit in the IO. All plots for IO are represented with respect to this minimum.

Chapter 2

Cosmology of an expanding universe

The Universe is a vast extension both in time and space, what makes very suitable the use of statistical techniques in order to handle the study of its components. Therefore, as strange as it might sound, the evolution of the Universe can be analysed from the point of view of its "macroscopic" properties, even though its "microscopic" entities are at least of galactic size. In cosmological scales, galaxies are hence like molecules when studying a gas. This thermodynamic approach makes it easier to understand the Universe as a whole.

Nowadays, the best theoretical model to study the Universe and its evolution is the so-called Λ-*cold dark matter* (ΛCDM) model. It is based in just a few assumptions: the *cosmological principle*, an *expanding* universe and *inflation*, and it also assumes that the dark components of the Cosmos are in form of cold dark matter and a cosmological constant Λ. These assumptions have been tested with observations and no clear deviation from them has been found so far.

The cosmological principle implies that the Universe is homogeneous and isotropic at scales larger than $\sim 100\,\mathrm{Mpc}$, huge distances for us that are nonetheless ridiculously small when compared to the size of the horizon. The most general metric describing such a universe is the Friedmann-Robertson-Walker (FRW) metric,

$$g_{\mu\nu}\mathrm{d}x^\mu \mathrm{d}x^\nu = \mathrm{d}t^2 - a^2(t)\left(\frac{\mathrm{d}r^2}{1-kr^2} + r^2\mathrm{d}\theta^2 + r^2\sin^2\theta\,\mathrm{d}\phi^2\right), \tag{2.1}$$

where r, θ and ϕ are comoving spherical coordinates. They are called *comoving* because they represent observers that are insensitive to the expansion dynamics, i.e. the values of these coordinates are invariant with the course of time. The variable t is the proper (physical) time as measured by our comoving observers. The relation between comoving distances $d_{\rm c}$, expressed in terms of comoving coordinates, and physical distances $d_{\rm p}(t) = a(t)d_{\rm c}$, is given by the scale factor $a(t)$, whose value increases with time enclosing the augmentation of physical distances in an expanding universe. The exact value of $a(t)$ depends upon an arbitrary constant rescaling, which for a flat universe is typically fixed to be $a = 1$ today. Finally, the value of the parameter k specifies the spatial curvature.

In order to study the Universe we need to control not only the properties of the container (the space-time), but also the properties of the content itself. We use General Relativity to link them, via the Einstein's equations

$$G_{\mu\nu} \equiv R_{\mu\nu} - \frac{1}{2}Rg_{\mu\nu} = 8\pi G T_{\mu\nu} + \Lambda g_{\mu\nu}, \tag{2.2}$$

where $R_{\mu\nu}$ is the Ricci tensor and R is the Ricci scalar; $T_{\mu\nu}$ is the energy-momentum tensor, G the gravitational constant and $g_{\mu\nu}$ stands, as above, for the metric tensor. Finally, Λ represents the Einstein's cosmological constant. The gravitational constant defines a mass scale in natural units: the Planck mass [10]

$$m_{\rm Pl} = G^{-1/2} = 1.22 \cdot 10^{19}\,{\rm GeV}. \tag{2.3}$$

When referring to the early Universe we are going to describe gases of photons, electrons, neutrinos and other particles as perfect fluids with no viscosity. Hence, the energy-momentum tensor is expressed like

$$T^{\mu}_{\ \nu} = (\rho + P)\, u^{\mu} u_{\nu} + P\delta^{\mu}_{\nu}, \tag{2.4}$$

where ρ and P are the energy density and the pressure of the fluid, respectively. We also consider fluids with zero velocity in the comoving frame, so the fluid 4-velocity u^{μ} takes the form

$$u^{\mu} = (1, 0, 0, 0) \tag{2.5}$$

and

$$T^{0}_{\ 0} = -\rho, \qquad T^{i}_{\ j} = P\delta^{i}_{j}. \tag{2.6}$$

Solving the time-time component $(0,0)$ of the Einstein equation (2.2) with this energy-momentum tensor gives the Friedmann equation

$$H^2(t) = \left(\frac{\dot{a}}{a}\right)^2 = \frac{8\pi G\rho}{3} - \frac{k}{a^2} + \frac{\Lambda}{3}, \tag{2.7}$$

where now ρ stands for the total energy density of the Universe[1], which is linked in this equation to the cosmological expansion rate at a time t. Such rate is given by the Hubble parameter $H(t)$, whose value today is $H_0 \sim 70\,\mathrm{km\,s^{-1}\,Mpc^{-1}}$ with differences depending on the dataset used to derive it.

In addition, the space-space component of the Einstein equation gives rise to

$$2\frac{\ddot{a}}{a} + \left(\frac{\dot{a}}{a}\right)^2 + \frac{k}{a^2} = -8\pi GP + \Lambda. \tag{2.8}$$

Combining Eqs. (2.7) and (2.8) we get

$$\frac{\ddot{a}}{a} = -\frac{4\pi G}{3}(\rho + 3P) + \frac{\Lambda}{3}, \tag{2.9}$$

that can be used together with the derivative of Eq. (2.7) with respect to time,

$$2\dot{a}\ddot{a} = \frac{8\pi G}{3}\left(\dot{\rho}a^2 + 2a\dot{a}\rho\right) + \frac{2\Lambda}{3}a\dot{a}, \tag{2.10}$$

to get the fluid equation

$$\dot{\rho} = -3H(\rho + P), \tag{2.11}$$

which can also be obtained from the conservation of the energy-momentum tensor for a perfect fluid.

This equation can be solved for a given component of the Universe once the connection among pressure and energy density is fixed. This relation is given by the equation of state, that we use in a simple linear form

$$P = w\rho, \tag{2.12}$$

where w is a parameter that depends on the nature of the chosen component. Non-relativistic particles, for instance, whose kinetic energy is very small with respect to their mass, behave as a pressureless gas (also referred to as dust or

[1] Technically speaking, in the way we have written Eq. (2.7) it does not account for the total energy density, because dark energy, here in form of a cosmological constant Λ, is not included inside ρ. However we explain later that Λ can be absorbed within ρ and P.

matter), so $w = 0$ for a non-relativistic component. However, relativistic particles (also referred to as *radiation*) have $w = 1/3$ regardless of their statistics (bosonic or fermionic). Finally, a cosmological constant will take a value $w = -1$. This last example is easy to see if we absorb Λ inside the energy-momentum tensor in Eq. (2.2), defining

$$T_{\mu\nu,\Lambda} \equiv -\frac{\Lambda}{8\pi G} g_{\mu\nu}, \tag{2.13}$$

from which

$$\rho_\Lambda = -P_\Lambda = \frac{\Lambda}{8\pi G}. \tag{2.14}$$

Additionally, we can generalise the cosmological constant and think about a generic form of dark energy, whose role is to ensure $\ddot{a} > 0$ in order to have an accelerated expansion. Under this condition, Eq. (2.9) tells us that $w < -1/3$ for dark energy, which can be interpreted as a fluid with negative pressure.

Integrating Eq. (2.11) we get the dependence of the energy density with the scale factor

$$\rho(a) \propto a^{-3(1+w)}. \tag{2.15}$$

From this equation it is obvious that a cosmological constant will have a parameter $w = -1$. Furthermore, focusing on a single component in the Friedmann equation (2.7) and substituting Eq. (2.15), after integrating we get

$$a(t) \propto \begin{cases} t^{\frac{2}{3(1+w)}}, & w \neq -1, \\ \mathrm{e}^{\bar{H}t}, & w = -1, \end{cases} \tag{2.16}$$

where $\bar{H}$ is the Hubble parameter that is asymptotically reached when Λ dominates the expansion of the Universe.

As we have already commented, Friedmann equation (2.7) shows that the expansion rate of the Universe depends on its content through its total energy density ρ, in which we include from now on the dark energy contribution. In addition, from this equation we notice that the relation is fixed for a given curvature. Our Universe is experimentally compatible with a flat space curvature (i.e. $k = 0$), but cosmology also works for a close ($k = +1$) or an open ($k = -1$) universe. The total energy density of a flat universe is typically called *critical density*,

$$\rho_{\mathrm{crit}}(t) = \frac{3}{8\pi G} H^2(t). \tag{2.17}$$

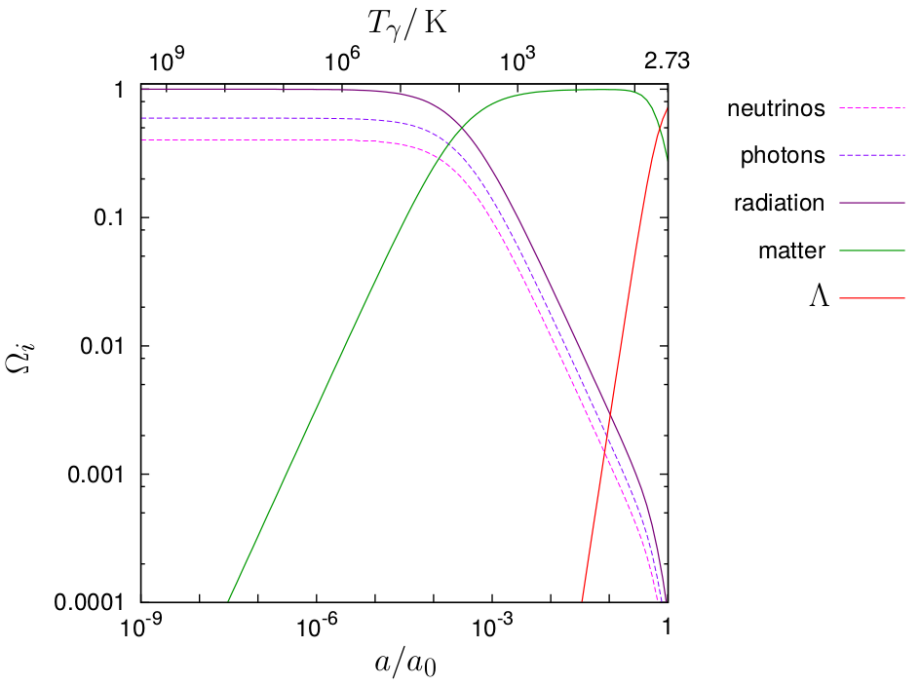

Figure 2.1: Evolution of different components of the Universe in terms of their density parameter. Neutrinos are taken to be massless and Λ stands for a cosmological constant.

Using $\rho_{\rm crit}$ to define the dimensionless *density parameter* of a given component i,

$$\Omega_i = \frac{\rho_i}{\rho_{\rm crit}}, \tag{2.18}$$

we can rewrite the Friedmann equation (2.7) as

$$H^2(a) = H_0^2 \left(\Omega_{\rm r,0}\, a^{-4} + \Omega_{\rm m,0}\, a^{-3} + \Omega_{k,0}\, a^{-2} + \Omega_{\Lambda,0} \right), \tag{2.19}$$

where the subscript 0 in one parameter means that it is evaluated today. Additionally, the components of the Universe are classified according to their dependence with the scale factor. The dependence of radiation $\Omega_{\rm r}$ (relativistic particles) and matter $\Omega_{\rm m}$ (non-relativistic particles) with a is obtained from Eq. (2.15); the factor a^{-2} for Ω_k is fixed directly from the Friedmann equation, and Λ is constant by definition. Expressed in this way, the Friedmann equation shows more clearly

the dependence of the Universe's expansion rate with its components and its expected evolution with time. For a flat universe only radiation, matter and dark energy are present. In figure 2.1 we show the evolution of the different components expressed in terms of their density parameter. At first, since the Universe was more compact and its temperature was higher, its energy density was almost completely ruled by radiation. The softer dependence with a of $\Omega_{\rm m}$ with respect to $\Omega_{\rm r}$ reflects the subsequent dominance of matter, after the cooling down of the Universe due to its expansion. Finally, at present we are entering an epoch of dark energy dominance, here expressed in terms of a cosmological constant Λ.

2.1 Thermodynamic relations in cosmology

The interplay between the dynamics of the Universe and its different constituents has already been established. In accordance with the cosmological principle, we are treating those components as isotropic and homogeneously distributed fluids, whose energy densities affect the expansion rate of the Cosmos. This thermodynamic quantity, as well as others, hinges on the distribution function $f(t, \mathbf{x}, \mathbf{p})$ of the individual particles of the gas. Because of isotropy and homogeneity, f does not depend on the direction of the momentum $\mathbf{p}$ nor on the spatial coordinates $\mathbf{x}$, and if we further consider thermodynamic equilibrium, the time dependence also disappears. This is not strictly correct in an expanding universe and we will see later that particles in equilibrium at a given time may abandon such condition when the expansion rate overcomes the rate of interactions. Therefore, when considering equilibrium in the expanding Universe, we actually deal with *local* thermodynamic equilibrium, in particular in the early Universe where we can describe it as a succession of nearly thermal states with temperature T (almost) constantly decreasing. Thus we end up with distribution functions that only depend on the magnitude $p = |\mathbf{p}|$ of the momentum, with the effect of expansion encoded in the evolution of T.

Under the simplifications that we just stated, the distribution function of a gas formed by particles in equilibrium at a temperature T takes the form

$$f(p) = \frac{1}{\mathrm{e}^{(E(p)-\mu)/T} \pm 1}, \tag{2.20}$$

where the energy of a particle of mass m is given by

$$E^2(p) = p^2 + m^2. \tag{2.21}$$

The plus sign (+) in Eq. (2.20) gives rise to a Fermi-Dirac distribution and the minus sign (−) to a Bose-Einstein, representing fermions and bosons respectively. The parameter μ is the chemical potential, that is related to a difference in the number of particles and antiparticles. Throughout this thesis, however, we study neutrinos, whose chemical potential is highly constrained from cosmological observations and neutrino oscillations and is found to be compatible with zero [82]. Therefore it can be ignored.

From the distribution functions (2.20) we can compute thermodynamic quantities such as the number density n, the energy density ρ and the pressure P of the gas:

$$n = \frac{g}{(2\pi)^3} \int_0^\infty f(p)\, \mathrm{d}^3\mathbf{p}, \tag{2.22}$$

$$\rho = \frac{g}{(2\pi)^3} \int_0^\infty f(p) E(p)\, \mathrm{d}^3\mathbf{p}, \tag{2.23}$$

$$P = \frac{g}{(2\pi)^3} \int_0^\infty f(p) \frac{p^2}{3E(p)}\, \mathrm{d}^3\mathbf{p}, \tag{2.24}$$

where g stands for the number of internal degrees of freedom. The entropy density

$$s = \frac{\rho + P}{T} \tag{2.25}$$

can also be computed from the previous relations.

In the relativistic limit ($T \gg m$), particles follow a Fermi-Dirac or a Bose-Einstein distribution (2.20) according to their spin[2]. However, both statistics converge in the non-relativistic limit ($T \ll m$) to a Maxwell-Boltzmann distribution.

When local thermodynamic equilibrium holds, the number density, energy density and pressure for relativistic (distinguishing between statistics) and non-relativistic gases of particles are shown in table 2.1. From the displayed values of the pressure it is clear why the parameter in the equation of state (2.12) takes the value $w = 0$ for matter and $w = 1/3$ for radiation.

During radiation-domination the energy density of the Universe is that of its relativistic components. Based on the results of table 2.1, we can write

$$\rho_\mathrm{r} = g_* \frac{\pi^2}{30} T^4, \tag{2.26}$$

[2]In chapter 5 we relax this condition for neutrinos and study experimental constraints on the spin-statistics theorem for these particles.

	relativistic		non-relativistic
	fermions	bosons	
n	$\frac{3}{4} g \frac{\zeta(3)}{\pi^2} T^3$	$g \frac{\zeta(3)}{\pi^2} T^3$	$g \left(\frac{mT}{2\pi}\right)^{3/2} \mathrm{e}^{-m/T}$
ρ	$\frac{7}{8} g \frac{\pi^2}{30} T^4$	$g \frac{\pi^2}{30} T^4$	$m\, n$
P	$\frac{1}{3}\rho$		$n\, T \ll \rho$

Table 2.1: Thermodynamic variables in the relativistic and non-relativistic regimes.

where T is the temperature of the cosmic plasma and therefore it is shared for all particle fluids in equilibrium. The quantity g_* determines the effective relativistic degrees of freedom,

$$g_* = \sum_{i,\mathrm{boson}} g_i \left(\frac{T_i}{T}\right)^4 + \frac{7}{8} \sum_{j,\mathrm{fermion}} g_j \left(\frac{T_j}{T}\right)^4, \tag{2.27}$$

where T_i and T_j are the temperatures of the different bosonic and fermionic species, respectively, that can be different from T if they are not in equilibrium. We will come back to this later.

A similar definition can be done for the entropy density, that from Eq. (2.25) and the values in table 2.1 can be expressed as

$$s_{\mathrm{r}} = g_s \frac{2\pi^2}{45} T^3, \tag{2.28}$$

where g_s represents the entropy relativistic degrees of freedom,

$$g_s = \sum_{i,\mathrm{boson}} g_i \left(\frac{T_i}{T}\right)^3 + \frac{7}{8} \sum_{j,\mathrm{fermion}} g_j \left(\frac{T_j}{T}\right)^3. \tag{2.29}$$

2.2 Stages of the early Universe

Most of the present thesis is dedicated to studies where relic neutrinos have a leading role. Within the SM of particle physics, neutrino interactions happen through the interchange of Z and $W^{\pm}$ bosons, meaning that they interact very

weakly and therefore decouple early from the cosmic plasma, even before the synthesis of the first nuclides. Therefore, among the different stages of the Cosmos we will concentrate on those that occurred during the early Universe.

2.2.1 Inflation and reheating

Although the standard cosmological model works well, it has problems in explaining some observational facts related to its initial conditions. For example, it does not provide a proper explanation for the observed isotropy and homogeneity of the cosmic microwave background (CMB). Within the standard cosmological model, photons from the last scattering surface coming from different directions, larger than about 1°, were not in casual contact in the past, yet they show the same temperature today. This apparent contradiction is called the *horizon problem*.

Another difficulty is connected with the curvature of the Universe. Experimentally, we seem to live in a flat universe ($|\Omega_k| < 0.005$ at 95% CL [83]). If we rewrite the Friedmann equation (2.7) using the definition of the critical density of the Universe, which we remind it is that of a flat curvature, and the Ω parameters (Eqs. (2.17) and (2.18) respectively) we end up with

$$\Omega_{\text{tot}} - 1 = \frac{k}{H^2 a^2}. \tag{2.30}$$

For a flat universe $k = 0$ and $\Omega_{\text{tot}} = 1$. However, if we assume that some deviation from flatness might exist today, this deviation should have been much smaller in the past. For instance, a deviation of about the per mil level today would imply a value of $|\Omega_{\text{BBN}} - 1| \sim \mathcal{O}\left(10^{-16}\right)$ when Big Bang nucleosynthesis (BBN) took place, at a time when the cosmic plasma had a temperature of $T \sim 0.1\,\text{MeV}$. This is known as the *flatness problem*.

These and other issues, regarding the lack of some expected relics as well as the generation of initial perturbations, are solved if we assume that there existed a primeval epoch during which the Universe expanded in an accelerated way. The need for such acceleration can be easily understood from the Friedmann equation expressed in the previous form (2.30) while enforcing the solution of the flatness problem. We can soften the fine tuning needed for the values of $\Omega - 1$ at early times if there was a primeval epoch in which its value quickly tended towards zero, i.e. if

$$\frac{\mathrm{d}\left(Ha\right)}{\mathrm{d}t} > 0, \tag{2.31}$$

which implies $\ddot{a} > 0$ and therefore represents an accelerating time.

This epoch is called *inflation*.

Despite being so efficient in solving problems of the cosmological model, inflation must be taken with care. It is not clear if it really existed and many models following different strategies and assumptions are currently available (see for example the lecture notes [84] and references therein). Experimentally, a smoking gun of inflation would be the detection of primordial gravitational waves, but inflation might still be possible with extremely small production of them [85]. Nonetheless, given how difficult it is to make observations about the early Universe and given the success of inflation as a trouble solver, it is undoubtedly the best solution today to set the ground for the reheating and post-reheating stages of the Universe.

During the inflationary epoch, a common assumption is to consider that the energy density of the Universe (at very large temperatures) was dominated by the potential energy of a scalar field, usually called *inflaton*. As the study of inflation is not crucial for the topics discussed in this thesis, we will not enter in the details of the different available models. It is enough to know that, typically, the scalar field leading inflation is coupled to standard fields, in such a way that at the end of inflation, when the kinetic energy of the inflaton becomes comparable to its potential energy, it can decay into the particles it is coupled to, populating the Universe with relativistic products that thermalise and give rise to a radiation-dominated epoch. This process is called *reheating*.

It is also possible that unstable non-relativistic particles, other than the inflaton, were responsible of more than one reheating phase at different times in the evolution of the Universe, leading to a series of matter and radiation-dominated stages.

What one can say is that there was a final period dominated by relativistic particles in thermal equilibrium starting at a maximum temperature T_{RH}, at least before Big Bang nucleosynthesis so that the primordial production of light elements is in agreement with the observed abundances.

2.2.2 Neutrino decoupling and electron-positron annihilation

Many interesting processes occurred in the first moments after inflation, whose consequences translate into a reduction of the effective relativistic degrees of freedom (see Fig. 2.2). Baryon asymmetry was generated; particles acquired mass after the electroweak phase transition in which the standard model gauge symmetry $SU(2)_L \times U(1)_Y$ was spontaneously broken to $U(1)_Q$; the most massive particles decayed into the lightest ones, hadrons were formed in the QCD transi-

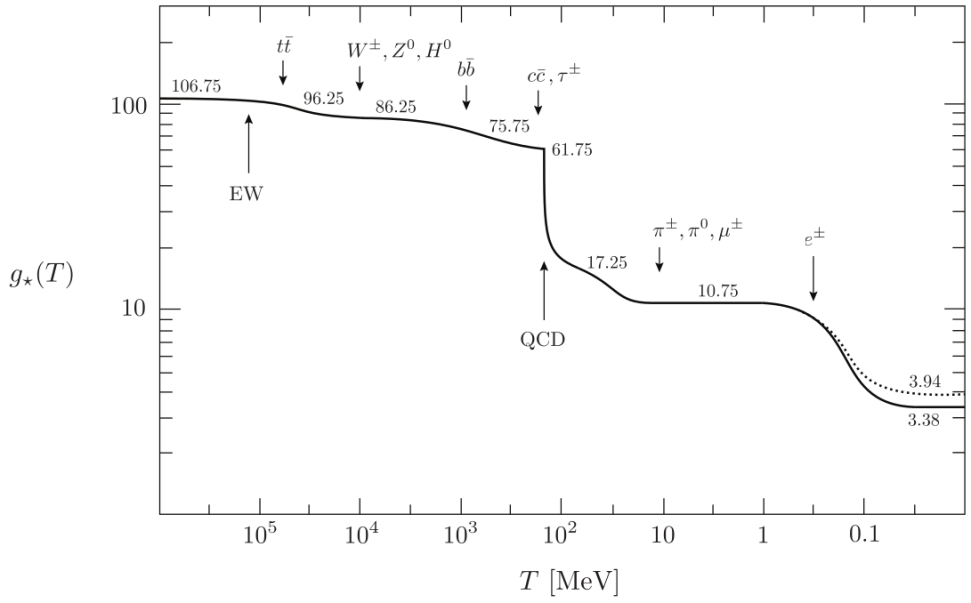

Figure 2.2: Change in the effective degrees of freedom g_* along the early Universe. The dotted line stands for the entropy relativistic degrees of freedom g_s. Figure taken from [86].

tion at a temperature of $\sim 200\,\mathrm{MeV}$ from unbound quarks and gluons; neutrinos decoupled right before the $e^{\pm}$-annihilation stage, and, finally, primordial nucleosynthesis occurred. After it, the Universe evolved more or less calmly until matter domination.

Among all these processes, the first event taking place during radiation domination that is interesting for us is the *neutrino decoupling*.

At first approximation, a particle fluid is kept in local thermodynamic equilibrium when the interaction rate Γ of their constituents is larger than the rate of expansion of the Universe, given by the Hubble parameter H,

$$\Gamma > H. \tag{2.32}$$

This is equivalent to saying that there are more than one interaction in a Hubble time, so the expansion does not spoil equilibrium.

The temperature at this stage and, as a consequence, the energy of the particles of the different fluids (still) in equilibrium, is much lower than the mass of the gauge bosons $W^{\pm}$ and Z^0. Hence the electroweak cross section goes approx-

imately as

$$\sigma \sim G_{\mathrm{F}}^2 T^2, \tag{2.33}$$

so the interaction rate of relativistic, weakly interactive particles, from the relation of the number density with temperature $n(T) \propto T^3$ (see Tab. 2.1) is

$$\Gamma = \langle n\sigma v \rangle \sim G_{\mathrm{F}}^2 T^5. \tag{2.34}$$

Additionally, in the radiation-dominated epoch, Friedmann equation (2.7) gets the form

$$H(T) = \left(\frac{8\pi G}{3} g_* \frac{\pi^2}{30} T^4 \right)^{1/2} \sim \sqrt{g_*} \frac{T^2}{m_{\mathrm{Pl}}}, \tag{2.35}$$

where we have used the expressions in Eqs. (2.26) and (2.27). Comparing the rates of interaction and expansion,

$$\frac{\Gamma}{H} \approx \frac{m_{\mathrm{Pl}} G_{\mathrm{F}}^2 T^5}{\sqrt{g_*}\, T^2} \sim \left(\frac{T}{g_*^{1/6}\, \mathrm{MeV}} \right)^3, \tag{2.36}$$

we see that for temperatures below $T_{\nu,\mathrm{dec}} \sim$ MeV, electroweak interactions are not efficient in keeping neutrinos in thermodynamic equilibrium and therefore they decouple from the cosmic bath.

The average kinetic energy of an ideal gas is related to its temperature through

$$\langle E_k \rangle = \frac{3}{2} T. \tag{2.37}$$

With this in mind, when the temperature of the cosmic plasma decreased below a third of the electron mass $m_e = 0.511\,\mathrm{MeV}$, these leptons annihilated with their antiparticles into photons, that could no longer keep the equilibrium with them. When this happened neutrinos had already decoupled and the entropy of electrons and positrons was only transferred to photons, in a sort of reheating that caused their temperature (thus the temperature of the cosmic plasma as well) to increase with respect to that of neutrinos, which continued to decrease proportionally to a^{-1}. We remind the reader that, after decoupling, neutrinos keep a Fermi-Dirac distribution with a "temperature"

$$T_\nu = \frac{T_{\nu,\mathrm{dec}} a_{\mathrm{dec}}}{a}, \tag{2.38}$$

being $T_{\nu,\mathrm{dec}}$ and a_{dec} the temperature and scale factor at decoupling. However, T_ν in (2.38) is an effective parameter related to the frozen distribution of neutrinos, in spite of its given name, since they are not in equilibrium any more.

As we discuss in detail in chapter 3, this leads to an enhancement of photon temperature T_γ over neutrino "temperature" T_ν close to

$$\frac{T_\gamma}{T_\nu} \approx \left(\frac{11}{4}\right)^{1/3}. \tag{2.39}$$

This relation is exact only in the so-called *instantaneous* decoupling approximation. In other cases, when part of the entropy released by electrons is not absorbed by photons, $T_\gamma/T_\nu \lesssim (11/4)^{1/3}$.

2.2.3 Primordial nucleosynthesis

Shortly after electron-positron annihilations, primordial nuclides were synthesised. The binding energies per nucleon of the order of $(1, 8)\,\mathrm{MeV}$ seem to indicate that nucleosynthesis should have taken place when the cosmic plasma reached that temperature. However, that was not the case, as a quick check can reveal studying a reaction

$$(A - Z)\, n + Zp \leftrightarrows N(A, Z) + \gamma \tag{2.40}$$

among Z free protons, $(A - Z)$ free neutrons (where A is the mass number) and the nuclei $N(A, Z)$ whose binding energy is $B(A, Z)$. Applying the Saha equation to this process we get

$$\frac{n_{N(A,Z)}}{n_B} \sim A^{3/2}\, \eta_B^{A-1} \left(\frac{2\zeta(3)}{\pi^2}\right)^{A-1} \left(\frac{2\pi T}{m_p}\right)^{3(A-1)/2} \mathrm{e}^{B_{N(A,Z)}/T}, \tag{2.41}$$

which indicates the dependence of the fraction between the number density of $N(A, Z)$ and that of baryons, n_B, on both the temperature T of the bath and the baryon-to-photon parameter $\eta_B = n_B/n_\gamma$. $\zeta(3) \approx 1.202$ is the Riemann zeta function evaluated at 3. Knowing that at the time of BBN the amount of baryons is several orders of magnitude smaller than the number of photons, $\eta_B \sim 10^{-9}$, the expression (2.41) applied to deuterium, whose binding energy is $B_{^2\mathrm{H}} \sim 2.2\,\mathrm{MeV}$, gives a fraction of $\frac{n_{^2\mathrm{H}}}{n_B} \sim 10^{-12}$ at $T = B_{^2\mathrm{H}}$. Notice that the smallness of this fraction mostly comes from the tiny baryon-to-photon number density. This shows that, even though the plasma temperature is smaller than the binding energy, there are yet too many high-energy photons from the tail of

the distribution inhibiting deuterium formation. From Eq. (2.41) we see that the factor η_B^{A-1} further suppresses the number density of a heavier nucleus. Moreover, the ratio $\frac{n_{^2\mathrm{H}}}{n_B}$ is approximately 1 only at a temperature $T \sim 0.07\,\mathrm{MeV}$.

Nuclides with mass number $A \geq 3$ need the presence of deuterium[3] d in order to be created, and this nuclide is forged through the reaction

$$p + n \leftrightarrows d + \gamma, \tag{2.42}$$

which depends on the number of neutrons and protons, being the former less abundant because of its larger mass. In fact, if local thermodynamic equilibrium holds, we can easily obtain that the neutron-to-proton number density

$$\frac{n}{p} = \frac{n_n}{n_p} \approx \mathrm{e}^{-\frac{\Delta m}{T}}, \tag{2.43}$$

where $\Delta m = m_n - m_p \approx 1.3\,\mathrm{MeV}$. The balance between protons and neutrons is maintained through the weak reactions

$$\begin{aligned} n &\leftrightarrows p + e^- + \bar{\nu}_e, \\ \nu_e + n &\leftrightarrows p + e^-, \\ e^+ + n &\leftrightarrows p + \bar{\nu}_e, \end{aligned} \tag{2.44}$$

until weak interactions become too slow, at a temperature $T \lesssim T_{\mathrm{dec}} \sim 0.7\,\mathrm{MeV}$, and the neutron-to-proton ratio freezes out at a value

$$\left.\frac{n}{p}\right|_{\mathrm{dec}} = \mathrm{e}^{-\frac{\Delta m}{T_{\mathrm{dec}}}} \sim \frac{1}{6}. \tag{2.45}$$

From this moment, free neutrons decay into protons reducing the fraction n/p. However, although the synthesis of deuterium (2.42) is suppressed because of the large amount of photons from the tail of their energy distribution compared to the baryon density, this element is already being produced at $T \lesssim T_{\mathrm{dec}}$. This causes neutrons to bind in deuterium nuclei and other nuclides whose production is also triggered. Therefore, the neutron-to-proton ratio reduction is effectively stopped when all remaining neutrons are bound into primordial nuclides, reaching a final value $n/p \sim 1/7$. As we have already mentioned, nuclides with $A \geq 3$ need the presence of d, which means that neutron decay is stopped at $T \sim 0.07\,\mathrm{MeV}$ when $n_{^2\mathrm{H}}/n_B \approx 1$.

[3]We name deuterium indistinctly d and $^2\mathrm{H}$ along the text of this thesis.

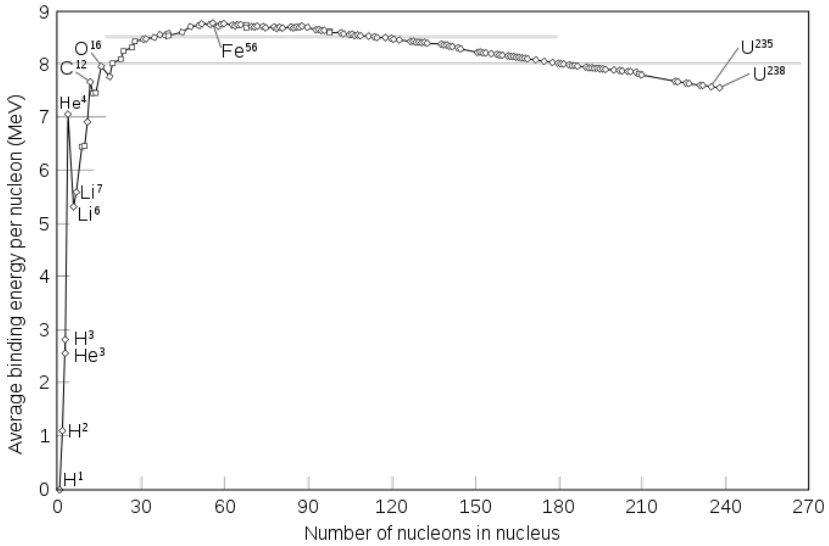

Figure 2.3: Average binding energy per nucleon per number of nucleons.

Once deuterium is produced, a chain reaction evolves quite fast into the production of heavier nuclides such as helium (^{3}He and ^{4}He) and a bit of lithium (^{7}Li). Other light nuclides are also synthesised, but in small quantities and most of them quickly decay into the lightest ones. The expansion of the Universe, together with the lack of stable nuclides with $A = 5$ and $A = 8$, hinders the yield of heavier elements. Among the lightest nuclides, ^{4}He is the one with the largest binding energy per nucleon (see figure 2.3), which translates into a great production of this element with respect to the others. In fact, if we assume that only ^{4}He and hydrogen[4] H are produced after primordial nucleosynthesis, all neutrons are bound in helium nuclei and the remaining protons form hydrogen nuclei. Therefore, defining the fraction of the number density of an element n_i with respect to that of hydrogen n_{H} as

$$X_{i,\mathrm{H}} \equiv \frac{n_i}{n_{\mathrm{H}}}, \tag{2.46}$$

and considering that $n/p \sim 1/7$ after freeze out of weak interactions,

$$X_{p,\mathrm{H}} = \frac{n_{^4\mathrm{He}}}{n_{\mathrm{H}}} = \frac{n_n/2}{7n_n - n_n} = \frac{1}{12}. \tag{2.47}$$

[4]Do not confuse the Hubble parameter H with the symbol of an hydrogen nucleus H.

From this we can obtain a very good approximation of the helium mass fraction

$$Y_p \approx \frac{4n_{^4\mathrm{He}}}{n_{\mathrm{H}} + 4n_{^4\mathrm{He}}} = \frac{4X_{p,\mathrm{H}}}{1 + 4X_{p,\mathrm{H}}} = 0.25, \tag{2.48}$$

where we have assumed $m_p \simeq m_n$.

A complete evolution of the reactions that generate the different nuclides during BBN implies the solution of a set of differential equations that can not be solved analytically. If we consider N_{nuc} species of nuclides and normalise their number densities n_i with respect to the number density of baryons n_B,

$$X_{i,B} = \frac{n_i}{n_B}, \qquad i = n, p, {}^2\mathrm{H}, {}^3\mathrm{He}, ..., \tag{2.49}$$

then the equations that we need to solve involve the conservation of the total baryon number per comoving volume,

$$\dot{n}_B = -3Hn_B; \tag{2.50}$$

the N_{nuc} Boltzmann equations describing the evolution of each species,

$$\dot{X}_{i,B} = \sum_{j,k,l} N_i \left(\Gamma_{kl\to ij} \frac{X_{k,B}^{N_k} X_{l,B}^{N_l}}{N_k! N_l!} - \Gamma_{ij\to kl} \frac{X_{i,B}^{N_i} X_{j,B}^{N_j}}{N_i! N_j!} \right), \tag{2.51}$$

and the cosmological charge neutrality in terms of the electron chemical potential,

$$n_B \sum_j Z_j X_{j,B} = n_{e^-} - n_{e^+}, \tag{2.52}$$

where Z_j is the electric charge of the nucleus j.

In Eq. (2.51) N_i is the number of nuclides of type i entering a given reaction (analogously of type j, k and l), whereas the Γ's stand for the reaction rates. For instance, when considering the decay of the species i, $N_i = 1$, $N_j = 0$ and $\Gamma_{i\to jk}$ is the inverse lifetime of the nuclide i. On the other hand, a two-body collision is described by $N_i = N_j = N_k = N_l = 1$ and in this case $\Gamma_{ij\to kl}$ denotes the thermal average of the product of the cross section times the $i - j$ relative velocity, $\langle \sigma_{ij\to kl}\, v \rangle$.

The set of equations must be completed by the Hubble parameter (Eq. (2.19)), evaluated during radiation domination, and the conservation of the total energy density (Eq. (2.11)).

		$A-Z$								
		0	1	2	3	4	5	6	7	8
	0		n							
	1	H	^{2}H	^{3}H						
	2		^{3}He	^{4}He						
	3				^{6}Li	^{7}Li	^{8}Li			
Z	4				^{7}Be		^{9}Be			
	5				^{8}B		^{10}B	^{11}B	^{12}B	
	6						^{11}C	^{12}C	^{13}C	^{14}C
	7						^{12}N	^{13}N	^{14}N	^{15}N
	8							^{14}O	^{15}O	^{16}O

Table 2.2: Nuclei of elements whose abundances are typically tracked in BBN codes.

Given the fast decrease in density of the nuclei with an increasing number of nucleons A, the numerical codes computing their abundances usually account for a small amount of elements. Table 2.2 shows the nuclides typically tracked in BBN codes.

The evolution of the main nuclides, in terms of their number density normalised to the number density of protons, is shown in Fig. 2.4. The tag M/H stands for *metals*, which here is considered to be the sum of the elements with $Z > 4$. The abundance of ^{4}He is provided as the *helium mass fraction*, approximated[5] to be

$$Y_p \approx \frac{4n_{^4\mathrm{He}}}{n_B}. \tag{2.54}$$

Since neutrinos decoupled just before primordial nucleosynthesis occurred, special care must be taken when dealing with them. In particular, their distribution functions slightly deviate from an equilibrium form. Although neutrino decoupling is discussed in detail in chapter 3, we can advance its importance from the point of view of primordial nucleosynthesis. Neutrinos affect BBN in three different ways:

[5]The true helium mass fraction

$$Y_m = \frac{m_{^4\mathrm{He}} n_{^4\mathrm{He}}}{\sum_i m_i n_i}, \tag{2.53}$$

where i are all elements, differs from our definition of Y_p in Eq. (2.54) by a 0.5%.

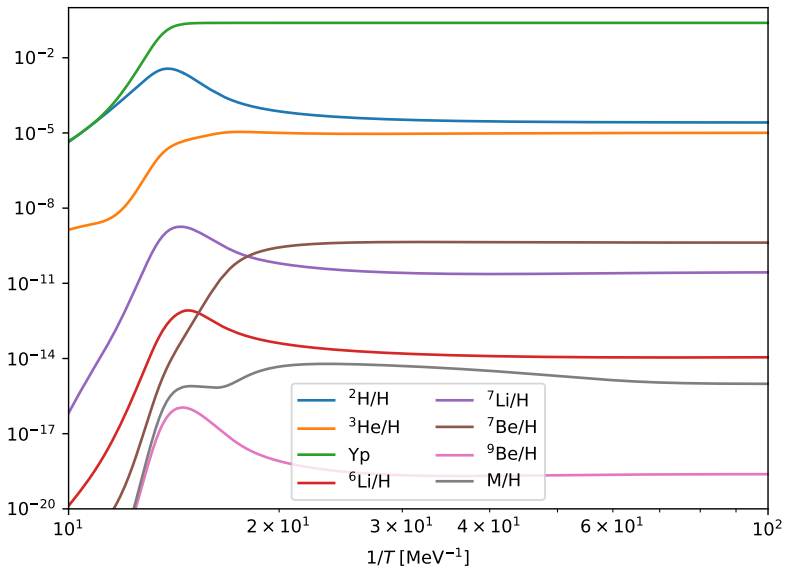

Figure 2.4: Evolution of the abundances of the light elements produced during BBN, represented by the number density of each nuclide normalised to that of protons. Elements with $Z > 4$ are summed in the contribution M/H and the abundance of ^{4}He is expressed as the helium mass fraction Y_p defined in Eq. (2.54). All abundances have being computed using the BBN code `PArthENoPE` [87, 88] for a baryon-to-photon ratio $\eta_B = 6 \cdot 10^{-10}$.

1. A larger contribution from neutrinos to the energy density of radiation $\rho_{\rm r}$, which translates into a larger value of $N_{\rm eff}$, would speed up the expansion of the Universe H. The opposite effect would happen if neutrinos contribute less to $\rho_{\rm r}$.

2. A modification of the energy distribution of electron-type neutrinos implies a change in the neutron-to-proton ratio n/p, since electron neutrinos enter in the weak interactions leading their equilibrium.

3. A delayed freeze out of weak interactions, induced by a modification of the tail of neutrino distribution towards larger energies, also influence the neutron-to-proton ratio.

When the amount of neutrinos is enhanced at higher energies, the second and third effects point towards the same direction: a decrease of n/p. This is so

because an effectively stronger weak interaction delays the moment of n/p freeze out, which happens at a lower temperature, and from Eq. (2.43) we see that the expansion of the Universe dilutes neutrons more efficiently than protons. However, the same change in neutrino distributions would have an opposite impact on n/p from the point of view of the first enumerated effect: A larger amount of more energetic neutrinos implies a larger energy density, what means a higher expansion rate; therefore, weak interactions become less efficient than the expansion of the Universe at higher temperatures, and the neutron-to-proton ratio freezes out with a larger value. As we will show later through different scenarios (very-low-reheating in chapter 4 and mixed neutrino statistics in chapter 5), in general the effect through weak interactions (second and third points) is more important and its influence wins over the change in the expansion rate (first point).

It is worth mentioning that during the development of the works included in this thesis we have also improved the `PArthENoPE`[6] code, whose update is presented in Ref. [88]. The main changes have been the creation of a graphical user interface (GUI) and the substitution of the previously used NAG libraries (which in spite of being very powerful are not easily available) by more portable ones.

2.3 Late time cosmology

Although the works presented in this thesis that are related to cosmology are focused on the study of neutrino properties, which mainly depends on the physics at neutrino decoupling (and therefore before BBN), a lot of useful information can be also extracted from processes taking place at later cosmological times. In particular, the study of the CMB anisotropies, together with the statistical distribution of cosmological structures, can be used complementary to nuclide-abundance measurements of BBN yields in order to constrain the parameters of some models. In the present thesis we make use of them in our study of non-standard scenarios (chapters 4 and 5).

2.3.1 Cosmic microwave background

The expansion of the Universe cooled down the cosmic plasma. From Friedmann equation (2.19) we notice that its earliest stages were dominated by radiation. This predominance of radiation is followed by a phase of matter domination

[6]Public Algorithm Evaluating the Nucleosynthesis of Primordial Elements.

at a redshift (given the measured values of $\Omega_{\mathrm{m},0}$ and $\Omega_{\mathrm{r},0}$)

$$1 + z_{\mathrm{rm}} = \frac{\Omega_{\mathrm{m},0}}{\Omega_{\mathrm{r},0}} \sim 3400, \tag{2.55}$$

which corresponds to a temperature $T_{\mathrm{rm}} = 0.8\,\mathrm{eV}$. If we recall that the binding energy of hydrogen is 13.59 eV, we would naively expect no free electrons at the time of matter-radiation equality. However, similarly to what we discussed in section 2.2.3 about BBN, there are enough photons in the energetic tail of its distribution to make the binding ineffective. For this reason, free electrons get bound to ionised nuclei, in a process called *recombination*, at a redshift $z_{\mathrm{reco}} \sim 1100$. This value corresponds to a temperature $T_{\mathrm{reco}} \sim 0.3\,\mathrm{eV}$.

When free electrons are captured by the ionised nuclei, photons no longer interact through Thomson scattering and they free stream. This leads to the formation of their *last scattering surface*, which follows a perfect black-body spectrum due to the previous state of local thermodynamic equilibrium. This relic radiation, homogeneously and isotropically distributed (in agreement with the cosmological principle) is what we call the *cosmic microwave background*. Its temperature today has been measured to be [89]

$$T_0 = (2.7255 \pm 0.0006)\ \mathrm{K}, \tag{2.56}$$

with small deviations of order μK depending on the direction. Despite being so small, these anisotropies carry a useful wealth of information, encoded in the power spectrum coefficients of the expansion in Legendre polynomials P_ℓ of the two-point correlation function. For instance, in the case of the angular fluctuations $\Delta T(\hat{n})/\overline{T}$ of the temperature,

$$\left\langle \frac{\Delta T(\hat{n})}{\overline{T}} \frac{\Delta T(\hat{n}')}{\overline{T}} \right\rangle = \sum_{\ell=0}^{\infty} \frac{2\ell+1}{4\pi} C_\ell^{TT} P_\ell\left(\hat{n}\cdot\hat{n}'\right), \tag{2.57}$$

where $\overline{T}$ is the average CMB temperature and C_ℓ^{TT} the coefficient of the multipole ℓ. Similar expressions can be written for the polarisation field and its correlation with temperature.

The Planck satellite has recently measured the power spectra coefficients (see Fig. 2.5), and it has been able to determine the parameters of the standard cosmological model with unprecedented accuracy. Planck data on CMB anisotropies are used in order to put constraints on the relevant parameters in some of the works discussed in this thesis.

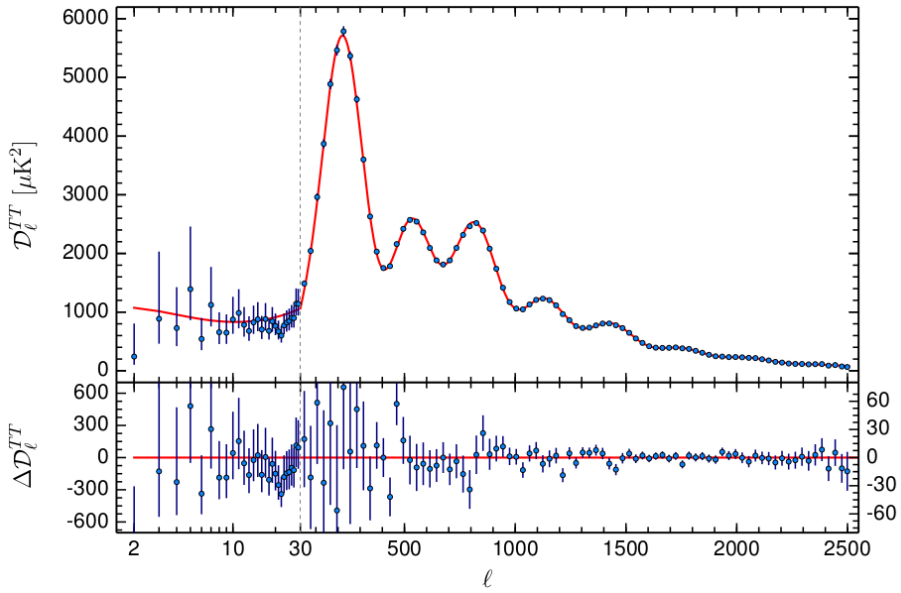

Figure 2.5: The CMB TT power spectrum measured by the Planck satellite, in terms of $\mathcal{D}_\ell^{TT} \equiv \ell\,(\ell+1)\,C_\ell^{TT}/\,(2\pi)$. The blue points are Planck data including 1σ uncertainties and the red line corresponds to the best fit in the ΛCDM framework. The lower panel shows the residuals with respect to the best fit, where the vertical scale is different for multipoles smaller or larger than $\ell = 30$. Figure taken from [90].

2.3.2 Large-scale structure formation

The epochs between the last scattering surface and the formation of the first stars are usually known as *dark ages*. During this time, the potential wells of DM attracted baryons into them. Therefore, from small perturbations in density

$$\delta = \frac{\rho - \bar{\rho}}{\bar{\rho}}, \tag{2.58}$$

where $\bar{\rho}$ is the average density of the Universe, the current large-scale structures (LSS) formed [91].

To understand the formation of first galaxies and their impact on the Universe's evolution, one needs to model and follow the non-linear evolution of perturbations. Many numerical simulations (N-body) have been performed for this purpose. However, simpler analytical models also help us to understand the

formation of LSS. For example, the collapse model allows us to compute the linearised density contrast of a shell of dark matter collapsing at redshift z_c for a spherical top-hat perturbation [92].

Experimentally, observations of LSS are carried out by instruments that observe millions of objects at different redshifts. The statistical properties of the corresponding surveys encode a great wealth of information. Among other things, we can access the early Universe (and the origin of LSS), in particular the *baryon acoustic oscillations* (BAO). The matter overdensities of the primordial plasma attracted more matter into them; this accretion at a stage of the Universe when interactions were very common generated outward electromagnetic pressure, and the interplay of these two forces made baryons oscillate analogously to sound waves in the air. The imprints of BAO can be measured not only in the distribution of LSS, but also from the Lyman-α absorption lines of hydrogen clouds and even from the 21 cm emission line of neutral hydrogen.

2.3.3 Minimal ΛCDM model

The minimal model that can explain the evolution of the Universe after the Big Bang is the ΛCDM model, in which dark energy takes the form of a cosmological constant and dark matter is cold (non-relativistic). Its great success is accomplished with only six parameters whose values are perfectly fit from CMB observations. Only a few tensions remain between the measurements from CMB anisotropies and other cosmological observations, like those constraining BAO or BBN.

The six parameters of the ΛCDM model are the DM and baryon energy densities, $\omega_{\rm dm} = \Omega_{\rm dm} h^2$ and $\omega_{\rm b}$; the optical depth to reionisation τ; the ratio of the sound horizon to the angular diameter distance at decoupling θ, and the tilt and amplitude of the power spectrum of primordial curvature perturbations n_s and A_s. Here we list the main aspects of the parameters:

- *DM and baryon energy densities* $\omega_{\rm dm}$ and $\omega_{\rm b}$, which account for the amount of matter in the Universe. Their quantities are relevant to determine the time of matter dominance as well as the creation and evolution of LSS.

- *Optical depth to reionisation* τ. During matter domination baryons fall into the gravitational potential of DM and first stars are formed. Therefore the neutral elements (in particular hydrogen) reionise and the Cosmos turns into an ionised plasma once more, although very diluted due to the cosmic expansion. Measuring the optical depth of photons to reionisation we can have an estimate of the redshift in which this phase occurred.

- *Angular size of the sound horizon* θ. In the peak location of the CMB anisotropies there is an angular scale encoded, which corresponds to the distance that the sound waves could have travelled before reionisation. This connects with BAO.

- *Amplitude and tilt of the primordial power spectrum* $P(k) = A_s(k/k_0)^{n_s-1}$, which are important for inflation, that predicts a nearly scale-invariant power spectrum (with $n_s \sim 1$). Both A_s and n_s can be related to the amplitude and shape of the inflaton potential.

Other useful quantities, like the expansion rate, can be derived from these six.

2.3.4 Extensions of the minimal model: $\sum m_\nu$ and $N_{\rm eff}$

The six parameters of the ΛCDM model can fit very well cosmological data. However, some extensions to this minimal model are useful in order to access other physical quantities. One extension that can be made regards neutrino masses, which are zero in the minimal ΛCDM as in the SM of particle physics.

Since the mass scale of neutrinos can not be determined by oscillation experiments, a great effort is put in other ways of measuring its value. For instance, neutrino masses can be studied through precise measurements of the endpoint of β-decay spectra, which is shifted at lower energies an amount equal to the neutrino mass. This is the chosen technique in the KATRIN experiment [93], which uses molecular tritium as its β-decay source. Tritium could also be exploited in a future experiment, PTOLEMY [94], whose main purpose is however the detection of relic neutrinos through their capture in this isotope.

Another way of measuring neutrino masses, provided that they are Majorana particles, is by means of the measurement of the lifetime of the $0\nu\beta\beta$ decay of some nuclei, which is connected with neutrino masses through the effective Majorana mass (Eq. (1.70)).

From cosmology it is also possible to access neutrino masses. Due to their expected values, smaller than for any other known massive particle, neutrinos behave as radiation at the early Universe but act as matter when they become non-relativistic. Depending on the moment in which this transition happens and on the value of the sum of their masses, they affect in a given way both the CMB anisotropies and LSS formation. From the point of view of CMB anisotropies, the general effect is a damping in the tail of the power spectrum (see Fig. 2.6), while regarding LSS, their formation is impeded for smaller masses due to neutrino free-streaming. The current upper bound at 95% CL, including Planck CMB temperature and polarisation data only, is $\sum m_\nu = m_1 + m_2 + m_3 < 0.34\,\text{eV}$. If

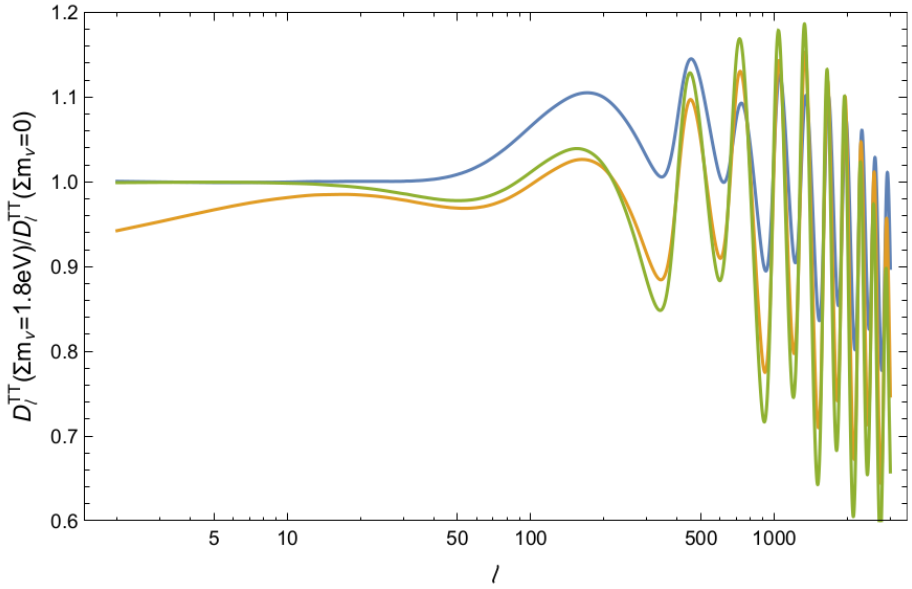

Figure 2.6: CMB TT power spectra for a cosmology with degenerate neutrinos, with $m_\nu = 0.6\,\mathrm{eV}$ each, with respect to the case when neutrinos are massless. In all curves $\Omega_{\mathrm{tot}} = 1$, which is forced by changing h (green), Ω_Λ (yellow) or ω_c (blue). This shows the degeneracy between different parameters with neutrino masses. Figure taken from [95].

Planck high-ℓ temperature, low-ℓ polarisation, CMB lensing and BAO are also accounted for, the limit strengthens up to $\sum m_\nu < 0.17\,\mathrm{eV}$ [96].

Other cosmological analyses conclude that even the minimal value of $\sum m_\nu$ in the inverted mass hierarchy is disfavoured by some combinations of cosmological data, see e.g. Ref. [97]. Anyway, one must remember that all these limits are obtained in the context of the ΛCDM model, and may change if a different cosmological model is considered. The changes range from loosen upper limits for simple extensions of the ΛCDM model (see e.g. Refs. [98, 99]) to a preference for a positive $\sum m_\nu$ when one considers some kind of modified gravity, see e.g. Refs. [100, 101]. In the opposite direction, other analyses try to understand the model dependence and build model independent constraints [102].

Concerning the energy density of radiation (relations (2.26) and (2.27)), we can now parametrise the contribution of neutrinos to ρ_{r} in the early Universe

after the electron-positron annihilation phase,

$$\rho_{\rm r} = \left(1 + N_{\rm eff}\frac{7}{8}\left(\frac{4}{11}\right)^{4/3}\right)\rho_\gamma, \tag{2.59}$$

where $N_{\rm eff}$ is known as the *effective number of neutrinos*. In the approximation that neutrinos keep an exact Fermi-Dirac distribution function after decoupling, and assuming that the freeze out was complete when $e^\pm$ annihilated (with the further consideration that only photons and neutrinos contribute to radiation afterwards), the value $N_{\rm eff} = 3$ is obtained. A slightly different value is found in chapter 3 including other effects, such as the fact that neutrino decoupling is not instantaneous and that they propagate in a plasma rather than in vacuum. However, before LEP experiments at CERN measured the number of light, active (weakly interactive) neutrinos to be $N_\nu = 2.9840 \pm 0.0082$ [103], $N_{\rm eff}$ gave us an idea of the existing amount of light, active neutrinos, which is why this parameter nowadays is called effective number of neutrinos. Actually, $N_{\rm eff}$ measures *any* contribution different from photons to the energy density in the early Universe, in terms of the contribution of a relativistic fermion that decoupled instantaneously before $e^\pm$ annihilations.

The most precise experimental value of this parameter is currently obtained from CMB anisotropies by the Planck satellite (PlanckTT,TE,EE + SIMlow) [96],

$$N_{\rm eff}^{\rm Planck} = 2.91^{+0.39}_{-0.37}\ (95\%\,{\rm CL})\,, \tag{2.60}$$

although the central value and error estimate vary depending on the polarisation maps accounted for. Forthcoming cosmological data from future CMB experiments, large-volume galaxy surveys, etc, are expected to improve the sensitivity on $N_{\rm eff}$ down to values such as $\sigma\left(N_{\rm eff}\right) \leq 0.04$ [104].

2.4 Dark matter

The energy density of the Universe today is dominated by its dark components. One of them (the dark energy) behaves as a fluid with negative pressure, and the other one (the dark matter) as a gas made of non-relativistic objects.

Observational evidences in favour of dark matter started very early. Fritz Zwicky studied in 1933 the properties of the Coma cluster, measuring the distance and velocity of galaxies within the cluster. Applying the virial theorem he estimated its mass, and he found that it was larger than its visible mass by more

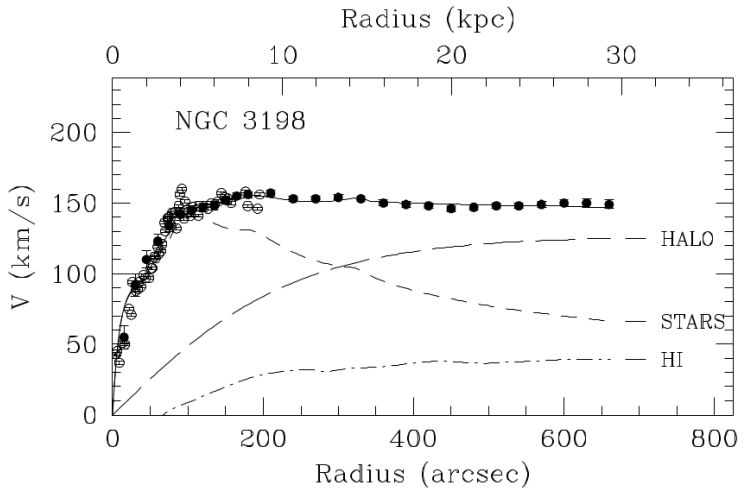

Figure 2.7: Best-fit mass model of NGC 3198. Dots are experimental data and the solid line represents the sum of the components: a DM halo (long dashed), stars (short dashed) and gas (dashed dotted) expressed in terms of hydrogen (HI). Figure taken from [105].

than two orders of magnitude. Then he concluded that this difference was due to some invisible mass in which the galaxies of the cluster were embedded.

Nowadays there are other hints pointing towards the existence of DM. Among them, probably the most famous are the rotational curves of spiral galaxies. The velocity of a test mass m orbiting at a distance r inside a galaxy with mass distribution $M(r)$ is

$$v = \sqrt{\frac{GM(r)}{r}}. \tag{2.61}$$

At sufficiently large distances we expect $v \propto 1/\sqrt{r}$, but a much flatter profile is measured instead. This can be explained if a dark, invisible halo is added to the gravitational contributors of galaxies (see Fig. 2.7).

Other proofs in favour of DM comes from the Bullet cluster, which consists of two colliding clusters of galaxies; gravitational lensing; the anisotropies of the CMB, from which a current amount of $\Omega_{\rm dm} \sim 0.25$ can be inferred, and the baryon acoustic oscillations described before.

Physicists explain the presence of DM as a new, non-baryonic particle arising from some extension to the standard model of particle physics. If this is the

case, the search for this component of the Universe can be broaden to a whole new set of experiments, apart from those aiming at its gravitational imprints. For instance, direct searches can be performed looking at the recoil energy of nuclei after the scattering of a dark matter particle, and in models in which both DM particles and antiparticles are currently present in similar amounts, its presence could be observed indirectly in astroparticle excesses (due to DM self annihilation), especially from dense regions like the galactic centre. In addition, depending on the properties of the particles that constitute the DM, they could be created in accelerators. However, despite the great effort devoted to this search, no dark matter particle has been found so far. Other attempts to explain the gravitational puzzle associated to DM rely on modified theories of gravity.

From the observation of galaxy rotation curves [106,107] and N-body numerical simulations [108,109], one may conclude that the shape of the DM distribution in galaxies follows a universal, spherical profile. Given the extremely weak interaction character associated to DM, a spherical symmetry is a very good approximation, since there are no tidal forces that can form a dark matter disc. In cosmological simulations where the properties of large scale structure formation are studied, the position and velocity of N representative massive bodies (which usually only interact gravitationally) is followed. Commonly these objects represent galaxies, and they are described only in terms of its dark matter mass. Several distributions are used, which mainly differ in the treatment of the central region. Along this thesis we make use of three of such parameterisations:

- An isothermal profile [110]

$$\rho_{\rm iso}(r) = \mathcal{N}_{\rm iso} \left(1 + \frac{r}{r_s}\right)^{-2}, \tag{2.62}$$

  where the normalisation $\mathcal{N}_{\rm iso}$ sets the value of the density at the galactic centre, that falls down with a logarithmic slope of -2 from a scale radius r_s.

- A Navarro-Frenk-White (NFW) profile [111,112]

$$\rho_{\rm NFW}(r) = \mathcal{N}_{\rm NFW} \left(\frac{r_s}{r}\right) \left(1 + \frac{r}{r_s}\right)^{-2}, \tag{2.63}$$

  with a logarithmic slope that now varies from -1 at a radius below r_s to -3 at larger radii. This profile diverges at the centre. In order to avoid this issue, it is common (in particular in numerical codes) to fix a radius for which the density is kept constant at smaller values of r.

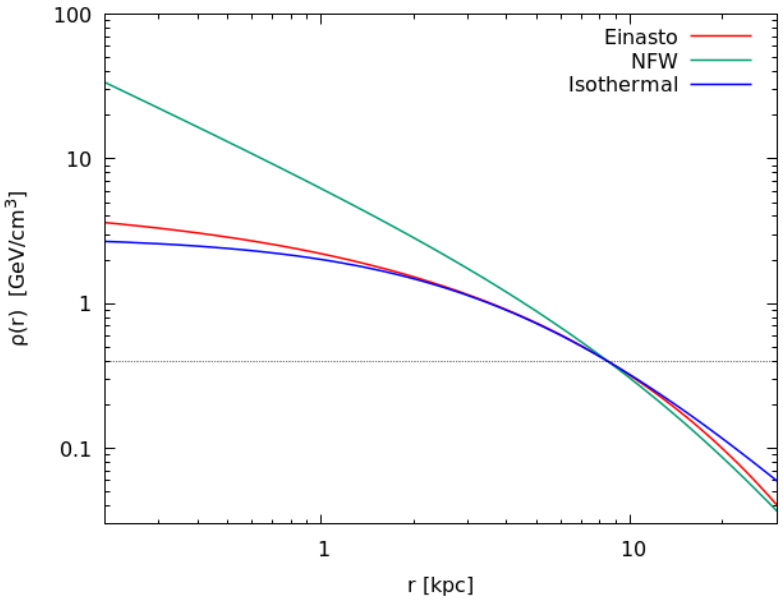

Figure 2.8: Energy density profiles of DM, normalised so $\rho_\oplus = 0.4\,\mathrm{GeV/cm^3}$ evaluated at $r_\oplus = 8.5\,\mathrm{kpc}$. The isothermal profile is chosen for a scale radius $r_s = 5\,\mathrm{kpc}$ according to Eq. (2.62), the NFW profile is parameterised with $r_s = 20\,\mathrm{kpc}$ in Eq. (2.63), and the parameters $r_s = 20\,\mathrm{kpc}$ and $\alpha = 0.5$ are chosen for the Einasto profile (2.64).

- An Einasto profile [113]

$$\rho_{\mathrm{Ein}}(r) = \mathcal{N}_{\mathrm{Ein}} \exp\left\{-\frac{2}{\alpha}\left(\left(\frac{r}{r_s}\right)^{\alpha} - 1\right)\right\}, \tag{2.64}$$

  where $\mathcal{N}_{\mathrm{Ein}} = \rho_{\mathrm{Ein}}(r_s)$ and α controls the slope of the profile and its value at the centre.

Figure 2.8 shows the three parameterisations of a DM profile normalised so that $\rho_\oplus(r_\oplus = 8.5\,\mathrm{kpc}) = 0.4\,\mathrm{GeV/cm^3}$, where $\rho_\oplus$ is the estimated DM density at the Earth location $r_\oplus$ from the galactic centre (see e.g. Refs. [114, 115]).

Chapter 3

Relic neutrino decoupling

The process of neutrino decoupling was briefly introduced in section 2.2.2. In this chapter we study the different effects leading to distortions with respect to the approximated scenario when neutrinos are assumed to decouple instantaneously. In particular we focus on the work published in Ref. [116], where we revisited the effect of neutrino oscillations, using the density matrix formalism and relaxing for the first time some approximations related to its non-diagonal terms. Although this relaxation has almost no impact on the final value of the effective number of neutrinos (defined in section 2.3.4), some deviations on the individual distortions in the flavour-dependent energy densities are found. We also study how much neutrino decoupling can be affected by the presence of a non-standard interaction (NSI) between these neutral leptons and electrons and positrons.

3.1 Instantaneous decoupling

As mentioned in section 2.2.2, neutrinos decoupled just before electron-positron pairs annihilated in the primeval plasma. A first (and very good) approximation is to treat both processes as completely independent, assuming that neutrino freeze-out happened instantaneously at $T_{\nu,\mathrm{dec}} \sim 1\,\mathrm{MeV}$ and therefore their contact with the cosmic fluid was completely lost when $e^- e^+$ pairs annihilated.

This leads to an enhancement of the photon temperature T_γ over the neutrino "temperature" T_ν, that can be computed from entropy conservation in a comoving volume (because the expansion is adiabatic), so that at two different times, implying two different scale factors a_1 and a_2, we have the relation

$$s(a_1)a_1^3 = s(a_2)a_2^3. \tag{3.1}$$

Before e^+e^- annihilations, $T_\gamma = T_\nu$. After electrons and positrons reheat photons, they behave as non-relativistic particles and their distribution is further suppressed by $\exp(-m_e/T_\gamma)$. Thus, except for a tiny fraction related to the baryon-to-photon density $\eta_{\rm B}$, practically all $e^\pm$ disappear. Since the neutrino contribution to entropy per comoving volume is not affected by these annihilations, we can follow the evolution of photon temperature during this stage from the conservation of entropy in the electromagnetic plasma,

$$s_{e^\pm,\gamma}\, a^3 = \frac{2\pi^2}{45}\left(\frac{T_\gamma}{T_\nu}\right)^3 g_{s,(e^\pm,\gamma)}(T), \tag{3.2}$$

where we have considered that $T_\nu \sim a^{-1}$. From relation (2.28) and the definition of entropy in Eq. (2.25) we can compute the entropy degrees of freedom for $e^\pm$ and photons,

$$g_{s,(e^\pm,\gamma)}(T_\gamma) = 2 + \frac{45}{\pi^4}\int_0^\infty \left(\sqrt{x^2+\frac{m_e^2}{T_\gamma^2}} + \frac{x^2}{3\sqrt{x^2+\frac{m_e^2}{T_\gamma^2}}}\right)\frac{x^2 {\rm d}x}{\exp\sqrt{x^2+\frac{m_e^2}{T_\gamma^2}}+1}, \tag{3.3}$$

where we remind that T_γ is the temperature of the cosmic electromagnetic bath. The value of $g_{s,(e^\pm,\gamma)}$ converges towards what we expect (see Fig. 3.1). On the one hand, when $T_\nu = T_\gamma \gg m_e$ both photons and $e^\pm$ contribute, so

$$g_{s,(e^\pm,\gamma)}(T_\gamma \gg m_e) \to 2 + \frac{7}{8}4 = \frac{11}{2}. \tag{3.4}$$

On the other limit, when $m_e \gg T_\gamma > T_\nu$ the degrees of freedom are only those of photons, therefore

$$g_{s,(e^\pm,\gamma)}(T_\gamma \ll m_e) \to 2. \tag{3.5}$$

From conservation of relation (3.2) we have that

$$\left(\frac{T_\gamma}{T_\nu}\right)^3 g_{s,(e^\pm,\gamma)}(T) = \text{constant}, \tag{3.6}$$

so when electron-positron annihilations are complete and $T_\gamma \ll m_e$,

$$\frac{11}{2} = \left(\frac{T_\gamma}{T_\nu}\right)^3 2, \tag{3.7}$$

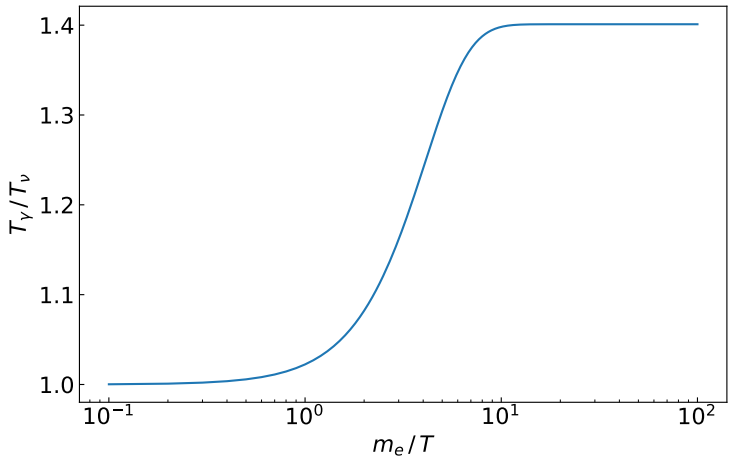

Figure 3.1: Increment of photon temperature over that of neutrinos during electron-positron annihilation in the instantaneous decoupling approximation.

that leads to the well-known quantity

$$\frac{T_\gamma}{T_\nu} = \left(\frac{11}{4}\right)^{1/3} \simeq 1.40102. \tag{3.8}$$

Given the value of T_γ^0 today (2.56), from this relation $T_\nu^0 = 1.95\,\mathrm{K}$.

3.2 Finite temperature QED corrections

The fact that particles in the early Universe move inside a plasma with temperature T makes the consideration of quantum electrodynamics (QED) corrections important. These corrections imply the modification of the dispersion relations

$$E_i^2 = k^2 + m_i^2 + \delta m_i^2(T) \tag{3.9}$$

of the particles (labeled as i), which translates into an effective variation of the electron mass squared $\delta m_e^2(T)$ and the acquisition by photons of an effective mass $\delta m_\gamma^2(T)$. At the temperatures of interest, $T \lesssim 1\,\mathrm{MeV}$, neutrino interactions are suppressed and any correction to their dispersion relation can be neglected.

As shown in [117, 118], photons acquire an effective mass given by

$$\delta m_\gamma^2(T) = \frac{8\alpha}{\pi}\int_0^\infty \mathrm{d}k \frac{k^2}{\sqrt{k^2+m_e^2}} \frac{1}{\left(\mathrm{e}^{\sqrt{k^2+m_e^2}/T}+1\right)} \tag{3.10}$$

at $\mathcal{O}(\alpha)$, being $\alpha \equiv e^2/(4\pi)$ the finite structure constant (where e is the electromagnetic charge of the electron). Additionally, electrons get a correction to their mass squared in the form

$$\begin{aligned}\delta m_e^2(p,T) = &\frac{2\pi\alpha T^2}{3} + \frac{4\alpha}{\pi}\int_0^\infty \mathrm{d}k \frac{k^2}{\left(\mathrm{e}^{\sqrt{k^2+m_e^2}/T}+1\right)\sqrt{k^2+m_e^2}} \\ &- \frac{2m_e^2\alpha}{\pi p}\int_0^\infty \mathrm{d}k \frac{k}{\sqrt{k^2+m_e^2}} \ln\left|\frac{p+k}{p-k}\right| \frac{1}{\left(\mathrm{e}^{\sqrt{k^2+m_e^2}/T}+1\right)}\end{aligned} \tag{3.11}$$

up to the same order in α. The third term in this expression gives δm_e^2 a dependence on the momentum p. Nevertheless, the contribution of this term represents less than 10% of δm_e^2, so in favour of a faster numerical performance we simply neglect it.

Corrections (3.10) and (3.11) change the total pressure and energy density of the plasma [119, 120],

$$P = \frac{T}{\pi^2}\int_0^\infty \mathrm{d}k\, k^2 \ln\left(\frac{\left(1+\mathrm{e}^{-E_e/T}\right)^2}{\left(1-\mathrm{e}^{-E_\gamma/T}\right)}\right), \tag{3.12}$$

$$\rho = -P + T\frac{\mathrm{d}P}{\mathrm{d}T}, \tag{3.13}$$

where the energies E_e and E_γ are obtained from the modified dispersion relations (3.9).

Expanding P with respect to δm_γ^2 and δm_e^2 we obtain the first order correction

$$P^{(1)} = -\int_0^\infty \frac{\mathrm{d}k}{2\pi^2}\left(\frac{k^2\,\delta m_e^2(T)}{\left(\mathrm{e}^{\sqrt{k^2+m_e^2}/T}+1\right)\sqrt{k^2+m_e^2}} + \frac{k\,\delta m_\gamma^2}{2\left(\mathrm{e}^{k/T}-1\right)}\right), \tag{3.14}$$

from which the total pressure is

$$P = P^{(0)} + P^{(1)}, \tag{3.15}$$

where $P^{(0)}$ is the pressure for the non-interacting particle gas. Using Eq. (3.14) in Eq. (3.13) we also obtain the correction $\rho^{(1)}$ to the energy density.

Almost independently of which other corrections to the instantaneous approximation are included, those of finite temperature QED enlarge the value of $N_{\rm eff}$ by ~ 0.01.

3.3 Non-instantaneous decoupling without oscillations

The instantaneous decoupling approximation implies that neutrinos keep undistorted distribution functions f_{ν_α} after freezing out, where $\alpha = \{e, \mu, \tau\}$. This translates, from Boltzmann equations, into

$$(\partial_t - Hp\partial_p)\, f_{\nu_\alpha} = 0, \tag{3.16}$$

where t is the proper time, H the Hubble parameter and p the modulus of the neutrino momentum.

Henceforth along this chapter we adopt dimensionless comoving variables defined as follows:

$$x \equiv m_e\, R(t), \qquad y \equiv p\, R(t), \qquad z \equiv T_\gamma\, R(t), \tag{3.17}$$

where $R(t)$ plays the role of the scale factor when it is defined such that

$$R(t) = \frac{1}{T_\nu} = \frac{1}{T_\gamma} \tag{3.18}$$

at large temperatures, and $R(t) = 1/T_\nu$ when neutrinos decouple and lose its contact with the rest of the plasma, since photons are reheated because of $e^\pm$ annihilations. We remind the reader that T_ν is not a physical temperature since neutrino freeze-out, and it merely represents the temperature that a gas of fermions would have if its distribution function were that of decoupled neutrinos in the instantaneous approximation, being constantly diluted by the cosmological expansion. Therefore, our comoving variable x plays the role of cosmic expansion, y is the neutrino momentum in comoving space and z the enhancement of photon temperature with respect to T_ν. The use of these units is especially convenient for numerical calculations.

When neutrino decoupling is not treated instantaneously, some deviation from equilibrium appears in the distribution function of these particles. Denoting $\bar{\rho} = (x/m_e)^4\, \rho$ the energy density expressed in the comoving variables (3.17), one

can compute the deviation from equilibrium of each neutrino flavour as

$$\delta_{\nu_\alpha} = \frac{\bar{\rho}_{\nu_\alpha} - \bar{\rho}_{\nu_{\rm eq}}}{\bar{\rho}_{\nu_{\rm eq}}}, \tag{3.19}$$

where

$$\bar{\rho}_{\nu_\alpha} = \frac{1}{\pi^2}\int_0^\infty {\rm d}y\, y^3 f_{\nu_\alpha}(x,y) \tag{3.20}$$

and

$$\bar{\rho}_{\nu_{\rm eq}} = \frac{1}{\pi^2}\int_0^\infty {\rm d}y\, \frac{y^3}{{\rm e}^y+1} = \frac{7\pi^2}{120}. \tag{3.21}$$

Since relic neutrinos are ultra-relativistic particles at this epoch, we have considered $E_\nu = p$. We also take $f_\nu = f_{\bar{\nu}}$, assuming zero neutrino chemical potential and accounting for a number of internal degrees of freedom $g_{\nu_\alpha} = 2$ per flavour. Notice that this is valid for both Dirac and Majorana neutrinos, since in the first case we have left-chiral neutrinos and right-chiral antineutrinos, while in the second case there are both left and right-chiral neutrinos.

In order to compute the distortions in the distribution functions of neutrinos, we need the corresponding Boltzmann equations, that in comoving variables (3.17) read

$$\frac{\rm d}{{\rm d}x} f_{\nu_\alpha}(x,y) = \frac{1}{xH} I_{\rm coll}, \tag{3.22}$$

where

$$I_{\rm coll} = \frac{1}{2E_1}\int (2\pi)^4 \delta^{(4)}(p_1+p_2-p_3-p_4) F(f) S|\mathcal{M}|^2_{12\to 34} \prod_{i=2}^{4} \frac{{\rm d}^3\mathbf{p}_i}{2E_i(2\pi)^3} \tag{3.23}$$

is the collision integral for a process $1+2 \to 3+4$. We have expressed $I_{\rm coll}$ in physical variables for simplicity. In equation (3.23) p_i are the 4-momenta,

$$F(f) = f_3 f_4 (1-f_1)(1-f_2) - f_1 f_2 (1-f_3)(1-f_4) \tag{3.24}$$

is the statistical factor, including Pauli blocking of the final states since we are dealing with fermions, and $S|\mathcal{M}|^2_{12\to 34}$ is the matrix element squared summed over spins of all particles, except the first one. Finally, S represents the symmetry factor for identical particles.

Apart from Boltzmann equations, we need to account for the effect of expansion, which is encoded in the evolution of $z(x)$. This evolution is obtained from

the continuity equation (2.11) expressed in comoving variables (3.17),

$$\frac{\mathrm{d}z}{\mathrm{d}x} = \frac{\dfrac{x}{z}F_1(x/z) + G_1(x/z) - \dfrac{1}{2\pi^2 z^3}\displaystyle\int_0^\infty \mathrm{d}y y^3 \sum_{\alpha=e,\mu,\tau} \frac{\mathrm{d}f_{\nu_\alpha}}{\mathrm{d}x}}{\dfrac{x^2}{z^2}F_1(x/z) + F_2(x/z) + \dfrac{2\pi^2}{15} + G_2(x/z)}, \tag{3.25}$$

where the functions $F_1(w)$, $F_2(w)$, $G_1(w)$ and $G_2(w)$ are given in the appendix A. Among them, G_1 and G_2 appear because of finite temperature QED corrections. Therefore, in the instantaneous neutrino decoupling approximation, where $\mathrm{d}f_{\nu_\alpha}/\mathrm{d}x = 0$, the equation (3.25) looks simpler,

$$\frac{\mathrm{d}z}{\mathrm{d}x} = \frac{\dfrac{x}{z}F_1(x/z)}{\dfrac{x^2}{z^2}F_1(x/z) + F_2(x/z) + \dfrac{2\pi^2}{15}}, \tag{3.26}$$

and its resolution leads to the same behaviour of T_γ/T_ν shown in figure 3.1.

From the frozen values of δ_{ν_α} and $z(x)$, after electron-positron annihilations, the final effective number of neutrinos can be computed as

$$N_{\mathrm{eff}} = \left(3 + \delta_{\nu_e} + \delta_{\nu_\mu} + \delta_{\nu_\tau}\right)\left(\frac{11}{4}\right)^{4/3}\frac{1}{z^4}. \tag{3.27}$$

The results are shown in the tables and plots of section 3.5. Before flavour oscillations are taken into account, the final values entering Eq. (3.27) are $z = 1.39784$, $\delta_{\nu_e} = 0.0092$ and $\delta_{\nu_\mu} = \delta_{\nu_\tau} = 0.00392$, what gives $N_{\mathrm{eff}} = 3.045$.

3.4 Including three-flavour oscillations

The study of neutrino decoupling is more complex when flavour oscillations are taken into account. We need to deal with interacting particles in a medium with changing temperature due to the cosmic expansion, where the density of electrons and positrons decreases, and to this we need to add the fact that mass neutrino states are not eigenstates of the interaction hamiltonian, leading to flavour oscillations as explained in chapter 1.

Equations derived in this section and subsequent results, presented in section 3.5, were published in [116]. Both standard and non-standard scenarios involving non-standard neutrino interactions are discussed.

3.4.1 Boltzmann equations

The process of neutrino decoupling in the early Universe takes place at a temperature of the order of MeV, when weak interactions are no longer effective to keep neutrinos in thermal contact with electrons, positrons and, indirectly, with photons. It has been shown in previous works (see e.g. [121]) that neutrino oscillations become effective at similar temperatures, if the mixing parameters have the values required to explain the data from solar, atmospheric, reactor and accelerator neutrino experiments. In order to take into account the effects of both interactions and oscillations, we consider the evolution of the neutrino density matrix ϱ_p,

$$\varrho_p(t) = \begin{pmatrix} \varrho_{ee} & \varrho_{e\mu} & \varrho_{e\tau} \\ \varrho_{\mu e} & \varrho_{\mu\mu} & \varrho_{\mu\tau} \\ \varrho_{\tau e} & \varrho_{\tau\mu} & \varrho_{\tau\tau} \end{pmatrix} = \begin{pmatrix} f_{\nu_e} & a_1 + i a_2 & b_1 + i b_2 \\ a_1 - i a_2 & f_{\nu_\mu} & c_1 + i c_2 \\ b_1 - i b_2 & c_1 - i c_2 & f_{\nu_\tau} \end{pmatrix}, \tag{3.28}$$

where the diagonal terms are the occupation numbers f_{ν_α} of flavour neutrinos with momentum p and the off-diagonal terms, non-zero in the presence of mixing, are described by the real parameters a_k, b_k and c_k ($k = \{1, 2\}$). Since we neglect a potential neutrino asymmetry, quite constrained due to the measured value of the mixing angle θ_{13} [82,122], neutrinos and antineutrinos share the same density matrices.

The equations of motion for the neutrino density matrices are the corresponding set of Boltzmann equations in an expanding universe [123] (see also [124])

$$(\partial_t - H p\, \partial_p)\, \varrho_p(t) = -i \left[\left(\frac{1}{2p} \mathsf{M}_\mathrm{F} - \frac{8\sqrt{2} G_\mathrm{F} p}{3 m_\mathrm{W}^2} \mathsf{E} \right), \varrho_p(t) \right] + \mathcal{I}\left[\varrho_p(t)\right], \tag{3.29}$$

where the commutator term includes the vacuum oscillation term, proportional to

$$\mathsf{M}_\mathrm{F} = U \begin{pmatrix} 0 & 0 & 0 \\ 0 & \Delta m_{21}^2 & 0 \\ 0 & 0 & \Delta m_{31}^2 \end{pmatrix} U^\dagger, \tag{3.30}$$

the mass-squared matrix in the flavour basis that is related to the diagonal one in the mass basis via the neutrino mixing matrix (1.48). Here we have considered the best-fit values from [125] for the neutrino mixing parameters, for both ways of ordering neutrino masses and assuming CP conservation.

The second term inside the commutator in Eq. (3.29) appears because of matter effects in neutrino oscillations. It corresponds to neutrino forward scattering in the primeval medium, proportional to $G_{\rm F}$ and the diagonal matrix E, that represents the energy densities of charged leptons. For the range of temperatures we are interested in, only the contribution of electrons and positrons is relevant (i.e. the only non-zero component of E is $\mathsf{E}_{11} = \rho_{ee} \equiv \rho_{e^-} + \rho_{e^+}$). We neglect other refractive terms that appear in the general form of Eq. (3.29): the usual term proportional to the charged-lepton asymmetries (that was derived in section 1.2 using a different formalism, but which is always smaller than either the vacuum or the E term) and the contribution of neutrino-neutrino interactions, that vanishes for zero neutrino-antineutrino asymmetry.

The last term in Eq. (3.29) includes the effect of non-forward neutrino interactions, proportional to $G_{\rm F}^2$. The most general form of $\mathcal{I}[\varrho_p(t)]$, for each of the interaction processes with neutrinos, is a matrix with a collision integral for each of the components of ϱ_p [123]. For instance, the collision term for the annihilation process $\nu(p_1) + \bar{\nu}(p_2) \leftrightarrow e^-(p_3) + e^+(p_4)$ is

$$\begin{aligned}\mathcal{I}_{\nu\bar{\nu}\to e^-e^+} = \frac{1}{2}\frac{2^5 G_{\rm F}^2}{2|\vec{p}_1|}\int \frac{{\rm d}^3\vec{p}_2}{(2\pi)^3 2|\vec{p}_2|}\frac{{\rm d}^3\vec{p}_3}{(2\pi)^3 2E_3}\frac{{\rm d}^3\vec{p}_4}{(2\pi)^3 2E_4}(2\pi)^4\delta^{(4)}(p_1+p_2-p_3-p_4)\\ \times\Big\{4(p_1\cdot p_4)(p_2\cdot p_3)F_{\rm ann}^{LL}(\nu^{(1)},\bar{\nu}^{(2)},e^{(3)},\bar{e}^{(4)})\\ +4(p_1\cdot p_3)(p_2\cdot p_4)F_{\rm ann}^{RR}(\nu^{(1)},\bar{\nu}^{(2)},e^{(3)},\bar{e}^{(4)})\\ +2(p_1\cdot p_2)m_e^2\left(F_{\rm ann}^{RL}(\nu^{(1)},\bar{\nu}^{(2)},e^{(3)},\bar{e}^{(4)})+F_{\rm ann}^{LR}(\nu^{(1)},\bar{\nu}^{(2)},e^{(3)},\bar{e}^{(4)})\right)\Big\},\end{aligned} \tag{3.31}$$

where $\nu^{(1)}$ is our way of denoting p_1 with a direct indication of the particle to which the momentum is associated, and equivalently for the other inputs in the F functions, that we have defined as

$$\begin{aligned}F_{\rm ann}^{ab}(\nu^{(1)},\bar{\nu}^{(2)},e^{(3)},\bar{e}^{(4)}) = f_3\bar{f}_4\left(G^a(1-\bar{\varrho}_2)G^b(1-\varrho_1)+(1-\varrho_1)G^b(1-\bar{\varrho}_2)G^a\right)\\ -(1-f_3)(1-\bar{f}_4)\left(\varrho_1 G^b\bar{\varrho}_2 G^a + G^a\bar{\varrho}_2 G^b\varrho_1\right).\end{aligned} \tag{3.32}$$

Here $f_i = f_{e^-}(p_i)$ and $\bar{f}_i = f_{e^+}(p_i)$ are the distribution functions of charged leptons and G^a is a matrix of couplings ($a = \{L, R\}$, left-handed L or right-handed R). In the absence of non-standard neutrino interactions, $G^{L,R}$ are diagonal with components

$$G^L = {\rm diag}\,(g_L, \tilde{g}_L, \tilde{g}_L)\,, \qquad\qquad G^R = {\rm diag}\,(g_R, g_R, g_R)\,, \tag{3.33}$$

where

$$g_L = \frac{1}{2} + \sin^2\theta_{\rm W}, \qquad \tilde{g}_L = g_L - 1, \qquad g_R = \sin^2\theta_{\rm W}, \tag{3.34}$$

with $\theta_{\rm W}$ the weak mixing angle. In order to avoid confusion with particle fields p_i when referring to the vector moduli, we have deliberately changed our vector notation in equation (3.31) to $\vec{p}_i$ instead of $\mathbf{p}_i$, whose moduli are now expressed as $|\vec{p}_i|$. The same applies to equations (3.35) and (3.36), which we introduce below.

For the scattering process with electrons we have

$$\begin{aligned}\mathcal{I}_{\nu e^-\to\nu e^-} = \frac{1}{2}\frac{2^5 G_{\rm F}^2}{2|\vec{p}_1|}\int \frac{{\rm d}^3\vec{p}_2}{(2\pi)^3 2E_2}\frac{{\rm d}^3\vec{p}_3}{(2\pi)^3 2|\vec{p}_3|}\frac{{\rm d}^3\vec{p}_4}{(2\pi)^3 2E_4}(2\pi)^4\delta^{(4)}(p_1+p_2-p_3-p_4)\\ \times\Big\{4(p_1\cdot p_4)(p_2\cdot p_3)F_{\rm sc}^{RR}(\nu^{(1)},e^{(2)},\nu^{(3)},e^{(4)})\\ +4(p_1\cdot p_2)(p_3\cdot p_4)F_{\rm sc}^{LL}(\nu^{(1)},e^{(2)},\nu^{(3)},e^{(4)})\\ -2(p_1\cdot p_3)m_e^2\Big(F_{\rm sc}^{RL}(\nu^{(1)},e^{(2)},\nu^{(3)},e^{(4)})+F_{\rm sc}^{LR}(\nu^{(1)},e^{(2)},\nu^{(3)},e^{(4)})\Big)\Big\},\end{aligned} \tag{3.35}$$

and for the scattering with positrons

$$\begin{aligned}\mathcal{I}_{\nu e^+\to\nu e^+} = \frac{1}{2}\frac{2^5 G_{\rm F}^2}{2|\vec{p}_1|}\int \frac{{\rm d}^3\vec{p}_2}{(2\pi)^3 2E_2}\frac{{\rm d}^3\vec{p}_3}{(2\pi)^3 2|\vec{p}_3|}\frac{{\rm d}^3\vec{p}_4}{(2\pi)^3 2E_4}(2\pi)^4\delta^{(4)}(p_1+p_2-p_3-p_4)\\ \times\Big\{4(p_1\cdot p_4)(p_2\cdot p_3)F_{\rm sc}^{LL}(\nu^{(1)},\bar{e}^{(2)},\nu^{(3)},\bar{e}^{(4)})\\ +4(p_1\cdot p_2)(p_3\cdot p_4)F_{\rm sc}^{RR}(\nu^{(1)},\bar{e}^{(2)},\nu^{(3)},\bar{e}^{(4)})\\ -2(p_1\cdot p_3)m_e^2\Big(F_{\rm sc}^{RL}(\nu^{(1)},\bar{e}^{(2)},\nu^{(3)},\bar{e}^{(4)})+F_{\rm sc}^{LR}(\nu^{(1)},\bar{e}^{(2)},\nu^{(3)},\bar{e}^{(4)})\Big)\Big\}.\end{aligned} \tag{3.36}$$

In both cases we use the definition

$$\begin{aligned}F_{\rm sc}^{ab}(\nu^{(1)},e^{(2)},\nu^{(3)},e^{(4)}) = f_4(1-f_2)\Big(G^a\varrho_3 G^b(1-\varrho_1)+(1-\varrho_1)G^b\varrho_3 G^a\Big)\\ -f_2(1-f_4)\Big(\varrho_1 G^b(1-\varrho_3)G^a+G^a(1-\varrho_3)G^b\varrho_1\Big),\end{aligned} \tag{3.37}$$

where $f_i = f(p_i)$ is the distribution function of the electron or positron, depending on which particle we are considering for the scattering. The collision terms for the neutrino-neutrino processes are similar to equations (3.31), (3.35) and (3.36),

but with more complicated expressions that are non-linear in the neutrino density matrices [123].

As in previous analyses of neutrino decoupling in the early universe [119, 126–131], in our calculations the collision terms for the diagonal components $\varrho_{\alpha\alpha}$ (the distribution functions of flavour neutrinos f_{ν_α}) are solved numerically after they are analytically reduced to two-dimensional integrals, following the process described in [127]. However, previous works have approximated the off-diagonal collision terms of $\mathcal{I}_{\alpha\beta}[\varrho_p]$ in Eq. (3.29) as damping factors with an expression $-D_{\alpha\beta}(p,t)\varrho_{\alpha\beta}$, where $\alpha \neq \beta$ and the D functions can be obtained under some approximations in a similar way as in [132–134]. With this prescription, one assumes that each time neutrinos interact in a process that distinguishes among flavours they collapse into weak-interaction eigenstates. In our analysis we relax that approximation and deal with the off-diagonal collision terms in the same way as for the diagonal variables for the processes that involve neutrinos and $e^\pm$. We do not consider the full off-diagonal terms for weak reactions involving only neutrinos, such as $\nu\nu \leftrightarrow \nu\nu$ or $\nu\bar{\nu} \leftrightarrow \nu\bar{\nu}$, that play a less important role in the process of neutrino heating (see e.g. the detailed discussion in [131]). This assumption also allows us to reduce the computing time.

As we did in section 3.3 without flavour oscillations, the Boltzmann equations for the neutrino density matrices must be solved simultaneously with the continuity equation (3.25) for the total energy density of radiation ρ and total pressure P of the relativistic plasma, that includes the electromagnetic components γ and $e^\pm$ (in equilibrium with temperature T_γ) and the three neutrino states. This equation gives, as before, the time evolution of the photon temperature T_γ. Finite temperature QED corrections are included as described in section 3.2.

3.4.2 Non-standard neutrino-electron interactions

Neutrino decoupling in the early Universe would be modified in the presence of interactions beyond the weak processes present in the SM of particle physics. Since neutrinos are massless in the framework of the SM, many extended models have been proposed where neutrinos acquire mass. Most of these models naturally lead to new non-standard interactions involving neutrinos, whose value strongly depends on the particular model.

Here we follow Refs. [135–137] and assume that new physics induces NSI only through the four-fermion operators $(\bar{\nu}\nu)(\bar{f}f)$, where f is a charged lepton or a quark. Moreover, for the decoupling of cosmological neutrinos only the NSI that involve electrons are important. They are described, together with the standard

weak interactions, by the effective lagrangian

$$\mathcal{L} = \mathcal{L}_{\rm SM} + \sum_{\alpha,\beta} \mathcal{L}^{\alpha\beta}_{\rm NSI} \tag{3.38}$$

which, in addition to the SM term [137], contains the contribution from NSI

$$\mathcal{L}^{\alpha\beta}_{\rm NSI} = -2\sqrt{2} G_{\rm F} \sum_{P} \varepsilon^{P}_{\alpha\beta} (\bar{\nu}_\alpha \gamma^\mu L \nu_\beta)(\bar{e}\gamma_\mu P e) \tag{3.39}$$

where $\alpha, \beta = \{e, \mu, \tau\}$ and $P = L, R = (1 \mp \gamma_5)/2$ are the chiral operators. The NSI parameters $\varepsilon^{P}_{\alpha\beta}$ can lead to a flavour-changing contribution ($\alpha \neq \beta$) or induce a breaking of lepton universality ($\alpha = \beta$). Their values are constrained by data from various laboratory experiments, as it was reviewed in [138], but due to possible cancellations the limits depend on the number of NSI parameters that are simultaneously included.

The effect of NSI on relic neutrino decoupling was studied in [137], where it was analytically shown how NSI parameters lead, in general, to a larger interaction between neutrinos and $e^{\pm}$, although in some particular regions of ε they could reduce the collision rate (see Fig. 3 in [137]). In any case, the presence of NSI modifies the evolution of the relevant parameters, and in particular the final value of $N_{\rm eff}$. For a particular combination of ε values, then allowed by experiments, it was shown that the deviation of $N_{\rm eff}$ from 3 was three times the enhancement from neutrino heating with SM interactions.

The Boltzmann equations (3.29) are modified due to NSI interactions as follows:

$$(\partial_t - Hp\partial_p)\, \varrho_p(t) = -i \left[\left(\frac{1}{2p} \mathsf{M}_{\rm F} - \frac{8\sqrt{2} G_{\rm F} p}{3 m_{\rm W}^2}\, \rho_{ee} \mathsf{E}_{\rm NSI} \right), \varrho_p(t) \right] + \mathcal{I}\left[\varrho_p(t), \varepsilon\right], \tag{3.40}$$

where the matrix

$$\mathsf{E}_{\rm NSI} = \begin{pmatrix} 1+\varepsilon_{ee} & \varepsilon_{e\mu} & \varepsilon_{e\tau} \\ \varepsilon_{e\mu} & \varepsilon_{\mu\mu} & \varepsilon_{\mu\tau} \\ \varepsilon_{e\tau} & \varepsilon_{\mu\tau} & \varepsilon_{\tau\tau} \end{pmatrix}, \tag{3.41}$$

is no longer diagonal and contains the effect of non-standard interactions via the combinations of NSI parameters

$$\varepsilon_{\alpha\beta} = \varepsilon^{L}_{\alpha\beta} + \varepsilon^{R}_{\alpha\beta}. \tag{3.42}$$

The presence of NSI also modifies the statistical factors of equations (3.32) and (3.37) in the collision integrals. The coupling matrices adopt the form

$$G^L = \begin{pmatrix} g_L + \varepsilon^L_{ee} & \varepsilon^L_{e\mu} & \varepsilon^L_{e\tau} \\ \varepsilon^L_{e\mu} & \tilde{g}_L + \varepsilon^L_{\mu\mu} & \varepsilon^L_{\mu\tau} \\ \varepsilon^L_{e\tau} & \varepsilon^L_{\mu\tau} & \tilde{g}_L + \varepsilon^L_{\tau\tau} \end{pmatrix}, \tag{3.43}$$

$$G^R = \begin{pmatrix} g_R + \varepsilon^R_{ee} & \varepsilon^R_{e\mu} & \varepsilon^R_{e\tau} \\ \varepsilon^R_{e\mu} & g_R + \varepsilon^R_{\mu\mu} & \varepsilon^R_{\mu\tau} \\ \varepsilon^R_{e\tau} & \varepsilon^R_{\mu\tau} & g_R + \varepsilon^R_{\tau\tau} \end{pmatrix}. \tag{3.44}$$

In our analysis we restrict the calculation of neutrino decoupling with NSI and full collision terms, as described in section 3.4.1, to two combinations of ε parameters with ε^P_{ee} and $\varepsilon^P_{\tau\tau}$, that are still allowed by present data [138–140].[1] We do not consider the contribution of ε that affect muon-neutrino interactions because they are strongly constrained by observations [141].

3.4.3 Computation and technical issues

We solve the system of Boltzmann equations (3.29) and the continuity equation (3.25) with the dimensionless comoving variables (3.17). The expressions of the Boltzmann equations in terms of these comoving variables are listed in the appendix B.

The system of kinetic equations to be solved is integro-differential due to the presence of the neutrino density matrices in the collision terms. In previous analyses of neutrino decoupling, this system was solved either using a discretisation in a grid for the neutrino momenta y_i (as in [126, 127, 129, 131, 142, 143]) or expanding the non-thermal distortions of the neutrino distribution functions in moments (as was done in [119, 128, 130]). Here we choose the first method and use a grid of values for the neutrino momenta y_i in the range $[0.01, 20]$. We found good convergence for 100 bins. The system of integro-differential equations is solved using the free `FORTRAN77` library `ODEPACK`[2], which includes several solvers for differential equations.

We start the numerical computation at a value $x_{\rm in} = m_e/T^0_\gamma$, where $T^0_\gamma = 10\,\text{MeV}$, while neutrinos are still in good thermal contact with the electromagnetic plasma via weak interactions and flavour oscillations are suppressed by the

[1] The constraints on NSI parameters depend on the number of parameters considered in the analyses, so they should be taken with caution.

[2] See the URL: `http://computation.llnl.gov/casc/odepack/`

medium. Therefore, the initial values of the off-diagonal components of $\varrho(y_i)$ are zero, while the diagonal terms are $[\exp(y_i/z_{\rm in}) + 1]^{-1}$, with $z_{\rm in} = 1.00003$ the initial value of the dimensionless photon temperature. This number is found solving the continuity equation (2.11) with neutrinos fully coupled to electrons and positrons [143] until $x_{\rm in}$. In our comoving variables (3.17) this equation gives rise to

$$\frac{{\rm d}z}{{\rm d}x} = \frac{\dfrac{x}{z}F_1(x/z) + G_1(x/z)}{\dfrac{x^2}{z^2}F_1(x/z) + F_2(x/z) + G_2(x/z) + \dfrac{2\pi^2}{15} + \dfrac{7\pi^2}{20}}\,. \tag{3.45}$$

Finally, after initial conditions are set, the system is solved up to a value $x_{\rm fin} = 30$ when the neutrino distribution functions and z have reached their asymptotic values.

3.5 Results

In this section, results for the different effects considered during neutrino decoupling (namely finite temperature QED corrections, non-instantaneous freeze-out and three-flavour oscillations) are presented, both in the standard case and in a couple of NSI scenarios.

3.5.1 Standard case with flavour oscillations

First, we consider the case with standard weak interactions, with and without neutrino oscillations. In the presence of neutrino mixing, we are mainly interested in the possible effects of including the full expressions for the off-diagonal collision terms in the kinetic equations. On the other hand, once the collision terms are fixed, we also want to check whether there are differences between the two options for the neutrino mass ordering.

We show in Fig. 3.2 the evolution of the flavour neutrino spectra for a particular value of the neutrino momentum ($y = 5$). The corresponding distortions $f_{\nu_\alpha}/f_{\rm eq}$, where $f_{\rm eq} = [\exp(y) + 1]^{-1}$, are shown as a function of the photon temperature or the cosmological expansion in terms of x. The behaviour of this evolution has been discussed in previous works (see e.g. [127, 129]). At large temperatures ($T_\gamma \gtrsim 2$ MeV) neutrinos are still interacting with $e^\pm$ and their energy spectra keep an equilibrium form with T_γ. Later the cosmological expansion renders less efficient the weak processes and neutrinos decouple from the electromagnetic plasma in a momentum-dependent way. The residual interactions lead to spectral distortions for neutrinos, which are larger for the electronic flavour.

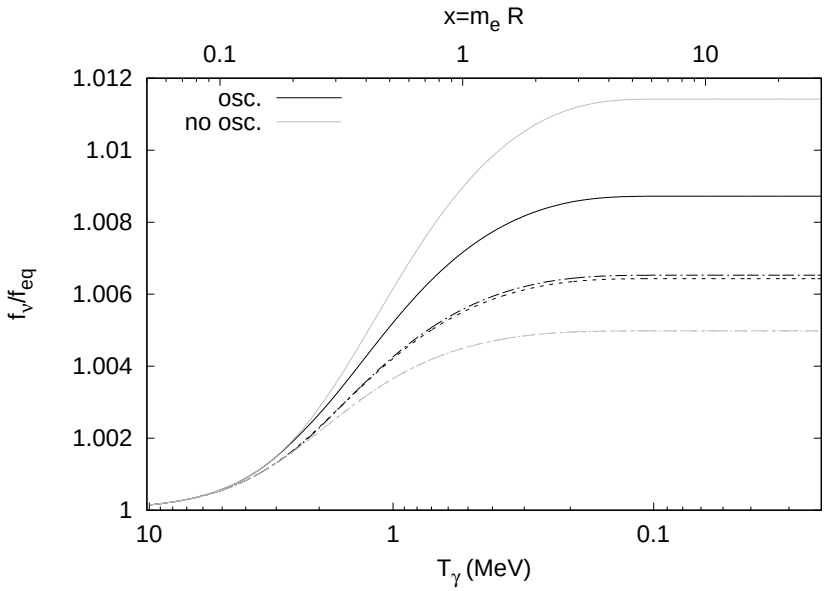

Figure 3.2: Evolution of the distortions of the neutrino spectra for the dimensionless momentum $y = 5$ with standard neutrino interactions, as a function of x or the photon temperature. Outer lines correspond to the case with no neutrino mixing, and inner ones to that with oscillations and masses in the NO. The upper two (solid) lines correspond to electron neutrinos and the lower lines to muon (dashed lines) and tau (dash-dotted lines) neutrinos, which are slightly different in the case with oscillations.

Neutrino oscillations, effective after $T_\gamma \lesssim 3$ MeV when the medium potential is diluted by the expansion, reduce the difference in the spectral distortions of electron neutrinos with respect to the other flavours.

The results shown in Fig. 3.2 when oscillations are taken into account were found with the full collision terms (the matrices $\mathcal{I}[\varrho_y]$) for neutrino-electron processes, avoiding the damping functions for the off-diagonal elements. In order to have an idea of the difference, we show in Fig. 3.3 the evolution of the collision terms for the real parts of the off-diagonal components $\varrho_{\alpha\beta}$ in Eq. (3.28), for a particular neutrino momentum ($y = 5$). For each case (a_1, b_1 and c_1), the result

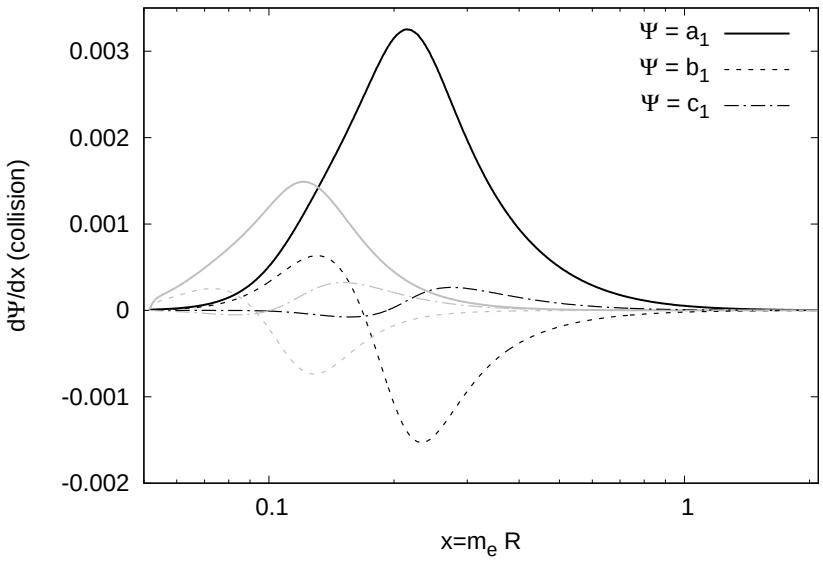

Figure 3.3: Collision terms for the real parts of the off-diagonal elements of the neutrino density matrix (3.28): a_1 (full lines), b_1 (dashed lines), and c_1 (dash-dotted lines). They are shown for a dimensionless momentum $y = 5$ and were calculated with the full expression (black lines) or with damping functions (grey lines), accounting only for the processes involving the interactions of neutrinos and $e^{\pm}$.

of the full integral is compared with the corresponding damping term. One can see that, while the overall behaviour is similar for each case, the full calculation presents a smoother evolution starting from zero at large temperatures. It is also interesting that the largest (absolute) values of the collision terms with the full integrals appear later than in the simple damping prescription. Since collisional damping leads to a loss of flavour coherence, a difference in the off-diagonal terms can modify the evolution of neutrino oscillations and eventually change the final distortions in the neutrino spectra.

The final values of the momentum-dependent distortions in the spectra of flavour neutrinos are shown in Fig. 3.4. Their non-thermal character is evident

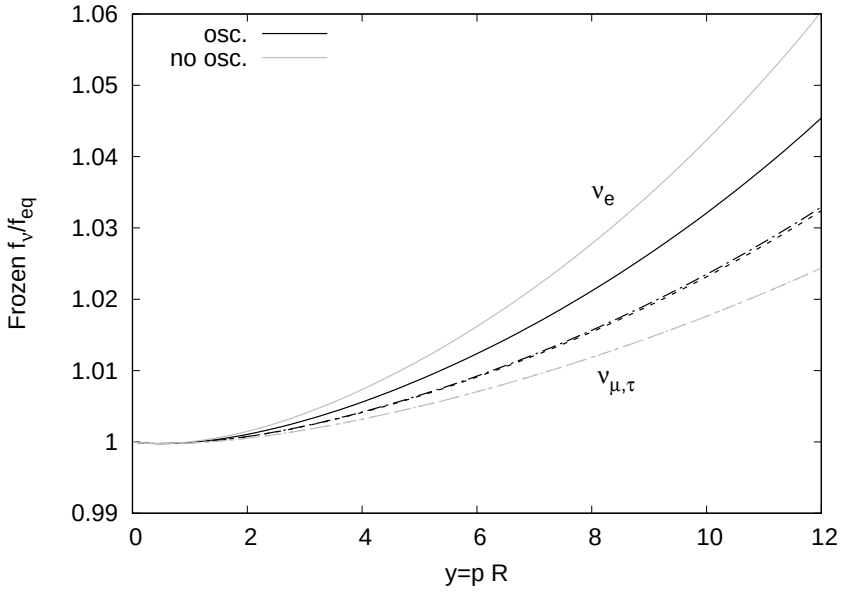

Figure 3.4: Final distortions of the flavour neutrino spectra as a function of the comoving momentum. Outer lines correspond to the case with no neutrino mixing, and inner lines to that with oscillations and masses in the NO. The IO case overlaps the NO one at this scale. Solid, dashed and dash-dotted lines are, respectively, for electron, muon and tau neutrinos.

and can be understood from the fact that more energetic neutrinos are interacting with $e^{\pm}$ at smaller temperatures. The presence of neutrino oscillations leads to a reduced difference between the distortions of electron neutrinos and those of the other flavours. The case with oscillations shown in Fig. 3.4 corresponds to the normal neutrino mass ordering, but the calculation with an inverted ordering leads to very similar results and the final distortions basically overlap with those found with NO.

We use the frozen values of the neutrino spectra to calculate how the energy density of each flavour state is enhanced with respect to the instantaneous decoupling approximation. The results are given in table 3.1 in terms of $\delta\bar{\rho}_{\nu_\alpha} = \delta_{\nu_\alpha}$ as defined in Eq. (3.19). In all cases the enhancement is at the sub-percent level,

Case	$z_{\rm fin}$	$\delta\bar{\rho}_{\nu_e}(\%)$	$\delta\bar{\rho}_{\nu_\mu}(\%)$	$\delta\bar{\rho}_{\nu_\tau}(\%)$	$N_{\rm eff}$
Instantaneous decoupling	1.40102	0	0	0	3.000
Inst. dec. (with QED corr.)	1.39975	0	0	0	3.011
No oscillations	1.39784	0.920	0.392	0.392	3.045
Normal ordering (NO)	1.39779	0.699	0.511	0.519	3.045
NO (damping terms)	1.39778	0.673	0.529	0.533	3.045
Inverted ordering (IO)	1.39779	0.697	0.512	0.520	3.045
NSI ee (NO)	1.39812	0.592	0.460	0.467	3.040
NSI $\tau\tau$ (NO)	1.39708	0.862	0.784	0.812	3.059

Table 3.1: Final values of the dimensionless photon temperature, the distortion of the energy density of flavour neutrinos and the effective number of neutrinos, computed for several cases as discussed in the text.

which indicates the well-known result that the non-thermal distortions for cosmological neutrinos are very small. The main effect is a slightly larger contribution of neutrinos to the cosmological energy density of radiation $\rho_{\rm r}$, usually given, as in the case of any other contribution of relativistic particles other than photons, in terms of the effective number of neutrinos,

$$N_{\rm eff} = \frac{8}{7}\left(\frac{11}{4}\right)^{4/3}\left[\frac{\rho_{\rm r}-\rho_\gamma}{\rho_\gamma}\right], \tag{3.46}$$

that can be also written as in equation (3.27) for $z_{\rm fin}$, the asymptotic value of the dimensionless photon temperature for each case in our calculations. The final values of $z_{\rm fin}$ for each case and the calculated ones for $N_{\rm eff}$ are given in table 3.1.

Our main results correspond to the cases NO and IO in table 3.1, computed with the full collision terms. Both cases lead to almost equal values of the enhanced neutrino energy densities and $z_{\rm fin}$, and to the same final effective number of neutrinos, $N_{\rm eff} = 3.045$, which is almost the same as 3.046, found in [129] and usually taken as reference for the standard value of $N_{\rm eff}$. Such a difference (0.001) is smaller than the accuracy quoted in [129] and corresponds to what we estimate for our own numerical calculations (performed with a completely independent code). We conclude that the value of $N_{\rm eff}$ does not depend on the ordering of neutrino masses. However, the NO and IO cases are not exactly equivalent; there is a resonance for IO when neutrino oscillations become effective at $T_\gamma \sim 3\,{\rm MeV}$ (see figure 3.5) that leads to an interchange among the mass states, although they evolve in a similar way after the resonance for both mass orderings. The

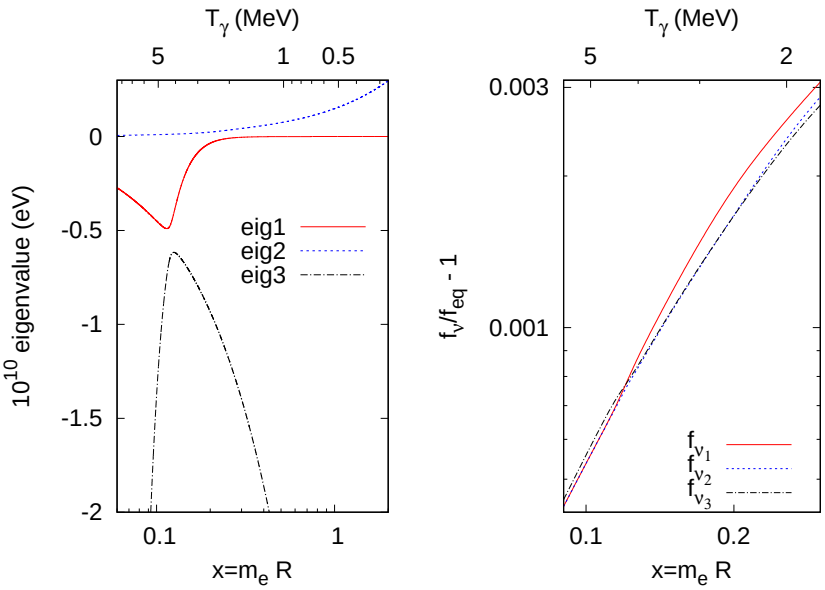

Figure 3.5: Resonance appearing in the IO when neutrino oscillations are becoming effective, due to the dilution of the medium density because of expansion. The left panel shows the eigenvalues obtained from the diagonalisation of the hamiltonian, with the change in tendency between eigenvalues 1 and 3 leading to the crossing of f_{ν_1} that appears in the right panel.

difference is therefore not appreciable for the range of temperatures after $e^{\pm}$ have annihilated and neutrinos are completely decoupled, as can be seen in table 3.2 and Fig. 3.6, where our main results are shown for the mass neutrino eigenstates $\nu_{1,2,3}$. The corresponding neutrino distribution functions are the relevant energy spectra for all cosmological calculations at temperatures much smaller than the neutrino decoupling value (MeV), both when neutrinos are still relativistic or when they start to behave as non-relativistic particles.

It is interesting to check if, fixing the mass ordering to NO, the differences shown in Fig. 3.3 between the off-diagonal collision terms calculated with the full integrals or the simple damping prescription, have any effect on the final values that characterise relic neutrino decoupling. We find that the value of $N_{\rm eff}$ is,

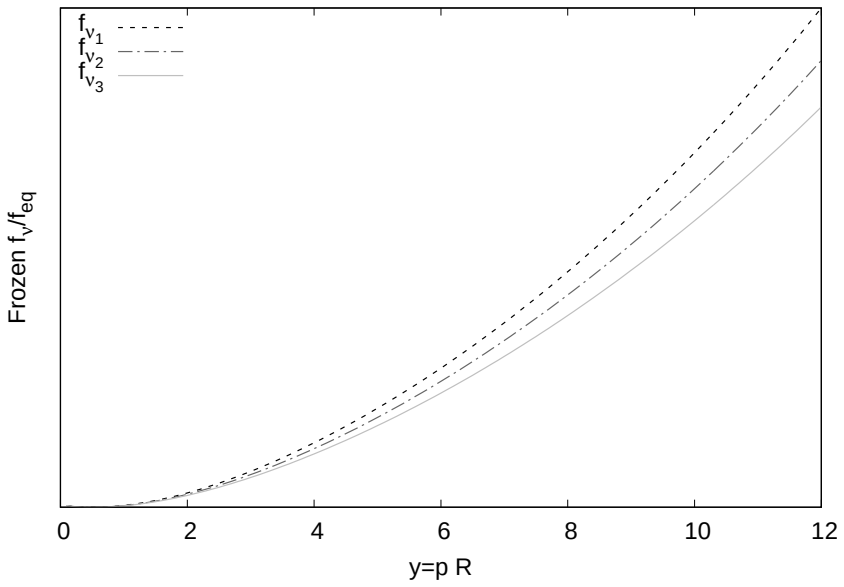

Figure 3.6: Same as figure 3.4 for the mass neutrino states and NO. The spectral distortions of the mass states for the IO case overlap with those for NO at this scale.

within the accuracy of our numerical calculations, the same in both cases (3.045), while there exist small differences in the values of the energy density distortions $\delta\bar{\rho}_{\nu_\alpha}$, that are slightly smaller for muon or tau neutrinos (and slightly larger for electron neutrinos) when the damping approximation is not used. However, one can conclude that for practical purposes, in particular concerning the final value of $N_{\rm eff}$, the inclusion of the full collision integrals in the evolution equation of the off-diagonal components of ϱ_p is not necessary.

We have also included in table 3.1 our results for the case when neutrino oscillations are not considered. As shown in previous analyses, the energy densities of the neutrino flavour states in absence of mixing are quite different with respect to those found with neutrino oscillations, but the final value of $N_{\rm eff}$ is again 3.045. This can be compared with the values found in previous works for zero neutrino mixing but including QED corrections: 3.046 [129], 3.044 [130] and 3.052 [131].

Case	$z_{\rm fin}$	$\delta\bar{\rho}_{\nu_1}(\%)$	$\delta\bar{\rho}_{\nu_2}(\%)$	$\delta\bar{\rho}_{\nu_3}(\%)$	$N_{\rm eff}$
Normal ordering (NO)	1.39779	0.636	0.574	0.518	3.045
Inverted ordering (IO)	1.39779	0.635	0.574	0.520	3.045
NSI ee (NO)	1.39812	0.548	0.504	0.465	3.040
NSI $\tau\tau$ (NO)	1.39708	0.839	0.821	0.798	3.059

Table 3.2: Same as the table 3.1 for the mass neutrino eigenstates.

While some of the small differences among these values could be due to different methods for the numerical evaluation, we believe that a new, specific study of the effects of finite temperature QED radiative corrections on relic neutrino decoupling could be useful in order to understand the approximations assumed.

3.5.2 Non-standard neutrino-electron interactions

Here our aim is not to explore the whole space of NSI parameters allowed by laboratory data, but to show the effects of the new interactions on relic neutrino decoupling with a couple of examples. We consider two sets of diagonal parameters ε^P_{ee} and $\varepsilon^P_{\tau\tau}$ that are not ruled out by experimental data, as described in [139]. The two chosen sets are $\varepsilon_{\tau\tau} \neq 0$ ($\varepsilon^R_{\tau\tau} = -\varepsilon^L_{\tau\tau} = 0.37$) and $\varepsilon_{ee} \neq 0$ ($\varepsilon^R_{ee} = -0.42$, $\varepsilon^L_{ee} = -0.09$), setting in both cases the rest of NSI parameters to zero, and including neutrino oscillations with a normal ordering of neutrino masses.

We chose these values because they correspond to allowed NSI parameters that are the furthest from the standard case, where all $\varepsilon = 0$. In addition, with this selection of values we want to illustrate the two possible effects on neutrino decoupling: the first case ($\varepsilon_{\tau\tau} \neq 0$) leads to an increase in the effective number of neutrinos with respect to $N_{\rm eff} = 3.045$, while the case with $\varepsilon_{ee} \neq 0$ gives a smaller value of $N_{\rm eff}$. An explanation of this effect in terms of the effective decoupling temperature of neutrinos can be found in [137] (see in particular their Figs. 3 and 4).

We show in Fig. 3.7 the evolution of the neutrino spectral distortions $f_{\nu_\alpha}/f_{\rm eq}$, as a function of the photon temperature or our comoving variable x, for both sets of NSI parameters and for a particular neutrino momentum ($y = 5$). The asymptotic values of the flavour neutrino distortions as a function of y are depicted in Fig. 3.8. The final values of the dimensionless photon temperature, neutrino energy distortions and $N_{\rm eff}$ are listed in the lower rows of tables 3.1 (flavour neutrino states) and 3.2 (mass neutrino states). The presence of non-zero NSI

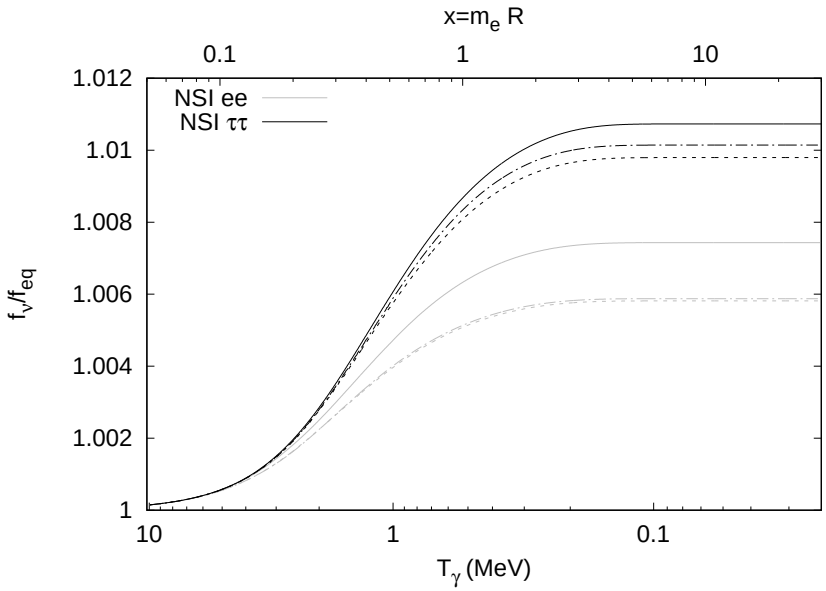

Figure 3.7: Same as figure 3.2 for the two scenarios with non-standard neutrino interactions, including flavour oscillations and masses in the NO case. The classification of lines corresponding to each neutrino flavour is the same as in Fig. 3.2.

parameters modifies the neutrino spectral distortions and leads to small changes in the final value of $N_{\rm eff}$: $+0.014$ for the case $\varepsilon_{\tau\tau} \neq 0$ and -0.005 when $\varepsilon_{ee} \neq 0$.

3.6 Chapter remarks

We have revisited the decoupling process of neutrinos in the early Universe in the presence of three-flavour oscillations, both with standard weak interactions and with non-standard neutrino interactions with electrons. We have calculated the evolution of the momentum spectra of neutrinos and found their final contribution to the cosmological energy density in the form of radiation, given by the effective number of neutrinos, $N_{\rm eff}$.

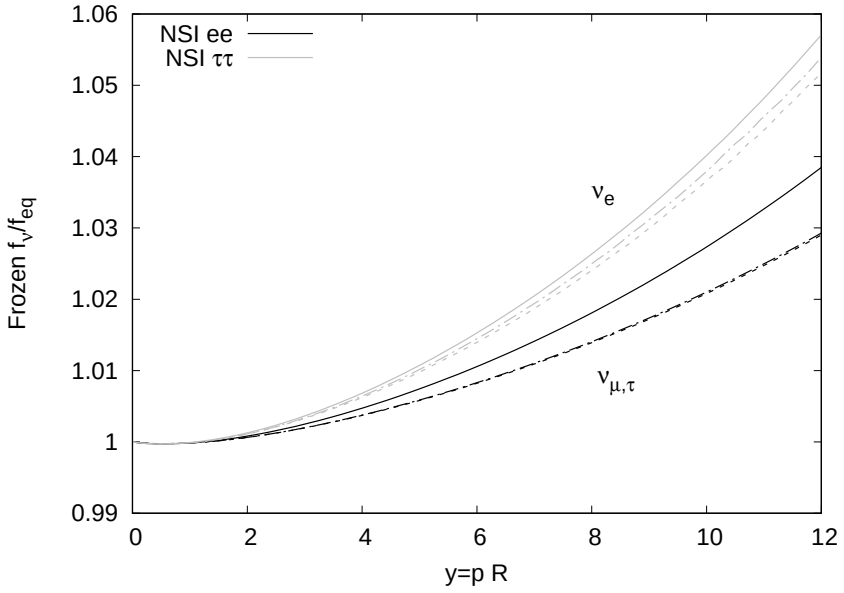

Figure 3.8: Same as figure 3.4 for the two cases with non-standard neutrino interactions, including flavour oscillations and masses in the NO case. The classification of lines corresponding to each neutrino flavour is the same as in Fig. 3.4.

This problem requires the numerical solution of the corresponding momentum-dependent kinetic equations for the neutrino density matrix, that we have performed including the full collision terms for neutrino-electron processes. In the case of the off-diagonal components, these collision integrals replace the damping terms usually assumed in previous analyses. We find that, while this improved calculation does change the evolution of the off-diagonal elements, it does not modify the final value of the effective number of neutrinos, given by $N_{\rm eff} = 3.045$. The impact of including the off-diagonal collision terms calculated with the full integrals or the simple damping prescription could be more important for other cases, such as active-sterile neutrino oscillations [144] or very low-reheating scenarios [145], where the spectral flavour distortions could be significantly larger than in the standard case.

Finally, we have also studied the decoupling process of relic neutrinos for two sets of NSI parameters allowed by present data, finding that the final value of $N_{\rm eff}$ can be reduced down to 3.040 or enhanced up to 3.059.

Chapter 4

Very low reheating scenarios

As we have introduced in a previous chapter (in section 2.2.1), an assumption commonly made about the history of the Universe is that its expansion was fixed by relativistic particles at early epochs. This radiation-dominated era usually arises as a result of the thermalisation of the decay products of a massive particle, a process called reheating. The best example is the reheating process after primordial inflation that occurred at very large temperatures. However, several reheating processes due to consequent (unstable) non-relativistic particles might have occurred, leading to more than one radiation-dominated phase, each preceded by a very short, matter dominated epoch. Here we are only interested in the last radiation-dominated phase, that started at a temperature ($T_{\rm RH}$) which can be bounded from below using BBN and CMB data.

The main consequence of very low reheating scenarios concerns the production of neutrinos, because they are the relativistic particles with the largest decoupling temperature. As we saw, weak processes involving neutrinos are only effective at cosmological temperatures above $\sim 1\,\mathrm{MeV}$. Therefore, for $T_{\rm RH} \sim \mathcal{O}(\mathrm{MeV})$, the thermalisation of the neutrino background could be incomplete due to the lack of interactions. In such a case, neutrino spectra would not present an equilibrium form with the same temperature as the electromagnetic plasma, and in particular the contribution of neutrinos to the energy density of radiation, measured in terms of the parameter $N_{\rm eff}$ (see section 2.3.4), would be smaller than the standard value of 3.045 [116]. This would affect the expansion rate during BBN, as well as the influence of electron neutrinos and antineutrinos on weak processes relating neutrons and protons, both effects leading to the lower bound on $T_{\rm RH}$ mentioned above. The effect of neutrino flavour oscillations was found in [146] to be quite

relevant, shifting the lower bound from BBN on the reheating temperature from $T_{\rm RH} \gtrsim [0.5, 0.7]$ MeV (as obtained in [147–151]) to $T_{\rm RH} \gtrsim 2\,{\rm MeV}$.

In addition to primordial nucleosynthesis, other cosmological measurements such as the distribution of CMB anisotropies or LSS can test the radiation content of the Universe, which can provide an independent lower bound on $T_{\rm RH}$, as discussed in [147]. Using CMB (from WMAP) and LSS (from 2dF) data in combination with BBN, the analysis described in [151] found $T_{\rm RH} > 4\,{\rm MeV}$ at 95% CL. A less stringent bound, $T_{\rm RH} > 2\,{\rm MeV}$ (also at 95% CL), was obtained in [152] from WMAP data and galaxy clustering power spectrum of the Sloan Digital Sky Survey (SDSS) luminous red galaxies (LRGs), translating the bound on the radiation content with the relation between $T_{\rm RH}$ and $N_{\rm eff}$. A similar analysis performed in [153] found, at 95% CL, $T_{\rm RH} > 2\,{\rm MeV}$ from WMAP-5 data alone and $T_{\rm RH} > 3.2\,{\rm MeV}$ including external priors from cosmic age constraints and the SDSS-LRG galaxy survey.

In this chapter we review the results published in Ref. [145], where we updated previous analyses of very low reheating scenarios [147, 148, 151], and in particular that of Ref. [146] where the effect of neutrino flavour oscillations was included, motivated by the present availability of very precise cosmological data. We improve previous calculations of the production and thermalisation of neutrinos in the low-reheating case solving the momentum-dependent equations of motion of the neutrino spectra taking into account three-flavour oscillations, as in the works on the standard case [116, 129]. The impact on BBN is found with a modified version of the `PArthENoPE` code [87, 88], while the bounds on $T_{\rm RH}$ from late-time cosmological observables are obtained from the latest results of the Planck satellite, among other data, including also the case of massive neutrinos.

In particular, this chapter is focused on the role of neutrino oscillations in the BBN analysis, since it was the part in which the author of the present thesis most contributed. The CMB analysis is summarised for completeness, but for more details about it we refer the reader to the original publication [145].

4.1 Neutrino production in low-reheating scenarios

Let us call ϕ the massive particle that decays with a rate Γ_ϕ into relativistic particles other than neutrinos, reheating the Universe. With this assumption, neutrinos are populated via weak interactions with charged leptons such as $e^\pm$. The cases where hadrons or neutrinos can be directly produced in ϕ decays were considered in [148] and [151], respectively.

We follow the convention of previous analyses and define the reheating temperature $T_{\rm RH}$ as

$$\Gamma_\phi = 3H(T_{\rm RH}), \tag{4.1}$$

where we assume that at this point the Universe is already dominated by radiation with $T_{\rm RH}$ (therefore implying that ϕ has already decayed and $\mathrm{d}\rho_\phi/\mathrm{d}t = 0$). For the range of temperatures that we are interested in, if all relativistic particles are the standard ones with an energy density $\rho_{\rm r}$, the Hubble parameter is given by

$$H = \sqrt{\frac{8\pi\rho_r}{3m_{\rm Pl}^2}} = \sqrt{g_*\frac{8\pi^3}{90}}\frac{T^2}{m_{\rm Pl}}, \tag{4.2}$$

where $m_{\rm Pl}$ is the Planck mass (2.3) and the number of effective relativistic degrees of freedom is $g_* = 10.75$ in the standard case. In our low-reheating scenario we use this value for the definition of $T_{\rm RH}$, despite the fact that neutrinos might be far from being in equilibrium with the electromagnetic plasma. Therefore, $T_{\rm RH}$ is just a different way of referring to the decay rate of the massive particles

$$T_{\rm RH} \simeq 0.7\left(\frac{\Gamma_\phi}{\mathrm{s}^{-1}}\right)^{1/2}\mathrm{MeV}. \tag{4.3}$$

The particle content of the Universe as a function of time in a low-reheating scenario is found solving three types of evolution equations: one for the ϕ's, another one for the electromagnetic particles and a third one for neutrinos. The equation for the energy density of ϕ's is that of a decaying non-relativistic species,

$$\frac{\mathrm{d}\rho_\phi}{\mathrm{d}t} = -\Gamma_\phi\rho_\phi - 3H\rho_\phi, \tag{4.4}$$

where inverse decays are neglected and the Hubble parameter depends on the total energy density of the Universe.

Those particles that are coupled through electromagnetic interactions are in equilibrium with a common temperature T_γ, including photons, $e^\pm$ and $\mu^\pm$. Therefore, we just need to compute the time evolution of T_γ, which is obtained from the continuity equation (2.11) for the total energy-momentum ρ in the expanding Universe,

$$\frac{\mathrm{d}T_\gamma}{\mathrm{d}t} = \frac{-\Gamma_\phi\rho_\phi + 4H(\rho_\gamma+\rho_\nu) + 3H(\rho_l+P_l) + \mathrm{d}\rho_\nu/\mathrm{d}t}{\partial\rho_\gamma/\partial T_\gamma + \partial\rho_l/\partial T_\gamma}. \tag{4.5}$$

In this equation, l stands for the charged leptons. We have further modified this equation in our calculations, including finite temperature QED corrections to the electromagnetic plasma, as described in section 3.2.

The evolution of the momentum distribution of the three flavour neutrinos is calculated taking into account that, at MeV temperatures, neutrinos are interacting while oscillations start to be effective. Hence, as it was explained in section 3.4, we make use of the density matrix formalism, where neutrino distributions are described with 3×3 matrices in flavour space $\varrho_{\mathbf{p}}$ for each neutrino momentum $\mathbf{p}$. Its evolution is that of equation (3.29), where for this study we need to include in E the contribution of $e^{\pm}$ and $\mu^{\pm}$. We have used momentum-dependent damping factors in order to account for the collisional integrals in the off-diagonal terms. However, as it was mentioned later in [116], relaxing this approximation might have a non-negligible effect, although we suspect it will not be very relevant.

The neutrino oscillation parameters (two mass-squared differences and three mixing angles) were fixed in this work to the best-fit values found in [125] for the normal mass ordering of neutrino masses.

In summary, with respect to the previous calculation of neutrino production in low-reheating scenarios [146] we include three-flavour oscillations and solve two-dimensional collision integrals for the weak processes (with $m_e \neq 0$ and using Fermi-Dirac distributions for $e^{\pm}$). For comparison, we have also performed the calculations in the absence of neutrino oscillations. As in [146] we neglect neutrino-neutrino processes, that do not increase the energy density of neutrinos and are expected to have small effects, and use comoving variables for the expansion rate, the photon temperature and the neutrino momenta as described in equation (3.17).

For each value of the reheating temperature, we start our calculations at $t = 10^{-3}\,\mathrm{s}$, imposing that the Universe is strongly dominated by matter, and end the evolution when $T_\gamma < 10\,\mathrm{keV}$ in a radiation-dominated regime. The results do not depend on the choice of the initial time, provided that the maximum value of T_γ (which is not exactly T_{RH}) that is reached is significantly larger than the neutrino decoupling temperature. The value of ρ_ϕ is obtained from the Friedmann equation [151],

$$\frac{3}{2} t_i = \left(\frac{8\pi \rho_\phi}{3 m_{\mathrm{Pl}}^2} \right)^{-1/2} , \tag{4.6}$$

while we fix the initial $T_\gamma = 2\,\mathrm{MeV}$. This last choice speeds up the initial phase of the numerical calculations, until the expected evolution is obtained: T_γ decreases

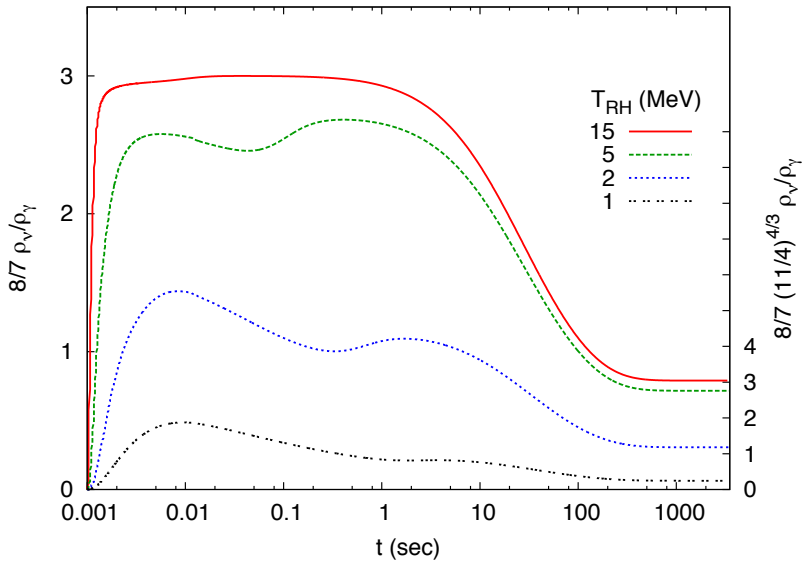

Figure 4.1: Time evolution of the ratio of energy densities of neutrinos and photons, normalised in such a way that it corresponds to $N_{\rm eff}$ before (left) and after (right) $e^{\pm}$ annihilations. Four cases with different values of the reheating temperature are shown.

as $t^{-1/4}$ when matter dominates and as $t^{-1/2}$ when relativistic particles fix the cosmological expansion.

A few examples of our numerical calculations are depicted in Fig. 4.1, where the time evolution of the ratio of energy densities ρ_ν/ρ_γ is shown for four values of $T_{\rm RH}$. This ratio is normalised in two different ways in the y-axis, so that it corresponds to the effective number of neutrinos before and after $e^{\pm}$ annihilations (3 in both cases in the approximation of instantaneous neutrino decoupling). In particular, at late times $N_{\rm eff}$ is defined as $\rho_r/\rho_\gamma = 1 + 7/8(4/11)^{4/3}N_{\rm eff}$. For values of the reheating temperature of 15 MeV, the evolution of ρ_ν/ρ_γ is similar to the standard case (except at the very initial phase) with a fast drop at $t \sim 1\,$s due to photon heating by $e^{\pm}$ annihilations. Instead, for smaller values of $T_{\rm RH}$ one can see that ρ_ν/ρ_γ decreases while the ϕ's decay, followed by a period where this ratio slightly increases but never reaches the value expected in the standard

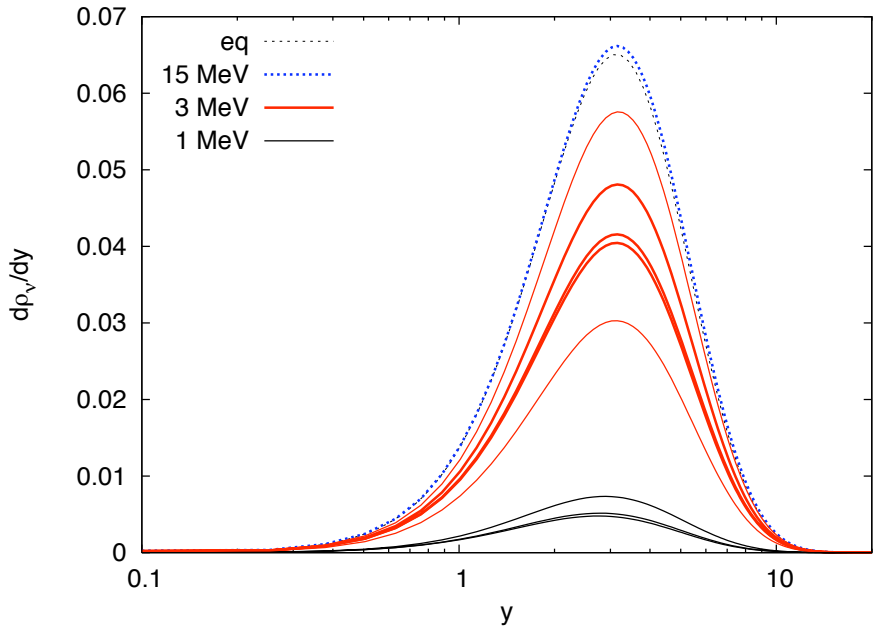

Figure 4.2: Final differential spectra of neutrino energies as a function of the comoving momentum for three values of $T_{\rm RH}$, compared to an equilibrium spectrum (thin dotted black line). The three thick solid lines for $T_{\rm RH} = 3\,{\rm MeV}$ (middle red lines) and $1\,{\rm MeV}$ (lower black lines) correspond, from larger to smaller values, to ν_e, ν_μ and ν_τ, respectively. For $T_{\rm RH} = 3$ MeV we also include the case without flavour oscillations (thin red lines, upper for ν_e and lower for $\nu_{\mu,\tau}$).

case. Hence, neutrinos do not reach equilibrium and the final $N_{\rm eff}$ is clearly below three. This fact can be easily seen in Fig. 4.2, where the differential energy spectrum of neutrinos at the end of the evolution is shown for three values of $T_{\rm RH}$, compared to the case of an equilibrium Fermi-Dirac spectrum. For $T_{\rm RH} = 15\,{\rm MeV}$ the energy distribution is very close to equilibrium, actually slightly above for large momenta as expected in the standard decoupling case that leads to $N_{\rm eff} = 3.045$ [116]. Nonetheless, for smaller values of the reheating temperature there exists a significant reduction in the production of neutrinos, in particular for $T_{\rm RH} = 1\,{\rm MeV}$.

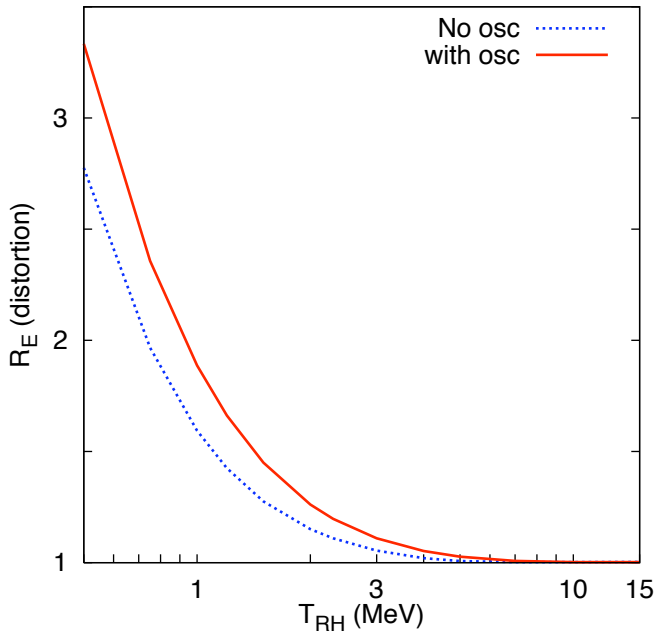

Figure 4.3: Distortion of the electron neutrino spectrum parameterised with R_E (equation (4.7)) as a function of the reheating temperature. A value $R_E > 1$ indicates a significant spectral distortion with respect to equilibrium. The red, solid curve is for oscillating neutrinos, while the blue, dotted line is for the no oscillation case and it is reported for comparison.

The distortion of the neutrino spectra from an equilibrium form can be described by the parameter R_E, defined as [148]

$$R_E = \frac{1}{3.151\, T_{\mathrm{eff},\nu}} \frac{\rho_\nu}{n_\nu}\,, \tag{4.7}$$

where the neutrino energy density ρ_ν, number density n_ν and effective temperature $T_{\mathrm{eff},\nu} = [2\pi^2 n_\nu/\zeta(3)]^{1/3}$ are found by integrating the spectrum. The parameter R_E represents the ratio of the mean neutrino energy to the value in thermal equilibrium and it is shown for electron neutrinos as a function of T_{RH} in Fig. 4.3. A value around unity indicates that the neutrino spectrum has a form close to equilibrium, while larger R_E point to significant distortions as it happens for $T_{\mathrm{RH}} \lesssim 3\,\mathrm{MeV}$ (more noticeable if flavour oscillations are included).

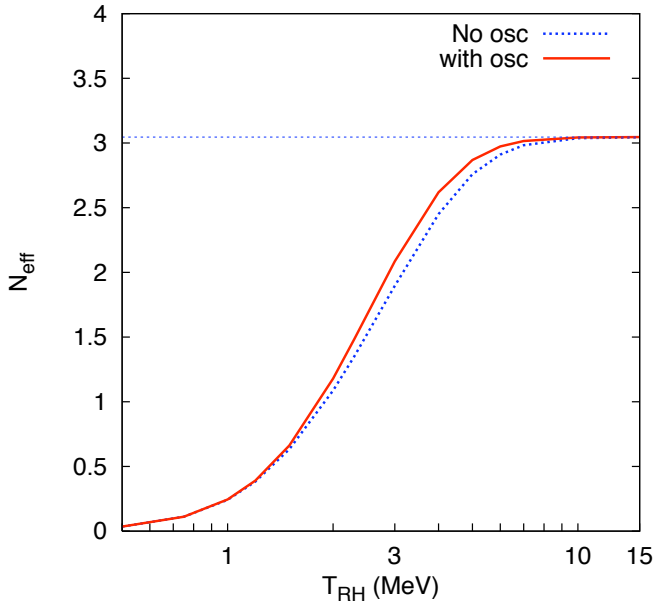

Figure 4.4: Final contribution of neutrinos to the radiation energy density in terms of $N_{\rm eff}$, as a function of the reheating temperature. The horizontal line indicates the standard value $N_{\rm eff} = 3.045$.

Finally, we present in Fig. 4.4 the final contribution of neutrinos to the energy density of radiation in terms of $N_{\rm eff}$. Its value drops below 3 if $T_{\rm RH} \lesssim 7\,{\rm MeV}$. Our results are similar to those shown in [151] (figure 1) and [146] (figure 3). In particular, we agree with reference [146] in the fact that the final value of $N_{\rm eff}$ in the middle range of MeV reheating temperatures is slightly larger in the case where flavour oscillations are included.

4.2 Bounds from primordial nucleosynthesis

The effect of neutrino distributions on the production of primordial yields of light elements during BBN can be summarised as follows:

1. The energy density of all neutrino flavours $\rho_\nu = \sum_\alpha \rho_{\nu_\alpha}$ contributes to the energy density of radiation $\rho_{\rm r}$, which leads the Hubble expansion rate.

2. The momentum distribution of electron neutrinos directly enters the charged current weak rates, which govern the neutron-proton chemical equilibrium.

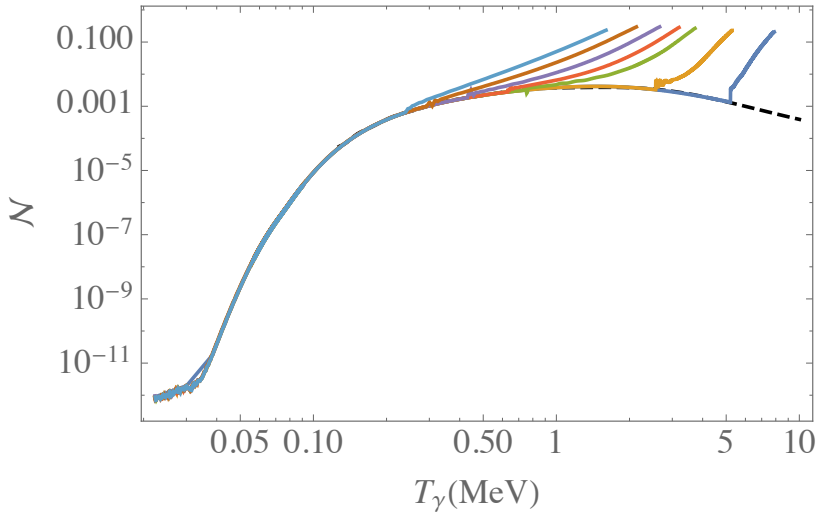

Figure 4.5: The function $\mathcal{N}$ (as defined in Eq. (4.8)) for values of $T_{\rm RH} = (15, 10, 7, 6, 5, 4, 3)$ MeV (from right to left) compared to the standard one (black dashed line). The initial (large temperature) decreasing branch of each curve is due to neutrino heating from electromagnetic plasma, which smoothly tends toward the standard behaviour due to $e^{\pm}$ annihilation stage.

3. The time evolution of ρ_ν explicitly enters the fluid equation (2.11). In particular, one can define the function [154]

$$\mathcal{N} = \frac{1}{z^4}\left(x\frac{\mathrm{d}}{\mathrm{d}x}\bar{\rho}_\nu\right) , \tag{4.8}$$

with $\bar{\rho}_\nu \equiv a^4\rho_\nu$. This function measures the neutrino heating by electromagnetic plasma, and in the standard scenario it is not vanishing only during the $e^{\pm}$ annihilation stage, due to the small entropy transfer (at $\mathcal{O}(1\%)$) to neutrinos. For sufficiently low $T_{\rm RH}$ scenarios we expect this function to be non-zero in the BBN relevant temperature range, during the neutrino production stage.

In order to put constraints on the reheating temperature, the time evolution of ρ_ν, $\mathcal{N}$, and of the ν_e and $\bar{\nu}_e$ distribution functions have been fitted for different values of $T_{\rm RH}$, and used as input in a modified version of the `PArthENoPE` code [87, 88]. Fig. 4.5 shows the evolution with photon temperature of $\mathcal{N}$ for different

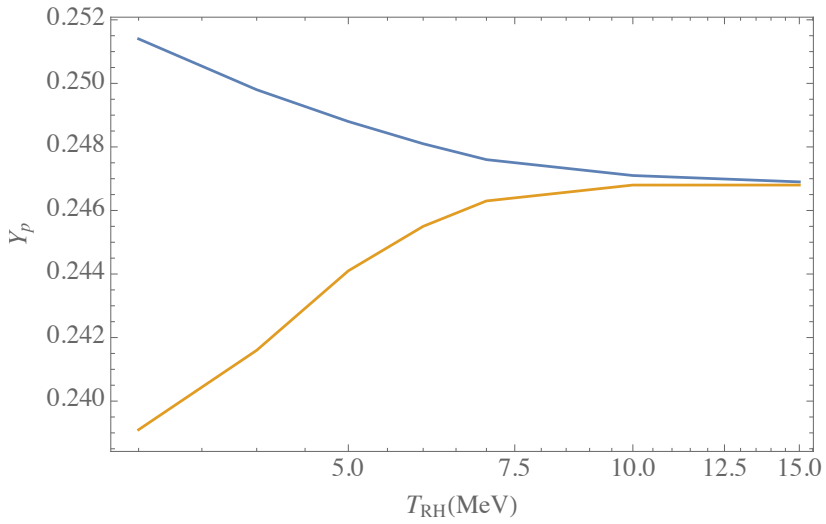

Figure 4.6: Primordial helium yield Y_p for different values of $T_{\rm RH}$, taking into account neutrino oscillations (upper blue line) and in absence of the oscillations (lower yellow line).

values of $T_{\rm RH}$. As expected, the lower $T_{\rm RH}$ is, the smaller the value of T_γ at which the standard expression is recovered.

The values of the final abundances of helium, Y_p, and deuterium, ^{2}H/H, for a baryon density $\omega_b = \Omega_b h^2 = 0.02226$ are reported in figures 4.6 and 4.7, where we show for comparison the data obtained both in presence and in the absence of neutrino oscillations.

We use the most recent data available (at the time of making this work) on the primordial abundances of ^{4}He and deuterium. For the helium mass fraction, the result of new observations of He (and H) emission lines in extragalactic HII regions, including a near infrared line at λ10830 [155] that helps in breaking the degeneracy between gas density and temperature, leads to a reduction in the uncertainty and to a better defined regression value [156],

$$Y_p = 0.2449 \pm 0.0040. \tag{4.9}$$

On the other hand, after a very precise observation of deuterium abundance in 2012 [157], which reduced the uncertainty from about $(10, 20)\,\%$, to about 2%,

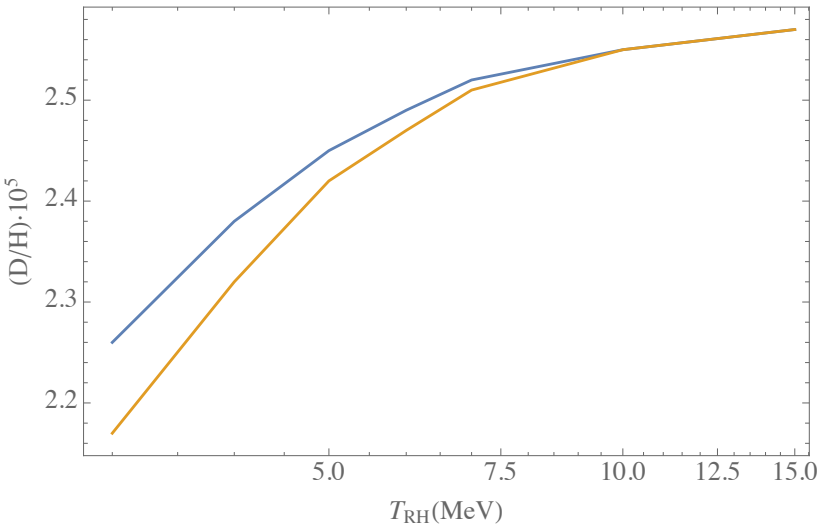

Figure 4.7: Same as Fig. 4.6 for the deuterium to hydrogen ratio ^{2}H/H.

the result of a reanalysis of deuterium data gives [158]

$$^2\mathrm{H/H} = (2.53 \pm 0.04) \cdot 10^{-5}. \tag{4.10}$$

For each nuclide we have defined a χ^2-function as follows ($i = {}^4\mathrm{He}, {}^2\mathrm{H/H}$):

$$\chi_i^2 = \frac{\left(X_i^{\mathrm{th}}(\Omega_b h^2, T_{\mathrm{RH}}) - X_i^{\mathrm{exp}}\right)^2}{\sigma_{i,\mathrm{th}}^2 + \sigma_{i,\mathrm{exp}}^2}, \tag{4.11}$$

where X_i^{th} is the theoretical value computed with `PArthENoPE` as a function of baryon density and T_{RH}, and σ_{th}^2 the corresponding uncertainty due to propagation of nuclear process rates ($\sigma_{^4\mathrm{He,th}} = 0.0003$, $\sigma_{\mathrm{D,th}} = 0.07 \cdot 10^{-5}$) [159]. The corresponding experimental mean value and uncertainty are denoted by X_i^{exp} and $\sigma_{i,\mathrm{exp}}$. We have used a prior on the value of $\Omega_b h^2$ from the recent Planck collaboration results [83]. Of course each χ_i^2 tends to a constant value for sufficiently large values of T_{RH}, which corresponds to a standard cosmology at BBN epoch, whereas it increases quite rapidly when T_{RH} becomes smaller and smaller. From these χ_i^2 equations we find the 2σ BBN bound

$$T_{\mathrm{RH}} \geq 4.1\,\mathrm{MeV}. \tag{4.12}$$

Actually, this constraint is essentially provided by deuterium.

As a final consideration, we should mention that our result was obtained using the present best fit of experimental data on the $d(p,\gamma)^3$He S-factor [160]. A theoretical ab-initio calculation for this process has been presented in [161], resulting in a larger reaction cross section in the BBN energy range, and a lower theoretical value of ^{2}H/H, in better agreement with the experimental result of Eq. (4.10), see [162]. Using this theoretical value for the $d(p,\gamma)^3$He thermal rate, assuming conservatively the same error on its determination $\sigma_{\rm D,th} = 0.07 \cdot 10^{-5}$, the BBN bound on the reheating temperature becomes even stronger:

$$T_{\rm RH} \geq 5.1\,{\rm MeV}. \tag{4.13}$$

4.3 Bounds from CMB observations

We now summarise the bounds obtained on the reheating temperature from the observed spectrum of CMB temperature and polarisation anisotropies as measured by the Planck satellite [83, 90, 163].

In order to compute the CMB power spectrum in models with a low-reheating temperature, we have modified the Boltzmann code `CAMB` [164] to allow for an arbitrary form of the neutrino distribution function (in principle different for each neutrino state). We use the results on the evolution of the neutrino spectra, as described in section 4.1, to obtain the distribution functions of the flavour neutrinos, to be given as an input to `CAMB` for a given value of the reheating temperature $T_{\rm RH}$. Only the last step of the time integration is actually relevant, since at the redshift of interest for the calculation of the CMB anisotropies, as well as other late-time observables, the neutrino distribution functions keep a constant shape and are only redshifted by the expansion of the Universe. Please notice that the cosmological perturbation equations are written in terms of the momentum distributions for the mass eigenstates, f_{ν_i} (with $i = \{1,2,3\}$), which are related to the flavour distributions f_{ν_α} by means of the relation

$$f_{\nu_i}(y) = \sum_{\alpha=e,\,\mu,\,\tau} |U_{\alpha i}|^2 \, f_{\nu_\alpha}(y). \tag{4.14}$$

The distorted flavour distributions as a function of $T_{\rm RH}$ have been expressed in terms of four parameters (a_α, b_α, c_α and d_α) such that

$$f_{\nu_\alpha}(y) = \frac{1}{{\rm e}^{a_\alpha y - b_\alpha + c_\alpha y^2 + d_\alpha y^3} + 1}, \tag{4.15}$$

with the dependence on the reheating temperature encoded in the values of these parameters.

We have seen in section 4.1 that in low-reheating scenarios the effective number of relativistic species $N_{\rm eff}$ is smaller than its standard value. However, this is not an independent parameter from the neutrino distribution functions, which subsequently depend on $T_{\rm RH}$. Therefore, the correct value of $N_{\rm eff}$ for each reheating temperature is automatically obtained internally in the Boltzmann code by means of the integration of the neutrino spectra.

The CMB anisotropy spectrum is also sensitive to the primordial helium abundance Y_p. Assuming standard BBN, the helium fraction can be determined once the baryon density ω_b and $N_{\rm eff}$ are given. We generalise this treatment to the models with a low-reheating temperature using `PArthENoPE` to generate a grid of values of Y_p as a function of ω_b and $T_{\rm RH}$, from which we interpolate to obtain the helium abundance for arbitrary values of these two parameters.

Finally, in order to compute Bayesian confidence intervals and sample the posterior distributions for the parameters of the model, given the data, we use the Metropolis-Hastings (MH) algorithm [165, 166] as implemented in `CosmoMC` [167] (interfaced with our modified version of `CAMB`). The MH algorithm is used to generate Markov chains of samples for a set of cosmological parameters. The models under investigation here can be described by the values of the six parameters of the standard ΛCDM model, as described in section 2.3.3 (with the amplitude of the spectrum of primordial scalar fluctuations, A_s, evaluated at the pivot scale $k_0 = 0.05\,{\rm Mpc}^{-1}$), with the addition of the reheating temperature $T_{\rm RH}$ and the mass of the lightest neutrino eigenstate (m_1 in normal ordering). The masses of the remaining eigenstates are derived from the best fit of the mass differences of Ref. [125].

We compute the constraints of the parameters from different datasets. Our basic one consists of Planck 2015 data on the CMB temperature anisotropies up to a multipole $\ell = 2500$ and on large-scale ($\ell < 30$) polarisation anisotropies [163]. This is the same basic dataset used by the Planck collaboration for parameter estimation [83], and we follow the tendency of referring to this dataset as "PlanckTT+lowP". We also consider the so-called "PlanckTT,TE,EE+lowP" dataset, that includes, in addition to the data just mentioned, the high-ℓ polarisation measurements from Planck [163].

As a first step, we have performed a test run by fixing $T_{\rm RH} = 15\,{\rm MeV}$. For this value of the reheating temperature, the scenario should be basically indistinguishable from standard ΛCDM, and in fact we have checked that we can reliably reproduce the corresponding results presented in Ref. [83], up to small

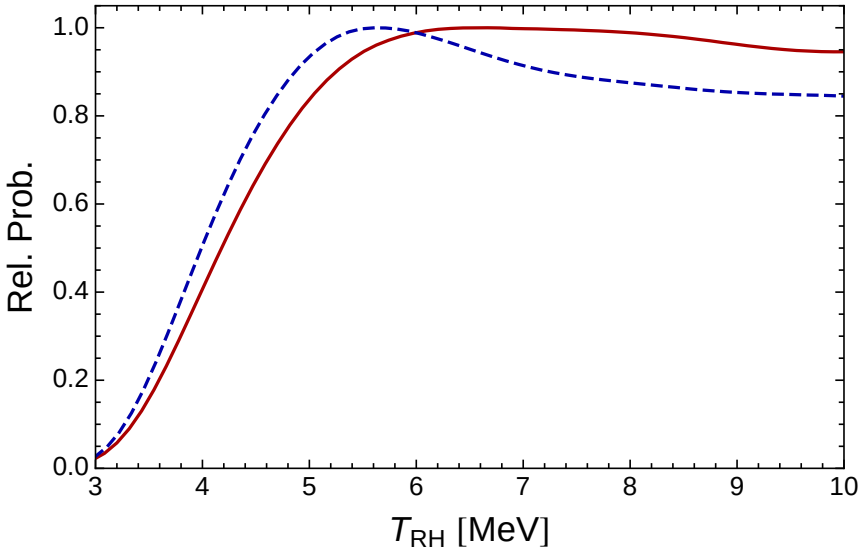

Figure 4.8: One-dimensional probability distribution for $T_{\rm RH}$, from the PlanckTT+lowP (red solid) and PlanckTT,TE,EE+lowP (blue dashed) datasets.

(below one standard deviation) shifts in the parameters, but we have traced them to the different parameterisation of neutrino masses between our code and the standard version of `CosmoMC` used by the Planck collaboration. We will comment about this point in further detail later.

After having checked the consistency with the standard ΛCDM, we turn to the Monte Carlo runs with $T_{\rm RH}$ as a free parameter. We get the following 95% lower limits on the reheating temperature:

$$\begin{aligned} T_{\rm RH} &\geq 4.7\,{\rm MeV} \quad ({\rm PlanckTT} + {\rm lowP}), \\ T_{\rm RH} &\geq 4.4\,{\rm MeV} \quad ({\rm PlanckTT, TE, EE} + {\rm lowP}). \end{aligned} \tag{4.16}$$

The corresponding posterior distributions for $T_{\rm RH}$ are shown in Fig. 4.8. Concerning the effective number of neutrinos we get (again at 95% CL)

$$\begin{aligned} N_{\rm eff} &\geq 2.81 \quad ({\rm PlanckTT} + {\rm lowP}), \\ N_{\rm eff} &\geq 2.75 \quad ({\rm PlanckTT, TE, EE} + {\rm lowP}). \end{aligned} \tag{4.17}$$

It is interesting to test the robustness of the cosmological limits on neutrino masses in low-reheating scenarios. In the following we will focus on the PlanckTT+lowP dataset only. Computing the 95% credible interval for the sum of neutrino masses $\sum m_i$ from our chains yields [1]

$$\sum m_i \leq 0.83\,\mathrm{eV} \qquad (\text{for } T_{\rm RH} \leq 15\,\mathrm{MeV}). \tag{4.18}$$

We have checked that we basically obtain the same result ($\sum m_i \leq 0.80\,\mathrm{eV}$) when $T_{\rm RH}$ is fixed to 15 MeV. However, one should not conclude from this that the neutrino mass limits stay unchanged in a low-reheating scenario. The reason is that, by considering the full allowed range for $T_{\rm RH}$, we are exploring a parameter space that for the most part (approximately $T_{\rm RH} > 7\,\mathrm{MeV}$) reproduces the standard ΛCDM+m_ν scenario. This is also the region where most of the probability mass is concentrated. When marginalizing over all other parameters to obtain the posterior for m_ν, this region dominates the probability integral and thus the procedure returns a constraint that is very close to the one found in standard ΛCDM. A possibly more sensible way to assess the effect of low-reheating scenarios on cosmological neutrino mass limits is to focus on the models with the lowest reheating temperature, by assuming a more stringent prior on $T_{\rm RH}$. Assuming different (*a priori*) upper limits on $T_{\rm RH}$, we get the following 95% credible intervals for $\sum m_i$:

$$\sum m_i \leq \begin{cases} 0.89\,\mathrm{eV} & (T_{\rm RH} \leq 7\,\mathrm{MeV}) \\ 0.93\,\mathrm{eV} & (T_{\rm RH} \leq 6\,\mathrm{MeV}) \\ 0.96\,\mathrm{eV} & (T_{\rm RH} \leq 5\,\mathrm{MeV}) \end{cases} \tag{4.19}$$

In Fig. 4.9 we show the posterior distribution for the sum of neutrino masses with these and other assumptions on $T_{\rm RH}$. There is a clear trend here: the constraint relaxes for lower reheating temperatures. The reason is easy to understand: the lower the reheating temperature, the lower the neutrino number density. Since, within a good approximation, the CMB directly constraints the neutrino energy density, and thus the product of mass times number density, a low reheating temperature allows larger masses to be compatible with the data.

Finally, we have calculated the improvement in the goodness-of-fit of the low-reheating scenario with respect to standard ΛCDM. For the PlanckTT+lowP

[1] This limit is different from the one quoted in Planck's paper [83] for the ΛCDM+m_ν scenario ($\sum m_i \leq 0.72\,\mathrm{eV}$). This is because we have implemented the normal mass neutrino ordering in the code, and as a consequence the total mass is bound to be larger than 0.06 eV. Instead, the ΛCDM+m_ν analysis by the Planck collaboration assumes three degenerate mass states and a simple positivity prior $\sum m_i \geq 0$.

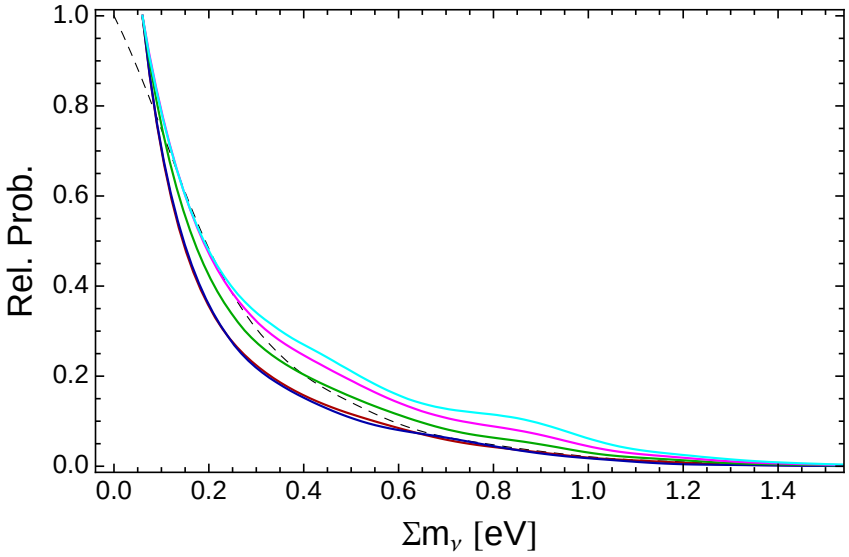

Figure 4.9: One-dimensional posterior distribution for $\sum m_i$ from the PlanckTT+lowP dataset, for different assumptions on the reheating temperature: $T_{\rm RH} \leq 15\,{\rm MeV}$ (red), $T_{\rm RH} = 15\,{\rm MeV}$ (blue, basically coinciding with the previous case), $T_{\rm RH} \leq 7\,{\rm MeV}$ (green), $T_{\rm RH} \leq 6\,{\rm MeV}$ (magenta), $T_{\rm RH} \leq 5\,{\rm MeV}$ (cyan). We also show a curve (black dashed) that reproduces the Planck collaboration results on $\sum m_i$ for the ΛCDM+m_ν model, for three neutrinos with equal mass.

dataset, we find $\Delta\chi^2 \ll 1$, signalling that low-reheating scenarios, in spite of the presence of one additional parameter, do not allow to improve significantly the fit to the CMB data.

4.4 Chapter remarks

We have studied the production of relic neutrinos in a generic cosmological model where the latest reheating phase of the Universe occurs at temperatures as low as 1 MeV. This low-reheating scenario is an exotic possibility where it is not easy to account for a proper baryogenesis (although some solutions exist [168, 169]), but it provides an interesting way to reduce the radiation content of the Universe (parameterised by $N_{\rm eff}$).

We have carefully solved the thermalisation of neutrinos in a low-reheating scenario, improving previous calculations and taking into account the effect of three-flavour neutrino oscillations. We have calculated the impact on the production of light elements, which in the case of ^{4}He strongly depends on the inclusion or not of neutrino oscillations, as originally found in [146]. The BBN lower limit on the reheating temperature is $T_{\rm RH}(\mathrm{BBN}) \geq 4.1\,\mathrm{MeV}$ (95% CL). A slightly more stringent bound can be obtained from the analysis of CMB anisotropies, from which we find $T_{\rm RH}(\mathrm{CMB}) \geq 4.7\,\mathrm{MeV}$ (95% CL).

Chapter 5

Testing neutrino statistics with cosmology

In this chapter, based on the publication [170], our aim is to investigate the possible cosmological bounds on a property of these tiny particles that is seldom discussed: the neutrino statistics. From the theoretical point of view, this issue was addressed in an original work by W. Pauli [171], which results in the well-known spin-statistics theorem. According to it, the wave function of integer-spin particles should be symmetric, meaning that it is invariant under permutations of the position of identical particles. Those particles are categorised as bosons, and an ensemble of bosons in thermal equilibrium obeys the *Bose-Einstein* (BE) distribution. On the other hand, particles with half-integer spin should be represented by antisymmetric wave functions, which change sign under position permutations. These particles are named fermions, and their thermal distribution is the *Fermi-Dirac* (FD) distribution. This is the case, for instance, of neutral leptons such as neutrinos. However, contrary to the case of electrons and nucleons, a possible violation of the Pauli exclusion principle for neutrinos is not yet experimentally excluded, although it affects elementary processes which involve identical neutrinos, such as double beta decay [172,173]. Such a violation was discussed in a series of theoretical papers, although no satisfactory model has been proposed so far (more discussion can be found in [172] and references therein).

Of course, from the theoretical point of view, many problems arise when assuming a violation of the Pauli exclusion principle. Among them, the spin-statistics theorem follows from the canonical quantisation to ensure a positive definiteness of energy, which might be spoilt if the Pauli principle is violated; the

CPT theorem follows, in particular, from the normal relation between spin and statistics, so CPT invariance could also be violated, and local observables would not commute, locality would be destroyed and Lorentz-invariance can be broken. In addition, since the standard electro-weak theory puts left-handed neutrinos and electrons in the same doublet, one would expect them to obey the same statistics.

In spite of all these complications, here we follow previous works and take a purely phenomenological approach for neutrino statistics, described by a single continuous parameter κ_ν which describes from purely fermionic ($\kappa_\nu = +1$) to purely bosonic ($\kappa_\nu = -1$) neutrinos. Previous analyses have described the main effects of $\kappa_\nu \neq 1$ on the early Universe, in particular on BBN [172, 174, 175], including a change in the contribution to the relativistic degrees of freedom (see also [176–178]). A modified neutrino statistics would also lead to a different behaviour as hot dark matter [179, 180] and, in the extreme case of bosonic relic neutrinos, even as light as axions, they could condense and act as the cosmological dark matter [172]. Other astrophysical consequence of the violation of the Pauli principle would be a different influence on the dynamics of the supernova collapse [172], as well as on a future detection of supernova neutrinos [181].

Our study extends previous works on the cosmological implications of a modified neutrino statistics, studying the bounds on κ_ν that can be obtained from the precise cosmological data currently available, both from BBN and the combined analysis of CMB measurements and BAO data, including for the first time the neutrino mass as a free parameter. In addition, we check how the currently known cosmological tensions are affected by a deviation from the purely fermionic nature of neutrinos. For instance, CMB measurements from the Planck satellite [83, 96] prefer a significantly lower value of the current expansion rate $H_0 = 100\,h\,\mathrm{km\,s^{-1}\,Mpc^{-1}}$ than what is derived from the type Ia Supernovae Survey [182]. Another tension that involves the same Planck mission affects matter fluctuations at small scales, quantified by the parameter σ_8 (a measure of the mean matter fluctuations in a sphere with a radius of 8 Mpc). Recent determinations of this parameter, using KiDS-450 [183] and Dark Energy Survey (DES) [184] data, result in a smaller value than the one obtained by Planck, exhibiting a discrepancy at a level of a bit more than 2σ in the pure ΛCDM model. Finally, concerning BBN, there is a discrepancy between the theoretical value of the primordial ^{7}Li abundance and its experimental determination from the Spite plateau [185], the so-called ^{7}Li *problem*. While these tensions may arise from not-yet-revealed observational systematics, they can also be viewed as signals that open doors to new physics.

In order to present this work we are going to discuss first the effects of a modified neutrino statistics on cosmology, moving later to the bounds obtained from BBN data (part in which the author of the present thesis has mostly contributed) and to those obtained from CMB observations. Finally we close the chapter with some remarks.

5.1 Cosmological effects of a modified neutrino statistics

In our phenomenological study we consider that the energy distribution of neutrinos in a thermal bath is different from that in equilibrium (Eq. (2.20)) by adding the *Fermi-Bose parameter* κ_ν, in such a way that they follow a distribution

$$f_\nu^{\rm eq}(E) = \frac{1}{{\rm e}^{E/T_\nu} + \kappa_\nu}, \tag{5.1}$$

with the substitution $E(p) \to p$ after decoupling. The parameter κ_ν characterises the neutrino statistics and can vary from -1 to $+1$. Such a parameterisation is motivated by earlier works on possible deviations of the neutrino statistics from the Fermi-Dirac distribution [172, 173, 175]. The strongest bound on the parameter κ_ν up to now comes from the observation of two-neutrino double beta decay processes, which leads to the lower bound $\kappa_\nu > -0.2$ [173, 186][1]. Thus, a 100% violation of Fermi statistics for neutrinos is disfavoured, but a large admixture of the bosonic component can still be present.

The parameter κ_ν should be also present in the statistical factor of the collision integral of any process involving neutrinos. For instance, in the case of the elastic scattering $\nu_1 + l_1 \leftrightarrow \nu_2 + l_2$ the corresponding statistical factor would be

$$F = f_\nu(k_1) f_l(p_1)[1 - f_l(p_2)][1 - \kappa_\nu f_\nu(k_2)] - f_\nu(k_2) f_l(p_2)[1 - f_l(p_1)][1 - \kappa_\nu f_\nu(k_1)]. \tag{5.2}$$

The generalised form $f_\nu^{\rm eq}(E)$ in Eq. (5.1) guarantees that, in thermal equilibrium, the collision integral of the process vanishes also for the case of mixed neutrino statistics.

[1] This bound could be improved soon from a careful analysis of NEMO-3 data (A.S. Barabash, private communication).

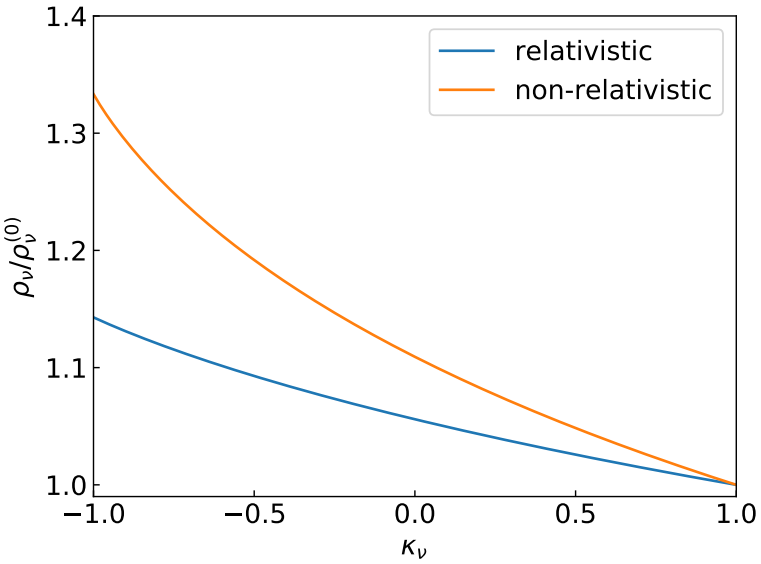

Figure 5.1: Ratio of neutrino energy densities $\rho_\nu/\rho_\nu^{(0)}$ as a function of κ_ν, where $\rho_\nu^{(0)}$ corresponds to the purely fermionic case.

The first and obvious effect of $\kappa_\nu \neq 1$ is a change in the contribution of neutrinos to the cosmological energy density, given by

$$\rho_\nu = \frac{g_\nu}{2\pi^2}\int_0^\infty \mathrm{d}p\, p^2 E(p)\, f_\nu(p) = \frac{g_\nu}{2\pi^2}\int_0^\infty \mathrm{d}p \frac{p^2 E(p)}{\exp(p/T_\nu)+\kappa_\nu}, \tag{5.3}$$

where $g_\nu = 2$ specifies the neutrino degrees of freedom per state. Therefore, varying the neutrino statistics has an impact on the neutrino energy density throughout the entire cosmic history.

For massless neutrinos, their modified energy density can be increased up to a factor 8/7 with respect to its value for fermionic neutrinos, as can be seen in Fig. 5.1 for different values of κ_ν. This factor arises from the calculation of the integral (5.3) for bosonic instead of fermionic particles (see Tab. 2.1). The modification in the energy density is fully equivalent to a change in the effective number of neutrinos N_{eff}. For three neutrino states, this amounts to a larger N_{eff}, with a maximum difference with respect to the standard value $N_{\mathrm{eff}}^{\mathrm{std}} = 3.045$ [116] of $\Delta N_{\mathrm{eff}} \equiv N_{\mathrm{eff}} - N_{\mathrm{eff}}^{\mathrm{std}} \simeq 0.43$ for purely bosonic neutrinos. The variation

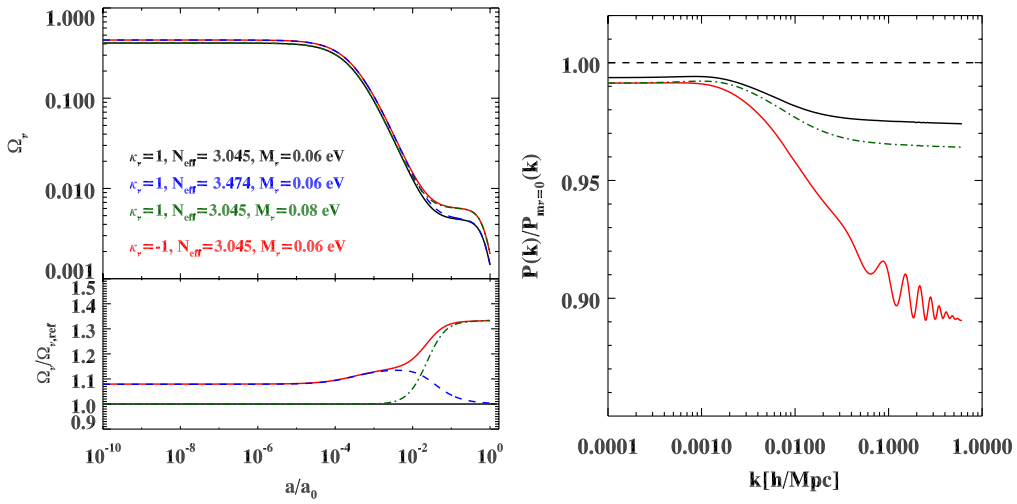

Figure 5.2: *Left panel:* Neutrino energy density in units of the critical energy density of the Universe, $\Omega_\nu = \rho_\nu/\rho_{\rm crit}$, as a function of the scale factor a, for different values of κ_ν, $N_{\rm eff}$, and the sum of the neutrino masses M_ν. $\Omega_{\nu,{\rm ref}}$ is the neutrino energy density fraction for $N_{\rm eff} = 3.045$ and $M_\nu = \sum m_\nu = 0.06\,{\rm eV}$. *Right panel:* Degree of late-time matter power suppression for different values of κ_ν and neutrino mass. Parameter values are the same for curves with the same colour in the two panels.

in $N_{\rm eff}$ is one of the required changes for a proper calculation of the outcome of primordial nucleosynthesis, together with the inclusion of the spectrum in Eq. (5.1) for electron neutrinos and antineutrinos in the weak processes that relate neutrons and protons, as we discuss in section 5.2.

For the more realistic case of massive neutrinos, the effect of a mixed statistics to the energy density is different at early and current times. At the epochs when relic neutrinos are still ultra-relativistic, their contribution to ρ_ν can be parametrised with an enhanced $N_{\rm eff}$, as we have just described. However, after their non-relativistic transition the neutrino energy in Eq. (5.3) is replaced by the neutrino mass. In this case, the ratio of the energy densities $\rho_\nu(\kappa_\nu)/\rho_\nu^{(0)}$ also grows for smaller values of κ_ν, but now reaching a maximum of 4/3 for purely bosonic neutrinos (see again Tab. 2.1), as depicted in Fig. 5.1.

Therefore, the full effect of having a modified neutrino statistics on the cosmological energy density is not equivalent to a global rescale of $N_{\rm eff}$ or of the neutrino masses. In the left panel of Fig. 5.2 we illustrate how the neutrino

energy density in different scenarios changes during the cosmological evolution, in comparison to the standard case of fermionic ($\kappa_\nu = 1$) neutrinos assuming $\sum m_\nu = 0.06\,\mathrm{eV}$ (solid black lines). Other three scenarios are shown: considering the same sum of neutrino masses, $\sum m_\nu = 0.06\,\mathrm{eV}$, we depict bosonic neutrinos with the standard value of $N_{\rm eff}$ (solid red lines), and also fermionic neutrinos when $N_{\rm eff}$ is manually increased by 0.43 (dashed blue lines). The last scenario (dashed-dotted green curves) shows fermionic neutrinos with their total mass increased by a factor of 4/3. As we can see, for a lower value of κ_ν both the early- and late-time neutrino energy densities are increased, as expected from Eq. (5.3). The case of FD neutrinos with an increased $N_{\rm eff}$ is equivalent at early times to the case of BE neutrinos, but not at late times, when neutrinos are no longer ultra-relativistic. On the other hand, neutrinos with an increased mass mimic the effect of the purely bosonic case only at late times, because the mass does not have any effect at the early stage. In the right panel of Fig. 5.2 we show the effect of the increased late-time neutrino energy on the current matter power spectrum. A larger late-time neutrino energy density causes more suppression to the matter power spectrum, an effect that is similar to having an increased neutrino mass. Therefore, if one wants to test a mixed neutrino statistics, it is clear that the entire cosmological evolution must be computed taking into account the neutrino distribution with a free κ_ν, as well as the possible values of neutrino masses.

Although current bounds are enough to forbid purely bosonic neutrinos, if this was the case their distribution function would include the possibility of a neutrino condensate,

$$f_{\nu,\mathrm{bose}} = (2\pi)^3 n_0 \delta(\mathbf{p}) + \frac{1}{\mathrm{e}^{(E-\mu)/T_\nu} - 1}, \tag{5.4}$$

where μ is the chemical potential of neutrinos and n_0 is the number density of neutrinos in a possible condensate. However, this term can only be non-zero if the chemical potential is maximum, $\mu = m_\nu$, because for smaller μ the collision integral vanishes only if $n_0 = 0$. Hence, the formation of a neutrino condensate is highly disfavoured.

5.2 Bounds from primordial nucleosynthesis

The implications on BBN of modified statistics for neutrinos were considered in the pioneering papers [172, 174, 175]. In particular, it was found that smaller values of κ_ν lead to a decrease both in the primordial mass fraction of helium-4, Y_p, and in the produced ^{7}Li abundance, while the amount of deuterium was

increased [175]. At that time, primordial nucleosynthesis did not exclude a purely bosonic nature of neutrinos, but a mixed neutrino statistics went in the direction of improving the agreement between the predicted value of the baryon asymmetry $\eta_{10} \equiv 10^{10} n_B/n_\gamma$ and its determination by CMB observations, which actually constrains the baryon energy density ω_b, related to η_{10} by

$$\omega_b \equiv \Omega_b h^2 = \frac{1 - 0.007125 Y_p}{273.279} \left(\frac{T_\gamma^0}{2.7255\,\mathrm{K}} \right)^3 \eta_{10}, \tag{5.5}$$

where T_γ^0 is the CMB temperature today (Eq. (2.56)).

The effect that neutrino statistics has on BBN enters in two main ways through the form of the modified neutrino distribution functions:

a) The total energy density of neutrino flavours, ρ_ν, contributes to the energy density of radiation, which in turn determines the Hubble expansion rate.

b) The electron-neutrino distribution functions directly appear in the weak rates that determine the neutron-proton chemical equilibrium.

Both effects can significantly affect the final abundances of primordial nuclides produced during BBN.

We have used a modified version of the `PArthENoPE` code [87, 88] to find the theoretical prediction of primordial abundances when neutrinos present mixed statistics. On the one hand, we have accounted for the modification of the neutrino energy density in the non-standard case of $\kappa_\nu \neq 1$. Since neutrinos are always ultra-relativistic at BBN, we have included the corresponding multiplicative factor on ρ_ν, as depicted in Fig. 5.1. On the other hand, implementing a modified statistics in the calculation of the weak rates is a more complex problem, due to the fact that the standard operation requires a high degree of accuracy, which forces us to take into account radiative corrections to neutron-proton exchange rates (see [187] for a review on BBN physics). In order to make a reliable estimate of the primordial abundances, we use in the modified `PArthENoPE` the Born weak rates. Additionally, we use the difference between the calculation including full radiative corrections and the one using Born rates, both computed for $\kappa_\nu = 1$ and for the same values of the other parameters, to revise the result and compensate for the lack of radiative corrections when using the mixed statistics (the same procedure is followed in the modified version of `PArthENoPE` used in the low-reheating study of chapter 4).

Our BBN results for a particular value of the baryon asymmetry ($\eta_{10} = 6.094$) are shown in Fig. 5.3, where the relative change of the primordial abundances is

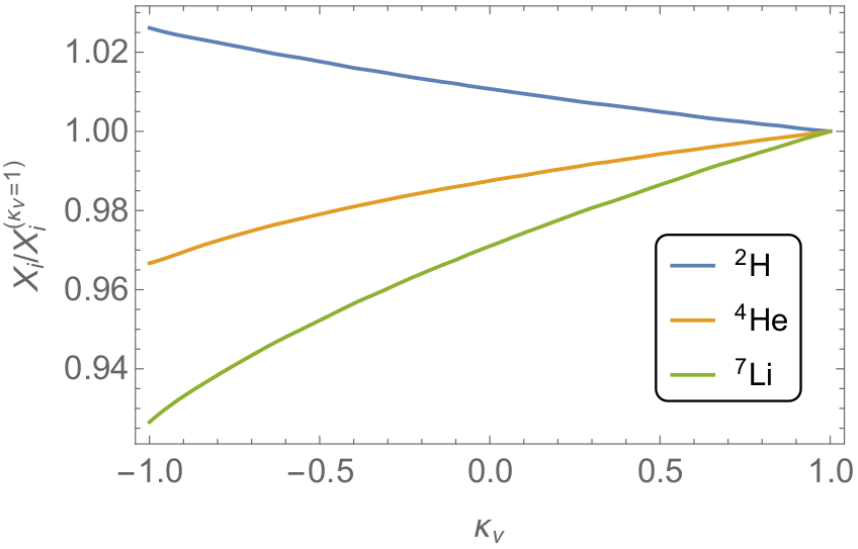

Figure 5.3: Relative change of the primordial abundances, $X_i/X_i^{(\kappa_\nu=1)}$, as a function of κ_ν, for $\eta_B = 6.094 \cdot 10^{-10}$.

plotted as a function of the effective Fermi-Bose parameter. The relative change in the primordial abundances is of the order of a few per cent, negative for ^{4}He and ^{7}Li and slightly positive for ^{2}H. This behaviour is in fair agreement with the results in figure 2 (lower panel) of [175]. Interestingly, we can note from the reduction of the produced ^{4}He for smaller values of κ_ν that the direct effect of the neutrino distribution on the weak rates is more important than the increased neutrino contribution to the energy density.

For the BBN analysis we consider the following experimental determinations of the primordial abundances of deuterium [188], helium-4 [156] and lithium-7 [189]:

$$^2\mathrm{H/H} = (2.527 \pm 0.030) \cdot 10^{-5}, \tag{5.6}$$

$$Y_p = 0.2449 \pm 0.0040, \tag{5.7}$$

$$^7\mathrm{Li/H} = (1.58 \pm 0.31) \cdot 10^{-10}. \tag{5.8}$$

Notice that the value of deuterium abundance used here (5.6) comes from a recent analysis and it is more precise than the one that we used in the previous chapter (Eq. (4.10)). The theoretical values of the primordial abundances are compared

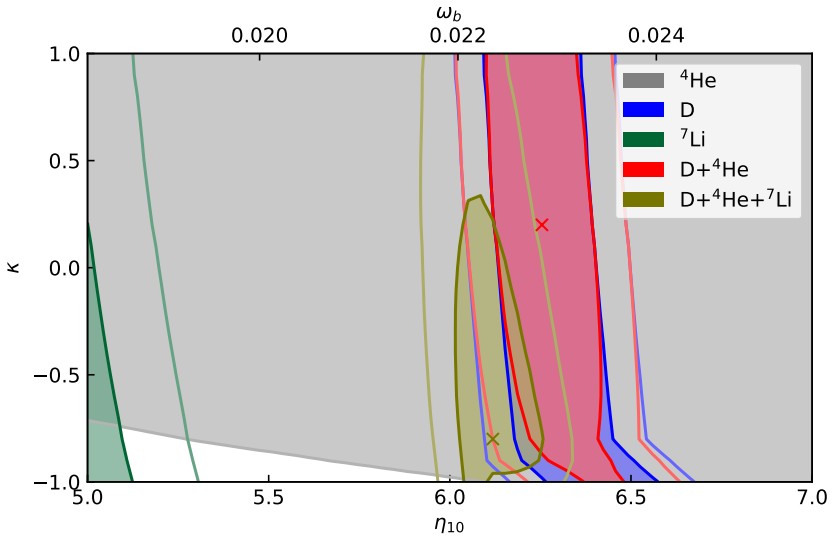

Figure 5.4: 1σ and 2σ contours in the plane $(\eta_{10},\, \kappa_\nu)$ from our BBN analysis. Areas in colour indicate the 1σ region and the corresponding line the 2σ one. In addition to the single abundance cases, we report the results for the combinations D+^{4}He and D+^{4}He+^{7}Li. Crosses mark the best-fit values for the combined cases.

with their measurements by the following χ^2-functions:

$$\chi^2_i\left(\kappa_\nu, \eta_{10}\right) = \frac{\left(X_i^{\rm th}\left(\kappa_\nu, \eta_{10}\right) - X_i^{\rm exp}\right)^2}{\sigma^2_{i,\rm th} + \sigma^2_{i,\rm exp}}\,, \tag{5.9}$$

where $i = \{\,^2{\rm H/H}\,,\, Y_p\,,^7{\rm Li/H}\}$, $\sigma_{i,\rm exp}$ are the experimental errors as given above and $\sigma_{i,\rm th}$ is the uncertainty due to propagation of nuclear process rates: $\sigma_{^2{\rm H/H,th}} = 0.05 \cdot 10^{-5}$, $\sigma_{Y_p,\rm th} = 0.0003$ and $\sigma_{^7{\rm Li/H,th}} = 0.26 \cdot 10^{-10}$ [159].

The results of our analysis are shown in Fig. 5.4 as 1σ and 2σ contours in the plane $(\eta_{10},\, \kappa_\nu)$, separately for each of the abundances and for the combined cases, D+^{4}He and D+^{4}He+^{7}Li. Some comments are in order. While deuterium prefers a restricted region in η_{10} (as it is a well known "baryometer"), the 1σ region from ^{4}He extends to almost all the plotted range and, at 2σ, the whole plane is allowed. At the same time, no evident indication for a preferred κ_ν value can be established, with the exception of the bottom left corner that is excluded by ^{4}He, but only with 1σ significance and for values of ω_b in tension

with CMB estimations. The lithium problem is evident in the displacement of the 1σ lithium region to the extreme left (and almost out of the considered region). The combined analysis without lithium essentially coincides with the area fixed by deuterium, with a mild preference for $\kappa_\nu \neq -1$. Instead, when ^{7}Li is included, the preference of this nuclide for a lower value of η_{10} tends to favour the "bosonic" character of neutrinos. Again, this is a consequence of the existence of the ^{7}Li problem, which is only slightly alleviated but cannot be solved with non-fermionic neutrinos.

5.3 Bounds from CMB and BAO data

In this section we study whether CMB and BAO measurements can provide any bound on neutrino statistics. We base our study on the standard ΛCDM cosmological model, parametrised by the usual six parameters (see section 2.3.3), with the following extensions: one with fermionic neutrinos and free neutrino masses (ΛCDM + m_ν model), one where we fix the neutrino masses and vary the parameter κ_ν describing the neutrino statistics (ΛCDM + κ_ν model) and the case where both κ_ν and m_ν are free (ΛCDM + κ_ν + m_ν model). When considering the models with varying neutrino masses, we adopt a degenerate case for the neutrino mass eigenstates, i.e. three identical masses such that $\sum m_\nu = 3m_\nu$. For this study this is a good approximation, since current cosmological experiments are not yet precise enough to discriminate the three separate mass eigenstates. When fixing the neutrino masses, we assume $m_\nu = 0.02\,\text{eV}$, corresponding to the (almost) minimum $\sum m_\nu = 0.06\,\text{eV}$ allowed by neutrino oscillations.

The theoretical models are computed with a modified version of the Boltzmann code `CLASS` [190], while to explore the parameter space we employ its companion code `MontePython` [191] together with the `MultiNest` [192–194] nested sampling algorithm. Concerning the experimental measurements, we use CMB data from the Planck 2015 release[2]: the high-ℓ ($30 \leq \ell \leq 2508$) and the low-ℓ ($2 \leq \ell \leq 29$) temperature auto-correlation likelihoods, the Planck polarisation likelihood at low-multipoles ($2 \leq \ell \leq 29$) and the lensing likelihood from the 4-point correlation function [83, 90, 163, 195]. BAO measurements are also considered, including data from the 6dF galaxy survey [196] at $z = 0.106$, SDSS DR7 main galaxy sample [197] at $z = 0.15$ and the two BOSS DR10 and DR11 results [198], from LOWZ at $z = 0.32$ and from CMASS at $z = 0.57$.

We do not show here a full comparison between the results obtained in the standard ΛCDM model and the extended ΛCDM + κ_ν model. The reason is that

[2]The Planck likelihoods are publicly available at www.cosmos.esa.int/web/planck/pla.

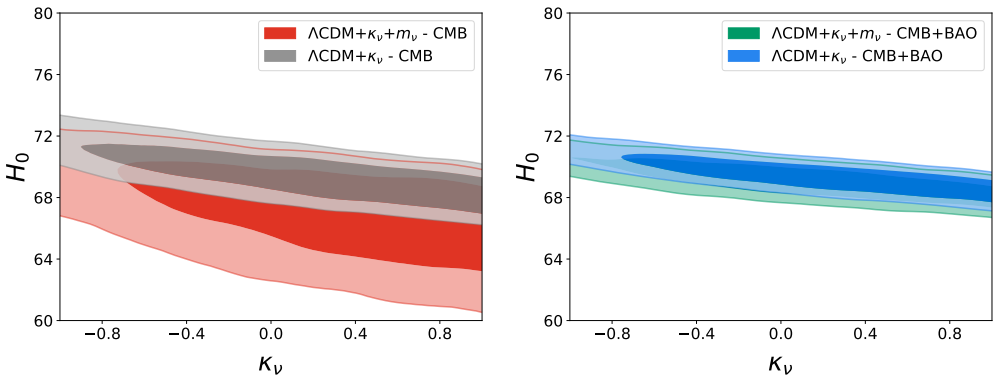

Figure 5.5: Degeneracy between κ_ν and H_0, considering two different data combinations (CMB and CMB+BAO) and theoretical models ($\Lambda\mathrm{CDM} + \kappa_\nu$ and $\Lambda\mathrm{CDM} + \kappa_\nu + m_\nu$). Areas represent 1σ and 2σ credible regions.

most of the cosmological parameters are affected by the new varying quantity κ_ν only through its partial degeneracy with $N_{\rm eff}$, discussed before, and the constraints do not change significantly. For example, we show in Fig. 5.5 that this degeneracy forces an expected correlation of κ_ν with the present value of the Hubble parameter H_0, which in turn impacts all the other parameters. Since m_ν and κ_ν have some degree of degeneracy and the neutrino mass is also correlated with H_0, the size of the 2-dimensional allowed contours is much larger in the $\Lambda\mathrm{CDM} + \kappa_\nu + m_\nu$ model. On the contrary, since BAO data strongly constrain m_ν, the degeneracy is reduced when the CMB+BAO dataset is considered.

The 1-dimensional marginalised posteriors on κ_ν from our analysis are presented in Fig. 5.6. Since from the CMB point of view a change in κ_ν is nearly equivalent to increasing $N_{\rm eff}$ by 0.43 or less, the current experimental sensitivity is not sufficient to obtain a strong bound on neutrino statistics. We obtain therefore a lower limit

$$\kappa_\nu > -0.18 \ (68\%,\ \mathrm{CMB},\ \Lambda\mathrm{CDM} + \kappa_\nu). \tag{5.10}$$

The purely bosonic case, although disfavoured at more than 68% CL, is still allowed at the 95% CL. This result is consistent with the lower bound obtained from the analysis of two-neutrino double beta decay ($\kappa_\nu > -0.2$), and implies that mixed statistics of neutrinos is still allowed given the current CMB data. The 68% lower limit changes only a bit if one considers a different data combination

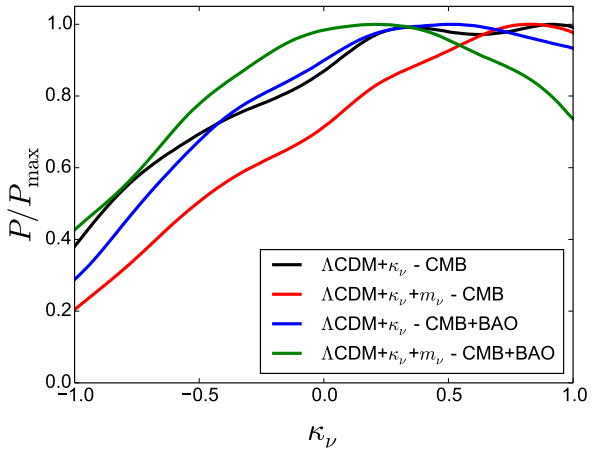

Figure 5.6: Marginalised posterior distribution for the parameter κ_ν from CMB data alone and in combination with BAO, in the ΛCDM+κ_ν and ΛCDM+κ_ν+m_ν models.

for the same model or an extended cosmological model with CMB data only,

$$\kappa_\nu > -0.15 \ (68\%,\ \text{CMB+BAO},\ \Lambda\text{CDM} + \kappa_\nu), \tag{5.11}$$

$$\kappa_\nu > -0.06 \ (68\%,\ \text{CMB},\ \Lambda\text{CDM} + \kappa_\nu + m_\nu). \tag{5.12}$$

Instead, a difference appears in the analysis of the $\Lambda\text{CDM} + \kappa_\nu + m_\nu$ model with CMB+BAO data. In this case, indeed, we find a 68% range of $-0.38 < \kappa_\nu < 0.83$, that does not include the pure FD and BE distributions. As demonstrated in Ref. [199], however, we recall that a flat prior is not the best way to sample the parameter space of a constrained parameter like m_ν or κ_ν, and the bounds on these parameters may be influenced by the chosen prior. We think that this is exactly the case. In addition, volume effects or shot noise problems are more likely to appear in this particular case, since BAO data strongly prefer values of m_ν close to the lower allowed value and there is some correlation between m_ν and κ_ν (see Fig. 5.7) that might affect the bound. Moreover, as reported in Eq. (5.11), when we fix the neutrino masses to the minimum of our prior (i.e. when we consider the $\Lambda\text{CDM} + \kappa_\nu$ model), the bound is perfectly compatible with the one obtained from CMB data alone and there is no exclusion of the FD distribution. Another interesting thing we can learn from Fig. 5.7 is that there is less freedom for BE neutrinos when they have large masses. The reason is that

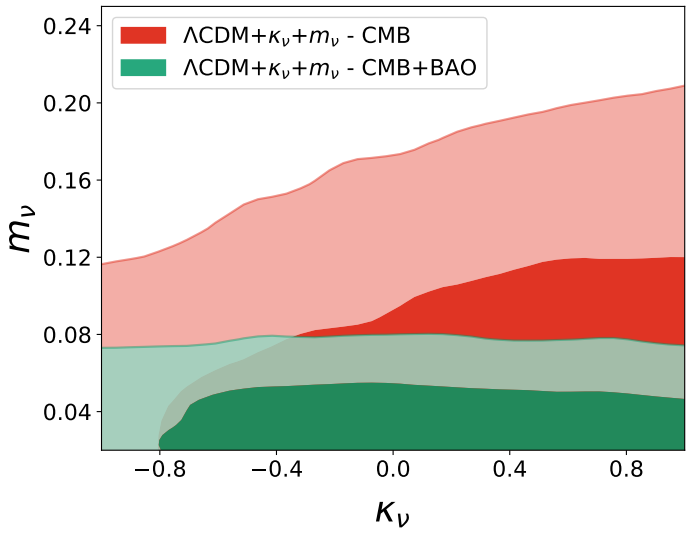

Figure 5.7: Correlations between κ_ν and m_ν in the $\Lambda\text{CDM} + \kappa_\nu + m_\nu$ model, using CMB data alone or in combination with BAO. Areas represent 1σ and 2σ credible regions.

the late time energy density for bosonic neutrinos is 4/3 larger than the FD one for the same masses, and consequently the neutrino mass is more constrained for $\kappa_\nu \simeq -1$.

We have also studied the impact of a mixed neutrino statistics on the H_0 and σ_8 tensions mentioned at the beginning of the chapter. In Fig. 5.8, we show the comparison of the constraints on H_0 and σ_8 from the standard ΛCDM model and the extended models with free neutrino statistics. As it is clear from the 1-dimensional posterior distributions, the extended models produce a higher H_0 but similar values of σ_8 with respect to the standard ΛCDM model predictions. Since the value of the Hubble parameter is larger, the tension between CMB-based H_0 estimates and its determinations from local measurements [182] is alleviated. Unfortunately, the 2-dimensional plot in the lower panel of Fig. 5.8 shows very well that there is a strong correlation between σ_8 and H_0, telling us that if H_0 increases, σ_8 cannot be significantly smaller than its value in the ΛCDM model. This result indicates that a modified neutrino statistics alone would not be enough to solve both the H_0 and σ_8 tensions simultaneously, regardless of the assumptions on neutrino masses.

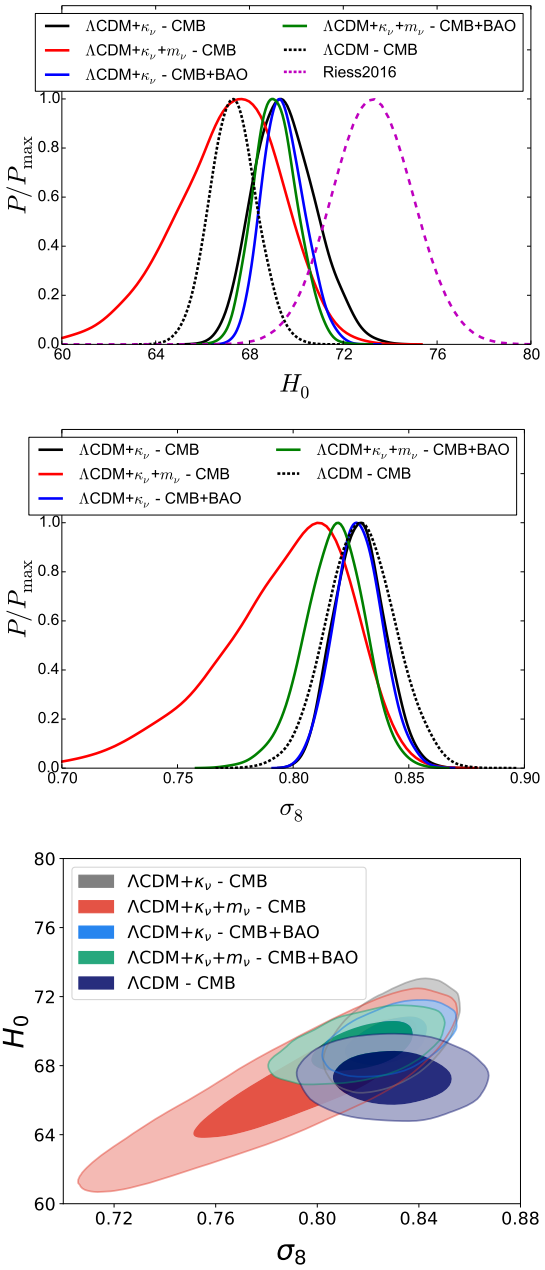

Figure 5.8: Constraints on H_0 and σ_8 in the $\Lambda\mathrm{CDM} + \kappa_\nu$ and $\Lambda\mathrm{CDM} + \kappa_\nu + m_\nu$ models, using CMB data alone and in combination with BAO, in comparison with the result from the base ΛCDM model (CMB only). We also plot the local measurement of H_0 (Riess2016 [182]) in the corresponding panel. Areas represent 1σ and 2σ credible regions.

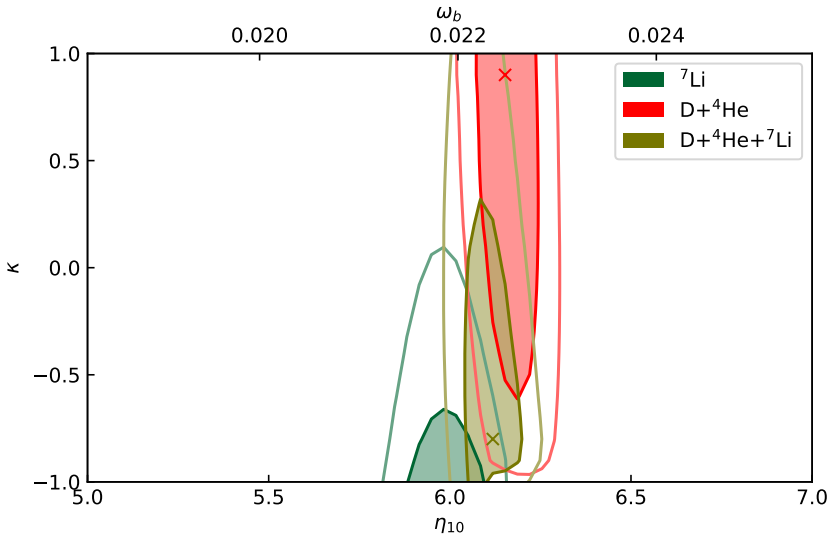

Figure 5.9: Same as Fig. 5.4 including a prior on ω_b from CMB (see text).

5.4 Combined bounds and chapter remarks

We want to investigate if a joint analysis of BBN, CMB and late-time cosmological observables could provide a stronger bound on neutrino statistics. We do it by the inclusion of a gaussian prior on ω_b from CMB on the BBN analysis. The prior, $\omega_b = 0.02230 \pm 0.00027$, was derived accounting properly for neutrino statistics, i.e., it is the result of a marginalisation over all the parameters except κ_ν of the full posteriors obtained using the extended model $\Lambda\text{CDM} + \kappa_\nu + m_\nu$ and only CMB data, discussed in section 5.3. The results are shown in Fig. 5.9, where one can see that the prior helps in reducing the allowed η_{10} region and, as a consequence, to improve the significance of the allowed region in κ_ν. In both cases, with or without prior, it is evident that D+^{4}He and ^{7}Li prefer *more fermionic* and *more bosonic* neutrinos, respectively. However, as we have already mentioned, the preference of ^{7}Li for negative values of κ_ν should be taken with care, since it is an artefact of the disagreement between the experimental value and the prediction for the lithium abundance.

In this chapter, based on the work [170], we have considered cosmological bounds on neutrino statistics, as well as the implications of a scenario where neutrinos violate the Pauli principle and do not follow the spin-statistics relation.

This assumption, which immediately arises theoretical problems that are difficult to solve, is analysed with a phenomenological approach via the introduction of the so-called Fermi-Bose parameter κ_ν, that characterises mixed neutrino statistics.

Our study shows that, despite the availability of very precise cosmological data, only very weak bounds are obtained on neutrino statistics. Using either CMB data alone or in combination with BAO results, we find that the region of κ_ν close to the purely bosonic case is weakly disfavoured, but only at less that 2σ, with lower bounds at the level of $\kappa_\nu > -0.18$ to $\kappa_\nu > -0.06$. The same applies to the BBN analysis, where only the smallest values of κ_ν are disfavoured, but at very low significance, once a prior on the baryon asymmetry from CMB is taken into account. We also find that the possibility of mixed neutrino statistics does not provide a way to solve current cosmological tensions.

Chapter 6

Local density of relic neutrinos

The direct detection of the cosmic neutrino background (CνB) is hindered by the feebleness of the weak interaction and the smallness of relic neutrino energies, diluted by the expansion. Neutrino oscillations, together with cosmic expansion, guarantee that at least two of the mass states of relic neutrinos are non-relativistic at present times, being that their mass is larger than their effective temperature $T_\nu^0 \simeq 1.6 \times 10^{-4}\,\mathrm{eV}$. This represents the only known situation in which neutrinos behave as non-relativistic particles, and allows them the possibility of being gravitationally trapped under the influence of large potentials, such as our own galaxy. This is of interest for experiments aiming at their detection, such as those that focus on capturing relic neutrinos in tritium.

Since the time of the first proposal by Weinberg [200], several techniques have been studied to detect relic neutrinos (see e.g. [201–206]), but the task still looks very challenging. Given the present tiny values of the neutrino kinetic energy, the most promising approach is to consider an interaction process with no energy threshold. In particular, the case of neutrino capture on β-decaying nuclei ($\overset{(-)}{\nu}_e + A \to e^\pm + A'$) has been considered in Refs. [207–211]. A relic neutrino capture by a nucleus A that can spontaneously β decay stimulates the emission of an electron with an energy at $2m_\nu$ above the β-decay endpoint[1], producing a characteristic peak shifted beyond the end of the β spectrum. Accordingly, an experiment based on this process should measure the shape of the energy spectrum of the electrons

[1]This is true for degenerate neutrino masses. If the energy resolution of an hypothetical relic neutrino detector is good enough to resolve the difference in the masses of the neutrinos, then it will be sensitive to three peaks (assuming a non-zero mass for the lightest neutrino) corresponding to the three neutrino masses, each of them at a distance $m_{\nu,\mathrm{lightest}} + m_i$ from the β-decay endpoint.

produced by the β-decaying nuclei with exquisite precision near the endpoint. A detection of relic neutrinos could be achieved if the energy resolution Δ was smaller than the neutrino mass. This is a very challenging requirement, because one would need at least $\Delta \lesssim 0.7 m_\nu$ [211] in order to be able to distinguish the events due to neutrino capture from standard β-decay events.

Among the available β-decaying nuclei, tritium is considered as the best candidate. This isotope has a high neutrino capture cross section, a low Q-value and a long lifetime. Tritium is used as a radioactive source in the KATRIN experiment [93, 212], whose aim is to determine the absolute neutrino mass by measuring the endpoint region of the β spectrum. KATRIN has started collecting data in 2018, but its effective amount of tritium is far too small for detecting relic neutrinos, with an estimated event rate of $\mathcal{O}(10^{-6})$ per year [213, 214]. On the other hand, a dedicated experiment based on neutrino capture by tritium was proposed recently: the PonTecorvo Observatory for Light, Early-universe, Massive-neutrino Yield (PTOLEMY) [94]. For a PTOLEMY-like experiment, working with about 100 g of pure atomic tritium, a number of around 10 events per year from CνB interactions is expected, taking into account the present average number density of relic neutrinos [94, 207, 211, 215, 216]. Its phenomenology and potential for CνB detection was studied in detail in Ref. [211]. Unfortunately, the designed energy resolution of PTOLEMY, $\Delta \simeq 150\,\text{meV}$, is too large for C$\nu$B detection if the heaviest neutrino state has the minimal mass guaranteed by flavour oscillations, of the order of $m_\nu \simeq 50\,\text{meV}$. However, the experiment could be sensitive to larger masses $m_\nu \gtrsim 150\,\text{meV}$, that are disfavoured but not completely ruled out by the current cosmological limits on the sum of neutrino masses (see the discussion in section 2.3.4).

Here we present the results published in [215] on the calculation of the local overdensity of relic neutrinos, a subject that was already studied in the past. In particular, we use the same simulation technique as in Ref. [217]. With respect to it, however, we consider lighter neutrino masses, closer to the limits imposed by cosmological observations. In addition, we also improve the treatment of the matter distribution in the local neighbourhood of the Earth, using the results of recent estimates and N-body simulations of objects similar to the Milky Way (MW) for both DM and baryon densities.

Along this chapter, we first describe the method used to compute the gravitational clustering of massive neutrinos in section 6.1 and how we parameterise the matter distribution (DM and baryons) in our galaxy in section 6.2. Our results on the local overdensity of massive relic neutrinos and the consequences for PTOLEMY-like experiments are discussed in section 6.3.

6.1 Gravitational clustering of massive neutrinos

In our work we adopt the "N-one-body" simulation method described in Ref. [217] to calculate the clustering of light neutrinos in the local environment. The N-one-body technique is based on the assumption that the growth of the neutrino overdensity does not influence in a significant way the evolution of the DM halo and the baryon accretion. Therefore, it is possible to calculate independently the clustering of each single neutrino in the evolving DM+baryon distribution and to obtain the total overdensity as the sum of the contributions of N selected neutrinos. The crucial difference with respect to an N-body simulation is that, instead of evolving N particles at the same time, one evolves N times one single particle. Thus one can increase arbitrarily the number of sample neutrinos without modifying the complexity of the code.

The N-one-body approach is valid as long as we can assume that:

1. the only interaction that matters is gravitational;
2. DM and baryons evolve independently of neutrinos: this follows from the small contribution of neutrinos to the total non-relativistic matter density;
3. neutrinos evolve according to the gravitational effects of DM and baryons, and independently of other neutrinos: this is another consequence of the same fact.

6.1.1 Equations of motion

We can write the lagrangian for our test neutrino with mass m_ν, moving in a gravitational potential well $\phi(\mathbf{x}, \tau)$, as

$$L(\mathbf{x}, \dot{\mathbf{x}}, \tau) = a \left(\frac{1}{2} m_\nu v^2 - m_\nu \phi(|\mathbf{x}|, \tau) \right), \tag{6.1}$$

where $a = 1/(1+z)$ is the cosmological scale factor (normalised to 1 today), $\mathbf{v} = \dot{\mathbf{x}}$ the peculiar velocity of the particle, $\mathbf{x}$ the comoving distance and τ the conformal time. For simplicity we choose a spherically symmetric gravitational potential $\phi(\mathbf{x}, \tau)$, so we can rewrite the lagrangian in comoving polar coordinates $\{r, \theta\}$,

$$L\left(r, \theta, \dot{r}, \dot{\theta}, \tau\right) = \frac{a}{2} m_\nu \left(\dot{r}^2 + r^2 \dot{\theta}^2 - 2\,\phi(r, \tau) \right), \tag{6.2}$$

from where we get the hamiltonian

$$H\left(r,\theta,p_r,l,\tau\right)=\frac{1}{2am_\nu}\left(p_r^2+\frac{l^2}{r^2}\right)+am_\nu\phi(r,\tau), \tag{6.3}$$

where

$$p_r=\frac{\partial L}{\partial\dot{r}}=am_\nu\dot{r}, \qquad l=rp_\theta=\frac{\partial L}{\partial\dot{\theta}}=am_\nu r^2\dot{\theta} \tag{6.4}$$

are the canonical momenta conjugate to r and θ respectively. We obtain then the Hamilton equations

$$\begin{aligned}
\frac{\partial H}{\partial p_r}&=\frac{\mathrm{d}r}{\mathrm{d}\tau}=\frac{p_r}{am_\nu}, & \frac{\partial H}{\partial l}&=\frac{\mathrm{d}\theta}{\mathrm{d}\tau}=\frac{l}{am_\nu r^2},\\
-\frac{\partial H}{\partial r}&=\frac{\mathrm{d}p_r}{\mathrm{d}\tau}=\frac{l^2}{am_\nu r^3}-am_\nu\frac{\partial\phi}{\partial r}, & -\frac{\partial H}{\partial\theta}&=\frac{\mathrm{d}l}{\mathrm{d}\tau}=0,
\end{aligned} \tag{6.5}$$

where the gravitational potential $\phi(r,\tau)$ is known from the Poisson equation

$$\nabla^2\phi=\frac{1}{r^2}\frac{\partial}{\partial r}\left(r^2\frac{\partial\phi}{\partial r}\right)=4\pi Ga^2\rho_{\mathrm{matter}}\left(r,\tau\right). \tag{6.6}$$

G is the gravitational constant and we remind the reader that ρ_{matter} is taken to be spherically symmetric. Then we have

$$\frac{\partial\phi}{\partial r}=\frac{G}{ar^2}M_{\mathrm{matter}}(r,\tau), \tag{6.7}$$

where

$$M_{\mathrm{matter}}(r,\tau)=4\pi a^3\int_0^r\rho_{\mathrm{matter}}(r',\tau)r'^2\mathrm{d}r' \tag{6.8}$$

is the total matter at a distance r and a proper time τ.

6.1.2 Technical details

The result of our simulations is a mapping between sets of initial and final neutrino coordinates in phase space. There are regions in the initial phase space such that today neutrinos are still inside the dark matter halo, and regions such that they escape and leave to infinity. Only the first category of trajectories is relevant for us, since our goal is to evaluate the neutrino density in the halo at present time. However, there is no way to know in advance where the boundaries of the relevant region are in the initial phase space, and we cannot afford to spend

most of the computing time on the calculation of irrelevant neutrino trajectories. We address this problem with an iterative approach. We first launch a set of representative particles for a coarse-grained discretisation of the full initial phase space. Among these particles, those ending up inside a certain $r_{\rm cut}$ radius are traced back, finer discretised and relaunched. The procedure is repeated until we have a sufficient number of relevant trajectories to estimate the neutrino density profile at $r \simeq r_\oplus = 8\,{\rm kpc}$ with good precision.

The raw result of the simulations consists in a set of final neutrino coordinates in phase space. We need to go from this discrete set to a smooth number density profile $n(r)$. This can be done, first, by assigning an appropriate statistical weight to each trajectory, in order to correctly sample the initial phase space, and to properly take into account the initial Fermi-Dirac isotropic distribution of neutrino momenta; and second, by applying a smoothing kernel to the discrete results, in order to estimate the underlying continuous density distribution. For these two steps, we follow the procedure described in [218] and already employed in [217]. In particular, since we assume spherical symmetry for simplicity, we must choose a smoothing kernel that will automatically enforce such a symmetry. Our kernel consists in a gaussian function of the radial coordinate; in other words, we perform gaussian smoothing on the surface of spheres of radius r. We refer to appendix A.3 of [217] for the mathematical expressions.

For each r, this kernel has only one arbitrary parameter: the gaussian width ξ (indicated as h in [217]). Choosing a too small ξ would lead to a small number of simulated neutrinos per smoothing shell, and the results would be dominated by shot noise and statistical fluctuations, unless a prohibitive number of trajectories is computed. Choosing a too large ξ would erase the details of the radial density profile $n(r)$ that we want to reconstruct. Hence the goal of the game is to resolve a sufficient number of trajectories in order to get results which remain independent of ξ within an extended range of ξ values. As long as the result varies strongly with ξ in the whole range $0 < r < r_{\rm cut}$, we know that the results are not yet converged, and that we need to increase the number of samples.

In the following results, we use this method to define our convergence criteria. For each simulated model, the optimal value of ξ is chosen in such a way that the results are stable against small variations of ξ. The dependence of the result on ξ is used to estimate the numerical error coming from discrete sampling, which is reported as error bands in our final plots. Following this method, we find that smaller neutrino masses require a larger number of neutrino trajectories to achieve the same precision. This was expected, since lighter neutrinos have larger velocities and escape more easily from the DM halo. Hence they require

a finer discretisation of the initial phase space. For the smallest mass considered here, our numerical error is limited by large needs in terms of computing time. However, even in that case, the total errors are dominated by the uncertainty on the shape of the DM distribution in the MW, rather than by discretisation issues and shot noise.

6.2 Matter distribution in our galaxy

The results of our N-one-body simulations depend on the *total* matter distribution in our galaxy, regardless of the nature of its different components. However, in order to show the relative impact of DM and baryons on the clustering of relic massive neutrinos, we have run simulations with only one component at a time, in addition to full simulations including the whole matter distribution. This will also help us to understand the impact of various approximations and the uncertainty coming from each distribution.

For simplicity, our simulations do not feature a feedback of baryons on the evolution of DM and vice versa. In the real Universe, these feedbacks are important (see e.g. [219, 220]), but we will see later how we cope with this approximation. Note also that the DM and baryon profiles implemented here are estimated from actual observation of the current matter distribution in the MW, which is the result of a self-consistent evolution including feedback effects: hence, we do take them into account in some indirect way.

6.2.1 Dark matter distribution

For the DM density profile in the MW, we follow [221] and use two different assumptions:

a) A generalised NFW profile, with a logarithmic slope varying from γ below a scale radius r_s to -3 in the outer region. We do not fix $\gamma = 1$ like in the original NFW proposal (see Eq. (2.63)), but leave it as a free parameter. Therefore, the NFW profile gets the form

$$\rho_{\rm NFW}(r) = \mathcal{N}_{\rm NFW} \left(\frac{r}{r_s}\right)^{-\gamma} \left(1 + \frac{r}{r_s}\right)^{-3+\gamma}, \tag{6.9}$$

where $\mathcal{N}_{\rm NFW}$ is a normalisation parameter related to the halo mass. Note that there is a unique relation between this parameter and the DM density at the core radius,

$$\mathcal{N}_{\rm NFW} = 2^{3-\gamma} \rho_{\rm NFW}(r_s). \tag{6.10}$$

b) An Einasto profile with the same parameterisation as in equation (2.64),

$$\rho_{\rm Ein}(r) = \mathcal{N}_{\rm Ein} \exp\left\{-\frac{2}{\alpha}\left(\left(\frac{r}{r_s}\right)^{\alpha} - 1\right)\right\}. \tag{6.11}$$

The normalisation parameter is now related to the DM density at the core radius by

$$\mathcal{N}_{\rm Ein} = \rho_{\rm Ein}(r_s), \tag{6.12}$$

and α is left as a free parameter in the model.

We now fit Milky Way data with our two DM distribution models, described by three parameters ($\mathcal{N}$, r_s, η), where ($\mathcal{N}$, η) can be either ($\mathcal{N}_{\rm NFW}$, γ) in the NFW model or ($\mathcal{N}_{\rm Ein}$, α) in the Einasto model.

The experimental data are taken from the non-parametric reconstruction of the DM density in the MW performed in [222]. In particular, we use the data presented in their figure 2, taking the central value of their so-called baryonic bracketing as the experimental values for $\rho_{\rm DM}(r)$, and the extreme values as the edge of the 1σ errors. Since uncertainties coming from the determination of the galactocentric radius r are included in those on $\rho_{\rm DM}(r)$, we identify r with the central radius of each bin. Note that [222] converted angular circular velocities $\omega_{\rm DM}$ to a DM density profile under the assumption of spherical symmetry; this matches perfectly with our own simplifying assumptions. Following the same reference, we assume that the solar radial distance to the galactic centre and the local circular velocity are respectively given by $r_\odot = 8\,{\rm kpc}$ and $v_\odot = 230\,{\rm km/s}$.

In order to have an idea of the spread of the DM profile parameters in reasonable agreement with the data, we generated a large amount of possible spectra with a Markov Chain Monte Carlo method. We used the Metropolis-Hastings to accept or reject models on the basis of their χ^2 statistics. In each of the two cases (Eqs. (6.9) and (6.11)), this approach provides the best-fit model (black lines in figure 6.1) and the 1, 2 and 3σ confidence intervals (gray bands). We also define in each case what we call the optimistic model (dashed red lines), obtained by picking parameters that nearly saturates the upper 2σ bounds. We use these optimistic profiles to obtain an upper limit on the clustering of relic neutrinos at the Sun/Earth distance from the galactic centre (shown in green on the figure). Table 6.1 summarises the values of the parameters that describe the best-fit and optimistic NFW and Einasto profiles of figure 6.1, and gives in addition the corresponding virial mass and the parameter β (defined and computed below), the density at the Sun/Earth radius, and the χ^2 of the fit to the data points.

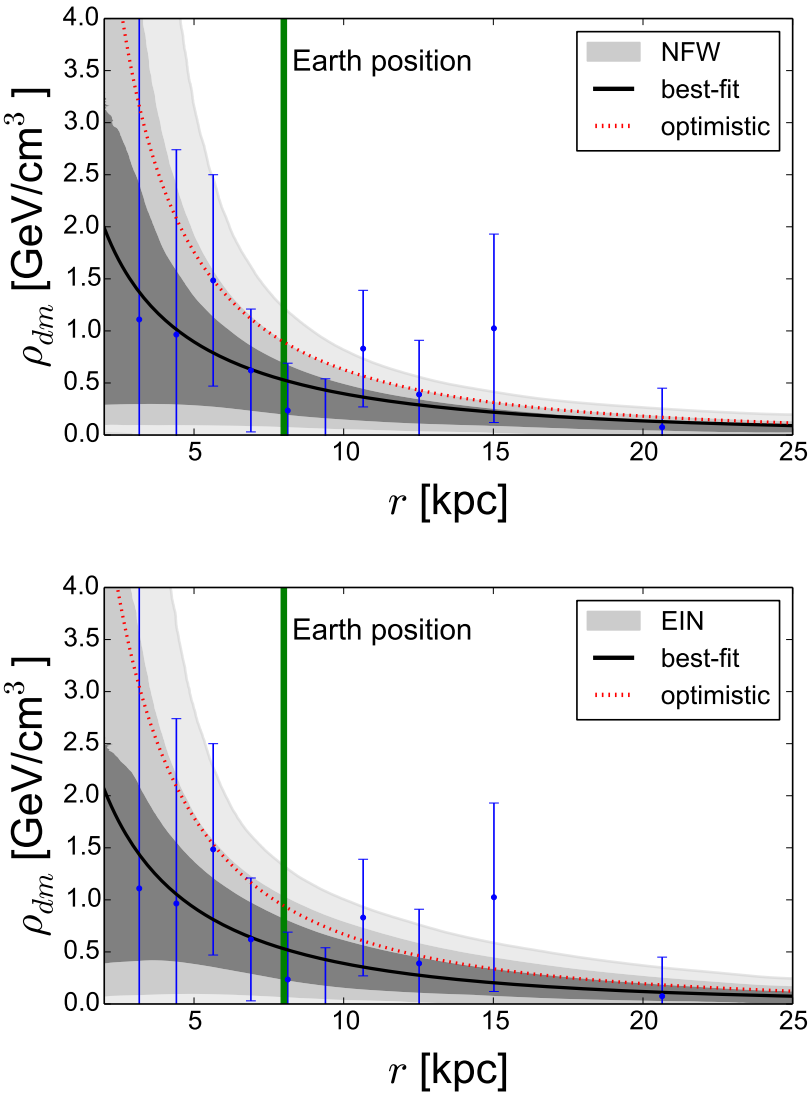

Figure 6.1: Profiles of the dark matter halo that we adopt in the calculations: we show the best-fit and optimistic cases (solid and dotted lines) together with the 1, 2 and 3σ regions. The upper (lower) panel is for an NFW (Einasto) profile of the DM halo. The green line represents the Earth position. The blue points are from Ref. [222].

	$\mathcal{N}$	r_s/kpc	η	$M_{\rm vir}/(10^{12}\,{\rm M}_\odot)$	$\rho_{\rm DM}(r_\oplus)/({\rm GeV/cm^3})$	β	χ^2
NFW best fit	0.73	20.29	0.53	3.76	0.53	2.09	3.06
NFW optimistic	0.73	20.28	0.95	4.25	0.89	2.21	5.79
Ein. best fit	0.12	20.28	0.45	1.13	0.53	1.10	3.08
Ein. optimistic	0.19	20.27	0.33	2.52	0.94	1.58	6.37

Table 6.1: Values of the parameters for the best-fit and optimistic profiles fitted to data and shown in Fig. 6.1.

In order to compute the effect of the gravitational potential ϕ on cosmological neutrinos through Eqs. (6.5) and (6.7) *today*, we need the DM distribution not only at present time, but also in the past. We assume that the η parameter is fixed, while $\mathcal{N}(z)$ and $r_s(z)$ are functions of the redshift, with values at $z = 0$ given by table 6.1. We compute the scaling of $\mathcal{N}(z)$ and $r_s(z)$ with redshift using two constraints (one coming from analytical modelling and one from N-body simulations) on the virial quantities $\Delta_{\rm vir}(z)$ and $c_{\rm vir}(M_{\rm vir}, z)$ defined below.

In any spherical halo, the virialised matter forms a sphere with fixed mass $M_{\rm vir}$, varying virial radius $r_{\rm vir}(z)$, and varying overdensity with respect to the critical density

$$\Delta_{\rm vir}(z) \equiv \frac{M_{\rm vir}}{\frac{4\pi}{3} a^3 r_{\rm vir}^3(z) \rho_{\rm crit}(z)}. \tag{6.13}$$

A second obvious relation fulfilled by $M_{\rm vir}$ and $r_{\rm vir}$ is

$$M_{\rm vir} = 4\pi a^3 \int_0^{r_{\rm vir}(z)} \rho_{\rm DM}(r', z) r'^2 dr'. \tag{6.14}$$

The function $\Delta_{\rm vir}(z)$ can be inferred from analytic calculations, by following the collapse of a spherical top-hat perturbation [223], but it is commonly approximated using a fixed value $\Delta \sim 200$. For each of the two parameterisations (NFW and Einasto) we follow the criteria of Ref. [224]:

$$\Delta_{\rm vir}(z) = \begin{cases} 18\pi^2 + 82\lambda(z) - 39\lambda(z)^2 & \text{for NFW,} \\ 200 & \text{for Einasto,} \end{cases} \tag{6.15}$$

where

$$\lambda(z) = \Omega_{\rm m}(z) - 1 \tag{6.16}$$

and $\Omega_{\rm m}(z)$ is the fractional matter density (as defined in Eq. (2.18)) at redshift z. For each of the four cases studied here (NFW/Einasto with best-fit/optimistic parameters), we know the density profile $\rho_{\rm DM}(r, 0)$ today, and $\Delta_{\rm vir}(0)$ is given

by (6.15). Then the two equations (6.13, 6.14) evaluated at $z = 0$ provide two relations between two unknowns $M_{\rm vir}$ and $r_{\rm vir}(0)$, that we find numerically.

We now need to relate the virial radius $r_{\rm vir}(z)$ to the scale radius $r_s(z)$ of the NFW or Einasto profile. The ratio between these two radii is called the concentration parameter,

$$c_{\rm vir}(M_{\rm vir}, z) = r_{\rm vir}(z)/r_s(z). \tag{6.17}$$

We use the average concentration parameter across several halos that has been measured in N-body simulations in [224], which provides two functions $a(z)$ and $b(z)$ such that

$$\log_{10} c_{\rm vir}^{\rm average} = a(z) + b(z) \log_{10} \left(M_{\rm vir} / \left[10^{12} h^{-1} M_\odot \right] \right), \tag{6.18}$$

where $M_\odot$ stands for the solar mass. Since this result denotes a statistical trend, we assume that in each halo $c_{\rm vir}(M_{\rm vir}, z) = \beta \times c_{\rm vir}^{\rm average}(M_{\rm vir}, z)$, where β is a redshift-independent number of order one, that might be different in each galaxy. Knowing $M_{\rm vir}$, $c_{\rm vir}^{\rm average}(M_{\rm vir}, 0)$, $r_{\rm vir}(0)$ and $r_s(0)$, we can easily compute β in the Milky Way for each of our four models. The β values reported in table 6.1 are kept fixed in the rest of the calculation. At this point, the only remaining unknowns are $r_{\rm vir}(z)$, $r_s(z)$ and $\mathcal{N}(z)$ for $z > 0$, but given that $\Delta_{\rm vir}(z)$ and $c_{\rm vir}(M_{\rm vir}, z)$ are known from equations (6.15) and (6.18), the three relations (6.13), (6.14) and (6.17) are sufficient for finding them with a numerical algorithm. Note that this algorithm also depends on the cosmological model through the scaling of the critical density with redshift, involved in equation (6.13). During matter or Λ domination, the scaling is given by

$$\rho_{\rm crit}(z) = \frac{3H_0^2}{8\pi G} \left(\Omega_{\rm m,0}(1+z)^3 + \Omega_{\Lambda,0} \right), \tag{6.19}$$

where $(H_0, \Omega_{\rm m,0}, \Omega_{\Lambda,0})$ are the present values of the Hubble parameter, the matter density fraction and the cosmological constant density fraction. For the study discussed in this chapter we assume that these parameters take the Planck best-fit values $(H_0, \Omega_{\rm m,0}, \Omega_{\Lambda,0}) = (67.27\,{\rm km/s/Mpc}, 0.3156, 0.6844)$ [83].

6.2.2 Baryonic distribution

The baryon distribution in our galaxy is very uncertain. For the DM distribution, we followed Ref. [221] and discussed only two plausible models. For the baryon distribution, the same reference proposes a total of 70 different models,

each of them coming from a different choice of 7 models for the bulge, 5 for the disc and 2 for the gas of the Milky Way.[2] Performing N-one-body simulations for each of these cases would require a prohibitively large computation time, and would not add much to the final results, since the gravitational potential mainly depends on DM. Actually, in our analysis, the relative uncertainties on the DM distribution correspond to a greater error than the relative uncertainties in the baryon component.

We choose to fix the baryon distribution according to the observation-driven model of Ref. [225]. This work fitted simplified axisymmetric distributions to the data for six distinct components: cold and warm dust, molecular and atomic hydrogen, stellar disc and stellar bulge. The latter two distributions are inferred from the star emissivity, which is converted into matter density assuming a global conversion factor determined from a total stellar mass of $6.43 \times 10^{10}\,\mathrm{M}_\odot$ [226] in the Milky Way.

We further assume that the baryonic profile is spherically symmetric in order to limit the computational time of our simulations. This approximation should be harmless for our purposes, since the total effect of baryons on the gravitational potential is smaller than that of the DM, except for a central region of radius $\sim 5\,\mathrm{kpc}$ [222] dominated by the bulge rather than the disc. In order to symmetrise the baryon profile, we simply compute the mass $M_\mathrm{b}(r)$ contained in each sphere of radius r, according to the true axisymmetric distribution. We then take the derivative of this function to obtain the symmetrised baryon density profile. Our assumptions for the baryonic profile are depicted in figure 6.2, where we show the total baryonic density, both in its spherically symmetrised approximation (solid blue) and on the galactic plane with the original axisymmetric profile (dashed-dotted blue, not used in the calculations). One can see that the two curves are closer at smaller radii, since the thickness of the disc is comparable with the distance from the galactic centre. In order to show that the main contribution to the baryon density comes from the stars, we include different lines for the contribution of stars (dotted black) and the sum of all the other components (dashed black), for the spherically symmetrised profile. The best-fit NFW DM profile is also shown for comparison.

We model the redshift dependence of the baryon profile through a simple redshift-dependent global normalisation factor $\mathcal{N}_\mathrm{b}(z)$. For higher precision, one should also introduce a redshift-dependent tilting of the profile, but the impact on our final results would be negligible compared to the uncertainty on the DM

[2] See table I in Ref. [221] for the corresponding list and references.

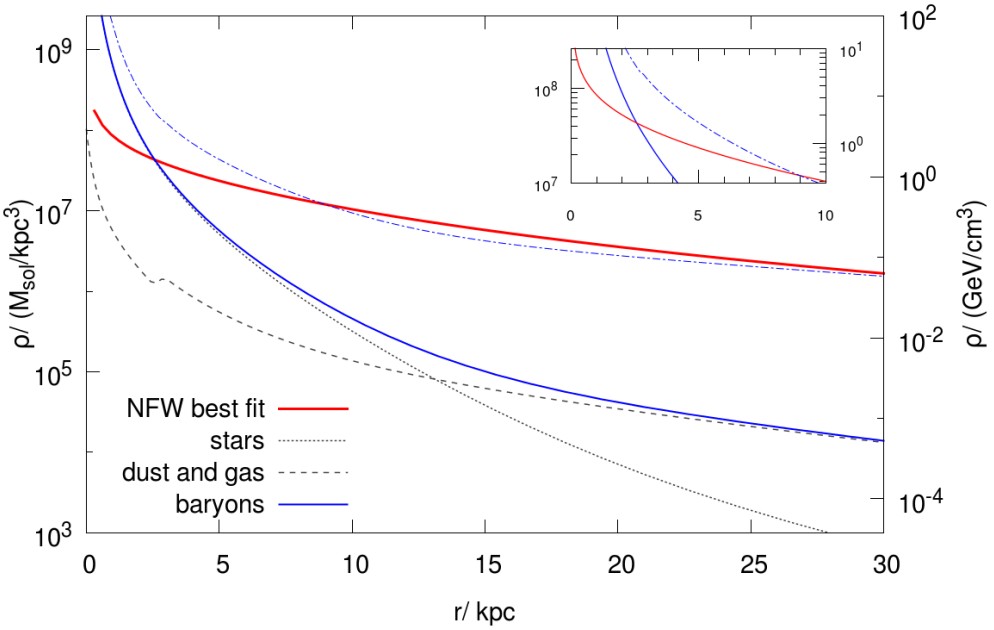

Figure 6.2: Spherically symmetrised baryonic density distribution used in our simulations (blue solid line), and its decomposition in stellar disc contribution (dotted) and other components (dashed). We also show the original axisymmetric baryonic profile evaluated on the galactic plane (dotted-dashed, not used in the calculations), and the best-fit NFW DM profile (red line).

profile. We obtain $\mathcal{N}_{\rm b}(z)/\mathcal{N}_{\rm b}(0)$ by averaging over the evolution of the stellar mass in eight Milky Way-sized simulated haloes, given in figure 18 of Ref. [219].

Concerning the mutual influence that baryons and DM have on each other during the gravitational accretion, it is true that there must be a correlation in the profile growth with redshift (see e.g. [219, 220]), but the effect is small when compared to the uncertainties coming from the shape of the DM profile. The presence of baryons tends to make the DM halo more clumpy near the galactic centre, but this is already taken into account in our DM profiles since they have been fitted to real data. At most, we expect that our model slightly overestimates the matter density in the past, because the leading component (DM) is being traced back in time independently, starting from a profile at $z = 0$ that includes the current baryonic feedback.

6.3 Estimating the local density of relic neutrinos

In this section we describe our results on the relic neutrino overdensity and the corresponding prospects for the event rate in a PTOLEMY-like experiment, computed for different values of the neutrino masses. We first assume nearly minimal neutrino masses (subsection 6.3.1), and then consider non-minimal masses, more favourable for a detection by PTOLEMY (subsection 6.3.2). Finally, in subsection 6.3.3 we show the detection prospects for a light sterile neutrino, such as the one proposed to solve the short-baseline neutrino oscillation anomalies.

6.3.1 Minimal neutrino masses

Using the method described in the previous sections, here we show the results obtained for nearly minimal neutrino masses, when the heaviest mass eigenstate has a mass $m_\nu \simeq 60\,\text{meV}$. We show in figure 6.3 the overdensity profile of such a neutrino state, for the different assumptions on the DM and baryon distributions previously discussed. For each DM profile, NFW or Einasto, we consider the best-fit case and the optimistic case (described in Sec. 6.2.1 and listed in table 6.1). We also show the effect of the baryonic component (discussed in section 6.2.2), alone or combined with each best-fit case of DM.

For a neutrino with $m_\nu \simeq 60\,\text{meV}$, we find that the total overdensity due to gravitational clustering at the Earth distance from the galactic centre is rather small, with a relative increase with respect to the average density of the CνB of 10%-20% at most. The values of the local neutrino overdensity are reported in table 6.2 for the different matter profiles.

For the same normalisation of $\rho_{\rm DM}(r)$ at the Earth distance, the NFW profile corresponds to a higher DM density than the Einasto profile at the galactic centre, and consequently to a stronger gravitational attraction of neutrinos. Thus, one can see in figure 6.3 that the local overdensity generated by NFW-distributed DM profiles is larger than in the Einasto cases. As expected, the effect of baryons is small, modifying the result by approximately 3% with respect to the CνB mean density.

These numbers depend slightly on the numerical factor ξ used in the reconstruction of the neutrino profile, and the corresponding numerical uncertainty is represented by the coloured band that enclose each curve in figure 6.3. These bands do not represent any kind of statistical or systematic error in the whole calculation; they just quantify the difficulty of computing robustly the neutrino clustering at decreasing distances from the centre of the matter halo.

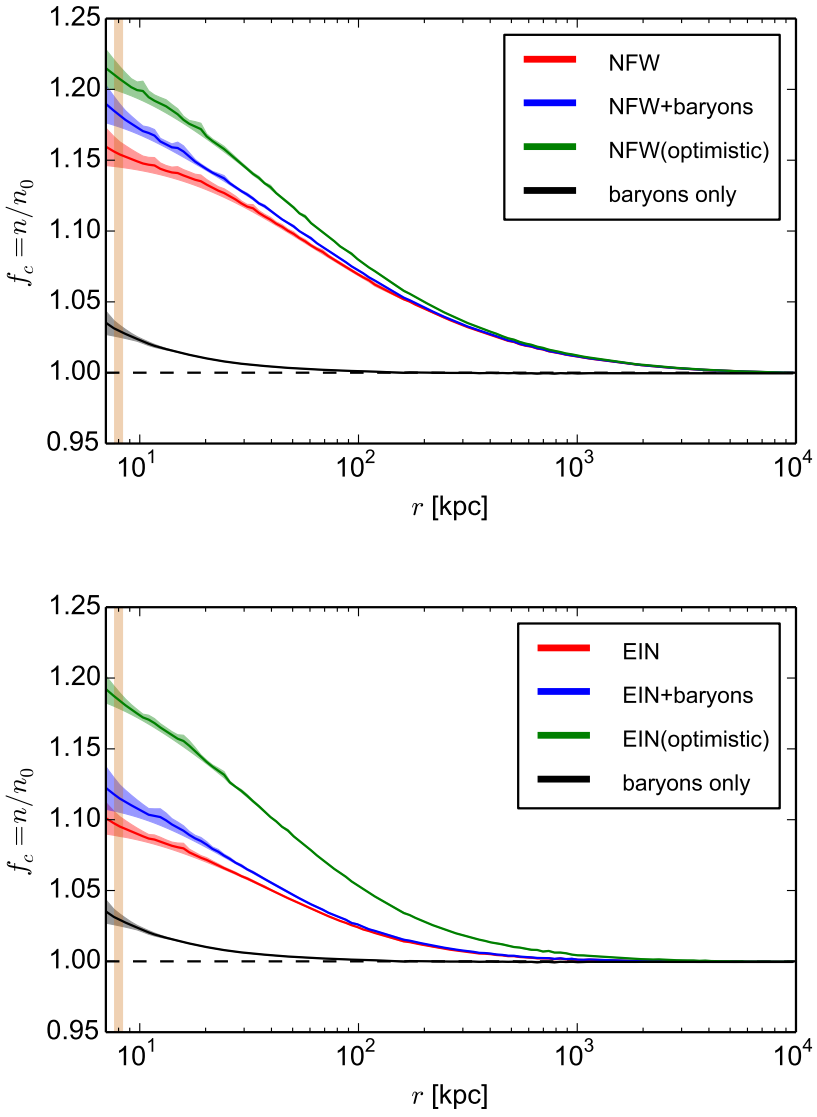

Figure 6.3: Neutrino overdensity for a single neutrino family with $m_\nu = 60\,\text{meV}$ as a function of the distance from the galactic centre, computed with different assumptions on the matter profiles. The upper (lower) panel is for an NFW (Einasto) DM profile. The orange band represents the Earth's position.

The final error is dominated by the uncertainty on the DM profile, since there is a significant difference between the NFW and the Einasto cases, and between the best-fit and optimistic distributions in each case. This last difference is of course expected, since we recall that our optimistic parameterisations can be considered as upper limits on the DM distributions, since they are chosen to be overestimates of the actual available data.

One can also see from figure 6.3 that the overdensity, as expected, depends on the distance from the centre of the MW. We see that neutrinos feel the gravitational attraction of the Milky Way halo and cluster at radii $r \leq r_{\rm over} \simeq \mathcal{O}(1\,{\rm Mpc})$.

The neutrino overdensity on sub-galactic scales was not previously computed for values of the neutrino mass as small as 60 meV. However, when comparing with the N-one-body results of Ref. [217] and the full N-body results of Ref. [227] obtained for heavier neutrinos, we find that the shape and the normalisation of our profiles are compatible with their results.

Let us comment the fact that the calculations we performed for such a (nearly) minimal value of the neutrino mass can be developed using the linear approximation with minor changes in the final results. The differences between the two methods have been studied in Ref. [217], where it was shown that the approximated results are very close to the simulated ones if the mass of the galaxy and the neutrino mass are small. However, since we also want to compute the overdensity for heavier neutrinos, it is mandatory to use the full computation.

In our N-one-body simulation, we only considered one isolated spherical galactic halo with homogeneous boundary conditions, and neglected the effect of neighbouring galaxies, satellite galaxies, etc. The impact of these objects should be negligible at redshift $z = 3$, when we start the simulation, but it could become important near $z = 0$. However, the computation of the neutrino clustering in a realistic environment where all DM clumps close to the MW are properly represented would be extremely demanding, so here we just present a qualitative discussion of their possible effects.

The satellite galaxies located at less than 1 Mpc from the centre of the Milky Way (the distance at which the DM halo starts to influence the neutrino overdensity) are much lighter than the MW, so we expect that their gravitational effect is very small. On the other hand, the Andromeda galaxy is slightly larger than the MW[3] and it is only $\sim 0.8\,{\rm Mpc}$ away (see e.g. [231, 232]). If we simply con-

[3] A recent study reanalysed the measurement of Andromeda's mass from the escape velocity of its high velocity tracers [228], finding a smaller value comparable to the MW mass. Previous analyses using different methodologies were compatible with this result [229, 230]. Therefore, to be in the safe side, it would be more adequate to say that Andromeda is, at least, as massive as the MW.

sider the superposition of two distinct (independently evolved) neutrino haloes for the two galaxies, we conclude from our results that the overdensity $f_{\rm c}$ at the Earth increases by ~ 0.02 to ~ 0.03 due to Andromeda; this is comparable to the effect of baryons, and smaller than the uncertainties due to the DM halo. For more distant galaxies with size comparable to the MW the effect would be even smaller. However, we need to take in consideration also larger objects, and in particular the Virgo cluster, the closest galaxy cluster to the MW. Its centre is located at approximately 16 Mpc, with a mass around $10^{15}\,{\rm M}_\odot$ [233, 234]. Interestingly, the neutrino clustering in a DM halo comparable to the one of the Virgo cluster has been studied with a full N-body simulation in Ref. [235], for neutrino masses ranging from 50 meV to 300 meV. One can see in their figure 2 that the Virgo neutrino halo probably extends beyond 10 Mpc. An extrapolation of the curve suggests that for a mass close to 50 meV or 60 meV, Virgo may create a neutrino overdensity at a radius of 16 Mpc of the same order as the one created by the MW halo itself. Therefore, the clustering factor due to Virgo should be kept into account when computing the local CνB neutrino density, but a full calculation involving different DM halos in the neighbourhood of the MW would be computationally too expensive to be performed with our method.

Let us now consider the effect of an enhanced local density of CνB neutrinos on the expected interaction rate in a future detector. Following [211], this can be estimated from

$$\Gamma_{\rm C\nu B} = \sum_{i=1}^{3} |U_{ei}|^2 [n_i(\nu_{h_R}) + n_i(\nu_{h_L})]\, N_T\, \bar{\sigma}, \tag{6.20}$$

where $n_i(\nu_{h_{R(L)}})$ is the number density of the i-th mass eigenstate neutrino with right (left) helicity, $N_T = M_T/m(^3{\rm H})$ is the approximate number of tritium nuclei in a sample of mass M_T, and $\bar{\sigma} \simeq 3.834 \times 10^{-45}\,{\rm cm}^2$ [211]. In the following we assume that the number density in vacuum of a single neutrino in a given helicity state is n_0, for all neutrinos, and independently of their mass. We use the values $|U_{ei}|^2 = (0.681, 0.297, 0.022)$ for the mixing matrix elements, and we fix the tritium mass to $M_T = 100\,{\rm g}$, having in mind the PTOLEMY proposal [94].

If the local density of each mass eigenstate is increased by a clustering factor $f_{\rm c}(m_i)$, the total neutrino capture rate can be obtained as

$$\Gamma_{\rm C\nu B} = [n_0(\nu_{h_R}) + n_0(\nu_{h_L})]\, N_T\, \bar{\sigma} \sum_{i=1}^{3} |U_{ei}|^2 f_{\rm c}(m_i). \tag{6.21}$$

We recall that the capture rate of Majorana neutrinos $\Gamma^{\rm M}_{\rm C\nu B}$ is twice the one of Dirac neutrinos $\Gamma^{\rm D}_{\rm C\nu B}$, because the capture is kinematically forbidden for Dirac antineutrinos, while in the Majorana case there is no distinction between a neutrino and an antineutrino particle. In both cases, both left and right helicity states are conserved during propagation; however, when neutrinos become non-relativistic both helicities share a left-chiral component, and only the one with positive lepton number interacts in the Dirac case. As a reference, we compare our results with the ones obtained when neglecting the neutrino clustering due to the MW [211],

$$\Gamma^{\rm D}_{\rm C\nu B} \simeq 4.06\,{\rm yr}^{-1}, \qquad \Gamma^{\rm M}_{\rm C\nu B} = 2\Gamma^{\rm D}_{\rm C\nu B} \simeq 8.12\,{\rm yr}^{-1}. \tag{6.22}$$

In table 6.2 we summarise our results for the normal and inverted mass ordering scenarios, assuming each time that the heaviest neutrino mass is $\simeq 60\,{\rm meV}$. We can see that the choice of mass ordering matters when computing the capture rate, since the three mass eigenstates are differently mixed with the electron neutrino flavour, the only one that interacts with the detector nuclei. In the case of normal mass ordering, gravitational clustering has practically no effect on the final event rate. For inverted ordering, there is a noticeable increase of the event rate of the order of 10% to 20%.

We conclude this discussion recalling that, unfortunately, a higher event rate does not necessarily lead to an easier detection of the CνB. Depending on the energy resolution of the detector, the events due to interactions with the CνB may be distinguished or not from those coming from the standard β decay of the detector material, that constitutes the main background for these kind of experiments. Since a resolution $\Delta \lesssim 0.7 m_\nu$ is required for a neutrino mass m_ν, while the PTOLEMY experiment targets $\Delta \sim (100, 150)\,{\rm meV}$, the cases that we have discussed so far are beyond the current capabilities of a PTOLEMY-like experiment.

6.3.2 Active neutrinos with non-minimal masses

After considering the most pessimistic neutrino mass scenarios from the point of view of CνB detection, we turn to an optimistic scenario in which the heaviest neutrino would have a mass $m_\nu \simeq 150\,{\rm meV}$. This assumption is motivated by the expected resolution of the PTOLEMY experiment, $\Delta \simeq (100, 150)$ meV [94]. In such a case, both squared-mass differences probed by oscillation experiments are much smaller than m_ν^2, and the three neutrino states share practically the same mass m_ν. In this degenerate scenario, in which the mass ordering is not so

masses (ordering)	matter halo	overdensity f_c		$\Gamma^{D}_{C\nu B}$ (yr^{-1})	$\Gamma^{M}_{C\nu B}$ (yr^{-1})
		$f_1 \simeq f_2$	f_3		
any	any	no clustering		4.06	8.12
$m_3 = 60\,\text{meV}$ (NO)	NFW (+bar.)	$\sim$1	1.15 (1.18)	4.07 (4.08)	8.15 (8.15)
	NFW opt.		1.21	4.08	8.16
	Ein. (+bar.)		1.09 (1.12)	4.07 (4.07)	8.14 (8.14)
	Ein. opt.		1.18	4.08	8.15
$m_1 \simeq m_2$ $m_2 = 60\,\text{meV}$ (IO)	NFW (+bar.)	1.15 (1.18)	$\sim$1	4.66 (4.78)	9.31 (9.55)
	NFW opt.	1.21		4.89	9.77
	Ein. (+bar.)	1.09 (1.12)		4.42 (4.54)	8.84 (9.07)
	Ein. opt.	1.18		4.78	9.55

Table 6.2: Clustering factors and expected event rates for Dirac or Majorana neutrinos in a PTOLEMY-like experiment, under different assumptions on the matter profile and on the neutrino mass ordering, when the heaviest mass is 60 meV. The first line shows the event rates in absence of clustering (for an homogeneous CνB).

relevant, the event rate is directly proportional to the overdensity factor f_c and the total neutrino mass is $\sum m_\nu \simeq 450\,\text{meV}$, a value already excluded by the most constraining combinations of cosmological data in the minimal ΛCDM framework (see e.g. [83, 97]), but still plausible in extended models (see e.g. Refs. [98–101]).

We repeated our N-one-body simulations for 150 meV neutrinos. Our results are summarised in figure 6.4 and table 6.3, using the same format as in the previous figures and tables. The general trends are the same as for 60 meV neutrinos, but the local overdensity factor is much larger: it reaches values around 2.4 and 1.9 for the best-fit NFW and Einasto profiles, respectively, with a maximum of 2.9 and 2.4 in the respective optimistic cases. As in the previous case, we can see that the neutrino halo of the Milky Way extends up to $r \simeq 1\,\text{Mpc}$.

Our results can be compared with those presented in Ref. [217] for the same neutrino mass. Since we are considering a different value for the DM halo mass, a direct comparison with their figure 5 is not possible, but our profiles are in good agreement with their results in figure 1. The same can be said about figure 8 of Ref. [227]: there is a qualitative agreement, but the different DM halo masses prevent a direct comparison.

Concerning the direct detection of relic neutrinos in a PTOLEMY-like experiment, table 6.3 shows that for a neutrino mass of order 150 meV, gravitational clustering in the Milky Way halo may enhance the expected event rates by a factor 1.7 to 2.5 depending on the DM profile. Under the most optimistic as-

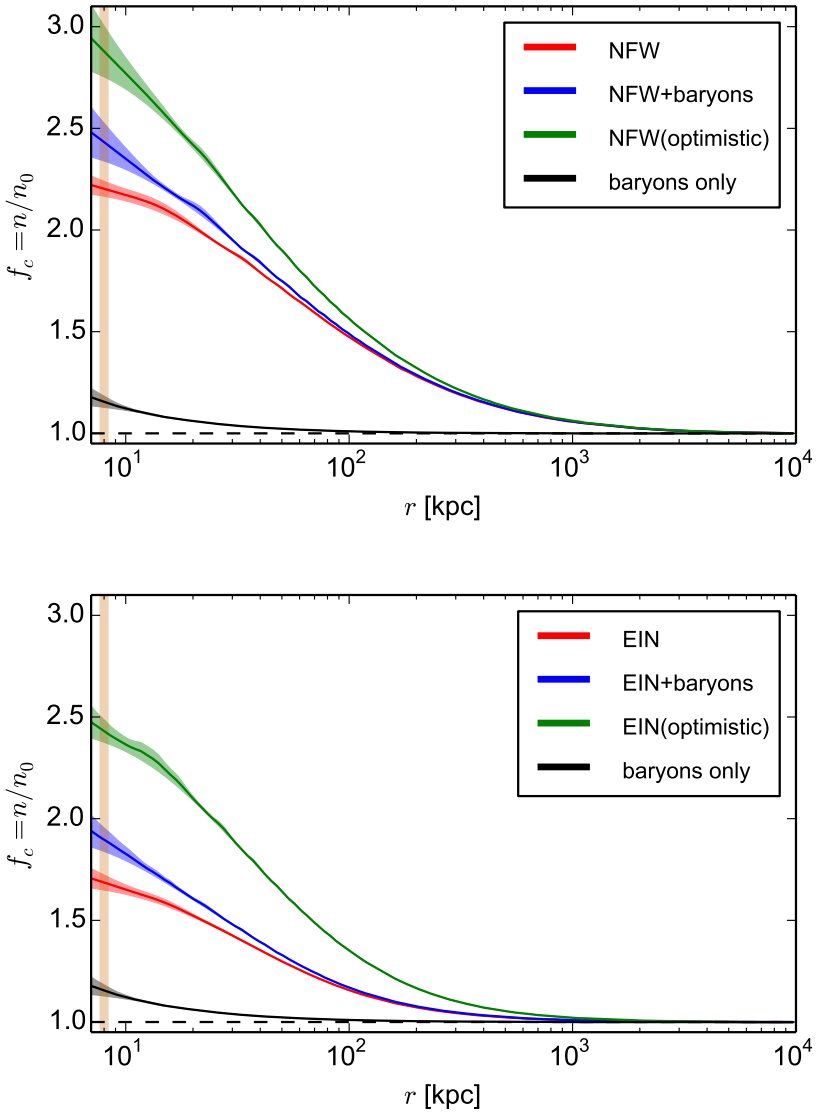

Figure 6.4: Same results as figure 6.3, but for a neutrino mass $m_\nu = 150\,\mathrm{meV}$.

sumptions and for Majorana neutrinos, one may expect more than 20 events per year.

matter halo	overdensity f_c $f_1 \simeq f_2 \simeq f_3$	$\Gamma^{D}_{C\nu B}$ (yr^{-1})	$\Gamma^{M}_{C\nu B}$ (yr^{-1})
any	no clustering	4.06	8.12
NFW (+baryons)	2.18 (2.44)	8.8 (9.9)	17.7 (19.8)
NFW optimistic	2.88	11.7	23.4
Ein. (+baryons)	1.68 (1.87)	6.8 (7.6)	13.6 (15.1)
Ein. optimistic	2.43	9.9	19.7

Table 6.3: Clustering factors and expected event rates in a PTOLEMY-like experiment for different assumptions on the matter profile, when neutrinos are approximately degenerate in mass and $m_\nu \simeq 150\,\text{meV}$.

6.3.3 Beyond active neutrinos: light sterile neutrinos

The masses of the active neutrinos can not be very large and therefore they are bound to travel through our galaxy almost unclustered. Instead, a different scenario opens up for a sterile neutrino with a mass $m_{\nu_s} \sim \mathcal{O}(1\,\text{eV})$, that could explain the short-baseline neutrino oscillation anomalies (see section 1.5).

In the framework of the so-called 3+1 active-sterile mixing scheme, the fourth mass eigenstate is heavier than the standard three ones, with a squared-mass difference

$$\Delta m^2_{\text{SBL}} = \Delta m^2_{41} \simeq \Delta m^2_{42} \simeq \Delta m^2_{43} \simeq 1\,\text{eV}^2 \gg |\Delta m^2_{31}| \gg \Delta m^2_{21}. \tag{6.23}$$

The 3×3 mixing matrix is extended to a 4×4 mixing matrix U.[4] Its elements in the fourth column quantify the mixing of the fourth mass eigenstate, ν_4, with the active neutrino flavours. Experimental data impose that they must be small, $|U_{\alpha 4}|^2 \ll 1$, where $\alpha = \{e, \mu, \tau\}$. Therefore the standard three neutrino mixing is not affected by the existence of the new mass eigenstate.

In such a scheme, the new neutrino oscillates with the active flavours in the early Universe and a population of ν_4 may be created, depending on the values of the new mixing parameters. We consider the usual parameterisation of the energy density of radiation in the early Universe in terms of the effective number of neutrinos N_{eff} (Eq. (2.59)). As we discuss in chapter 3, the effective number of neutrinos in presence of only active neutrinos is $N^{\text{active}}_{\text{eff}} = 3.045$ [116]. The

[4] We use the same name for the 3×3 and the 4×4 mixing matrix, since U refers to the 4×4 only in this section and there is no confusion.

additional contribution given by the sterile neutrino can be written as

$$\Delta N_{\rm eff} = \left[\frac{1}{\pi^2}\int {\rm d}p\, p^3 f_{\rm s}(p)\right] / \left[\frac{7}{8}\frac{\pi^2}{15}T_\nu^4\right] = N_{\rm eff} - 3.045, \tag{6.24}$$

where here $N_{\rm eff}$ is the true value of this parameter and $f_{\rm s}(p)$ is the energy distribution function of the sterile neutrino in terms of its momentum p.

The parameter $\Delta N_{\rm eff}$ is crucial to know how efficiently the fourth neutrino was created in the early Universe and, as a consequence, how much it contributes to the CνB. Its value depends on $f_{\rm s}(p)$, which in turn is fixed by the production mechanism of the sterile neutrinos. The simplest possibility is that the ν_4's were generated by active-sterile oscillations in the early Universe [144, 236–240] with the same temperature (and momentum distribution) of active neutrinos. In this case, considering the current best-fit results on active-sterile neutrino oscillation parameters, we would have $\Delta N_{\rm eff} = 1$, that is disfavoured with respect to the most recent CMB determinations [83]. Instead, if the production of sterile neutrinos occurs through non-thermal mechanisms, the fourth neutrino momentum distribution maintains approximately the same shape of the active neutrino ones [241–243] and can be written as a Fermi-Dirac spectrum times a constant scaling factor, that is $\Delta N_{\rm eff}$. Hence, in the following we will assume [241]

$$f_{\rm s}(p) = \frac{\Delta N_{\rm eff}}{1 + \exp(p/T_\nu)} \tag{6.25}$$

as an input for the calculation of the local overdensity of the fourth neutrino. As the mean neutrino number density today is defined by Eq. (2.22), for the fourth neutrino we have $\bar{n}_4 = n_0\,\Delta N_{\rm eff}$ (where $n_0 \approx 56\,{\rm cm}^{-3}$). This number needs to be multiplied by the clustering factor $f_{\rm c}(m_4)$, which is independent of $\Delta N_{\rm eff}$, in order to obtain the local number density of ν_4, $n_4 = n_0\, f_{\rm c}(m_4)\,\Delta N_{\rm eff}$, relevant for C$\nu$B detection.

In order to compute the expected number of events in PTOLEMY from the additional neutrino state, we must include the relevant element of the fourth column of the mixing matrix, $|U_{e4}|^2$. This parameter and the short-baseline squared-mass difference $\Delta m^2_{\rm SBL}$ are the only quantities needed to estimate the event rate in PTOLEMY. Both values should be obtained from a global fit of all neutrino oscillation data. A recent global fit that considers the anomalous SBL experiments reports the best fit values $\Delta m^2_{\rm SBL} = 1.7\,{\rm eV}^2$ and $|U_{e4}|^2 = 0.020$ [244] for the parameters we are interested in.

matter halo	overdensity f_4	$\Delta N_{\rm eff}$	$\Gamma^{\rm D}_{\rm C\nu B}$ (yr^{-1})	$\Gamma^{\rm M}_{\rm C\nu B}$ (yr^{-1})
NFW (+baryons)	159.9 (187.3)	0.2	2.6 (3.0)	5.2 (6.1)
		1.0	13.0 (15.2)	26.0 (30.4)
NFW optimistic	208.6	0.2	3.4	6.8
		1.0	16.9	33.9
Ein. (+baryons)	105.1 (139.5)	0.2	1.7 (2.3)	3.4 (4.5)
		1.0	8.5 (11.3)	17.1 (22.7)
Ein. optimistic	203.5	0.2	3.3	6.6
		1.0	16.5	33.0

Table 6.4: Clustering factors and expected event rates in a PTOLEMY-like experiment for different assumptions on the matter profile, for a sterile neutrino corresponding to different values of $\Delta N_{\rm eff}$. We consider a mass $m_4 = 1.3\,\text{eV}$ and a mixing matrix element $|U_{e4}|^2 = 0.02$ [244].

In the following we will assume that $m_4 \gg m_{1,2,3}$, so that we can approximate $m_4 \simeq \sqrt{\Delta m^2_{\rm SBL}} \simeq 1.3\,\text{eV}$. This is the value for which we calculate the clustering of sterile neutrinos in the local neighbourhood using N-one-body simulations. The overdensity profiles for a neutrino with mass $m_4 \simeq 1.3\,\text{eV}$ are shown in figure 6.5. As expected, the overdensity is much higher than in the previous cases because such neutrinos have a larger mass and smaller kinetic energies and they are more easily trapped by the galactic gravitational potential.

The total event rate for a Majorana (Dirac) fourth neutrino is given by [211]

$$\Gamma_4^{\rm M(D)} \simeq \Delta N_{\rm eff}\, |U_{e4}|^2\, f_{\rm c}(m_4)\, \Gamma^{\rm M(D)}_{\rm C\nu B}, \tag{6.26}$$

from which we obtain values that vary between 3.4 and 33.9 (1.7 and 16.9), depending on the assumptions on the matter profile of our galaxy and on the thermalisation of the fourth neutrino in the early Universe. We list in table 6.4 the expected event rates for two different values of $\Delta N_{\rm eff}$. In the first one we consider $\Delta N_{\rm eff} = 1$, corresponding to a fully thermalised sterile neutrino (disfavoured by present cosmological constraints [83]), and we also use a conservative $\Delta N_{\rm eff} = 0.2$, that is basically compatible with the 1σ cosmological limits regardless of the assumed dataset.

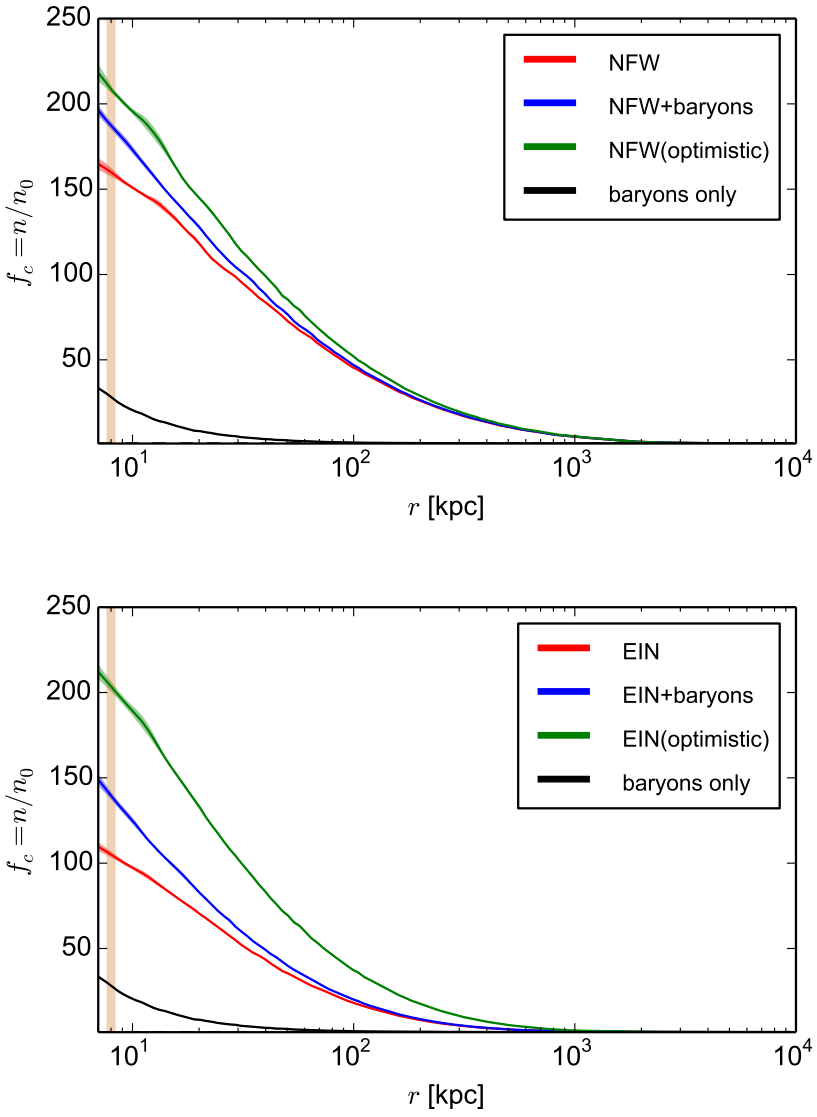

Figure 6.5: Same results as figures 6.3 and 6.4, but for a sterile neutrino with mass $m_4 = 1.3\,\mathrm{eV}$ and contribution to the radiation energy density $\Delta N_{\mathrm{eff}} = 1$.

6.4 Chapter remarks

In this chapter we have studied the gravitational clustering of massive neutrinos at galactic and subgalactic scales. In particular, we focused on the matter distribution in the Milky Way, that we parameterised with different profiles for the DM and the baryons. Using a method based on N-one-body simulations [217], we have computed the enhancement of the number density of relic neutrinos as a function of the distance from the galactic centre for different values of the neutrino masses. For a 150 meV mass, a value within the potential reach of PTOLEMY and not completely ruled out by present cosmological analyses including Planck data, we find that the local density of cosmological neutrinos can be as large as two or three times its average value, depending on the galactic matter profile. This result is in reasonable agreement with previous analyses [217, 227]. We have also considered, for the first time, smaller neutrino masses. A nearly minimal value for the heaviest neutrino is 60 meV, for which we find that the local population of relic neutrinos is also enhanced, but only up to 10% to 20% with respect to its average number density.

These very small enhancement factors can be compared with the significant overdensities that could be reached if neutrino masses were larger than 1 eV, a case that is not possible for standard, active neutrinos. As a non-standard example, we have shown the case of a fourth massive state, mostly sterile, finding that the gravitational clustering would lead to enhancement factors of order 140 to 210 for a 1.3 eV neutrino mass.

Finally, the main uncertainties in the calculation of our results on massive neutrino clustering in the Milky Way are related to the parameterisation of the galactic matter distribution, both for baryons and DM. We found that the differences obtained when modifying the matter content are much larger than the numerical uncertainties in the N-one-body calculations.

Chapter 7

Neutrino propagation in the dark matter halo

In this chapter we present the work published in [11], where we study how a possible neutrino-DM interaction affects the pattern of neutrino oscillations, with special attention to the unique imprints of a resonant MSW effect. Flavour oscillations in the energy range from a few hundreds of keV to the TeV scale are well known experimentally, including the presence of ordinary matter effects. However, at ultra-high energies (above TeV) they are barely constrained. Thanks to the ability of very-large volume neutrino telescopes to detect particles of such energies, this unexplored region has recently become available and in the near future we will have enough data to test flavour oscillations at a wider energy range.

Furthermore, as discussed in chapter 1, matter effects are more important at larger energies, since flavour oscillations become more sensitive to coherent forward scattering. Here we study the hypothetical scenario of a non-universal neutrino-DM interaction, faint enough to be accessible through its effect on neutrino oscillations only at extreme energies.

Similar hypotheses have been discussed in previous works. Some of them, however, consider neutrinos as the main component of the galactic DM [245, 246] or focus on the effect due to the interaction on the CνB [247]. The analysis in Ref. [248] follows a closer approach, although it does only account for an homogeneous DM distribution. In this work we show that the effect of the DM profile may be very important, specially for neutrinos generated near the galactic centre. This occurs because DM density variations can lead to a resonant behaviour in neutrino oscillations. Furthermore, this hypothesis may imply new conse-

quences in future high-energy neutrino observations. In particular, and given the anisotropic character of the phenomenon due to the non-central position of the Solar System inside the Milky Way, the presence of galactic DM may predict different neutrino flavour compositions for KM3NeT and IceCube, sensitive to complementary regions of the sky.

The origin of very-high-energy neutrinos is not completely understood. However, there are some estimates suggesting that, for energies larger than 60 TeV, 40% of the total neutrino flux has a galactic origin while the rest is extragalactic [56]. Even though galactic neutrinos are less abundant at these energies, the present study is focused in such component to analyse the effect of the DM halo of the Milky Way on the neutrino propagation.

7.1 Chosen dark matter distribution

For the scope of this work, we describe the DM distribution in the Milky Way using two extreme choices: the isothermal profile presented in Eq. (2.62) with $r_s = 5\,\mathrm{kpc}$ and an NFW profile (Eq. (2.63)) with $r_s = 20\,\mathrm{kpc}$, where the main difference between both distributions is the presence of a cusp at $r = 0$ in the NFW profile. In addition, we consider that the Solar System is located at $r_\oplus = 8.5\,\mathrm{kpc}$ from the galactic centre and the local DM energy density is $\rho_\oplus = 0.4\,\mathrm{GeV/cm^3}$, as indicated by several studies [114, 221, 249, 250].

The masses of most of the proposed DM candidates can range from eV to TeV. For the sake of simplicity, along this work we assume a generic value for the mass of the DM particle as well as a generic coupling to neutrinos. In the discussion of our results in the next sections we consider three different benchmark cases with particular values for these parameters.

7.2 Neutrino oscillations in dark matter

In order for neutrino oscillations to be modified by the presence of DM, a non-universal interaction is needed. Since the nature of DM is still unknown, we can assume such a general case.

Similarly to what happens when neutrinos travel across a medium like the Earth or the Sun, their interaction with the DM introduces a new term in the total hamiltonian describing the evolution of neutrinos in the medium (see Eq. (1.29)), where in this occasion V is the DM-induced effective potential matrix, expressed in the flavour basis. For the neutrino oscillation parameters we use the best-fit

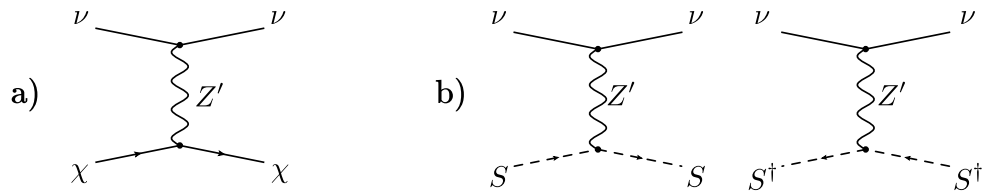

Figure 7.1: Examples of processes leading to the parameterisation in Eq. (7.1). Diagram a) corresponds to the case of asymmetric DM while diagrams in b) represent the case of scalar DM.

values in Ref. [125], with the exception of the phase related to CP violation, which we set to zero.

The effective potential describing the interaction between neutrinos and DM in the flavour basis can be parametrised as

$$\mathsf{V}_{\alpha\beta} = \lambda_{\alpha\beta}\, G_{\rm F}\, N_\chi, \tag{7.1}$$

where $\lambda_{\alpha\beta}$ is a hermitian matrix encoding the effective couplings between neutrinos and DM, and N_χ is the DM number density, which is related to its energy density by

$$N_\chi = \frac{\rho_{\rm DM}}{m_{\rm DM}}. \tag{7.2}$$

The parameterisation used in Eq. (7.1) is well motivated in scenarios with fermion asymmetric DM, where no anti-DM is present in the Universe, as well as in the case of scalar or vector DM candidates. Possible realisations are presented in Fig. 7.1. In the simplest scenario, we require a mediator particle that connects the DM and neutrino sectors without mixing them. This is shown in diagram a) for a fermion asymmetric DM.

Since neutrino oscillations are blind to global phases, we can reduce the number of free parameters in the effective potential by subtracting a term proportional to the identity matrix $\mathbb{I}$. In our case we subtract $\mathsf{V}_{\tau\tau}\,\mathbb{I}$. We also consider only real entries in the λ matrix. Then, the effective potential is reduced to

$$V = \mathsf{V} - \mathsf{V}_{\tau\tau}\mathbb{I} = G_{\rm F} N_\chi \begin{pmatrix} \lambda_{11} & \lambda_{12} & \lambda_{13} \\ \lambda_{12} & \lambda_{22} & \lambda_{23} \\ \lambda_{13} & \lambda_{23} & 0 \end{pmatrix}, \tag{7.3}$$

with five free parameters describing the effective interactions between DM and neutrinos. Let us remark that a relative sign may appear in V modelling the

effect for neutrinos and antineutrinos, although this sign would depend on the nature of the DM candidate. In our study, we consider all possible signs in the entries of the potential to cover the DM effect including both species without distinction.

In the case of a constant effective potential and starting with an initial flavour content $f^0 = \left(f_e^0, f_\mu^0, f_\tau^0\right)$, the final averaged flavour state is given by

$$f_\beta = \sum_{\alpha=e,\mu,\tau} \left(\sum_{i=1}^{3} |U_{\beta i} U_{\alpha i}^*|^2 \, f_\alpha^0 \right), \tag{7.4}$$

which is valid for distances much larger than the characteristic oscillation wavelength.

In a more realistic scenario, the effective potential depends on the neutrino position. In our case, the spatial dependence arises from the DM distribution. The solution to the flavour evolution equation requires the diagonalisation of the hamiltonian in matter at every instant, depending on the value of N_χ at the neutrino position. We describe that position in terms of the line of sight distance l, with respect to the Solar System, and the angle ϕ with respect to the galactic centre. The galactocentric radius r is then simply described by

$$r^2 = r_\oplus^2 + l^2 - 2\, l\, r_\oplus \cos\phi. \tag{7.5}$$

In this scheme, the evolution of the flavour states is given by

$$f_\beta(l_{n+1}, \phi) = \sum_{\alpha=e,\mu,\tau} \left(\sum_{i=1}^{3} |U_{\beta i}(l_n, \phi) U_{\alpha i}^*(l_n, \phi)|^2 \, f_\alpha(l_n, \phi) \right), \tag{7.6}$$

where the initial state corresponds to $f_\alpha(l_0, \phi) = f_\alpha^0$, with l_0 being the distance to the source; $U(l_n, \phi)$ is the matrix that diagonalises the hamiltonian evaluated at the neutrino position (l_n, ϕ), and $f_\beta(l = 0, \phi) = f_\beta^\oplus$ is the final state at Earth. The distances involved in these scenarios are of the order of 1 kpc, while the largest oscillation wavelength is much smaller for neutrino energies from TeV to PeV. Therefore, we can safely describe the neutrino flavour evolution by an averaged oscillation.

On the other hand, if neutrino propagation is adiabatic, the numerical integration of the evolution described above can be further simplified. In that case, the neutrino flavour evolution would only depend on the initial and final DM densities. As we show in Fig. 7.2, for the DM densities that we analyse the adiabaticity condition is satisfied in the neutrino propagation, so we can safely

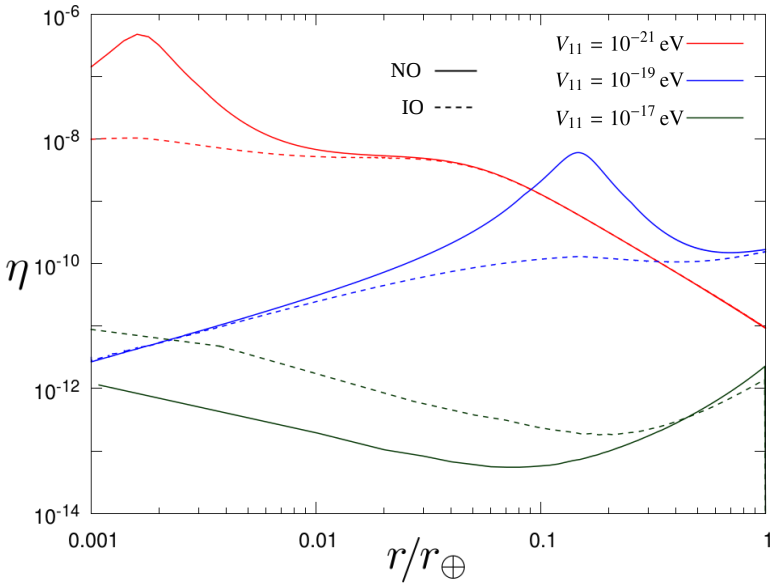

Figure 7.2: Adiabaticity parameter η for a 1 PeV neutrino crossing the galactic centre as a function of the radial distance, r, given in units of the distance to the Earth, $r_\oplus$. An NFW DM profile is assumed. The variation of η is shown for three different effective potentials at Earth, $V_{11}^\oplus$, assuming normal (solid line) and inverted (dashed line) neutrino mass orderings.

calculate the final flavour composition under this assumption. In the figure we depict the adiabaticity parameter (Eq. (1.45) for three neutrinos) for a 1 PeV neutrino crossing the galactic centre for three DM-neutrino interaction potentials and an NFW profile. The case with $V_{11}^\oplus = 10^{-17}$ eV corresponds to an effective potential that saturates neutrino oscillations. Therefore, the value of η is very small along the neutrino path. The other values of the potential shown in the figure, $V_{11}^\oplus = 10^{-19}$ eV and $V_{11}^\oplus = 10^{-21}$ eV, do not saturate oscillations at Earth but they do it instead at the very centre of the galaxy, due to the larger DM density. This explains the peaks in η followed by a decrease in the function when r approximates to zero. The peaks correspond to regions with maximum change in the potential previous to reach the saturation values, i.e. the regions where the effective oscillation parameters are more sensitive to variations in the DM potential.

In what follows, we consider two different approaches to evaluate the effect of neutrino interactions with dark matter: as a first approximation, we assume a homogeneous DM distribution; next, we proceed including the more realistic case of a varying DM density assuming either an NFW or an isothermal profile.

7.2.1 Case I: homogeneous DM halo

Here we search for values of the effective potential V leading to measurable effects on the neutrino oscillation pattern. As a first approximation to the problem, we focus on the effects of a homogeneous DM halo. This is equivalent to use a constant value of the effective potential and therefore the final flavour state is obtained from Eq. (7.4). The deviations between the DM-modified final state $f_\beta^{\rm DM}$ and the expected final state when neutrinos propagate in vacuum $f_\beta^{\rm vac}$ are described by

$$R_\beta(V,E) = \frac{f_\beta^{\rm DM} - f_\beta^{\rm vac}}{f_\beta^{\rm vac}}, \tag{7.7}$$

where the effective potential V is given in Eq. (7.3), E is the neutrino energy and $\beta = (e,\mu,\tau)$ is the neutrino flavour.

We calculate the deviations in the neutrino flavour content for different configurations of the effective potential (i.e. varying different entries of the potential V_{ij}) and we find that their effect qualitatively shows similar results. Therefore, for simplicity we show only the results of varying the entries V_{11} and V_{22}. We particularly look for regions where V_{ij} gives rise to strong modifications in the behaviour of the neutrino oscillations, with abrupt changes in the sign of $\partial R/\partial V_{ij}$, since these regions are a clear hint for a resonant behaviour. The transition can be observed in Fig. 7.3, where the sudden changes in colour are related to the presence of a resonance.

Due to the nature of neutrino oscillations in a medium, an increase in E_ν is equivalent to an increase in V_{ij}. Comparing the three panels in Fig. 7.3 we observe a linear change in the size of the regions due to the linear dependence on E_ν. In particular, the resonant behaviour of R_e around $V_{11} = 10^{-10}\,\text{eV}$ for $E = 1\,\text{MeV}$ is shifted to $V_{11} = 10^{-19}\,\text{eV}$ for $E = 1\,\text{PeV}$. This resonant pattern and its shift in energies also manifest in R_μ and R_τ. In consequence, the DM-neutrino interaction could explain a non-standard flavour composition in the high-energy neutrino flux observed at Earth without compromising lower energy observations. Additionally, we observe in the figure that the ratio R_β in Eq. (7.7) reaches a saturation value when E_ν grows and V_{ij} is fixed.

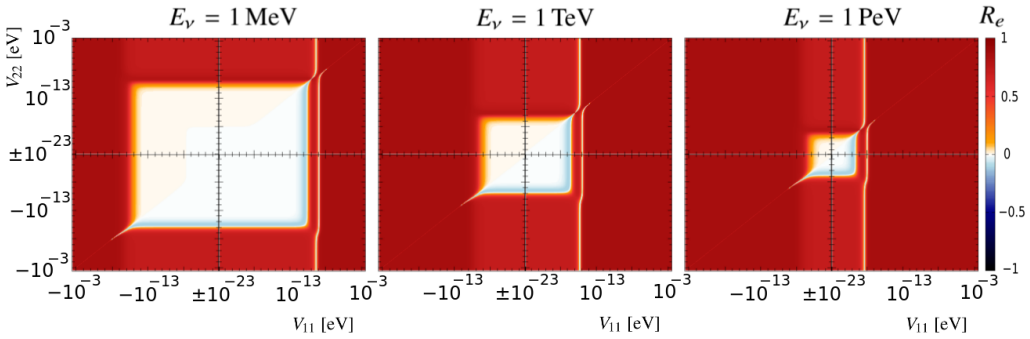

Figure 7.3: Map for the variable R_e in the plane (V_{11}, V_{22}) starting with a flavour content (1:0:0) for $E_\nu = 1\,\text{MeV}$ (left panel), $E_\nu = 1\,\text{TeV}$ (middle panel) and $E_\nu = 1\,\text{PeV}$ (right panel).

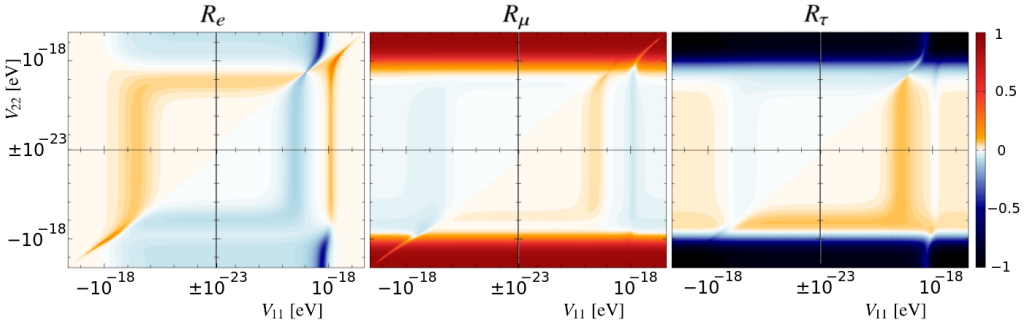

Figure 7.4: R_β (β = e, μ, τ) maps in the plane (V_{11}, V_{22}) for $E_\nu = 1\,\text{PeV}$ and an initial flavour content of (1:2:0).

We also study the case of an astrophysical source of neutrinos with initial flavour content equal to (1:2:0). In Fig. 7.4 we present the $R_{e,\mu,\tau}$ maps in the plane (V_{11}, V_{22}) for $E_\nu = 1\,\text{PeV}$. We have explored the effective potential V_{ii} in the range from 10^{-23} to $10^{-16}\,\text{eV}$. In our scan, the lower limit of V_{ii} does not produce appreciable deviations from the vacuum solution (i.e. $R_\beta \simeq 0$), while the upper limit saturates the flavour oscillations beyond the resonance and then R_β does not change for larger values of V_{ii}.

At this level, we can compare the patterns shown in the three panels of Fig. 7.4. To understand the difference we need to consider the definition of R_β in Eq. (7.7). The averaged oscillations in vacuum for an initial flavour content of

(1:2:0) lead to a final flavour composition

$$f^{\rm vac} = (0.331 : 0.347 : 0.322). \tag{7.8}$$

However, in the region where both $|V_{11}|$ and $|V_{22}|$ are larger than $10^{-18}\,$eV, the initial flavour content remains unchanged. This is because the effective potential dominates the neutrino hamiltonian and then flavour oscillations are suppressed. Therefore, in this case, for an initial flavour composition of (1:2:0) we keep the same composition at Earth,

$$f^{\rm DM} = (0.333 : 0.667 : 0), \tag{7.9}$$

which is equivalent to

$$(R_e : R_\mu : R_\tau) \approx (6 \times 10^{-3} : 0.92 : -1). \tag{7.10}$$

This explains the values of the deviations R_β at the corners.

In the region of Fig. 7.4 where $|V_{11}| \geq 10^{-18}\,$eV and $|V_{22}| \leq 10^{-18}\,$eV, only electron neutrino oscillations are suppressed, leaving $f_e^{\rm DM} \simeq f_e^0$ (i.e. $R_e \simeq 0$). However, oscillations for muon and tau neutrinos are still active. Since the atmospheric mixing angle θ_{23} in vacuum is almost maximal, the initial content of muon neutrinos, $f_\mu^0 = 0.667$, is equally distributed between muon and tau neutrinos. This leads to $f^{\rm DM} \approx (0.33 : 0.33 : 0.33)$, what explains the slightly negative value of R_μ and the slightly positive one of R_τ and R_e obtained after the comparison with the vacuum expectations in Eq. (7.8).

The final saturation region, where V_{11} is small and V_{22} is large, prevents the oscillation of muon neutrinos. The vacuum oscillations between electron and tau neutrinos are mainly controlled by the reactor mixing angle $\theta_{13} \approx 9^\circ$. This implies that just a small part of the initial electron neutrino content, $f_e^0 = 0.333$, is transferred to tau neutrinos. Consequently R_e remains small, but negative, while R_τ has a negative value close to -1.

A more general analysis, where all the entries of the effective potential V_{ij} are free to vary, is summarised in Fig. 7.5. The regions in colour cover all the possible flavour neutrino compositions at Earth predicted in the presence of DM. In the same figure, the black points indicate the predictions assuming neutrino oscillations in vacuum. We present our results for four different initial states: (1:0:0), (0:1:0), (1:2:0) and (0:0:1). The first three cases are motivated by astrophysical processes such as neutron decay, damped muon source and pion decay, respectively. The last case, (0:0:1), is shown for comparison. A compendium

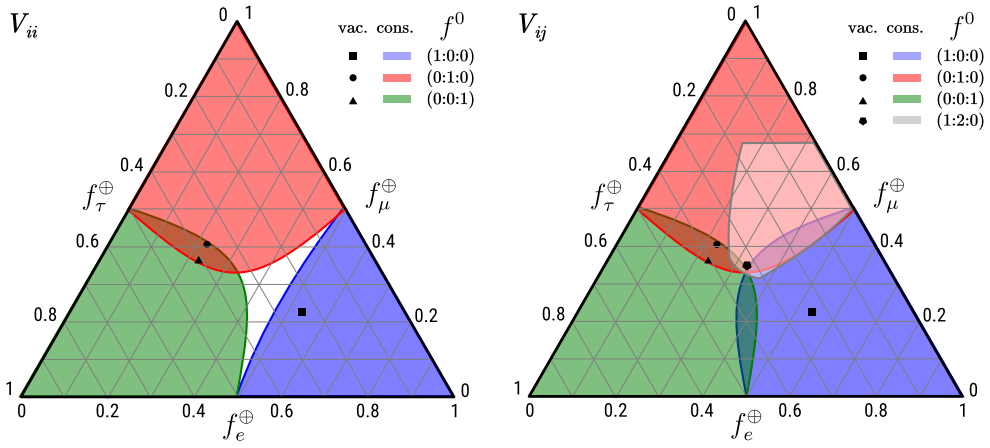

Figure 7.5: Flavour triangle for $E_\nu = 1\,\text{PeV}$ for the initial neutrino compositions (1:0:0), (0:1:0), (0:0:1) and (1:2:0). Colour regions include the possible flavour neutrino compositions at Earth predicted in the presence of DM, whereas the points correspond to the expected flavour composition in vacuum. Left panel results from the scan using only pure initial neutrino states and diagonal terms in the potential while the right panel has been obtained scanning over all entries, including the non-diagonal ones.

of possible astrophysical neutrino sources is described in Ref. [251]. In the left panel, we only vary the diagonal terms of the effective potential keeping the non-diagonal equal to zero, while in the right panel all terms are allowed to vary, showing the maximum deviation area. In both cases, $|V_{ij}|$ take values in the range $(10^{-23}, 10^{-13})$ eV. From the figure we see that there is no difference between the shape of the regions obtained for (0:1:0) and (0:0:1) in the two panels. On the contrary, for the initial flavour content (1:0:0) the diagonal-only scan does not cover all the region obtained in the right panel. Our results agree with the analysis presented in Ref. [252], which considers other possible new physics scenarios.

7.2.2 Case II: DM halo profile

In this section we consider non-homogeneous profiles for the galactic DM density distribution. This implies a spacial dependence in the effective matter potential along the neutrino path that may produce similar effects to the ones explaining the solar neutrino problem. In section 7.2.1, we estimated the values of

Benchmark	Case A	Case B	Case C
$V_{11}^{\oplus}$ $[10^{-21}\,\mathrm{eV}]$	4	20	40

Table 7.1: Benchmark cases A, B and C, defined by the effective potential value at Earth.

V_{ij} for which the neutrino flavour composition at Earth is different from the case of oscillations in vacuum. Here we combine that information with the spatial distribution of DM in the Milky Way assuming homogeneously produced neutrinos up to $r_{\max} = 20\,\mathrm{kpc}$ on the galactic plane. We consider three benchmark cases: A, B and C (see Table 7.1 for details). The values of each benchmark are chosen to give a very small value of R_β in the homogeneous DM case. However, thanks to the DM distribution profile, the effective potential for neutrinos is larger in regions closer to the galactic centre compared to the outskirts of the galaxy. In Fig. 7.6 we show how the effective potential changes with the DM distribution. We consider the isothermal and NFW profiles described in section 7.1 to analyse the impact of the DM distribution on neutrino oscillations.

In Fig. 7.7 we show the colour map of the deviation parameter R_β for an initial state (1:0:0) in terms of the neutrino production point in the galactic plane for the NFW profile. We consider neutrinos with energies of 1 PeV and the benchmark cases in Table 7.1. For simplicity, only $V_{11}^{\oplus}$ has been chosen different from zero. Each column of plots, from left to right, represents R_e, R_μ and R_τ, respectively, while each row corresponds to a different benchmark point. We observe that the impact of the spatial dependence is very important and the effect is different for each R_β. The use of different benchmarks has also an impact on the R_β maps. As expected, one can notice that the benchmark C presents the largest deviations over every R_β when it is compared with the cases A and B.

In Fig. 7.8 we present the R_β map using the benchmark C and the isothermal profile. The direct comparison of Figs. 7.7 and 7.8 shows that the flavour conversion is enhanced towards the galactic centre. One can notice that, thanks to the inner cusp, the NFW profile is rather different from the isothermal one only in the $\sim 1\,\mathrm{kpc}$ inner region. This promising feature might indicate that a DM–MSW effect can reveal relevant information about the centre of the galaxy.

We show in Fig. 7.9 the predicted flavour compositions at Earth for neutrinos produced with distributions (1:2:0) and (1:0:0). As initial neutrino positions we have considered all points inside a 20 kpc radius from the galactic centre. In the left panel, we compare the overall region for a constant potential (reddish area) with the region resulting from the NFW profile (blueish region). Also, we include

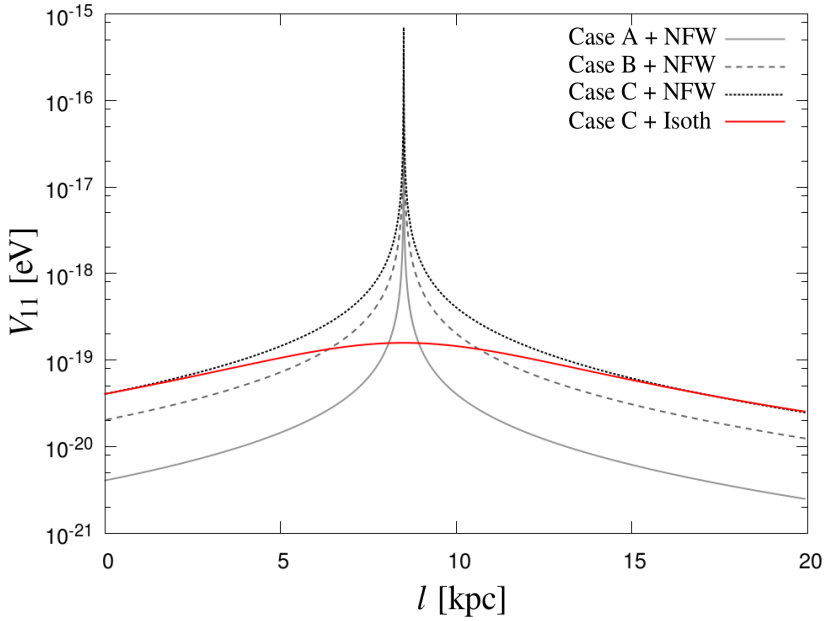

Figure 7.6: Effective potential V_{11} as a function of the distance from the Earth, l, for a path crossing the galactic centre. Different curves correspond to the benchmark cases A, B and C in Tab. 7.1 for an NFW DM profile. The benchmark case C with an isothermal profile is also shown.

the uncertainty bands as well as the best fit point obtained from the IceCube results on neutrino flavour composition [253]. The values of all entries of the potential $|V_{ij}^{\oplus}|$ have been chosen to vary in the range from 10^{-24} eV to 10^{-16} eV. The main difference between the blueish and reddish areas arises because the DM distributions are different near the galactic centre and in the outskirts of the galaxy. The strongest impact of the DM interaction on neutrino oscillations on these production zones broadens the blueish area beyond the expected region for a constant potential.

The right panel of Fig. 7.9 shows the possible flavour compositions produced from an initial flavour (1:0:0) and an NFW DM profile, where each coloured area arises as the result of a scan with a maximum value of $|V_{ij}^{\oplus}|$. We observe that values of $V_{ij}^{\oplus}$ as large as 10^{-17} eV can almost cover the full flavour triangle. However, as soon as the maximum value of $V_{ij}^{\oplus}$ is reduced, the obtained areas tend to converge to the vacuum solution, as expected. We observe that, for the same

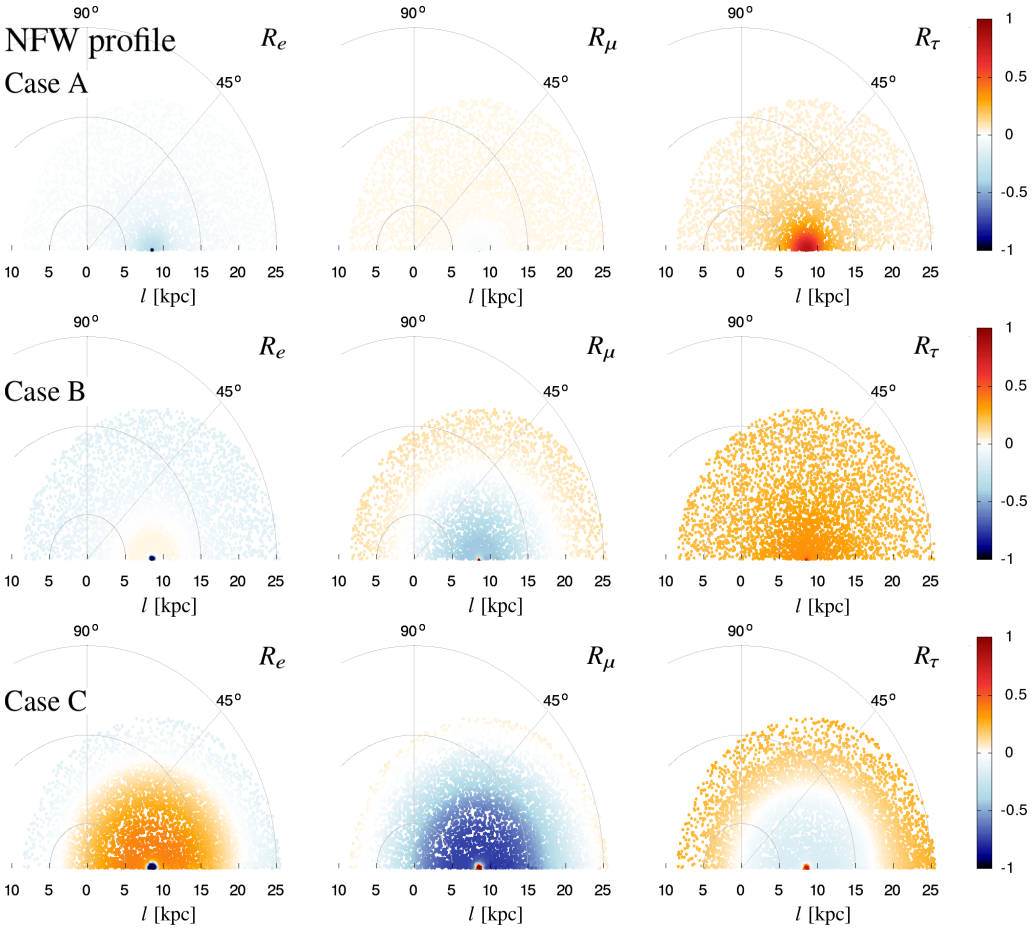

Figure 7.7: R_β maps for different neutrino production positions. $l = 0$ corresponds to the Earth's position. In all plots, the initial flavour state is (1:0:0), $E_\nu = 1\,\mathrm{PeV}$ and an NFW profile is assumed. Columns from left to right correspond to R_e, R_μ and R_τ respectively, and rows from top to bottom are benchmark cases A, B and C.

range of $V_{ij}^{\oplus}$, the area produced by a homogeneous dark matter profile (Fig. 7.5) is more restricted than the one obtained from an NFW profile.

As a final comment, we notice that the change in the effective potential felt by neutrinos depends on their arrival direction. For example, neutrinos coming from regions near the centre of the galaxy would feel larger modifications in their effective potential. This indicates that the flavour composition of ultra-

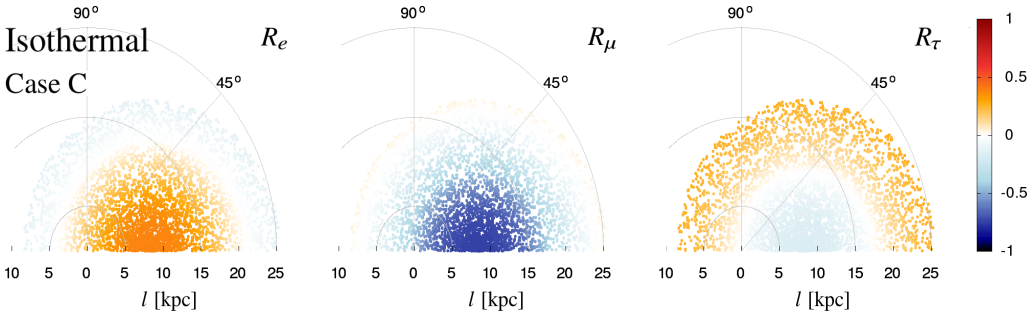

Figure 7.8: R_β maps for different neutrino production positions. Same initial state as in Fig. 7.7 for an isothermal DM profile. Panels from left to right correspond to R_e, R_μ, R_τ respectively and all plots are for the benchmark case C.

high-energy neutrinos might depend on the arrival angle, something that can be tested in the future with new neutrino telescopes.

7.3 Discussion

In the previous sections we have analysed the effect of DM on neutrino oscillations using an effective potential parameterised as in Eq. (7.3). In a more generic framework, considering new physics beyond the SM, the interaction between both particles can also be expressed as

$$V_{ij} = \lambda'_{ij}\, G'_{\rm F}\, \frac{\rho_{\rm DM}}{m_{\rm DM}}. \tag{7.11}$$

This equation allows us to reinterpret the effective potential in terms of a new interaction strength $G'_{\rm F}$ as well as on the DM mass, $m_{\rm DM}$. We highlight that Eqs. (7.3) and (7.11) are parameterisations of the potential where the structure of the λ_{ij} and λ'_{ij} parameters depends on the specific choice of a particle physics model. For simplicity, in this discussion we assume that the interaction between neutrinos and DM particles happens via the interchange of a Z'-like boson. In this case, the *primed* Fermi constant is related to the standard $G_{\rm F}$ by

$$G'_{\rm F} = \frac{m_Z^2}{m_{Z'}^2}\, G_{\rm F}, \tag{7.12}$$

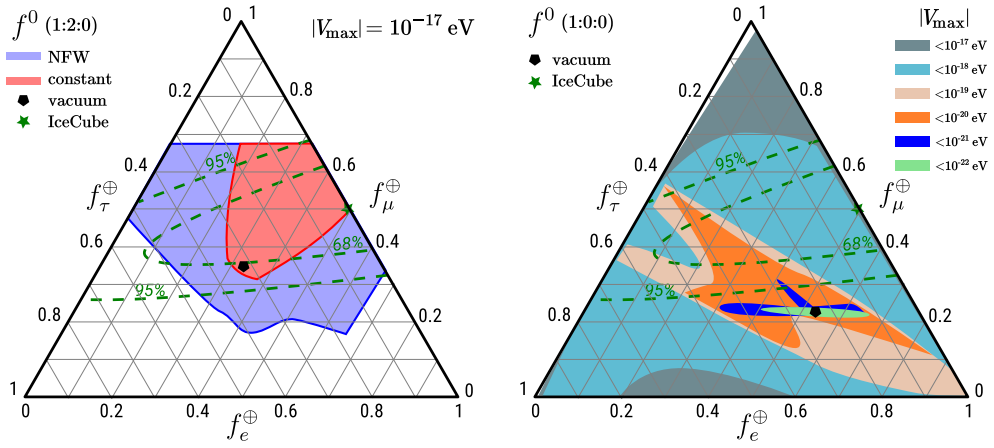

Figure 7.9: Flavour triangles for the initial states (1:2:0) (left) and (1:0:0) (right). The left panel shows the flavour area covered by a homogeneous DM profile (reddish area) and the one covered by the effect of an NFW profile (blueish area). The right panel shows the areas covered by imposing a maximum value for $\left|V_{ij}^\oplus\right|$ and an NFW profile. We observe that for smaller maximum values the area is closer to the solution in vacuum. The best-fit point and 68% and 95% CL allowed regions from IceCube data [253] are also shown for comparison.

with $m_Z \simeq 91\,\text{GeV}$. Here, the mass of the mediator and the interaction strength are tightly related. This scaling is valid only for the coherent scattering regime if there is no momentum transferred by the mediator, or if the mediator is so heavy that it can be integrated out.

It is important to mention that, besides the effect of forward coherent scattering encoded in the DM potential V, neutrinos might actually scatter on the DM halo. This could disrupt the effect of neutrino oscillations, modifying also their arrival directions and energy spectrum [254]. To this end, we have to ensure that the mean free path due to the neutrino-DM scattering cross section at Earth,

$$l_\nu = \left(\sigma_{\nu\chi}\frac{\rho_{\text{DM}}}{m_{\text{DM}}}\right)^{-1} = \left(\frac{\sigma_{\nu\chi}}{8.1\times10^{-22}\,\text{cm}^2}\right)^{-1}\left(\frac{m_{\text{DM}}}{1\,\text{GeV}}\right)\,\text{kpc}, \tag{7.13}$$

is large enough, allowing neutrinos to cross the galaxy and being affected only at the level of oscillations.

For the case of galactic neutrinos, we set l_ν at Earth to be 50 kpc, which corresponds to a cross section $\sigma_{\nu\chi} = 1.62\times10^{-23}\ (m_{\text{DM}}/\text{GeV})\ \text{cm}^2$. This value

guarantees that, apart from the effect of coherent forward scattering, neutrinos would rarely scatter along any trajectory, including the ones passing close to the galactic centre for an NFW profile. A complementary study for ultra-light DM, in the regime where neutrino-DM scattering cross section has a relevant role for the neutrino propagation is analysed in Ref. [255].

In a more extreme case, we also consider $\sigma_{\nu\chi} < 10^{-33}\ (m_{\rm DM}/{\rm GeV})\ {\rm cm}^2$, a bound that comes from the CMB analysis when DM-neutrino interactions are allowed [256]. This bound corresponds to $l_\nu > 10^6\,{\rm Gpc}$ at Earth.[1] However, let us remark that this bound applies for DM-neutrino cross sections at the MeV scale and therefore its value might be different for the neutrino energies considered in this work, depending on the particle physics model considered. In what follows, we use these two values of the neutrino mean free path as benchmarks to discuss the dependence of the effective potential on the remaining parameters: λ', $G'_{\rm F}$ and $m_{Z'}$. We also show the example of a particle physics scenario with unconstrained mean free path in order to better understand the role of the parameters.

In table 7.2, we present six different choices of the involved parameters that can reproduce three selected values of the effective potential at Earth. These values have been chosen in the range from $10^{-21}\,{\rm eV}$ to $10^{-17}\,{\rm eV}$, a representative range of the potential that might produce sizeable effects on the neutrino oscillation flavour content as it is shown in Fig. 7.9. In the table we have considered that the neutrino-DM cross section takes the form

$$\sigma \propto \lambda'^2 G'_{\rm F} \simeq 3.75 \times 10^{-29}\,\lambda'^2 \left(\frac{m_{Z'}}{1\,{\rm GeV}}\right)^{-2}\ {\rm cm}^2, \tag{7.14}$$

well motivated for the case $\sqrt{s} \gg m_{Z'}, m_{\rm DM}$. At this point, the functional relation between $V^\oplus$, l_ν and the rest of the parameters ($m_{\rm DM}$, λ' and $G'_{\rm F}$) allows us to describe the effect on neutrino oscillations by fixing only three of them.

The scenarios described in the table are the following:

- **Weak scale**. We assume for all cases that $G'_{\rm F} = G_{\rm F}$. If we further impose $\lambda' = 1$ (case **a**), the DM mass has to lie in the range from $10^{-12}\,{\rm eV}$ to $10^{-8}\,{\rm eV}$. This corresponds to an extremely light DM particle which is in the spirit of axion Bose-Einstein Condensates (BEC) [257], although the mass we obtain is (at best) two orders of magnitude smaller than the BEC case. One can find models with such extremely light candidates like in

[1] From this value it is obvious that, under such a small cross section, the problem is not that neutrinos might interact harder than through a coherent forward elastic scattering, but the loss of coherence itself. The message here is that galactic neutrinos would only suffer, at most, coherent forward elastic scattering.

scalar (wave) dark matter models [258]. As the result of the chosen λ' and $G'_{\rm F}$, the neutrino mean free path is in the sub-pc range. This small value of l_ν might imply that high energy neutrinos are screened due to their interaction with the DM halo [254]. If we now impose $l_\nu = 50\,\text{kpc}$ (case **b**), as discussed above, the values of λ' are reduced to the range between 10^{-7} and 10^{-11}, and the DM mass becomes even lighter, lying on the range from $10^{-15}\,\text{eV}$ to $10^{-23}\,\text{eV}$.

- **100 GeV DM**. Here we fix l_ν at Earth to the two values previously discussed. For $l_\nu = 50\,\text{kpc}$ (case **a**), we obtain the same values of λ' as before. In this case, $m_{Z'}$ takes sub-eV values, $10^{-2}\,\text{eV}$ to $10^{-6}\,\text{eV}$, which may be in the line of models with light mediators in the neutrino sector [259]. On the other hand, for $l_\nu = 10^6\,\text{Gpc}$ (case **b**), the values of λ' are in the range from 10^{-17} to 10^{-21}, significantly smaller than for larger values of l_ν. The same happens for $m_{Z'}$, that now takes values within the range from $10^{-7}\,\text{eV}$ to $10^{-11}\,\text{eV}$, well below the predictions of case **a**, In general terms, larger values of the mean free path imply lower values of λ' and $m_{Z'}$.

- **1 keV DM**. Here, the lower value of the DM mass results in an increased value of the number density of DM particles, N_χ. Depending on the value of $V^\oplus$, this could lead to a mediator mass of the order of few eV, in agreement with models including light mediators. The values of λ' remain unchanged with respect to the 100 GeV DM case.

In our calculations, we have parameterised the DM-neutrino interaction in a way that the DM interacts with both neutrinos and antineutrinos. Let us remark that the interaction with neutrinos and antineutrinos is intrinsically related to the nature of DM and the particle mediator. For instance, in models of asymmetric DM we might expect that the DM only affects either neutrinos or their antiparticles. On the other hand, this could also happen in symmetric DM scenarios (WIMP-like), where the nature of the mediator is responsible for the non-symmetric effect, for example through a coupling of DM to antineutrinos and anti-DM to neutrinos. Let us highlight that this asymmetry is already present in the standard MSW effect, since most of the media are mainly composed by matter and no antimatter. In a more general scenario, the predicted neutrino flavour composition at Earth would be different for neutrinos and antineutrinos.

Another aspect to be considered is the relation between the neutrino arrival direction and the observed flavour composition. The DM distribution moulds the observed neutrino flavour composition depending on its production point within the Milky Way, as discussed in section 7.2.2. This implies that the location of

$V_{11}^{\oplus}/\,\mathrm{eV}$	10^{-21}	10^{-19}	10^{-17}
Weak scale (a) assumptions:	$G'_{\mathrm{F}} = G_{\mathrm{F}}$, $\lambda_{11} = 1$		
$m_{\mathrm{DM}}/\,\mathrm{eV}$	10^{-8}	10^{-10}	10^{-12}
$l_\nu/\,\mathrm{pc}$	10^{-2}	10^{-4}	10^{-6}
Weak scale (b) assumptions:	$G'_{\mathrm{F}} = G_{\mathrm{F}}$, $l_\nu = 50\,\mathrm{kpc}$		
λ_{11}	10^{-7}	10^{-9}	10^{-11}
$m_{\mathrm{DM}}/\,\mathrm{eV}$	10^{-15}	10^{-19}	10^{-23}
100 GeV DM (a) assumptions:	$m_{\mathrm{DM}} = 100\,\mathrm{GeV}$, $l_\nu = 50\,\mathrm{kpc}$		
λ_{11}	10^{-7}	10^{-9}	10^{-11}
$m_{Z'}/\,\mathrm{eV}$	10^{-2}	10^{-4}	10^{-6}
100 GeV DM (b) assumptions:	$m_{\mathrm{DM}} = 100\,\mathrm{GeV}$, $l_\nu = 10^6\,\mathrm{Gpc}$		
λ_{11}	10^{-17}	10^{-19}	10^{-21}
$m_{Z'}/\,\mathrm{eV}$	10^{-7}	10^{-9}	10^{-11}
1 keV DM (a) assumptions:	$m_{\mathrm{DM}} = 1\,\mathrm{keV}$, $l_\nu = 50\,\mathrm{kpc}$		
λ_{11}	10^{-7}	10^{-9}	10^{-11}
$m_{Z'}/\,\mathrm{eV}$	10^{2}	1	10^{-2}
1 keV DM (b) assumptions:	$m_{\mathrm{DM}} = 1\,\mathrm{keV}$, $l_\nu = 10^6\,\mathrm{Gpc}$		
λ_{11}	10^{-17}	10^{-19}	10^{-21}
$m_{Z'}/\,\mathrm{eV}$	10^{-3}	10^{-5}	10^{-7}

Table 7.2: Particle physics interpretations for three given values of the effective potential at Earth, $V_{11}^{\oplus}$. Six different scenarios are displayed, with the corresponding assumptions shown in the upper row of each block. For each case, the second, third and fourth columns show the values of the remaining parameters for the corresponding values of $V_{11}^{\oplus}$. Implications of each case are described in the text.

the neutrino observatory plays an important role on the observation of the neutrino flavour content. For instance, ARCA and IceCube have access to different parts of the sky; consequently, the averaged flavour composition observed at each experiment may be different.

Although it has not been discussed in this work, the effect of DM on neutrino oscillations might also be relevant for extragalactic neutrinos. Accordingly, PeV neutrinos coming from regions above or below the galactic plane can also present different flavour compositions with respect to the expectations in vacuum. In this case the effect would depend on the properties of the DM halo where the neutrino source is located and on how it compares with the one of the Milky Way.

Besides that, a larger l_ν might be required, depending on the size and density of the departing DM halo. The distance to the source would also be relevant due to the loss of coherence in the neutrino propagation.

7.4 Chapter remarks

The observation of PeV neutrinos opens a new window to explore astrophysical processes and high-energy neutrino sources. Independently of the source location, neutrinos must travel across the galactic DM halo. Depending on the distance to the source, we can observe deviations with respect to neutrino oscillations in vacuum due to the interaction between dark matter and neutrinos. In this work, we have assumed the most generic interaction between dark matter and neutrinos, as described in Eq. (7.3). We have been interested in the study of the effects of a non-homogeneous distribution for the DM halo of the Milky Way. As a consequence, the effective potential acquires a spatial dependence, what implies a richer scenario than other new physics cases in which the detected flavour composition of ultra-high energy neutrinos is also changed.

Conclusions

Particle physics, astrophysics and cosmology have a great success in explaining most of the known processes happening in the Universe, but there are loose ends that resist the theoretical attempts to find an explanation and, sometimes, even a clarification from experiments becomes a challenging task. Therefore, physicists working on these topics need to collaborate, since the answer to the missing pieces in one of the subjects might come from a different one. In this regard, neutrino physics takes part in the three mentioned fields, so one can not deny that it is indeed an interesting subject. In the particular case of this PhD thesis, we have placed special emphasis on the role of these neutral leptons in cosmology.

One of the most intriguing aspects of neutrinos are their flavour oscillations, which we have revisited in chapter 1. They appear in almost all the works discussed in this thesis, and they play a leading role in most of them. We have discussed the basics of neutrino oscillations, highlighting the importance of matter effects, and we have explained the main results derived from a global fit of the leading experiments in the field. This work was published in Ref. [7] and it includes data from solar, reactor, accelerator and atmospheric experiments. Specifically, we have centred our attention on the atmospheric-neutrino analyses of the LVNTs ANTARES and IceCube DeepCore, in which the author mostly contributed. Although they are not the most relevant experiments nowadays, future neutrino telescopes such as ORCA (already under deployment) and PINGU will become extremely competitive. The major improvement that we have found in the global analysis of all relevant experiments (including the two mentioned LVNTs) has been a preference for normal over inverted mass ordering with a significance of 3.4σ, coming mostly from the atmospheric analysis of Super-Kamiokande and from the interplay between the measurements of the mixing angle θ_{13} from reactor and long-baseline accelerator data. Additionally, the determination of the CP-phase δ is also improved, and the best-fit value of θ_{23} is compatible with maximal mixing for both mass orderings.

From the point of view of cosmology, neutrinos are primarily important in the early stages of the Universe, when they contribute to radiation. After introducing in chapter 2 the basics of cosmology, in chapter 3 we have studied in detail the decoupling process of these weakly interacting particles. The discussion is based on the work [116], where we have revisited the treatment of flavour oscillations, relaxing some approximations with respect to the off-diagonal terms of the collisional matrix that enters the Boltzmann equations. We have computed the value of the effective number of neutrinos in the standard case, with no contribution from other relativistic species, obtaining $N_{\rm eff} = 3.045$, which is in full agreement with the previous standard value. We have also shown that oscillations do not change this value to this level of precision; however, they are very important in order to study the deviation from equilibrium of the distribution functions of the individual flavours. We have tested as well that the results are basically the same in both mass orderings. Finally, we have checked the influence of a non-standard interaction between neutrinos and electrons, for two given values of the parameters still compatible with the experimental bounds, and we found that in this scenario $N_{\rm eff}$ can vary from 3.040 to 3.059.

Another non-standard scenario in which the effective number of neutrinos can be affected is presented in chapter 4. There we have discussed the work published in Ref. [145] on a very low reheating scenario. Under the hypothesis that the last radiation dominated phase of the Universe started later than it is usually assumed, when the temperature of the cosmic plasma was of the order of MeV, neutrino thermalisation might be incomplete. This has a direct effect in both BBN and CMB anisotropies, due to the impact on the expansion rate of a lower amount of radiation and, in the specific case of BBN, because of the change in the neutron-to-proton ratio caused by the distortions in the distribution functions of electro neutrinos. In this study we also took into account flavour oscillations, that are extremely important when studying the modification of the neutrino distribution functions (as we saw in chapter 3). Actually, they even change the behaviour in the altered abundance of helium with respect to the reheating temperature. In the end, the bound from primordial nucleosynthesis that we have obtained gives $T_{\rm RH} > 4.1\,{\rm MeV}$ at 95% CL. Using the results on the baryon density ω_b from BBN we have further found a stringent bound from CMB observations, of $T_{\rm RH} > 4.7\,{\rm MeV}$ at 95% CL.

In chapter 5 we have also studied a non-standard scenario involving relic neutrinos in the early Universe. This work, published in Ref. [170], is based on the phenomenological study of neutrino statistics. Putting aside all possible theoretical problems, we have tested whether cosmological observations can say

something about the statistical properties of neutrinos. We have modified their distribution function introducing the parameter κ_ν, that can take any value from -1 (acquiring a bosonic distribution) to $+1$ (recovering a fermionic distribution). The main consequence of a non-fermionic statistics of neutrinos is a larger contribution to the energy density of the Universe, both in form of radiation at its earlier stages and in form of matter when neutrinos become non-relativistic. Hence, this non-standard scenario can be tested with BBN and CMB observables. However, despite the great success of recent cosmological observations, this scenario is far from being constrained with the current precision. In particular, the bounds that we have obtained from primordial nucleosynthesis alone are compatible with any value of κ_ν at 68% CL, and only when a prior is used on ω_b from CMB anisotropies we can tighten the bounds and a purely bosonic neutrino ($\kappa_\nu = -1$) is out of the region allowed at 2σ. From CMB alone we have found lower bounds from $\kappa_\nu > -0.18$ to $\kappa_\nu > 0.06$, depending on the dataset and on the particular extension of the ΛCDM model. As a final test, we have checked that the existing tensions on some cosmological observables can not be significantly reduced with the assumption of a mixed neutrino statistics.

In the next work [215], described in chapter 6, we have still studied relic neutrinos, but we moved towards lower energies and recent times. In this case we have studied the local density of such relics, taking into account the fact that they are non-relativistic nowadays and therefore they feel the gravitational potential of our galaxy. We have investigated the impact of the DM profile, using an NFW and an Einasto parameterisation which have been fit to data. Of course, no dark matter particle has been detected so far, so the data used to infer the DM distribution was obtained from a study where rotational velocities and luminous matter in our galaxy were compared. We have also included baryons in our calculations, improving the treatment of matter in the Milky Way made in previous works. In addition, we have made the computation (using N-one-body simulations) for neutrino masses close to minimal values. For a mass $m_\nu = 60\,\text{meV}$ we have obtained an enhancement from 10% to 20% in the local density, depending on the DM profile, which can rise up to 300% in the most optimistic case for $m_\nu = 150\,\text{meV}$. Knowing the overdensity of relic neutrinos is particularly important for future experiments aiming at their detection, as it is the case of PTOLEMY, whose expected number of relic neutrinos captured in tritium can rise almost a factor 3 in the most optimistic scenarios and for the largest neutrino masses allowed by cosmological constraints.

In chapter 7 (which is based on the publication [11]) we leave relic neutrinos and change to those accelerated at ultra-high energies, only reachable at VLVNTs

such as IceCube. Making the hypothesis of a non-universal DM-neutrino interaction, we have examined the imprints on flavour oscillations of the DM halo of the Milky Way for ultra-high energetic neutrinos. We know that matter effects modify the oscillatory patterns, and in media with a changing density there can be resonances further affecting this phenomenon. On the other hand, the larger the energy of the travelling neutrino the larger the effect. Therefore, if DM nature is such that its particles interact with neutrinos, and this interaction is not the same for all the flavours, matter effects could appear in the flavour composition of the most energetic neutrinos detectable by VLVNTs. In fact, we have shown that because of the non-homogeneous nature of the DM profile in our galaxy, galactic neutrinos could be influenced differently depending on their arrival direction. Moreover, larger modifications on the oscillatory patterns can be accessed with respect to other new physics scenarios that also affect oscillations, thanks to the distinctive impact that has the presence of resonances. The addition of ARCA in the Mediterranean sea and GVD at lake Baikal will complement IceCube and could test this hypothesis in the near future.

Throughout this thesis we have studied several aspects of neutrino physics, with the focus put on the role of the relics that decoupled very early in the history of the Universe. We have revisited neutrino flavour oscillations and their impact on cosmology, starting from the process of relic neutrino decoupling and moving later to non-standard scenarios. In addition, we have investigated these relics at present time, analysing their local density. And we have also studied ultra-energetic neutrinos and the possible influence on their oscillation pattern coming from a DM-neutrino interaction. All in all, we can say that neutrinos are an important piece in particle physics, astrophysics and cosmology, and even though they can not explain everything, they are one of the few particles that can serve as a bridge between fields, hopefully helping us to understand the missing explanations, when not creating new puzzles. Therefore, we may not trust our favourite supernatural entity, but we should certainly trust neutrinos.

Appendices

A Functions for the $z(x)$ evolution equation

The following functions appear in the evolution equations (3.25), (3.26) and (3.45) of $z(x)$. The first ones, $F_1(w)$ and $F_2(w)$, are present in all $z(x)$ evolution equations, and the next ones appear when the finite temperature corrections are included.

$$F_1(w) = \frac{1}{\pi^2}\int_0^\infty \mathrm{d}u \frac{u^2 \mathrm{e}^{\sqrt{u^2+w^2}}}{\left(\mathrm{e}^{\sqrt{u^2+w^2}}+1\right)^2}, \tag{1}$$

$$F_2(w) = \frac{1}{\pi^2}\int_0^\infty \mathrm{d}u \frac{u^4 \mathrm{e}^{\sqrt{u^2+w^2}}}{\left(\mathrm{e}^{\sqrt{u^2+w^2}}+1\right)^2}, \tag{2}$$

$$F_3(w) = \frac{1}{\pi^2}\int_0^\infty \mathrm{d}u \frac{u^2}{\sqrt{u^2+w^2}} \frac{1}{\left(\mathrm{e}^{\sqrt{u^2+w^2}}+1\right)}, \tag{3}$$

$$\begin{aligned} G_1(w) = 2\pi\alpha \Bigg[& \frac{1}{w}\left(\frac{F_3(w)}{3} + 2F_3(w)^2 - \frac{F_1(w)}{6} - F_3(w)F_1(w)\right) \\ & + \left(\frac{1}{6}\frac{\mathrm{d}F_3(w)}{\mathrm{d}w} - F_3(w)\frac{\mathrm{d}F_3(w)}{\mathrm{d}w} + \frac{1}{6}\frac{\mathrm{d}F_1(w)}{\mathrm{d}w} \right. \\ & \left. + F_3(w)\frac{\mathrm{d}F_1(w)}{\mathrm{d}w} + F_1(w)\frac{\mathrm{d}F_3(w)}{\mathrm{d}w}\right)\Bigg] \end{aligned} \tag{4}$$

and

$$G_2(w) = -8\pi\alpha\left(\frac{F_3(w)}{6} + \frac{F_1(w)}{6} - \frac{1}{2}F_3(w)^2 + F_3(w)F_1(w)\right) + 2\pi\alpha w\left(\frac{1}{6}\frac{\mathrm{d}F_3(w)}{\mathrm{d}w} - F_3(w)\frac{\mathrm{d}F_3(w)}{\mathrm{d}w} + \frac{1}{6}\frac{\mathrm{d}F_1(w)}{\mathrm{d}w} + F_3(w)\frac{\mathrm{d}F_1(w)}{\mathrm{d}w} + F_1(w)\frac{\mathrm{d}F_3(w)}{\mathrm{d}w}\right). \quad (5)$$

In (4) and (5) $\alpha = e^2/(4\pi)$ is the finite structure constant.

B Boltzmann equations and collision terms in comoving variables

In terms of the comoving variables (3.17) one can write the Boltzmann equations (3.29) as

$$\frac{\mathrm{d}\varrho_y}{\mathrm{d}x} = m_{\mathrm{P}}\sqrt{\frac{3}{8\pi\bar{\rho}}}\left\{-i\frac{x^2}{m_e^3}\left[\left(\frac{\mathsf{M}_{\mathrm{F}}}{2y} - \frac{8\sqrt{2}G_{\mathrm{F}}ym_e^6}{3m_{\mathrm{W}}^2x^6}\,\bar{\rho}_{ee}\mathsf{E}\right), \varrho_y\right] + \frac{m_e^3}{x^4}\,\bar{\mathcal{I}}\left[\varrho_y\right]\right\}, \quad (6)$$

where the bar over some quantities indicate that they are written in the comoving variables (3.17), such as the dimensionless energy density $\bar{\rho} = \rho(x/m_e)^4$. On the other hand, the continuity equation (2.11) can be translated into an equation for $\mathrm{d}z/\mathrm{d}x$ as in (3.25), including the contributions of finite temperature QED corrections.

Here we also present the two-dimensional collision integrals for neutrino-electron processes written in terms of the comoving variables. For the scattering with electrons one has

$$\begin{aligned}\bar{\mathcal{I}}_{\nu e^-\to\nu e^-} = \frac{G_{\mathrm{F}}^2}{(2\pi)^3 y_1^2}\int \mathrm{d}y_2\mathrm{d}y_4\,\frac{y_2}{\bar{E}_2}\frac{y_4}{\bar{E}_4}\Big\{&\Pi_2(y_1,y_4)F_{\mathrm{sc}}^{RR}(\nu^{(1)},e^{(2)},\nu^{(3)},e^{(4)}) \\ &+ \Pi_2(y_1,y_2)F_{\mathrm{sc}}^{LL}(\nu^{(1)},e^{(2)},\nu^{(3)},e^{(4)}) \\ &- (x^2+\delta\bar{m}_e^2)\,\Pi_1(y_1,y_3)\Big(F_{\mathrm{sc}}^{RL}(\nu^{(1)},e^{(2)},\nu^{(3)},e^{(4)}) \\ &+ F_{\mathrm{sc}}^{LR}(\nu^{(1)},e^{(2)},\nu^{(3)},e^{(4)})\Big)\Big\}, \end{aligned} \quad (7)$$

where $\bar{E}_i = \sqrt{x^2+\delta\bar{m}_e^2+y_i^2}$ and $\delta\bar{m}_e$ is the finite temperature QED correction to the electron mass (Eq. (3.11) expressed in our comoving variables). In the case

of the scattering with positrons the matrix with collision terms is

$$\begin{aligned}\bar{\mathcal{I}}_{\nu e^+\to\nu e^+} = \frac{G_{\rm F}^2}{(2\pi)^3 y_1^2}\int \mathrm{d}y_2\mathrm{d}y_4 \frac{y_2}{\bar{E}_2}\frac{y_4}{\bar{E}_4}\Big\{&\Pi_2(y_1,y_4)F_{\rm sc}^{LL}(\nu^{(1)},\bar{e}^{(2)},\nu^{(3)},\bar{e}^{(4)})\\ &+\Pi_2(y_1,y_2)F_{\rm sc}^{RR}(\nu^{(1)},\bar{e}^{(2)},\nu^{(3)},\bar{e}^{(4)})\\ &-\left(x^2+\delta\bar{m}_e^2\right)\Pi_1(y_1,y_3)\Big(F_{\rm sc}^{RL}(\nu^{(1)},\bar{e}^{(2)},\nu^{(3)},\bar{e}^{(4)})\\ &+F_{\rm sc}^{LR}(\nu^{(1)},\bar{e}^{(2)},\nu^{(3)},\bar{e}^{(4)})\Big)\Big\},\end{aligned} \tag{8}$$

and for the annihilation to an $e^\pm$ pair,

$$\begin{aligned}\bar{\mathcal{I}}_{\nu\bar{\nu}\to e^-e^+} = \frac{G_{\rm F}^2}{(2\pi)^3 y_1^2}\int \mathrm{d}y_3\mathrm{d}y_4 \frac{y_3}{\bar{E}_3}\frac{y_4}{\bar{E}_4}\Big\{&\Pi_2(y_1,y_4)F_{\rm ann}^{LL}(\nu^{(1)},\bar{\nu}^{(2)},e^{(3)},\bar{e}^{(4)})\\ &+\Pi_2(y_1,y_3)F_{\rm ann}^{RR}(\nu^{(1)},\bar{\nu}^{(2)},e^{(3)},\bar{e}^{(4)})\\ &+\left(x^2+\delta\bar{m}_e^2\right)\Pi_1(y_1,y_2)\Big(F_{\rm ann}^{RL}(\nu^{(1)},\bar{\nu}^{(2)},e^{(3)},\bar{e}^{(4)})\\ &+F_{\rm ann}^{LR}(\nu^{(1)},\bar{\nu}^{(2)},e^{(3)},\bar{e}^{(4)})\Big)\Big\}.\end{aligned} \tag{9}$$

Finally, the functions $\Pi_{1,2}(y_i,y_j)$ have the following structure:

$$\Pi_1(y_1,y_3) = \bar{E}_1\bar{E}_3 D_1 + D_2(y_1,y_3,y_2,y_4), \tag{10}$$

$$\Pi_1(y_1,y_2) = \bar{E}_1\bar{E}_2 D_1 - D_2(y_1,y_2,y_3,y_4), \tag{11}$$

$$\begin{aligned}\Pi_2(y_1,y_4) = 2\Big(&\bar{E}_1\bar{E}_2\bar{E}_3\bar{E}_4 D_1 + \bar{E}_2\bar{E}_3 D_2(y_1,y_4,y_2,y_3)\\ &+\bar{E}_1\bar{E}_4 D_2(y_2,y_3,y_1,y_4) + D_3\Big),\end{aligned} \tag{12}$$

$$\begin{aligned}\Pi_2(y_1,y_2) = 2\Big(&\bar{E}_1\bar{E}_2\bar{E}_3\bar{E}_4 D_1 - \bar{E}_1\bar{E}_2 D_2(y_3,y_4,y_1,y_2)\\ &-\bar{E}_3\bar{E}_4 D_2(y_1,y_2,y_3,y_4) + D_3\Big),\end{aligned} \tag{13}$$

$$\begin{aligned}\Pi_2(y_1,y_3) = 2\Big(&\bar{E}_1\bar{E}_2\bar{E}_3\bar{E}_4 D_1 + \bar{E}_1\bar{E}_3 D_2(y_2,y_4,y_1,y_3)\\ &+\bar{E}_2\bar{E}_4 D_2(y_1,y_3,y_2,y_4) + D_3\Big),\end{aligned} \tag{14}$$

where

$$\bar{E}_i = \begin{cases} \sqrt{x^2 + \delta\bar{m}_e^2 + y_i^2} & \text{for electrons or positrons,} \\ y_i & \text{for neutrinos.} \end{cases} \tag{15}$$

The D_l functions are obtained as in [127] from the following integrals:

$$D_1 = \frac{16}{\pi}\int_0^\infty \frac{\mathrm{d}\lambda}{\lambda^2}\sin(\lambda y_1)\sin(\lambda y_2)\sin(\lambda y_3)\sin(\lambda y_4), \tag{16}$$

$$\begin{aligned} D_2(y_i, y_j, y_k, y_l) = -\frac{16}{\pi}\int_0^\infty \frac{\mathrm{d}\lambda}{\lambda^4}\sin(\lambda y_k)\sin(\lambda y_l)\left[\lambda y_i\cos(\lambda y_i) - \sin(\lambda y_i)\right] \\ \times\left[\lambda y_j\cos(\lambda y_j) - \sin(\lambda y_j)\right], \end{aligned} \tag{17}$$

$$D_3 = \frac{16}{\pi}\int_0^\infty \frac{\mathrm{d}\lambda}{\lambda^6}\prod_{a=1}^{4}\left[\lambda y_a\cos(\lambda y_a) - \sin(\lambda y_a)\right], \tag{18}$$

that can be solved analytically. We have not explicitly written the dependence on y_i of D_1 and D_3 because they are symmetric in the dimensionless neutrino momenta.

Resum de la tesi

La present tesi doctoral s'enfoca en l'estudi fenomenològic d'algunes propietats dels neutrins, així com d'èpoques cosmològiques en les quals la participació d'aquestes partícules elementals és important. S'ha posat especial èmfasi tant en les oscil·lacions de sabor com en el seu paper en cosmologia, en particular durant les primeres etapes de l'Univers.

Els neutrins són uns dels components més extranys del Model Estàndard de la física de partícules. Amb masses pràcticament nul·les, els valors de les quals es resisteixen als experiments, presenten unes propietats quàntiques que rares vegades són patents amb tanta claredat. És el cas, per exemple, de les anomenades *oscil·lacions* de sabor dels neutrins. Aquests leptons neutres sols interaccionen feblement, bescanviant bosons $W^{\pm}$ o Z^0 en interaccions de *corrent carregat* o *corrent neutre*, respectivament, i sols ho fan els seus estats febles *electrònic*, *muònic* o *tauònic*, anomenats així pel leptó carregat que els acompanya en el cas d'una interacció de corrent carregat. Aquests estats s'anomenen estats de *sabor*, i el fet que no coincidisquen amb els estats de massa (aquells que es propaguen lliurement en el buit), sinó que en siguen una barreja, dóna lloc a les oscil·lacions esmentades.

Les oscil·lacions dels neutrins impliquen que si una d'aquestes partícules és generada amb un sabor α, on α pot ser qualsevol dels tres sabors possibles, es pot detectar amb certa probabilitat amb un sabor distint β. És aquesta probabilitat la que presenta un comportament oscil·latori que varia tant amb l'energia del neutrí en qüestió com amb la distància que separa els seus punts d'origen i de detecció. A més a més, el patró d'oscil·lacions depèn d'una sèrie de paràmetres, que en el cas estàndard de tres neutrins són: a) tres angles de mescla, b) una fase relacionada amb la violació de la simetria càrrega-paritat (anomenada simetria CP) i c) les dues diferències del quadrat de les masses dels neutrins. D'aquests últims paràmetres s'obté l'important resultat que els neutrins són partícules amb massa, ja que les oscil·lacions només són possibles si les diferències del quadrat de les seues masses no són nul·les. La primera part d'aquesta tesi se centra en la

determinació d'aquests paràmetres a partir de l'anàlisi conjunta de les mesures de diversos experiments.

A banda del fenomen de les oscil·lacions, els neutrins són també interessants des del punt de vista de la cosmologia. Atès que les seues masses són molt menudes, els neutrins de l'Univers primigeni eren ultrarrelativistes, és a dir, les seues energies estaven dominades pel terme cinètic, essent molt superiors al valor de les seues masses. Açò fa que als primers instants de l'Univers els neutrins formen part de la radiació dominant amb una contribució que s'estudia a partir del conegut paràmetre $N_{\rm eff}$, el *nombre efectiu de neutrins*. De la mateixa manera que els neutrins, qualsevol altra partícula que no interaccione electromagnèticament i siga ultrarrelativista en l'Univers primerenc contribueix a la seua densitat d'energia durant aquesta època. Aquest tipus de radiació, present en alguns models teòrics, es coneix com a radiació fosca i la seua existència es pot contrastar comparant el càlcul exacte de $N_{\rm eff}$ en el cas estàndard amb la seua mesura experimental. En la segona part de la tesi calculem el valor estàndard del nombre efectiu de neutrins, relaxant algunes aproximacions presents en càlculs previs. Així mateix, estudiem l'efecte que pot tenir la presència d'interaccions no estàndard neutrí-electró.

Com els neutrins interaccionen feblement, el ritme de les seues interaccions fou superat molt prompte pel corresponent a l'expansió de l'Univers. Aquest procés es coneix com desacoblament, a partir del qual els neutrins primigenis, també anomenats neutrins relíquia, solcaren l'Univers en solitari fins arribar als nostres dies, mantenint un espectre d'energies molt proper al d'una distribució de Fermi-Dirac. El paper dels neutrins en la fase primordial de l'Univers és una de les coses a tenir en compte a l'hora de posar fites a extensions del model estàndard de cosmologia. En especial, les petites desviacions trobades a la seua distribució després del seu desacoblament, a causa del caràcter no instantani d'aquest, tot plegat amb el paper que les oscil·lacions poden arribar a jugar, han demostrat ser importants en certs estudis. Precisament explotarem aquest fet en un parell de capítols de la tesi, on posem límits tant al començament de l'última època de l'Univers dominada per la radiació com a les propietats estadístiques dels neutrins.

Més enllà de provocar el seu desacoblament, l'expansió de l'Univers té altre efecte important sobre els neutrins relíquia. La contínua dilatació de l'espai-temps provoca una dilució en les energies de les partícules desacoblades, representada per una disminució de la temperatura que caracteritza la seua distribució. Com els neutrins són partícules massives, la qual cosa sabem per l'estudi de les oscil·lacions de sabor, arriba un moment en què deixen de contribuir a la radiació de l'Univers

i passen a fer-ho com matèria. Del moment exacte d'aquesta transició i del valor de les masses dels neutrins depèn la formació de les grans estructures. Nosaltres aprofitem la capacitat d'aquests neutrins, no relativistes avui en dia, de ser atrapats en grans potencials gravitatoris, per estudiar el seu agrupament a la nostra galàxia, especialment al voltant del Sistema Solar. Com veurem, açò és important per a futurs experiments l'objectiu dels quals és la detecció directa dels neutrins relíquia.

Finalment, en l'últim capítol assumim, de la manera més general possible, que existeix algun tipus d'interacció entre els neutrins i les partícules de matèria fosca (DM per les seues sigles en anglès), amb l'objectiu d'estudiar possibles desviacions en el sabor dels neutrins de molt alta energia. L'origen d'aquest tipus de neutrins, observats amb el telescopi IceCube, és desconegut, però una part pot procedir de fonts galàctiques. Com la presència de matèria modifica els patrons d'oscil·lació, si suposem una interacció neutrí-DM, les oscil·lacions es poden veure afectades per la presència de matèria fosca en la Via Làctia. A més a més, tenim en compte la seua distribució no homogènia a la nostra galàxia.

En les següents seccions veurem un resum dels distints treballs el desenvolupament dels quals ha fet possible aquesta tesi doctoral.

Estimació dels paràmetres d'oscil·lació dels neutrins

En aquest estudi, basat en la publicació [7], hem posat en comú les dades de diversos experiments sobre les oscil·lacions de sabor dels neutrins.

En l'aproximació de dos neutrins, útil en multitud d'ocasions, la probabilitat de detectar un neutrí com un estat de sabor ν_β quan havia estat produït com ν_α, amb $\alpha \neq \beta$, ve donada per

$$P_{\nu_\alpha \to \nu_\beta}(L, E) = \sin^2(2\theta) \sin^2\left(\frac{\Delta m^2 L}{4E}\right), \tag{1}$$

on θ és l'angle de mescla característic de l'oscil·lació, que regula l'amplitud de la mateixa; $\Delta m^2 = m_2^2 - m_1^2$ és la diferència del quadrat de les masses dels dos neutrins considerats, responsable de la freqüència de les oscil·lacions, i L és la distància recorreguda pel neutrí en qüestió, d'energia E.

En l'equació (1) hi ha dos paràmetres d'oscil·lació, θ i Δm^2. En el cas estàndard de tres neutrins són sis els paràmetres a tenir en compte: tres angles de mescla, θ_{12}, θ_{13} i θ_{23}; dos diferències quadràtiques de masses, Δm^2_{21} y Δm^2_{31}, i una fase δ relacionada amb la violació de la simetria CP en el sector leptònic.

Aquests paràmetres apareixen en la matriu de mescla que relaciona els autoestats de massa (aquells que es propaguen en el hamiltonià lliure) amb els de sabor, i que pot escriure's com el producte de tres matrius de rotació

$$U = \begin{pmatrix} 1 & 0 & 0 \\ 0 & c_{23} & s_{23} \\ 0 & -s_{23} & c_{23} \end{pmatrix} \begin{pmatrix} c_{13} & 0 & s_{13}\mathrm{e}^{-i\delta} \\ 0 & 1 & 0 \\ -s_{13}\mathrm{e}^{i\delta} & 0 & c_{13} \end{pmatrix} \begin{pmatrix} c_{12} & s_{12} & 0 \\ -s_{12} & c_{12} & 0 \\ 0 & 0 & 1 \end{pmatrix}, \qquad (2)$$

on $c_{ij} = \cos\theta_{ij}$ i $s_{ij} = \sin\theta_{ij}$.

Existeixen diferents experiments dedicats a l'estudi de les oscil·lacions dels neutrins. Uns es basen en la detecció de neutrins solars; altres en l'observació de neutrins atmosfèrics, i alguns en la captura dels neutrins procedents dels reactors de les centrals nuclears o d'aquells produïts després de la desintegració de pions i kaons creats en acceleradors. Cada experiment té uns valors de L i E característics, la qual cosa fa que siguen especialment sensibles a certs paràmetres d'oscil·lació. És per això que una estimació global dels sis paràmetres sols és possible mitjançant l'anàlisi conjunta d'experiments basats en tècniques diferents i, per tant, sensibles a diferents paràmetres.

En el nostre ajust global hem inclòs les dades dels experiments solars Homestake, GALLEX/GNO, SAGE, Super-Kamiokande, SNO i Borexino; dels experiments de reactor KamLAND, Daya Bay, RENO i Double Chooz; dels experiments d'accelerador K2K, MINOS, T2K i NOνA, i dels experiments atmosfèrics IceCube DeepCore, ANTARES i de nou Super-Kamiokande.

Per al desenvolupament d'aquesta tesi ha sigut especialment important l'anàlisi de les dades d'ANTARES i IceCube DeepCore. Tots dos són telescopis de neutrins de gran volum que aprofiten un mitjà material extens per a la detecció d'aquestes partícules. ANTARES està situat al fons del mar Mediterrani i IceCube a l'interior de la capa de gel del Pol Sud. Els dos basen la detecció dels neutrins en la llum Cherenkov generada pel pas, a velocitats majors que les de la llum en l'aigua o el gel, de les partícules carregades creades en la interacció d'un neutrí amb les molècules del medi. Per a ambdues anàlisis hem comparat dades reals observades pels telescopis amb dades simulades del flux de neutrins atmosfèrics que arriben als detectors.

Els resultats derivats de l'anàlisi conjunta de tots els experiments es mostren a la taula 3, on NO i IO fan referència als ordres normal i invers, respectivament, de les masses dels neutrins. Aquesta ambigüitat existeix perquè, si bé sabem que $\Delta m^2_{21} > 0$, es desconeix el signe de Δm^2_{31}, podent estar m_3 per damunt de m_1 i m_2 (ordre normal) o per baix (ordre invers). Per últim, tal volta el resultat més important d'aquest treball és l'evidència estadística a 3.4σ que les

paràmetre	millor ajust $\pm$ 1σ	rang a 2σ	rang a 3σ
Δm^2_{21} $[10^{-5}\text{eV}^2]$	$7.55^{+0.20}_{-0.16}$	7.20–7.94	7.05–8.14
$\lvert\Delta m^2_{31}\rvert$ $[10^{-3}\text{eV}^2]$ (NO)	2.50 ± 0.03	2.44–2.57	2.41–2.60
$\lvert\Delta m^2_{31}\rvert$ $[10^{-3}\text{eV}^2]$ (IO)	$2.42^{+0.03}_{-0.04}$	2.34–2.47	2.31–2.51
$\sin^2\theta_{12}/10^{-1}$	$3.20^{+0.20}_{-0.16}$	2.89–3.59	2.73–3.79
$\theta_{12}/^\circ$	$34.5^{+1.2}_{-1.0}$	32.5–36.8	31.5–38.0
$\sin^2\theta_{23}/10^{-1}$ (NO)	$5.47^{+0.20}_{-0.30}$	4.67–5.83	4.45–5.99
$\theta_{23}/^\circ$	$47.7^{+1.2}_{-1.7}$	43.1–49.8	41.8–50.7
$\sin^2\theta_{23}/10^{-1}$ (IO)	$5.51^{+0.18}_{-0.30}$	4.91–5.84	4.53–5.98
$\theta_{23}/^\circ$	$47.9^{+1.0}_{-1.7}$	44.5–48.9	42.3–50.7
$\sin^2\theta_{13}/10^{-2}$ (NO)	$2.160^{+0.083}_{-0.069}$	2.03–2.34	1.96–2.41
$\theta_{13}/^\circ$	$8.45^{+0.16}_{-0.14}$	8.2–8.8	8.0–8.9
$\sin^2\theta_{13}/10^{-2}$ (IO)	$2.220^{+0.074}_{-0.076}$	2.07–2.36	1.99–2.44
$\theta_{13}/^\circ$	$8.53^{+0.14}_{-0.15}$	8.3–8.8	8.1–9.0
δ/π (NO)	$1.21^{+0.21}_{-0.15}$	1.01–1.75	0.87–1.94
$\delta/^\circ$	218^{+38}_{-27}	182–315	157–349
δ/π (IO)	$1.56^{+0.13}_{-0.15}$	1.27–1.82	1.12–1.94
$\delta/^\circ$	281^{+23}_{-27}	229–328	202–349

Taula 3: Valors dels paràmetres de'oscilació dels neutrins obtinguts en l'anàlisi global portada a terme en [7]. Els rangs per a l'ordre invers (IO) es refereixen al mínim local d'aquest ordre concret de les masses dels neutrins.

masses dels neutrins estan ordenades de manera normal, una preferència que apareix únicament quan s'analitzen en conjunt els distints tipus d'experiments. No obstant això, encara haurem d'esperar alguns anys que algun experiment arribe en solitari a tal nivell d'evidència a fi que, amb sort, l'anàlisi global indique una preferència major que 5σ cap a un dels ordres.

El desacoblament dels neutrins i el càlcul de N_{eff}

El treball que ací es discuteix ha sigut publicat en [116], on ens centrem en el paper que juguen les oscil·lacions de sabor en el desacoblament dels neutrins relíquia.

Poc abans que els neutrins es desacoblaren del plasma còsmic, quan la temperatura d'aquest s'acostava als 10 MeV (en unitats naturals), aquests leptons neutres estaven en equilibri amb fotons, electrons i positrons. Posteriorment, la velocitat d'expansió de l'Univers va superar la freqüència a la qual els neutrins interaccionaven amb la resta de les partícules del plasma (això va ocórrer a unes temperatures de l'ordre del MeV), i van iniciar un viatge en solitari després de produir-se el seu desacoblament. Poc després, quan la temperatura del plasma còsmic va continuar descendint i va estar per davall de la massa de l'electró, aquests es van anihilar amb les seues antipartícules sense possibilitat de ser generats de nou. Com els neutrins ja s'havien desacoblat, l'entropia dels parells $e^{\pm}$ va passar als fotons, reescalfant-los respecte als neutrins, que des del seu desacoblament han seguit una distribució de Fermi-Dirac amb una temperatura ponderada per l'expansió.

Els efectes que estudiem en aquest treball estan relacionats amb la proximitat dels dos processos que hem comentat: el *desacoblament dels neutrins* i la *anihilació de parells* $e^{\pm}$. Si els considerem independents, aproximant un desacoblament *instantani*, la diferència entre les temperatures de neutrins i fotons és

$$\frac{T_\gamma}{T_\nu} = \left(\frac{11}{4}\right)^{1/3} \simeq 1.40102. \tag{3}$$

Després de l'anihilació dels electrons i positrons, les úniques partícules que contribueixen a la densitat d'energia de radiació de l'Univers són els fotons i els neutrins. Tenint en compte que hi ha un factor 7/8 entre la densitat d'energia de fermions i bosons per grau de llibertat, a causa de la diferència en la seua estadística, i que la densitat d'energia d'una partícula ultrarrelativista és proporcional a T^4, de la diferència de temperatures (3) podem escriure la densitat d'energia de radiació de l'Univers com

$$\rho_{\mathrm{r}} = \left(1 + N_{\mathrm{eff}} \frac{7}{8} \left(\frac{4}{11}\right)^{4/3}\right) \rho_\gamma, \tag{4}$$

on el nombre efectiu de neutrins, N_{eff}, és un paràmetre que té en compte la contribució a la radiació en l'Univers primerenc de qualsevol partícula ultrarrelativista diferent dels fotons.

En l'aproximació d'un desacoblament instantani dels neutrins, $N_{\mathrm{eff}} = 3$. No obstant això, hi ha diversos efectes que modifiquen aquest nombre en el cas estàndard. Per exemple, les partícules de l'Univers primerenc estan immerses en un plasma i no en el buit, la qual cosa modifica les seues relacions de dispersió amb un terme que actua com una massa efectiva (correccions QED). Així mateix,

el desacoblament no es produeix de manera instantània, la qual cosa afecta especialment als neutrins més energètics (ja que són els que més temps interaccionen amb $e^{\pm}$), els que participen lleugerament en l'anihilació de parells $e^{\pm}$ absorbint part de la seua entropia. A més, com els neutrins de tipus electrònic interaccionen tant a través de corrent neutre com carregat amb els parells $e^{\pm}$, a aquests efectes cal sumar-los la presència de les oscil·lacions de sabor, que modifiquen les densitats d'energia dels tres estats de neutrins.

En el nostre treball calculem tant el valor de $N_{\rm eff}$ com les desviacions en les densitats d'energia dels neutrins. Per a això resolem el sistema d'equacions acoblades integrodiferencials que ens permet estudiar l'evolució de la temperatura dels fotons i de les desviacions, respecte a l'equilibri, de les funcions de distribució dels neutrins. El conjunt d'equacions està compost per l'equació de continuïtat

$$\dot{\rho} = -3H\left(\rho + P\right) \tag{5}$$

i les equacions de Boltzmann aplicades a les funcions de distribució dels neutrins en un univers en expansió

$$\left(\partial_t - Hp\,\partial_p\right)\varrho_p(t) = -i\left[\left(\frac{1}{2p}\mathsf{M}_{\rm F} - \frac{8\sqrt{2}G_{\rm F}p}{3m_{\rm W}^2}\mathsf{E}\right), \varrho_p(t)\right] + \mathcal{I}\left[\varrho_p(t)\right], \tag{6}$$

on ρ i P són la densitat d'energia i la pressió de l'Univers, $H = \dot{a}/a$ el paràmetre de Hubble (sent a el factor d'escala) i el punt indica la derivada temporal. A més, p és el moment lineal del neutrí considerat, $G_{\rm F}$ la constant de Fermi, m_W la massa del bosó W i ϱ_p la matriu de densitat dels neutrins de moment lineal p, els termes diagonals de la qual indiquen els números d'ocupació i els no diagonals estan relacionats amb les oscil·lacions. La necessitat d'utilitzar aquest formalisme ve de l'efecte simultani de les interaccions, estudiades en la matriu de les integrals de col·lisió $\mathcal{I}\left[\varrho_p(t)\right]$, i les oscil·lacions dels neutrins. Finalment, les matrius $\mathsf{M}_{\rm F}$ i E fan referencia a les oscil·lacions; la primera és la matriu de massa en la base de sabor, relacionada amb les oscil·lacions en el buit, i la segona apareix pels efectes de matèria sobre els patrons d'oscil·lació i només té com a component no nul·la en el cas estàndard $\mathsf{E}_{11} = \rho_{e^-} + \rho_{e^+}$.

Respecte a treballs anteriors, nosaltres vam tenir en compte el càlcul exacte de les components no diagonals de la matriu de les integrals de col·lisió, per als termes d'interacció entre electrons i neutrins, que han estat tractades de manera aproximada en càlculs previs. També incloem un parell d'exemples amb interaccions no estàndard entre neutrins i electrons permeses per altres experiments. Els resultats principals es mostren en la taula 4. Convé destacar que el valor de

Cas	$z_{\rm fin}$	$\delta\bar{\rho}_{\nu_e}(\%)$	$\delta\bar{\rho}_{\nu_\mu}(\%)$	$\delta\bar{\rho}_{\nu_\tau}(\%)$	$N_{\rm eff}$
Desacoblament instantani	1.40102	0	0	0	3.000
Des. inst. (amb corr. QED)	1.39975	0	0	0	3.011
Sense oscil·lacions	1.39784	0.920	0.392	0.392	3.045
Ordre normal (NO)	1.39779	0.699	0.511	0.519	3.045
NO (integrals aproximades)	1.39778	0.673	0.529	0.533	3.045
Ordre invers (IO)	1.39779	0.697	0.512	0.520	3.045
NSI ee (NO)	1.39812	0.592	0.460	0.467	3.040
NSI $\tau\tau$ (NO)	1.39708	0.862	0.784	0.812	3.059

Taula 4: Valors finals de la temperatura adimensional dels fotons $z_{\rm fi} = T_\gamma/T$ (on $T = T_\nu$ en l'aproximació de desacoblament instantani), de la distorsió de la densitat d'energia dels estats de sabor dels neutrins i del nombre efectiu. Es mostren diversos casos. Els tres primers corresponen a l'aproximació de desacoblament instantani, sense i amb correccions QED, i al de desacoblament no instantani sense incloure les oscil·lacions de sabor. El segon bloc exposa els resultats principals del treball, on s'inclouen les oscil·lacions dels neutrins per als dos ordres de les seues masses. A més, es mostra el cas per a l'ordre normal on les integrals de col·lisió no diagonals han estat aproximades, com en treballs anteriors. Finalment, el tercer bloc mostra els casos que inclouen les interaccions no estàndard (NSI) en els acoblaments dels electrons amb els neutrins electrònic (NSI ee) i tauònics (NSI $\tau\tau$).

$N_{\rm eff}$ depèn que es consideren o no l'aproximació de desacoblament instantani i les correccions QED, però no de la inclusió d'un càlcul precís de les oscil·lacions de sabor. Tanmateix, aquestes últimes són importants a l'hora d'estudiar les distorsions en la densitat d'energia dels neutrins.

Límit inferior a la temperatura de reescalfament de l'Univers

L'estudi del desacoblament dels neutrins és necessari a l'hora de posar fites a certs paràmetres cosmològics. En aquest treball, basat en la publicació [145], estudiem el que es coneix com a *temperatura de reescalfament* de l'Univers ($T_{\rm RH}$) en escenaris on adquireix valors molt, molt baixos, de l'ordre del MeV. La temperatura de reescalfament mesura el començament de l'última etapa de l'Univers dominada per la radiació, per exemple després del final de la fase d'inflació.

En el nostre treball assumim que l'última fase dominada per la radiació apareix després d'una fase on la matèria és dominant, en la qual una partícula massiva decau en les partícules lleugeres (ultrarrelativistes en el moment en el qual són produïdes) del model estàndard excepte els neutrins. Aquests últims són generats a partir del seu acoblament feble amb les altres partícules. D'aquesta manera, l'efecte de tenir temperatures de reescalfament molt baixes, de l'ordre de les temperatures del plasma còsmic quan es produeix el desacoblament dels neutrins, és una termalització incompleta dels neutrins. Això influeix tant en les anisotropies del fons còsmic de microones (CMB per les seues sigles en anglès) com en la producció dels primers nuclis lleugers durant la nucleosíntesi primordial (BBN, també per les seues sigles en anglès). En aquesta tesi ens hem centrat en el segon aspecte.

Primerament vam resoldre les equacions necessàries per al càlcul del desacoblament dels neutrins en escenaris de $T_{\rm RH}$ molt baixes, tenint en compte (per primera vegada en aquest tipus d'anàlisi) funcions de distribució Fermi-Dirac per a $e^{\pm}$ (sense assumir que tenen massa zero) juntament amb l'efecte de les oscil·lacions dels tres estats de sabor dels neutrins. Posteriorment, utilitzant les funcions de distribució dels neutrins obtingudes, calculem la producció d'elements lleugers en BBN amb una versió modificada del codi `PArthENoPE` i la contrastem amb les mesures experimentals per a posar un límit inferior a $T_{\rm RH}$. De manera similar s'utilitza una versió modificada del codi CAMB per a l'estudi de les anisotropies del CMB en funció de la temperatura de reescalfament.

En la figura 10 es mostra l'efecte que una temperatura de reescalfament molt baixa té sobre la producció d'heli i deuteri. També comparem els casos en què les oscil·lacions de sabor dels neutrins s'han tingut o no en compte, mostrant que la seua inclusió pot arribar a modificar la tendència en la producció d'heli respecte al cas estàndard.

Com a resultat d'aquest treball hem obtingut els límits inferiors més restrictius fins hui sobre la temperatura de reescalfament:

$$T_{\rm RH}({\rm BBN}) \geq 4.1\,{\rm MeV} \qquad (95\%\ {\rm CL}), \tag{7}$$

$$T_{\rm RH}({\rm CMB}) \geq 4.7\,{\rm MeV} \qquad (95\%\ {\rm CL}), \tag{8}$$

on les sigles CL indiquen *nivell de confiança*.

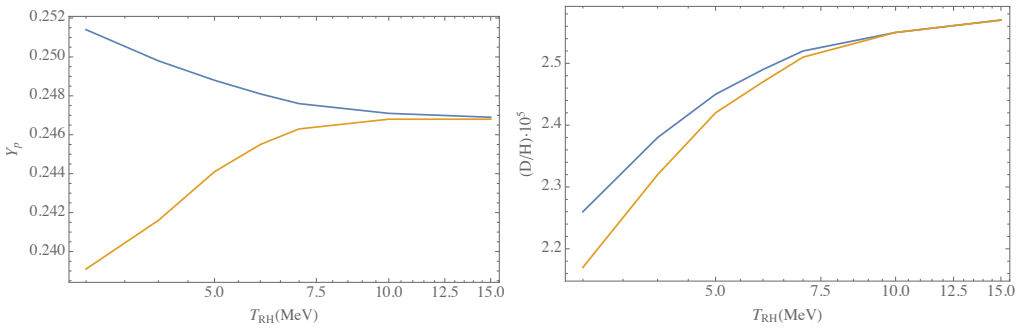

Figura 10: Producció primordial d'heli (en termes de la fracció de massa de l'heli Y_p) i deuteri (en termes de la seua abundància respecte a l'hidrogen ^{2}H/H), tenint en compte les oscil·lacions de sabor dels neutrins (línies blaves) i en l'absència d'aquestes (línies grogues).

Límits cosmològics a l'estadística dels neutrins

En el treball discutit en aquesta secció (publicat en [170]) estudiem les conseqüències que els neutrins incomplisquen el teorema espín-estadística. D'acord amb aquest teorema, les partícules amb espín enter segueixen una estadística de Bose-Einstein quan es troben en grans agrupaments, mentre que les partícules amb espín semienter, com és el cas dels neutrins, segueixen una distribució de Fermi-Dirac. A causa de la dificultat de trobar grans agrupacions de neutrins en equilibri i com aquestes partícules únicament interaccionen feblement, la comprovació que no violen el teorema espín-estadística continua pendent. Els millors límits actuals venen de mesures de desintegració doble beta, on es descarta un caràcter purament bosònic en els neutrins però no es confirma un comportament totalment fermiònic, malgrat tractar-se de partícules elementals d'espín 1/2. Una altra font que pot explotar-se per posar límits a l'estadística dels neutrins és el fons còsmic de neutrins relíquia (habitualment abreujat com a CνB), perquè constitueix un dels pocs casos on podem trobar una gran quantitat de neutrins que han estat en equilibri.

Aprofitant l'existència de noves dades cosmològiques de gran precisió, hem actualitzat els límits procedents d'observacions cosmològiques. En especial, i igual que per al treball en què vam posar límits a la temperatura de reescalfament, per al desenvolupament de la present tesi doctoral s'ha realitzat l'anàlisi de les dades procedents de mesures de la nucleosíntesi primordial. Per a això hem utilitzat una versió modificada de l'última actualització del codi `PArthENoPE` [88], en el

desenvolupament del qual també s'ha participat durant el període d'elaboració d'aquesta tesi.

Des del punt de vista teòric, un comportament anòmal en l'estadística dels neutrins implica multitud de problemes de difícil solució; per això, el desenvolupament d'aquest treball és estrictament fenomenològic. Per a estudiar l'estadística seguida pels neutrins utilitzem una modificació de la funció de distribució

$$f_\nu^{\mathrm{eq}}(E) = \frac{1}{\mathrm{e}^{E/T_\nu} + \kappa_\nu}, \tag{9}$$

on E i T_ν són l'energia i la temperatura dels neutrins, i on a més incloem el paràmetre κ_ν, que pot prendre valors des de -1 (cas purament bosònic) fins a $+1$ (cas purament fermiònic), passant per tota una gamma de casos intermedis. Posant límits a aquest paràmetre podem conéixer l'estadística seguida pels neutrins.

L'efecte principal d'un canvi d'estadística (diferent de l'esperada, purament fermiònica) és un augment de la densitat d'energia dels neutrins, que al seu torn afecta al ritme d'expansió de l'Univers primerenc. D'altra banda, les interaccions febles que mantenen l'equilibri entre neutrons i protons també es veuen afectades, la qual cosa repercuteix en la formació d'elements lleugers durant la nucleosíntesi.

Els resultats principals de l'anàlisi es resumeixen en la figura 11, on es mostren les regions de contorn en el pla (η_{10}, κ_ν), sent $\eta_{10}\, 10^{-10} = \eta_B = n_B/n_\gamma$ la mesura de la densitat numèrica de barions respecte a la corresponent als fotons. Els barions també poden estudiar-se a partir del paràmetre ω_b, que mesura la seua densitat d'energia respecte a la densitat crítica de l'Univers i el valor del qual està relacionat amb η_{10}. Les regions de contorn que inclouen les dades de ^{7}Li mostren clarament la tensió que existeix entre el valor estimat de producció d'aquest element i la seua mesura experimental. Un comportament altament bosònic dels neutrins podria alleujar aquesta tensió, però no serviria per a relaxar altres tensions existents en cosmologia, com la corresponent a l'estimació del paràmetre de Hubble H_0 o del paràmetre σ_8, i tampoc garanteix que el problema del ^{7}Li quede totalment resolt, mentre que afig moltes complicacions a nivell teòric. En definitiva, quan tenim en compte la combinació D+^{4}He i incloem la informació addicional sobre ω_b que s'obté de l'anàlisi utilitzant les anisotropies del CMB, les observacions cosmològiques només són capaces d'excloure un comportament purament bosònic a 2σ, sent compatible una estadística mesclada fins i tot en els casos on la mescla és més bosònica que fermiònica.

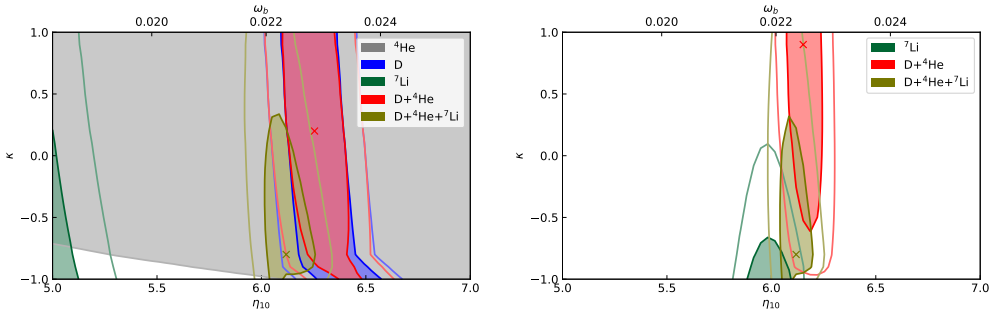

Figura 11: Regions de contorns a 1σ i 2σ en el pla $(\eta_{10},\, \kappa_\nu)$ obtingudes en la nostra anàlisi de BBN. Les àrees en color indiquen la regió a 1σ i les corresponents línies, aquelles a 2σ. En tots dos panells es mostren els resultats per a les anàlisis d'un únic element, així com per a les combinacions D+^{4}He i D+^{4}He+^{7}Li. Les creus indiquen el valor de millor ajust en els casos combinats. En el panell de la dreta s'ha inclòs la informació addicional sobre ω_b obtinguda de l'anàlisi a partir de les dades de les anisotropies del CMB.

Sobredensitat local dels neutrins relíquia

Els resultats que ací discutim es basen en la publicació [215]. A causa del seu important paper, sobretot en l'Univers primerenc, els neutrins relíquia constitueixen una de les prediccions del model estàndard de cosmologia més importants encara per determinar experimentalment. La seua existència ha sigut provada de manera indirecta per la seua contribució a la quantitat de radiació de l'Univers primerenc, però la seua mesura experimental directa no és tasca fàcil, especialment a causa del caràcter no relativista d'aquestes relíquies i, per tant, a la seua baixa energia cinètica. A pesar que les masses dels neutrins s'esperen per davall de l'eV, la temperatura del CνB és tan baixa a causa de l'expansió còsmica que, fins i tot en l'escenari on un dels neutrins no té massa, els altres dos estats de massa serien no relativistes a avui dia.

Diverses tècniques per a la detecció d'aquestes esquives relíquies han sigut discutides en la bibliografia; entre elles, la més prometedora és la que es basa en la seua captura en àtoms de triti, $\nu_e + {}^3\mathrm{H} \to {}^3\mathrm{He} + e^-$, per no tindre energia llindar. Especialment, la proposta de l'experiment PTOLEMY (basat en aquesta idea) està avançant favorablement, i tal vegada en un futur no gaire llunyà puguem celebrar la primera detecció del fons còsmic de neutrins.

Per a fer una estimació del nombre de neutrins capturats en triti per un experiment similar a PTOLEMY, és necessari conéixer la densitat numérica de neutrins relíquia als voltants del Sistema Solar. Calculant a partir d'una distribució de Fermi-Dirac, uns $n_0 = 56\,\mathrm{cm}^{-3}$ s'esperen per tipus de neutrí i grau de llibertat. No obstant això, a causa del caràcter no relativista d'aquestes relíquies, poden ser atretes per grans potencials gravitatoris, com per exemple el de la Via Làctia, i en el seu lloc tenim $n_\nu = n_0 f_c$, on f_c és un factor d'aglomeració que depèn de la massa del neutrí considerat.

En aquest treball calculem el valor del factor f_c, millorant el tractament dels models de matèria de la nostra galàxia respecte a treballs previs, així com estenent el rang estudiat en les masses dels neutrins cap a valors propers als mínims permesos per les mesures de les oscil·lacions de sabor.

Respecte al tractament de la distribució de matèria en la nostra galàxia, vam tindre en compte dues parametritzacions de la matèria fosca: una distribució del tipus Navarro-Frenk-White (NFW) i una altra del tipus perfil d'Einasto. La diferència principal entre les dues és que la distribució NFW divergeix en la part central de la galàxia i, per tant, s'espera un factor f_c major per a distàncies properes al centre galàctic. Tant la distribució de matèria fosca (en ambdues parametritzacions) com la de matèria bariònica han sigut ajustades a dades experimentals, i la seua evolució amb el temps s'ha calculat a partir de les dades proporcionades per simulacions cosmològiques de N cossos.

En la figura 12 mostrem la nostra estimació de f_c, en funció de la distància al centre galàctic, per a un neutrí de massa $m_\nu = 60\,\mathrm{meV}$ i per a les dues parametritzacions de la distribució de matèria fosca considerades. Els perfils etiquetats com a *optimistes* es refereixen a perfils de DM on s'ha sobreestimat la seua densitat en la nostra galàxia. Dels valors de f_c podem obtindre el nombre d'esdeveniments esperat en un experiment com PTOLEMY que utilitze 100 grams de triti. Aquests resultats es mostren en la taula 5 per a dos valors de les masses dels neutrins. El menor es correspon amb un escenari quasi minimalista i per tant l'estimació del nombre d'esdeveniments depèn de l'ordre de les masses, mentre que el major es correspon amb un escenari degenerat a la vora de la compatibilitat amb els límits provinents d'observacions cosmològiques. En la taula es distingeixen a més tres casos: aquell on únicament s'ha tingut en compte el millor ajust a les dades per als perfils de DM; un segon on s'afig el perfil de barions, i un tercer on només es considera la matèria fosca però amb els perfils optimistes. Finalment cal destacar que, si els neutrins són partícules de Majorana, esperaríem el doble de successos que en el cas en que siguen partícules de Dirac.

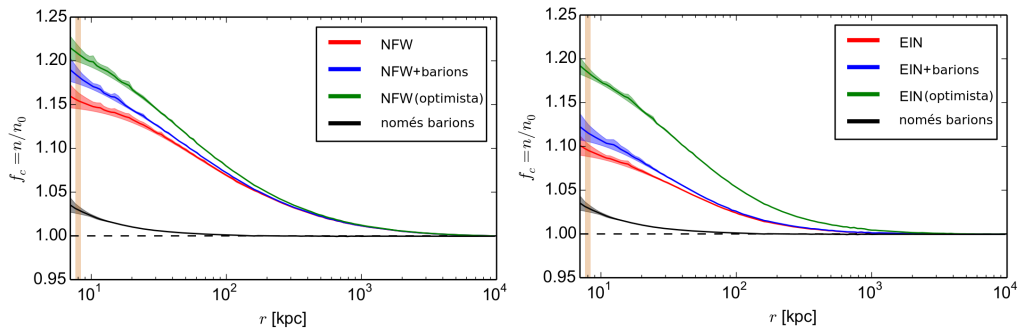

Figura 12: Sobredensitat numèrica per a un neutrí de massa $m_\nu = 60\,\text{meV}$, per grau de llibertat i en funció de la distància al centre galàctic. Les diferents línies es corresponen amb diferents perfils de matèria considerats, on NFW i EIN fan referència a les parametritzacions Navarro-Frenk-White i Einasto per a la matèria fosca. La línia vertical taronja representa la posició de la Terra, i les bandes en cada línia estan relacionades amb l'error numèric de les simulacions.

Efectes de matèria fosca en les oscil·lacions dels neutrins galàctics ultraenergètics

El treball descrit en aquesta secció està basat en la publicació [11]. És ben conegut que les oscil·lacions de sabor dels neutrins estan afectades per la presencia de matèria en el seu camí des del lloc de producció fins a la localització on són observats. En particular, l'efecte ocorre quan la interacció amb el medi no és universal per a tots els sabors; per exemple, els neutrins que travessen la Terra o aquells que s'originen a l'interior del Sol passen per un medi ric en electrons, amb els quals els neutrins de tipus electrònic poden interaccionar via corrent carregat, mentre que la interacció neutra, com és universal, només introdueix una fase global que no afecta les oscil·lacions. Els efectes de matèria depenen tant de la densitat de les partícules amb les quals els neutrins interaccionen com de l'energia d'aquests, de tal manera que un increment en la primera és equivalent a un increment en la segona.

D'altra banda, multitud de proves indirectes indiquen que galàxies com la nostra estan immerses en un halo de matèria fosca, predominant sobre la quantitat de matèria bariònica que podem veure. Per tant, assumint que les partícules de matèria fosca comparteixen una interacció amb els neutrins, i suposant que tal interacció no és universal, el patró de les oscil·lacions de sabor dels neutrins galàctics i extragalàctics podria veure's afectat per la presència de DM en la Via

masses (meV)	perfil	sobredens. f_c | $\Gamma^{\rm D}_{{\rm C}\nu{\rm B}}$ (any^{-1}) | $\Gamma^{\rm M}_{{\rm C}\nu{\rm B}}$ (any^{-1}) {millor ajust | m. a. + barions | optimista}		
qualsevol	qualsevol	1	4.06	8.12
degenerat	NFW	2.18|2.44|2.88	8.8 |9.9 |11.7	17.7|19.8|23.4
$m_{\nu_{1,2,3}} = 150$	Einasto	1.68|1.87|2.43	6.8 |7.6 |9.9	13.6|15.1|19.7
min. (IO)	NFW	1.15|1.18|1.21	4.07|4.08|4.08	8.15|8.15|8.16
$m_{\nu_3} = 60$	Einasto	1.09|1.12|1.18	4.07|4.07|4.08	8.14|8.14|8.15
min. (NO)	NFW	1.15|1.18|1.21	4.66|4.78|4.89	9.31|9.55|9.77
$m_{\nu_{1,2}} = 60$	Einasto	1.09|1.12|1.18	4.42|4.54|4.78	8.84|9.07|9.55

Taula 5: Factor d'agrupament f_c i nombre de captures esperades per any $\Gamma^{\rm D,M}_{{\rm C}\nu{\rm B}}$ per a neutrins de Dirac (D) o de Majorana (M). Els resultats es mostren per a distints perfils de matèria en la Via Làctia i diferents valors de la massa dels neutrins.

Làctia. Per descomptat, aquest efecte, si existeix, és prou xicotet com per a no aparèixer en el rang d'energies observat per la majoria d'experiments de neutrins, entre el MeV fins a diversos GeV, però bé podria entrar en joc a energies majors com les accessibles en IceCube. De fet, el continu augment en l'estadística de neutrins amb energies superiors al TeV (fins a diversos PeV) ha sigut una de les motivacions d'aquest treball.

Sens dubte, moltes altres fonts de nova física podrien portar a un efecte similar al d'una dispersió coherent i cap avant (el tipus d'interacció en matèria que modifica el patró d'oscil·lacions) per la presència de matèria fosca. No obstant això, en el nostre treball explotem la possible presència de ressonàncies, un senyal únic en un efecte de matèria. Depenent del tipus d'interacció, existeix una densitat crítica del medi per a la qual l'angle de mescla efectiu adquireix un valor màxim, independentment del seu valor en buit sempre que no siga nul. Quan un neutrí és produït en una regió saturada (és a dir, amb una densitat molt major que la crítica) i evoluciona adiabàticament fins a ser detectat en una regió on la densitat de matèria està per davall de la crítica, el terme mitjà de les oscil·lacions en el punt de detecció canvia respecte al seu valor en buit. Aquest efecte es coneix com MSW (Mikheyev–Smirnov–Wolfenstein) i, a causa del caràcter no homogeni de la distribució de matèria fosca en la nostra galàxia, podria aparèixer en els supòsits prèviament establits.

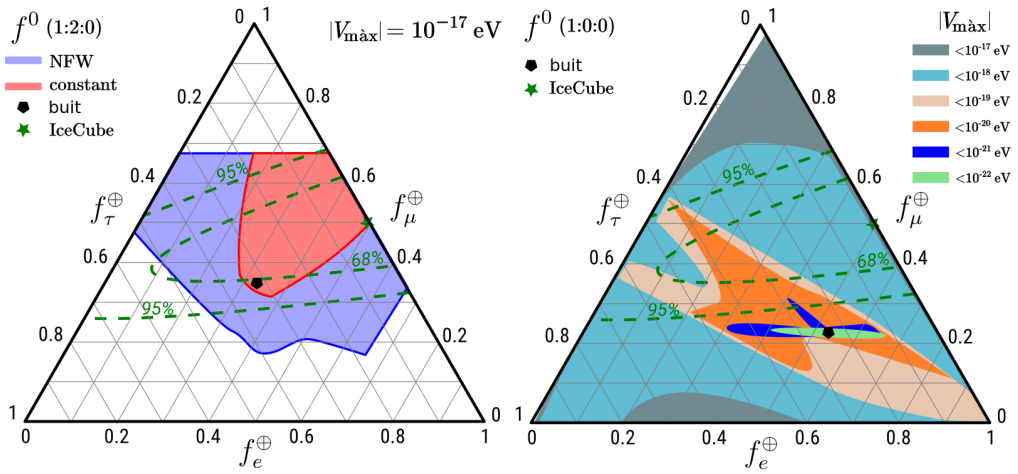

Figura 13: Triangles de sabor per a un flux d'estats inicials $(f^0_e : f^0_\mu : f^0_\tau) = (1{:}2{:}0)$ (esquerra) i (1:0:0) (dreta) on s'ha inclòs l'efecte en matèria per la presència de matèria fosca. El panell esquerre mostra l'àrea coberta per un perfil de DM homogeni (àrea vermellosa, compatible amb altres fonts de nova física) i aquella coberta per a un perfil NFW (àrea blava). El panell dret mostra les àrees cobertes per a un NFW després d'imposar un valor màxim $V^\oplus_{ij}$ concret. Observem que per a valors més xicotets, l'àrea s'acosta més a la solució en el buit, com s'espera.

Com a conseqüència, la regió dels possibles valors amitjanats per als sabors dels neutrins galàctics ultraenergètics, en la seua arribada a la Terra, s'obri considerablement (figura 13). Això podria explicar una possible mesura anòmala en un futur proper per part d'IceCube, en combinació amb altres telescopis de neutrins de gran volum (com per exemple el telescopi ARCA de la col·laboració KM3NeT), fins i tot si aquesta mesura caiguera fora de la zona permesa per l'efecte d'un altre tipus de nova física.

La figura 13 mostra els resultats principals d'aquest treball. En el panell esquerre s'indica la regió permesa en el triangle de sabor dels neutrins que arriben a la Terra, partint d'una distribució de sabors en el flux inicial amb valors $(f^0_e : f^0_\mu : f^0_\tau) = (1{:}2{:}0)$, típica en processos astrofísics on els neutrins es produeixen després de la desintegració de kaons o pions. La regió vermellosa s'ha generat amb un perfil de DM constant, mentre que la zona blava mostra l'eixamplament de la regió permesa en considerar un perfil NFW. Per cobrir tota la zona s'han generat punts variant els valors, en la posició de la Terra, de les entrades de la matriu del potencial que controla l'efecte en matèria, $V^\oplus_{ij}$, fins a un

valor màxim permés de $V^{\oplus}_{\max} = 10^{-17}\,\text{eV}$, corresponent a una saturació en tota la galàxia per a un neutrí de $E = 1\,\text{PeV}$. El punt negre indica la composició de sabor esperada per a una propagació en el buit. Per comparació també s'inclouen el valor de millor ajust i les regions de contorn permeses a 68% i 95% CL a partir de les dades d'IceCube publicades en [253]. L'àrea vermellosa és compatible amb altres fonts de nova física l'efecte de la qual és similar al generat per la presència de matèria constant.

En el panell de la dreta de la figura 13 s'ha utilitzat un perfil NFW de DM i un flux inicial de neutrins electrònics. Aquesta vegada es mostren les distribucions de sabor en la Terra per a diferents valors màxims del potencial en matèria. Pot apreciar-se que valors de $V^{\oplus}_{\max} = 10^{-17}\,\text{eV}$ poden explicar quasi tota la regió, mentre que valors més baixos del potencial s'acosten a la solució en buit.

Conclusions

En la present tesi doctoral s'han desenvolupat diversos treballs fenomenològics sobre la física dels neutrins, amb especial èmfasi en l'estudi de les oscil·lacions de sabor i en el seu paper en cosmologia. Entre ells, s'ha participat en un ajust global dels paràmetres d'oscil·lació, especialment important perquè permet aconseguir una precisió sense precedents en incloure experiments complementaris, com demostra l'evidència estadística a més de 3σ trobada en favor de l'ordre normal de les masses dels neutrins.

Respecte als neutrins relíquia, s'ha estudiat detalladament el fenomen de desacoblament en l'Univers primerenc, on s'han relaxat aproximacions referents al tractament de les oscil·lacions de sabor, i s'han posat fites a un parell d'extensions del model cosmològic estàndard afectades per la presència d'aquests neutrins en els primers instants de l'Univers. A més, hem calculat la sobredensitat local d'aquestes relíquies per a valors minimalistes de les seues masses, millorant així mateix el tractament de la distribució de matèria en la nostra galàxia en aquest tipus d'estudis.

Més enllà dels neutrins del fons còsmic, hem estudiat aquells amb energies que arriben fins a diversos PeV, centrant-nos en la possible implicació (en termes de les oscil·lacions de sabor) que una interacció neutrí-DM pot tindre en la distribució de sabor dels neutrins galàctics detectats per telescopis de gran volum com IceCube.

Finalment, durant el doctorat hem participat en el desenvolupament d'una actualització del codi `PArthENoPE` per a calcular la producció d'elements lleugers durant BBN, i, encara que no s'hagen inclòs completament en el manuscrit, també s'ha pres part en un parell d'estudis relacionats amb les fites a les masses dels neu-

trins i a l'ordre d'aquestes utilitzant tant les dades dels experiments d'oscil·lació com d'observacions cosmològiques.

Bibliography

[1] B. Pontecorvo. Mesonium and anti-mesonium. *Sov. Phys. JETP*, 6:429, 1957. [Zh. Eksp. Teor. Fiz.33,549(1957)].

[2] B. Pontecorvo. Inverse beta processes and nonconservation of lepton charge. *Sov. Phys. JETP*, 7:172–173, 1958. [Zh. Eksp. Teor. Fiz.34,247(1957)].

[3] Ziro Maki, Masami Nakagawa, and Shoichi Sakata. Remarks on the unified model of elementary particles. *Prog. Theor. Phys.*, 28:870–880, 1962.

[4] B. Pontecorvo. Neutrino Experiments and the Problem of Conservation of Leptonic Charge. *Sov. Phys. JETP*, 26:984–988, 1968. [Zh. Eksp. Teor. Fiz.53,1717(1967)].

[5] Q. R. Ahmad et al. Direct evidence for neutrino flavor transformation from neutral current interactions in the Sudbury Neutrino Observatory. *Phys. Rev. Lett.*, 89:011301, 2002, [nucl-ex/0204008].

[6] S. Abe et al. Precision Measurement of Neutrino Oscillation Parameters with KamLAND. *Phys. Rev. Lett.*, 100:221803, 2008, [0801.4589].

[7] P. F. de Salas, D. V. Forero, C. A. Ternes, M. Tortola, and J. W. F. Valle. Status of neutrino oscillations 2018: 3σ hint for normal mass ordering and improved CP sensitivity. *Phys. Lett.*, B782:633–640, 2018, [1708.01186].

[8] Valencia-globalfit. `http://globalfit.astroparticles.es/`.

[9] Evgeny Akhmedov. Do non-relativistic neutrinos oscillate? *JHEP*, 07:070, 2017, [1703.08169].

[10] M. Tanabashi et al. Review of Particle Physics. *Phys. Rev.*, D98:030001, 2018.

[11] P. F. de Salas, R. A. Lineros, and M. Tórtola. Neutrino propagation in the galactic dark matter halo. *Phys. Rev.*, D94(12):123001, 2016, [1601.05798].

[12] P. Mosteiro et al. Low-energy (anti)neutrino physics with Borexino: Neutrinos from the primary proton-proton fusion process in the Sun. *Nucl. Part. Phys. Proc.*, 265-266:87–92, 2015, [1508.05379].

[13] L. Wolfenstein. Neutrino Oscillations in Matter. *Phys. Rev.*, D17:2369–2374, 1978. [,294(1977)].

[14] S. P. Mikheev and A. Yu. Smirnov. Resonance Amplification of Oscillations in Matter and Spectroscopy of Solar Neutrinos. *Sov. J. Nucl. Phys.*, 42:913–917, 1985. [,305(1986)].

[15] S. P. Mikheev and A. Yu. Smirnov. Resonant amplification of neutrino oscillations in matter and solar neutrino spectroscopy. *Nuovo Cim.*, C9:17–26, 1986.

[16] Evgeny K. Akhmedov. Parametric resonance in neutrino oscillations in matter. *Pramana*, 54:47–63, 2000, [hep-ph/9907435].

[17] M. C. Gonzalez-Garcia and Michele Maltoni. Phenomenology with Massive Neutrinos. *Phys. Rept.*, 460:1–129, 2008, [0704.1800].

[18] Aldo M. Serenelli, W. C. Haxton, and Carlos Pena-Garay. Solar models with accretion. I. Application to the solar abundance problem. *Astrophys. J.*, 743:24, 2011, [1104.1639].

[19] W. C. Haxton, R. G. Hamish Robertson, and Aldo M. Serenelli. Solar Neutrinos: Status and Prospects. *Ann. Rev. Astron. Astrophys.*, 51:21–61, 2013, [1208.5723].

[20] B. T. Cleveland, Timothy Daily, Raymond Davis, Jr., James R. Distel, Kenneth Lande, C. K. Lee, Paul S. Wildenhain, and Jack Ullman. Measurement of the solar electron neutrino flux with the Homestake chlorine detector. *Astrophys. J.*, 496:505–526, 1998.

[21] F. Kaether, W. Hampel, G. Heusser, J. Kiko, and T. Kirsten. Reanalysis of the GALLEX solar neutrino flux and source experiments. *Phys. Lett.*, B685:47–54, 2010, [1001.2731].

[22] J. N. Abdurashitov et al. Measurement of the solar neutrino capture rate with gallium metal. III: Results for the 2002–2007 data-taking period. *Phys. Rev.*, C80:015807, 2009, [0901.2200].

[23] G. Bellini et al. Precision measurement of the 7Be solar neutrino interaction rate in Borexino. *Phys. Rev. Lett.*, 107:141302, 2011, [1104.1816].

[24] G. Bellini et al. Final results of Borexino Phase-I on low energy solar neutrino spectroscopy. *Phys. Rev.*, D89(11):112007, 2014, [1308.0443].

[25] J. Hosaka et al. Solar neutrino measurements in super-Kamiokande-I. *Phys. Rev.*, D73:112001, 2006, [hep-ex/0508053].

[26] J. P. Cravens et al. Solar neutrino measurements in Super-Kamiokande-II. *Phys. Rev.*, D78:032002, 2008, [0803.4312].

[27] K. Abe et al. Solar neutrino results in Super-Kamiokande-III. *Phys. Rev.*, D83:052010, 2011, [1010.0118].

[28] Y. Nakano. PhD Thesis, University of Tokyo. `http://www-sk.icrr.u-tokyo.ac.jp/sk/_pdf/articles/2016/doc_thesis_naknao.pdf`, 2016.

[29] K. Abe et al. Atmospheric neutrino oscillation analysis with external constraints in Super-Kamiokande I-IV. *Phys. Rev.*, D97(7):072001, 2018, [1710.09126].

[30] B. Aharmim et al. An Independent Measurement of the Total Active B-8 Solar Neutrino Flux Using an Array of He-3 Proportional Counters at the Sudbury Neutrino Observatory. *Phys. Rev. Lett.*, 101:111301, 2008, [0806.0989].

[31] B. Aharmim et al. Low Energy Threshold Analysis of the Phase I and Phase II Data Sets of the Sudbury Neutrino Observatory. *Phys. Rev.*, C81:055504, 2010, [0910.2984].

[32] K. Abe et al. Solar Neutrino Measurements in Super-Kamiokande-IV. *Phys. Rev.*, D94(5):052010, 2016, [1606.07538].

[33] A. Gando et al. Constraints on θ_{13} from A Three-Flavor Oscillation Analysis of Reactor Antineutrinos at KamLAND. *Phys. Rev.*, D83:052002, 2011, [1009.4771].

[34] J. H. Choi et al. Observation of Energy and Baseline Dependent Reactor Antineutrino Disappearance in the RENO Experiment. *Phys. Rev. Lett.*, 116(21):211801, 2016, [1511.05849].

[35] S. H. Seo et al. Spectral Measurement of the Electron Antineutrino Oscillation Amplitude and Frequency using 500 Live Days of RENO Data. 2016, [1610.04326].

[36] Myoung Youl Pac. Recent Results from RENO. 2018, [1801.04049].

[37] Feng Peng An et al. Measurement of electron antineutrino oscillation based on 1230 days of operation of the Daya Bay experiment. *Phys. Rev.*, D95(7):072006, 2017, [1610.04802].

[38] Y. Abe et al. Improved measurements of the neutrino mixing angle θ_{13} with the Double Chooz detector. *JHEP*, 10:086, 2014, [1406.7763]. [Erratum: JHEP02,074(2015)].

[39] M. Ishitsuka. Double Chooz Reactor Antineutrino Experiment. `https://indico.in2p3.fr/event/12279/session/3/contribution/173/material/slides/0.pdf`, March 2016.

[40] M. H. Ahn et al. Measurement of Neutrino Oscillation by the K2K Experiment. *Phys. Rev.*, D74:072003, 2006, [hep-ex/0606032].

[41] K. Abe et al. Updated T2K measurements of muon neutrino and antineutrino disappearance using 1.5×10^{21} protons on target. *Phys. Rev.*, D96(1):011102, 2017, [1704.06409].

[42] K. Abe et al. Combined Analysis of Neutrino and Antineutrino Oscillations at T2K. *Phys. Rev. Lett.*, 118(15):151801, 2017, [1701.00432].

[43] M. Hartz. T2K NEUTRINO OSCILLATION RESULTS WITH DATA UP TO 2017 SUMMER. `http://www.t2k.org/docs/talk/282`, August 2017.

[44] P. Adamson et al. Measurement of the neutrino mixing angle θ_{23} in NOvA. *Phys. Rev. Lett.*, 118(15):151802, 2017, [1701.05891].

[45] P. Adamson et al. Constraints on Oscillation Parameters from ν_e Appearance and ν_μ Disappearance in NOvA. *Phys. Rev. Lett.*, 118(23):231801, 2017, [1703.03328].

[46] Alexander Himmel. New neutrino oscillation results from NOVA. `https://indico.cern.ch/event/696410/`, January 2018.

[47] P. Adamson et al. Measurement of Neutrino and Antineutrino Oscillations Using Beam and Atmospheric Data in MINOS. *Phys. Rev. Lett.*, 110(25):251801, 2013, [1304.6335].

[48] P. Adamson et al. Electron neutrino and antineutrino appearance in the full MINOS data sample. *Phys. Rev. Lett.*, 110(17):171801, 2013, [1301.4581].

[49] P. Adamson et al. Combined analysis of ν_μ disappearance and $\nu_\mu \to \nu_e$ appearance in MINOS using accelerator and atmospheric neutrinos. *Phys. Rev. Lett.*, 112:191801, 2014, [1403.0867].

[50] T. K. Gaisser and M. Honda. Flux of atmospheric neutrinos. *Ann. Rev. Nucl. Part. Sci.*, 52:153–199, 2002, [hep-ph/0203272].

[51] M. Honda, M. Sajjad Athar, T. Kajita, K. Kasahara, and S. Midorikawa. Atmospheric neutrino flux calculation using the NRLMSISE-00 atmospheric model. *Phys. Rev.*, D92(2):023004, 2015, [1502.03916].

[52] M. Honda. Atmospheric neutrino flux updates. `http://www.icrr.u-tokyo.ac.jp/~mhonda/`, Feb 2015.

[53] M. G. Aartsen et al. PoS(ICRC2017)981. 2017, [1710.01191].

[54] M. G. Aartsen et al. Neutrino emission from the direction of the blazar txs 0506+056 prior to the icecube-170922a alert. *Science*, 2018.

[55] M. G. Aartsen et al. Multimessenger observations of a flaring blazar coincident with high-energy neutrino icecube-170922a. *Science*, 2018.

[56] Andrea Palladino and Francesco Vissani. Extragalactic plus Galactic model for IceCube neutrino events. *Astrophys. J.*, 826(2):185, 2016, [1601.06678].

[57] Peter B. Denton, Danny Marfatia, and Thomas J. Weiler. The Galactic Contribution to IceCube's Astrophysical Neutrino Flux. *JCAP*, 1708(08):033, 2017, [1703.09721].

[58] S. Adrian-Martinez et al. Letter of intent for KM3NeT 2.0. *J. Phys.*, G43(8):084001, 2016, [1601.07459].

[59] M. G. Aartsen et al. Letter of Intent: The Precision IceCube Next Generation Upgrade (PINGU). 2014, [1401.2046].

[60] S. Adrian-Martinez et al. Measurement of Atmospheric Neutrino Oscillations with the ANTARES Neutrino Telescope. *Phys. Lett.*, B714:224–230, 2012, [1206.0645].

[61] M. G. Aartsen et al. Determining neutrino oscillation parameters from atmospheric muon neutrino disappearance with three years of IceCube DeepCore data. *Phys. Rev.*, D91(7):072004, 2015, [1410.7227].

[62] IceCube Oscillations: 3 years muon neutrino disappearance data. `https://icecube.wisc.edu/science/data/nu_osc`, October 2016.

[63] A. M. Dziewonski and D. L. Anderson. Preliminary reference earth model. *Phys. Earth Planet. Interiors*, 25:297–356, 1981.

[64] M. G. Aartsen et al. Measurement of Atmospheric Neutrino Oscillations at 6–56 GeV with IceCube DeepCore. *Phys. Rev. Lett.*, 120(7):071801, 2018, [1707.07081].

[65] G. D. Barr, T. K. Gaisser, S. Robbins, and Todor Stanev. Uncertainties in Atmospheric Neutrino Fluxes. *Phys. Rev.*, D74:094009, 2006, [astro-ph/0611266].

[66] C. A. Argüelles Delgado. New Physics with Atmospheric Neutrinos, PhD Thesis, University of Wisconsin-Madison, 2015.

[67] S. Gariazzo, M. Archidiacono, P. F. de Salas, O. Mena, C. A. Ternes, and M. Tórtola. Neutrino masses and their ordering: Global Data, Priors and Models. *JCAP*, 1803(03):011, 2018, [1801.04946].

[68] P. F. de Salas, S. Gariazzo, O. Mena, C. A. Ternes, and M. Tórtola. Neutrino Mass Ordering in 2018: Global Status. 2018, [1806.11051].

[69] C. Athanassopoulos et al. Candidate events in a search for anti-muon-neutrino —> anti-electron-neutrino oscillations. *Phys. Rev. Lett.*, 75:2650–2653, 1995, [nucl-ex/9504002].

[70] A. Aguilar-Arevalo et al. Evidence for neutrino oscillations from the observation of anti-neutrino(electron) appearance in a anti-neutrino(muon) beam. *Phys. Rev.*, D64:112007, 2001, [hep-ex/0104049].

[71] J. N. Abdurashitov et al. Measurement of the response of a Ga solar neutrino experiment to neutrinos from an Ar-37 source. *Phys. Rev.*, C73:045805, 2006, [nucl-ex/0512041].

[72] Marco Laveder. Unbound neutrino roadmaps. *Nucl. Phys. Proc. Suppl.*, 168:344–346, 2007.

[73] Carlo Giunti and Marco Laveder. Short-Baseline Active-Sterile Neutrino Oscillations? *Mod. Phys. Lett.*, A22:2499–2509, 2007, [hep-ph/0610352].

[74] Carlo Giunti and Marco Laveder. Statistical Significance of the Gallium Anomaly. *Phys. Rev.*, C83:065504, 2011, [1006.3244].

[75] C. Giunti, M. Laveder, Y. F. Li, Q. Y. Liu, and H. W. Long. Update of Short-Baseline Electron Neutrino and Antineutrino Disappearance. *Phys. Rev.*, D86:113014, 2012, [1210.5715].

[76] G. Mention, M. Fechner, Th. Lasserre, Th. A. Mueller, D. Lhuillier, M. Cribier, and A. Letourneau. The Reactor Antineutrino Anomaly. *Phys. Rev.*, D83:073006, 2011, [1101.2755].

[77] I Alekseev et al. Search for sterile neutrinos at the DANSS experiment. 2018, [1804.04046].

[78] A. A. Aguilar-Arevalo et al. Observation of a Significant Excess of Electron-Like Events in the MiniBooNE Short-Baseline Neutrino Experiment. 2018, [1805.12028].

[79] Samoil M. Bilenky, C. Giunti, and W. Grimus. Phenomenology of neutrino oscillations. *Prog. Part. Nucl. Phys.*, 43:1–86, 1999, [hep-ph/9812360].

[80] J. M. Conrad, C. M. Ignarra, G. Karagiorgi, M. H. Shaevitz, and J. Spitz. Sterile Neutrino Fits to Short Baseline Neutrino Oscillation Measurements. *Adv. High Energy Phys.*, 2013:163897, 2013, [1207.4765].

[81] S. Gariazzo, C. Giunti, M. Laveder, Y. F. Li, and E. M. Zavanin. Light sterile neutrinos. *J. Phys.*, G43:033001, 2016, [1507.08204].

[82] Emanuele Castorina, Urbano Franca, Massimiliano Lattanzi, Julien Lesgourgues, Gianpiero Mangano, Alessandro Melchiorri, and Sergio Pastor. Cosmological lepton asymmetry with a nonzero mixing angle θ_{13}. *Phys. Rev.*, D86:023517, 2012, [1204.2510].

[83] P. A. R. Ade et al. Planck 2015 results. XIII. Cosmological parameters. *Astron. Astrophys.*, 594:A13, 2016, [1502.01589].

[84] Shinji Tsujikawa. Introductory review of cosmic inflation. In *2nd Tah Poe School on Cosmology: Modern Cosmology Phitsanulok, Thailand, April 17-25, 2003*, 2003, [hep-ph/0304257].

[85] Jerome Martin, Christophe Ringeval, and Vincent Vennin. Encyclopædia Inflationaris. *Phys. Dark Univ.*, 5-6:75–235, 2014, [1303.3787].

[86] Daniel Baumann. *Cosmology. Part III Mathematical Tripos.*

[87] O. Pisanti, A. Cirillo, S. Esposito, F. Iocco, G. Mangano, G. Miele, and P. D. Serpico. PArthENoPE: Public Algorithm Evaluating the Nucleosynthesis of Primordial Elements. *Comput. Phys. Commun.*, 178:956–971, 2008, [0705.0290].

[88] R. Consiglio, P. F. de Salas, G. Mangano, G. Miele, S. Pastor, and O. Pisanti. PArthENoPE reloaded. 2017, [1712.04378].

[89] D. J. Fixsen. The Temperature of the Cosmic Microwave Background. *Astrophys. J.*, 707:916–920, 2009, [0911.1955].

[90] R. Adam et al. Planck 2015 results. I. Overview of products and scientific results. *Astron. Astrophys.*, 594:A1, 2016, [1502.01582].

[91] S. Planelles, D. R. G. Schleicher, and A. M. Bykov. Large-Scale Structure Formation: from the first non-linear objects to massive galaxy clusters. *Space Sci. Rev.*, 188(1-4):93–139, 2015, [1404.3956].

[92] Nikhil Padmanabhan, Xiaoying Xu, Daniel J. Eisenstein, Richard Scalzo, Antonio J. Cuesta, Kushal T. Mehta, and Eyal Kazin. A 2 per cent distance to z=0.35 by reconstructing baryon acoustic oscillations - I. Methods and application to the Sloan Digital Sky Survey. *Mon. Not. Roy. Astron. Soc.*, 427(3):2132–2145, 2012, [1202.0090].

[93] J. Angrik et al. KATRIN design report 2004. 2005.

[94] S. Betts et al. Development of a Relic Neutrino Detection Experiment at PTOLEMY: Princeton Tritium Observatory for Light, Early-Universe, Massive-Neutrino Yield. In *Proceedings, 2013 Community Summer Study on the Future of U.S. Particle Physics: Snowmass on the Mississippi (CSS2013): Minneapolis, MN, USA, July 29-August 6, 2013*, 2013, [1307.4738].

[95] Massimiliano Lattanzi and Martina Gerbino. Status of neutrino properties and future prospects - Cosmological and astrophysical constraints. *Front.in Phys.*, 5:70, 2018, [1712.07109].

[96] N. Aghanim et al. Planck intermediate results. XLVI. Reduction of large-scale systematic effects in HFI polarization maps and estimation of the reionization optical depth. *Astron. Astrophys.*, 596:A107, 2016, [1605.02985].

[97] Sunny Vagnozzi, Elena Giusarma, Olga Mena, Katherine Freese, Martina Gerbino, Shirley Ho, and Massimiliano Lattanzi. Unveiling ν secrets with cosmological data: neutrino masses and mass hierarchy. *Phys. Rev.*, D96(12):123503, 2017, [1701.08172].

[98] Eleonora Di Valentino, Stefano Gariazzo, Martina Gerbino, Elena Giusarma, and Olga Mena. Dark Radiation and Inflationary Freedom after Planck 2015. *Phys. Rev.*, D93(8):083523, 2016, [1601.07557].

[99] Francesco Capozzi, Eleonora Di Valentino, Eligio Lisi, Antonio Marrone, Alessandro Melchiorri, and Antonio Palazzo. Global constraints on absolute neutrino masses and their ordering. *Phys. Rev.*, D95(9):096014, 2017, [1703.04471].

[100] Alexandre Barreira, Baojiu Li, Carlton Baugh, and Silvia Pascoli. Modified gravity with massive neutrinos as a testable alternative cosmological model. *Phys. Rev.*, D90(2):023528, 2014, [1404.1365].

[101] Yves Dirian. Changing the Bayesian prior: Absolute neutrino mass constraints in nonlocal gravity. *Phys. Rev.*, D96(8):083513, 2017, [1704.04075].

[102] Aoife Boyle and Eiichiro Komatsu. Deconstructing the neutrino mass constraint from galaxy redshift surveys. *JCAP*, 1803(03):035, 2018, [1712.01857].

[103] S. Schael et al. Precision electroweak measurements on the Z resonance. *Phys. Rept.*, 427:257–454, 2006, [hep-ex/0509008].

[104] Tim Sprenger, Maria Archidiacono, Thejs Brinckmann, Sébastien Clesse, and Julien Lesgourgues. Cosmology in the era of Euclid and the Square Kilometre Array. 2018, [1801.08331].

[105] Sebastien Blais-Ouellette, Claude Carignan, Philippe Amram, and Stephanie Cote. Accurate parameters of the mass distribution in spiral galaxies: 1. fabry - perot observations of ngc 5585. *Astron. J.*, 118:2123, 1999, [astro-ph/9911223].

[106] V. C. Rubin, W. K. Ford, Jr., N. Thonnard, M. S. Roberts, and J. A. Graham. Motion of the Galaxy and the local group determined from the velocity anisotropy of distant SC I galaxies. I - The data. *Astron. J.*, 81:687–718, September 1976.

[107] V. C. Rubin, N. Thonnard, W. K. Ford, Jr., and M. S. Roberts. Motion of the Galaxy and the local group determined from the velocity anisotropy of distant SC I galaxies. II - The analysis for the motion. *Astron. J.*, 81:719–737, September 1976.

[108] Ben Moore, Fabio Governato, Thomas R. Quinn, Joachim Stadel, and George Lake. Resolving the structure of cold dark matter halos. *Astrophys. J.*, 499:L5, 1998, [astro-ph/9709051].

[109] Sebastiano Ghigna, Ben Moore, Fabio Governato, George Lake, Thomas R. Quinn, and Joachim Stadel. Dark matter halos within clusters. *Mon. Not. Roy. Astron. Soc.*, 300:146–162, 1998, [astro-ph/9801192].

[110] John N. Bahcall and R. M. Soneira. The Universe at faint magnetidues. 2. Models for the predicted star counts. *Astrophys. J. Suppl.*, 44:73–110, 1980.

[111] Julio F. Navarro, Carlos S. Frenk, and Simon D. M. White. The Structure of cold dark matter halos. *Astrophys. J.*, 462:563–575, 1996, [astro-ph/9508025].

[112] Julio F. Navarro, Carlos S. Frenk, and Simon D. M. White. A Universal density profile from hierarchical clustering. *Astrophys. J.*, 490:493–508, 1997, [astro-ph/9611107].

[113] Alister W. Graham, David Merritt, Ben Moore, Juerg Diemand, and Balsa Terzic. Empirical models for Dark Matter Halos. I. Nonparametric Construction of Density Profiles and Comparison with Parametric Models. *Astron. J.*, 132:2685–2700, 2006, [astro-ph/0509417].

[114] Christopher F. McKee, Antonio Parravano, and David J. Hollenbach. Stars, Gas, and Dark Matter in the Solar Neighborhood. *Astrophys. J.*, 814(1):13, 2015, [1509.05334].

[115] S. Sivertsson, H. Silverwood, J. I. Read, G. Bertone, and P. Steger. The Local Dark Matter Density from SDSS-SEGUE G-dwarfs. *Mon. Not. Roy. Astron. Soc.*, 2017, [1708.07836].

[116] Pablo F. de Salas and Sergio Pastor. Relic neutrino decoupling with flavour oscillations revisited. *JCAP*, 1607(07):051, 2016, [1606.06986].

[117] A. F. Heckler. Astrophysical applications of quantum corrections to the equation of state of a plasma. *Phys. Rev.*, D49:611–617, 1994.

[118] N. Fornengo, C. W. Kim, and J. Song. Finite temperature effects on the neutrino decoupling in the early universe. *Phys. Rev.*, D56:5123–5134, 1997, [hep-ph/9702324].

[119] G. Mangano, G. Miele, S. Pastor, and M. Peloso. A Precision calculation of the effective number of cosmological neutrinos. *Phys. Lett.*, B534:8–16, 2002, [astro-ph/0111408].

[120] C.F. Barenghi and N.G. Parker. *A Primer on Quantum Fluids*. SpringerBriefs in Physics. Springer International Publishing, 2016.

[121] A. D. Dolgov, S. H. Hansen, S. Pastor, S. T. Petcov, G. G. Raffelt, and D. V. Semikoz. Cosmological bounds on neutrino degeneracy improved by flavor oscillations. *Nucl. Phys.*, B632:363–382, 2002, [hep-ph/0201287].

[122] Gianpiero Mangano, Gennaro Miele, Sergio Pastor, Ofelia Pisanti, and Srdjan Sarikas. Updated BBN bounds on the cosmological lepton asymmetry for non-zero θ_{13}. *Phys. Lett.*, B708:1–5, 2012, [1110.4335].

[123] G. Sigl and G. Raffelt. General kinetic description of relativistic mixed neutrinos. *Nucl. Phys.*, B406:423–451, 1993.

[124] Daniel N. Blaschke and Vincenzo Cirigliano. Neutrino Quantum Kinetic Equations: The Collision Term. *Phys. Rev.*, D94(3):033009, 2016, [1605.09383].

[125] D. V. Forero, M. Tortola, and J. W. F. Valle. Neutrino oscillations refitted. *Phys. Rev.*, D90(9):093006, 2014, [1405.7540].

[126] Steen Hannestad and Jes Madsen. Neutrino decoupling in the early universe. *Phys. Rev.*, D52:1764–1769, 1995, [astro-ph/9506015].

[127] A. D. Dolgov, S. H. Hansen, and D. V. Semikoz. Nonequilibrium corrections to the spectra of massless neutrinos in the early universe. *Nucl. Phys.*, B503:426–444, 1997, [hep-ph/9703315].

[128] S. Esposito, G. Miele, S. Pastor, M. Peloso, and O. Pisanti. Nonequilibrium spectra of degenerate relic neutrinos. *Nucl. Phys.*, B590:539–561, 2000, [astro-ph/0005573].

[129] Gianpiero Mangano, Gennaro Miele, Sergio Pastor, Teguayco Pinto, Ofelia Pisanti, and Pasquale D. Serpico. Relic neutrino decoupling including flavor oscillations. *Nucl. Phys.*, B729:221–234, 2005, [hep-ph/0506164].

[130] Jeremiah Birrell, Cheng-Tao Yang, and Johann Rafelski. Relic Neutrino Freeze-out: Dependence on Natural Constants. *Nucl. Phys.*, B890:481–517, 2014, [1406.1759].

[131] E. Grohs, G. M. Fuller, C. T. Kishimoto, M. W. Paris, and A. Vlasenko. Neutrino energy transport in weak decoupling and big bang nucleosynthesis. *Phys. Rev.*, D93(8):083522, 2016, [1512.02205].

[132] K. Enqvist, K. Kainulainen, and Mark J. Thomson. Stringent cosmological bounds on inert neutrino mixing. *Nucl. Phys.*, B373:498–528, 1992.

[133] Bruce H. J. McKellar and Mark J. Thomson. Oscillating doublet neutrinos in the early universe. *Phys. Rev.*, D49:2710–2728, 1994.

[134] Nicole F. Bell, Raymond R. Volkas, and Yvonne Y. Y. Wong. Relic neutrino asymmetry evolution from first principles. *Phys. Rev.*, D59:113001, 1999, [hep-ph/9809363].

[135] Zurab Berezhiani and Anna Rossi. Limits on the nonstandard interactions of neutrinos from e+ e- colliders. *Phys. Lett.*, B535:207–218, 2002, [hep-ph/0111137].

[136] S. Davidson, C. Pena-Garay, N. Rius, and A. Santamaria. Present and future bounds on nonstandard neutrino interactions. *JHEP*, 03:011, 2003, [hep-ph/0302093].

[137] Gianpiero Mangano, Gennaro Miele, Sergio Pastor, Teguayco Pinto, Ofelia Pisanti, and Pasquale D. Serpico. Effects of non-standard neutrino-electron interactions on relic neutrino decoupling. *Nucl. Phys.*, B756:100–116, 2006, [hep-ph/0607267].

[138] O. G. Miranda and H. Nunokawa. Non standard neutrino interactions: current status and future prospects. *New J. Phys.*, 17(9):095002, 2015, [1505.06254].

[139] D. V. Forero and M. M. Guzzo. Constraining nonstandard neutrino interactions with electrons. *Phys. Rev.*, D84:013002, 2011.

[140] Y. Farzan and M. Tortola. Neutrino oscillations and Non-Standard Interactions. *Front.in Phys.*, 6:10, 2018, [1710.09360].

[141] J. Barranco, O. G. Miranda, C. A. Moura, and J. W. F. Valle. Constraining non-standard neutrino-electron interactions. *Phys. Rev.*, D77:093014, 2008, [0711.0698].

[142] Nickolay Y. Gnedin and Oleg Y. Gnedin. Cosmological neutrino background revisited. *Astrophys. J.*, 509:11–15, 1998, [astro-ph/9712199].

[143] A. D. Dolgov, S. H. Hansen, and D. V. Semikoz. Nonequilibrium corrections to the spectra of massless neutrinos in the early universe: Addendum. *Nucl. Phys.*, B543:269–274, 1999, [hep-ph/9805467].

[144] Steen Hannestad, Rasmus Sloth Hansen, Thomas Tram, and Yvonne Y. Y. Wong. Active-sterile neutrino oscillations in the early Universe with full collision terms. *JCAP*, 1508(08):019, 2015, [1506.05266].

[145] P. F. de Salas, M. Lattanzi, G. Mangano, G. Miele, S. Pastor, and O. Pisanti. Bounds on very low reheating scenarios after Planck. *Phys. Rev.*, D92(12):123534, 2015, [1511.00672].

[146] Kazuhide Ichikawa, Masahiro Kawasaki, and Fuminobu Takahashi. The Oscillation effects on thermalization of the neutrinos in the Universe with low reheating temperature. *Phys. Rev.*, D72:043522, 2005, [astro-ph/0505395].

[147] M. Kawasaki, Kazunori Kohri, and Naoshi Sugiyama. Cosmological constraints on late time entropy production. *Phys. Rev. Lett.*, 82:4168, 1999, [astro-ph/9811437].

[148] M. Kawasaki, Kazunori Kohri, and Naoshi Sugiyama. MeV scale reheating temperature and thermalization of neutrino background. *Phys. Rev.*, D62:023506, 2000, [astro-ph/0002127].

[149] Gian Francesco Giudice, Edward W. Kolb, and Antonio Riotto. Largest temperature of the radiation era and its cosmological implications. *Phys. Rev.*, D64:023508, 2001, [hep-ph/0005123].

[150] Gian F. Giudice, Edward W. Kolb, Antonio Riotto, Dmitry V. Semikoz, and Igor I. Tkachev. Standard model neutrinos as warm dark matter. *Phys. Rev.*, D64:043512, 2001, [hep-ph/0012317].

[151] Steen Hannestad. What is the lowest possible reheating temperature? *Phys. Rev.*, D70:043506, 2004, [astro-ph/0403291].

[152] Kazuhide Ichikawa, Masahiro Kawasaki, and Fuminobu Takahashi. Constraint on the Effective Number of Neutrino Species from the WMAP and SDSS LRG Power Spectra. *JCAP*, 0705:007, 2007, [astro-ph/0611784].

[153] Francesco De Bernardis, Luca Pagano, and Alessandro Melchiorri. New constraints on the reheating temperature of the universe after WMAP-5. *Astropart. Phys.*, 30:192–195, 2008.

[154] Pasquale Dario Serpico, S. Esposito, F. Iocco, G. Mangano, G. Miele, and O. Pisanti. Nuclear reaction network for primordial nucleosynthesis: A Detailed analysis of rates, uncertainties and light nuclei yields. *JCAP*, 0412:010, 2004, [astro-ph/0408076].

[155] Y. I. Izotov, T. X. Thuan, and N. G. Guseva. A new determination of the primordial He abundance using the He i λ10830 Å emission line: cosmological implications. *Mon. Not. Roy. Astron. Soc.*, 445(1):778–793, 2014, [1408.6953].

[156] Erik Aver, Keith A. Olive, and Evan D. Skillman. The effects of He I λ10830 on helium abundance determinations. *JCAP*, 1507(07):011, 2015, [1503.08146].

[157] Max Pettini and Ryan Cooke. A new, precise measurement of the primordial abundance of Deuterium. *Mon. Not. Roy. Astron. Soc.*, 425:2477–2486, 2012, [1205.3785].

[158] Ryan Cooke, Max Pettini, Regina A. Jorgenson, Michael T. Murphy, and Charles C. Steidel. Precision measures of the primordial abundance of deuterium. *Astrophys. J.*, 781(1):31, 2014, [1308.3240].

[159] Alain Coc, Patrick Petitjean, Jean-Philippe Uzan, Elisabeth Vangioni, Pierre Descouvemont, Christian Iliadis, and Richard Longland. New reaction rates for improved primordial D/H calculation and the cosmic evolution of deuterium. *Phys. Rev.*, D92(12):123526, 2015, [1511.03843].

[160] E. G. Adelberger et al. Solar fusion cross sections II: the pp chain and CNO cycles. *Rev. Mod. Phys.*, 83:195, 2011, [1004.2318].

[161] L. E. Marcucci, M. Viviani, R. Schiavilla, A. Kievsky, and S. Rosati. Electromagnetic structure of A=2 and 3 nuclei and the nuclear current operator. *Phys. Rev.*, C72:014001, 2005, [nucl-th/0502048].

[162] Eleonora Di Valentino, Carlo Gustavino, Julien Lesgourgues, Gianpiero Mangano, Alessandro Melchiorri, Gennaro Miele, and Ofelia Pisanti. Probing nuclear rates with Planck and BICEP2. *Phys. Rev.*, D90(2):023543, 2014, [1404.7848].

[163] N. Aghanim et al. Planck 2015 results. XI. CMB power spectra, likelihoods, and robustness of parameters. *Astron. Astrophys.*, 594:A11, 2016, [1507.02704].

[164] Antony Lewis, Anthony Challinor, and Anthony Lasenby. Efficient computation of CMB anisotropies in closed FRW models. *Astrophys. J.*, 538:473–476, 2000, [astro-ph/9911177].

[165] N. Metropolis, A. W. Rosenbluth, M. N. Rosenbluth, A. H. Teller, and E. Teller. Equation of state calculations by fast computing machines. *J. Chem. Phys.*, 21:1087–1092, 1953.

[166] W. K. Hastings. Monte Carlo Sampling Methods Using Markov Chains and Their Applications. *Biometrika*, 57:97–109, 1970.

[167] Antony Lewis and Sarah Bridle. Cosmological parameters from CMB and other data: A Monte Carlo approach. *Phys. Rev.*, D66:103511, 2002, [astro-ph/0205436].

[168] Karim Benakli and Sacha Davidson. Baryogenesis in models with a low quantum gravity scale. *Phys. Rev.*, D60:025004, 1999, [hep-ph/9810280].

[169] Kazunori Kohri, Anupam Mazumdar, and Narendra Sahu. Inflation, baryogenesis and gravitino dark matter at ultra low reheat temperatures. *Phys. Rev.*, D80:103504, 2009, [0905.1625].

[170] P. F. de Salas, S. Gariazzo, M. Laveder, S. Pastor, O. Pisanti, and N. Truong. Cosmological bounds on neutrino statistics. *JCAP*, 1803(03):050, 2018, [1802.04639].

[171] W. Pauli. The Connection Between Spin and Statistics. *Phys. Rev.*, 58:716–722, 1940.

[172] A. D. Dolgov and A. Yu. Smirnov. Possible violation of the spin-statistics relation for neutrinos: Cosmological and astrophysical consequences. *Phys. Lett.*, B621:1–10, 2005, [hep-ph/0501066].

[173] A. S. Barabash, A. D. Dolgov, R. Dvornicky, F. Simkovic, and A. Yu. Smirnov. Statistics of neutrinos and the double beta decay. *Nucl. Phys.*, B783:90–111, 2007, [0704.2944].

[174] L. Cucurull, J. A. Grifols, and R. Toldrà. Spin statistics theorem, neutrinos, and big bang nucleosynthesis. *Astropart. Phys.*, 4:391–396, 1996, [astro-ph/9506040].

[175] A. D. Dolgov, Steen H. Hansen, and A. Yu. Smirnov. Neutrino statistics and Big Bang nucleosynthesis. *JCAP*, 0506:004, 2005, [astro-ph/0503612].

[176] Jun Iizuka and Teruyuki Kitabayashi. Fermi–Boltzmann statistics of neutrinos and relativistic effective degrees of freedom in the early universe. *Mod. Phys. Lett.*, A30(01):1550003, 2015, [1409.2964].

[177] Jun Iizuka and Teruyuki Kitabayashi. Statistics of neutrinos and relativistic effective degrees of freedom in the early universe. *Phys. Dark Univ.*, 11:54–63, 2016.

[178] Jun Iizuka and Teruyuki Kitabayashi. Relativistic effective degrees of freedom and quantum statistics of neutrinos. *Mod. Phys. Lett.*, A32(2):1750069, 2017, [1703.03120].

[179] Steen Hannestad, Andreas Ringwald, Huitzu Tu, and Yvonne Y. Y. Wong. Is it possible to tell the difference between fermionic and bosonic hot dark matter? *JCAP*, 0509:014, 2005, [astro-ph/0507544].

[180] Jacob Brandbyge and Steen Hannestad. Cosmological N-body simulations with generic hot dark matter. *JCAP*, 1710(10):015, 2017, [1706.00025].

[181] Sandhya Choubey and Kamales Kar. Possible violation of the spin-statistics relation for neutrinos: Checking through future galactic supernova. *Phys. Lett.*, B634:14–22, 2006, [hep-ph/0510261].

[182] Adam G. Riess et al. A 2.4% Determination of the Local Value of the Hubble Constant. *Astrophys. J.*, 826(1):56, 2016, [1604.01424].

[183] H. Hildebrandt et al. KiDS-450: Cosmological parameter constraints from tomographic weak gravitational lensing. *Mon. Not. Roy. Astron. Soc.*, 465:1454, 2017, [1606.05338].

[184] T. M. C. Abbott et al. Dark Energy Survey Year 1 Results: Cosmological Constraints from Galaxy Clustering and Weak Lensing. 2017, [1708.01530].

[185] F. Spite and M. Spite. Abundance of lithium in unevolved halo stars and old disk stars: Interpretation and consequences. *Astron. Astrophys.*, 115:357–366, 1982.

[186] A. S. Barabash. Experimental test of the Pauli Exclusion Principle. *Found. Phys.*, 40:703–718, 2010, [0908.3795].

[187] Fabio Iocco, Gianpiero Mangano, Gennaro Miele, Ofelia Pisanti, and Pasquale D. Serpico. Primordial Nucleosynthesis: from precision cosmology to fundamental physics. *Phys. Rept.*, 472:1–76, 2009, [0809.0631].

[188] Ryan J. Cooke, Max Pettini, and Charles C. Steidel. One Percent Determination of the Primordial Deuterium Abundance. *Astrophys. J.*, 855(2):102, 2018, [1710.11129].

[189] L. Sbordone et al. The metal-poor end of the Spite plateau. 1: Stellar parameters, metallicities and lithium abundances. *Astron. Astrophys.*, 522:A26, 2010, [1003.4510].

[190] Diego Blas, Julien Lesgourgues, and Thomas Tram. The Cosmic Linear Anisotropy Solving System (CLASS) II: Approximation schemes. *JCAP*, 1107:034, 2011, [1104.2933].

[191] Benjamin Audren, Julien Lesgourgues, Karim Benabed, and Simon Prunet. Conservative Constraints on Early Cosmology: an illustration of the Monte Python cosmological parameter inference code. *JCAP*, 1302:001, 2013, [1210.7183].

[192] F. Feroz, M. P. Hobson, and M. Bridges. MultiNest: an efficient and robust Bayesian inference tool for cosmology and particle physics. *Mon. Not. Roy. Astron. Soc.*, 398:1601–1614, 2009, [0809.3437].

[193] M. Bridges, F. Feroz, M. P. Hobson, and A. N. Lasenby. Bayesian optimal reconstruction of the primordial power spectrum. *Mon. Not. Roy. Astron. Soc.*, 400:1075–1084, 2009, [0812.3541].

[194] F. Feroz, M. P. Hobson, E. Cameron, and A. N. Pettitt. Importance Nested Sampling and the MultiNest Algorithm. 2013, [1306.2144].

[195] P. A. R. Ade et al. Planck 2015 results. XV. Gravitational lensing. *Astron. Astrophys.*, 594:A15, 2016, [1502.01591].

[196] Florian Beutler, Chris Blake, Matthew Colless, D. Heath Jones, Lister Staveley-Smith, Lachlan Campbell, Quentin Parker, Will Saunders, and Fred Watson. The 6dF Galaxy Survey: Baryon Acoustic Oscillations and the Local Hubble Constant. *Mon. Not. Roy. Astron. Soc.*, 416:3017–3032, 2011, [1106.3366].

[197] Ashley J. Ross, Lado Samushia, Cullan Howlett, Will J. Percival, Angela Burden, and Marc Manera. The clustering of the SDSS DR7 main Galaxy sample – I. A 4 per cent distance measure at $z = 0.15$. *Mon. Not. Roy. Astron. Soc.*, 449(1):835–847, 2015, [1409.3242].

[198] Lauren Anderson et al. The clustering of galaxies in the SDSS-III Baryon Oscillation Spectroscopic Survey: baryon acoustic oscillations in the Data Releases 10 and 11 Galaxy samples. *Mon. Not. Roy. Astron. Soc.*, 441(1):24–62, 2014, [1312.4877].

[199] Steen Hannestad and Thomas Tram. Optimal prior for Bayesian inference in a constrained parameter space. 2017, [1710.08899].

[200] Steven Weinberg. Universal Neutrino Degeneracy. *Phys. Rev.*, 128:1457–1473, 1962.

[201] Gintaras Duda, Graciela Gelmini, and Shmuel Nussinov. Expected signals in relic neutrino detectors. *Phys. Rev.*, D64:122001, 2001, [hep-ph/0107027].

[202] Graciela B. Gelmini. Prospect for relic neutrino searches. *Phys. Scripta*, T121:131–136, 2005, [hep-ph/0412305].

[203] Andreas Ringwald. How to detect big bang relic neutrinos? In *Eleventh International Workshop on Neutrino Telescopes, Venezia, February 22-25, 2005*, pages 473–491, 2005, [hep-ph/0505024].

[204] Yu-Feng Li. Detection Prospects of the Cosmic Neutrino Background. *Int. J. Mod. Phys.*, A30(12):1530031, 2015, [1504.03966]. [Adv. Ser. Direct. High Energy Phys.25,233(2015)].

[205] Petr Vogel. How difficult it would be to detect cosmic neutrino background? *AIP Conf. Proc.*, 1666:140003, 2015.

[206] Valerie Domcke and Martin Spinrath. Detection prospects for the Cosmic Neutrino Background using laser interferometers. *JCAP*, 1706(06):055, 2017, [1703.08629].

[207] Alfredo G. Cocco, Gianpiero Mangano, and Marcello Messina. Probing low energy neutrino backgrounds with neutrino capture on beta decaying nuclei. *JCAP*, 0706:015, 2007, [hep-ph/0703075].

[208] R. Lazauskas, P. Vogel, and C. Volpe. Charged current cross section for massive cosmological neutrinos impinging on radioactive nuclei. *J. Phys.*, G35:025001, 2008, [0710.5312].

[209] Mattias Blennow. Prospects for cosmic neutrino detection in tritium experiments in the case of hierarchical neutrino masses. *Phys. Rev.*, D77:113014, 2008, [0803.3762].

[210] Amand Faessler, Rastislav Hodak, Sergey Kovalenko, and Fedor Simkovic. Beta Decaying Nuclei as a Probe of Cosmic Neutrino Background. 2011, [1102.1799].

[211] Andrew J. Long, Cecilia Lunardini, and Eray Sabancilar. Detecting non-relativistic cosmic neutrinos by capture on tritium: phenomenology and physics potential. *JCAP*, 1408:038, 2014, [1405.7654].

[212] A. Osipowicz et al. KATRIN: A Next generation tritium beta decay experiment with sub-eV sensitivity for the electron neutrino mass. Letter of intent. 2001, [hep-ex/0109033].

[213] A. Kaboth, J. A. Formaggio, and B. Monreal. Sensitivity of Neutrino Mass Experiments to the Cosmic Neutrino Background. *Phys. Rev.*, D82:062001, 2010, [1006.1886].

[214] Amand Faessler, Rastislav Hodak, Sergey Kovalenko, and Fedor Simkovic. Can one measure the Cosmic Neutrino Background? *Int. J. Mod. Phys.*, E26(01n02):1740008, 2017, [1602.03347].

[215] P. F. de Salas, S. Gariazzo, J. Lesgourgues, and S. Pastor. Calculation of the local density of relic neutrinos. *JCAP*, 1709(09):034, 2017, [1706.09850].

[216] Jue Zhang and Xin Zhang. Gravitational clustering of cosmic relic neutrinos in the Milky Way. *Nature Commun.*, 9:1833, 2018, [1712.01153].

[217] Andreas Ringwald and Yvonne Y. Y. Wong. Gravitational clustering of relic neutrinos and implications for their detection. *JCAP*, 0412:005, 2004, [hep-ph/0408241].

[218] D. Merritt and B. Tremblay. Nonparametric estimation of density profiles. *Astron. J.*, 108:514–537, 1994.

[219] Federico Marinacci, Ruediger Pakmor, and Volker Springel. The formation of disc galaxies in high resolution moving-mesh cosmological simulations. *Mon. Not. Roy. Astron. Soc.*, 437(2):1750–1775, 2014, [1305.5360].

[220] Anne M Green. Astrophysical uncertainties on the local dark matter distribution and direct detection experiments. *J. Phys.*, G44(8):084001, 2017, [1703.10102].

[221] Miguel Pato, Fabio Iocco, and Gianfranco Bertone. Dynamical constraints on the dark matter distribution in the Milky Way. *JCAP*, 1512(12):001, 2015, [1504.06324].

[222] Miguel Pato and Fabio Iocco. The Dark Matter Profile of the Milky Way: a Non-parametric Reconstruction. *Astrophys. J.*, 803(1):L3, 2015, [1504.03317].

[223] G. L. Bryan and M. L. Norman. Statistical properties of x-ray clusters: Analytic and numerical comparisons. *Astrophys. J.*, 495:80, 1998, [astro-ph/9710107].

[224] Aaron A. Dutton and Andrea V. Macciò. Cold dark matter haloes in the Planck era: evolution of structural parameters for Einasto and NFW profiles. *Mon. Not. Roy. Astron. Soc.*, 441(4):3359–3374, 2014, [1402.7073].

[225] A. Misiriotis, E. M. Xilouris, J. Papamastorakis, P. Boumis, and C. D. Goudis. The distribution of the ISM in the Milky Way A three-dimensional large-scale model. *Astron. Astrophys.*, 459:113, 2006, [astro-ph/0607638].

[226] Paul J. McMillan. Mass models of the Milky Way. *Mon. Not. Roy. Astron. Soc.*, 414:2446–2457, 2011, [1102.4340].

[227] Francisco Villaescusa-Navarro, Simeon Bird, Carlos Pena-Garay, and Matteo Viel. Non-linear evolution of the cosmic neutrino background. *JCAP*, 1303:019, 2013, [1212.4855].

[228] Prajwal R. Kafle, Sanjib Sharma, Geraint F. Lewis, Aaron S. G. Robotham, and Simon P. Driver. The Need for Speed: Escape velocity and dynamical mass measurements of the Andromeda galaxy. 2018, [1801.03949].

[229] N. W. Evans, M. I. Wilkinson, P. Guhathakurta, E. K. Grebel, and S. S. Vogt. Dynamical mass estimates for the halo of m31 from keck spectroscopy. *Astrophys. J.*, 540:L9, 2000, [astro-ph/0008155].

[230] A. Tamm, E. Tempel, P. Tenjes, O. Tihhonova, and T. Tuvikene. Stellar mass map and dark matter distribution in M31. *Astron. Astrophys.*, 546:A4, 2012, [1208.5712].

[231] Alan W. McConnachie, M. J Irwin, A. M. N. Ferguson, R. A. Ibata, G. F. Lewis, and N. Tanvir. Distances and metallicities for 17 Local Group galaxies. *Mon. Not. Roy. Astron. Soc.*, 356:979–997, 2005, [astro-ph/0410489].

[232] Jorge Peñarrubia, Yin-Zhe Ma, Matthew G. Walker, and Alan McConnachie. A dynamical model of the local cosmic expansion. *Mon. Not. Roy. Astron. Soc.*, 443(3):2204–2222, 2014, [1405.0306].

[233] Simona Mei, John Blakeslee, Patrick Cote, John Tonry, Michael J. West, Laura Ferrarese, Andres Jordan, Eric Peng, Andre Anthony, and David Merritt. The ACS Virgo Cluster Survey. 13. SBF Distance Catalog and the Three-Dimensional Structure of the Virgo Cluster. *Astrophys. J.*, 655:144–162, 2007, [astro-ph/0702510].

[234] Pascal Fouque, Jose M. Solanes, Teresa Sanchis, and Chantal Balkowski. Structure, mass and distance of the virgo cluster from a tolman-bondi model. *Astron. Astrophys.*, 375:770, 2001, [astro-ph/0106261].

[235] Francisco Villaescusa-Navarro, Jordi Miralda-Escudé, Carlos Peña-Garay, and Vicent Quilis. Neutrino Halos in Clusters of Galaxies and their Weak Lensing Signature. *JCAP*, 1106:027, 2011, [1104.4770].

[236] A. D. Dolgov and F. L. Villante. BBN bounds on active sterile neutrino mixing. *Nucl. Phys.*, B679:261–298, 2004, [hep-ph/0308083].

[237] Marco Cirelli, Guido Marandella, Alessandro Strumia, and Francesco Vissani. Probing oscillations into sterile neutrinos with cosmology, astrophysics and experiments. *Nucl. Phys.*, B708:215–267, 2005, [hep-ph/0403158].

[238] Alessandro Melchiorri, Olga Mena, Sergio Palomares-Ruiz, Silvia Pascoli, Anze Slosar, and Michel Sorel. Sterile Neutrinos in Light of Recent Cosmological and Oscillation Data: A Multi-Flavor Scheme Approach. *JCAP*, 0901:036, 2009, [0810.5133].

[239] Steen Hannestad, Irene Tamborra, and Thomas Tram. Thermalisation of light sterile neutrinos in the early universe. *JCAP*, 1207:025, 2012, [1204.5861].

[240] Alessandro Mirizzi, Gianpiero Mangano, Ninetta Saviano, Enrico Borriello, Carlo Giunti, Gennaro Miele, and Ofelia Pisanti. The strongest bounds on active-sterile neutrino mixing after Planck data. *Phys. Lett.*, B726:8–14, 2013, [1303.5368].

[241] Scott Dodelson and Lawrence M. Widrow. Sterile-neutrinos as dark matter. *Phys. Rev. Lett.*, 72:17–20, 1994, [hep-ph/9303287].

[242] Mario A. Acero and Julien Lesgourgues. Cosmological constraints on a light non-thermal sterile neutrino. *Phys. Rev.*, D79:045026, 2009, [0812.2249].

[243] Thomas D. Jacques, Lawrence M. Krauss, and Cecilia Lunardini. Additional Light Sterile Neutrinos and Cosmology. *Phys. Rev.*, D87(8):083515, 2013, [1301.3119]. [Erratum: Phys. Rev.D88,no.10,109901(2013)].

[244] S. Gariazzo, C. Giunti, M. Laveder, and Y. F. Li. Updated Global 3+1 Analysis of Short-BaseLine Neutrino Oscillations. *JHEP*, 06:135, 2017, [1703.00860].

[245] R. Horvat. Resonant conversions of extremely high-energy neutrinos in dark matter halos. *Phys. Rev.*, D59:123003, 1999, [hep-ph/9812228].

[246] C. Lunardini and A. Yu. Smirnov. The Minimum width condition for neutrino conversion in matter. *Nucl. Phys.*, B583:260–290, 2000, [hep-ph/0002152].

[247] J. S. Diaz and F. R. Klinkhamer. Neutrino refraction by the cosmic neutrino background. *Phys. Rev.*, D93(5):053004, 2016, [1512.00817].

[248] O. G. Miranda, C. A. Moura, and A. Parada. Sterile neutrinos, dark matter, and resonant effects in ultra high energy regimes. *Phys. Lett.*, B744:55–58, 2015, [1308.1408].

[249] Riccardo Catena and Piero Ullio. A novel determination of the local dark matter density. *JCAP*, 1008:004, 2010, [0907.0018].

[250] Qiran Xia, Chao Liu, Shude Mao, Yingyi Song, Lan Zhang, R. J. Long, Yong Zhang, Yonghui Hou, Yuefei Wang, and Yue Wu. Determining the local dark matter density with LAMOST data. *Mon. Not. Roy. Astron. Soc.*, 458(4):3839–3850, 2016, [1510.06810].

[251] Mauricio Bustamante, John F. Beacom, and Walter Winter. Theoretically palatable flavor combinations of astrophysical neutrinos. *Phys. Rev. Lett.*, 115(16):161302, 2015, [1506.02645].

[252] Carlos A. Argüelles, Teppei Katori, and Jordi Salvado. New Physics in Astrophysical Neutrino Flavor. *Phys. Rev. Lett.*, 115:161303, 2015, [1506.02043].

[253] M. G. Aartsen et al. The IceCube Neutrino Observatory - Contributions to ICRC 2015 Part II: Atmospheric and Astrophysical Diffuse Neutrino Searches of All Flavors. In *Proceedings, 34th International Cosmic Ray Conference (ICRC 2015): The Hague, The Netherlands, July 30-August 6, 2015*, 2015, [1510.05223].

[254] Jonathan H. Davis and Joseph Silk. Spectral and Spatial Distortions of PeV Neutrinos from Scattering with Dark Matter. 2015, [1505.01843].

[255] Matías M. Reynoso and Oscar A. Sampayo. Propagation of high-energy neutrinos in a background of ultralight scalar dark matter. *Astropart. Phys.*, 82:10–20, 2016, [1605.09671].

[256] Ryan J. Wilkinson, Celine Boehm, and Julien Lesgourgues. Constraining Dark Matter-Neutrino Interactions using the CMB and Large-Scale Structure. *JCAP*, 1405:011, 2014, [1401.7597].

[257] P. Sikivie and Q. Yang. Bose-Einstein Condensation of Dark Matter Axions. *Phys. Rev. Lett.*, 103:111301, 2009, [0901.1106].

[258] Tonatiuh Matos and L. Arturo Urena-Lopez. A Further analysis of a cosmological model of quintessence and scalar dark matter. *Phys. Rev.*, D63:063506, 2001, [astro-ph/0006024].

[259] Yasaman Farzan and Steen Hannestad. Neutrinos secretly converting to lighter particles to please both KATRIN and the cosmos. *JCAP*, 1602(02):058, 2016, [1510.02201].

List of acronyms

ANTARES Astronomy with a Neutrino Telescope and Abyss environmental RESearch

ARCA Astroparticle Research with Cosmics in the Abyss

BAO Baryon Acoustic Oscillations

BBN Big Bang Nucleosynthesis

BE Bose-Einstein

BEC Bose-Einstein Condensate

BOSS Baryon Oscillation Spectroscopic Survey

CC Charged Current

CL Confidence Level

CMB Cosmic Microwave Background

CνB Cosmic Neutrino Background

CP Charge conjugation, Parity transformation

CPT Charge conjugation, Parity transformation, Time reversal

DES Dark Energy Survey

DM Dark Matter

DOM Digital Optical Module

DR Data Release

FD Fermi-Dirac

FRW Friedmann-Robertson-Walker

GALLEX GALLium EXperiment

GNO Gallium Neutrino Observatory

GUI Graphical User Interface

GVD Gigaton Volume Detector

ICAL Iron CALorimeter

INO India-based Neutrino Observatory

IO Inverted Ordering

JUNO Jiangmen Underground Neutrino Observatory

K2K KEK to Kamioka

KamLAND Kamioka Liquid-scintillator Anti-Neutrino Detector

KATRIN KArlsruhe TRItium Neutrino

KiDS Kilo Degree Survey

LAT Large Area Telescope

LBL Long BaseLine

ΛCDM Λ-Cold Dark Matter

LED Light-Emitting Diode

LRG Luminous Red Galaxy

LSND Liquid Scintillator Neutrino Detector

LSS Large Scale Structure

LVNT Large-Volume Neutrino Telescope

MAGIC Major Atmospheric Gamma-ray Imaging Cherenkov

MC Monte Carlo

MINOS Main Injector Neutrino Oscillation Search

MSW S. P. Mikheev, A. Smirnov and L. Wolfenstein

MW Milky Way

NC Neutral Current

***n*dF** n-degree Field

NEMO Neutrino Ettore Majorana Observatory

NFW Navarro-Frenk-White

NO Normal Ordering

NOνA NuMI Off-Axis ν_e Appearance

NSI Non-Standard Interactions

NuMI Neutrinos at the Main Injector

ORCA Oscillation Research with Cosmics in the Abyss

PArthENoPE Public Algorithm Evaluating the Nucleosynthesis of Primordial Elements

PINGU Precision IceCube Next Generation Upgrade

PMT PhotoMulTiplier

PREM Preliminary Reference Earth Model

PTOLEMY PonTecorvo Observatory for Light, Early-universe, Massive-neutrino Yield

QED Quantum Electrodynamics

RENO Reactor Experiment for Neutrino Oscillations

SAGE Soviet–American Gallium Experiment

SBL Short BaseLine

SDDR Savage-Dickey Density Ratio

SDSS Sloan Digital Sky Survey

SK Super-Kamiokande

SM Standard Model

SNO Sudbury Neutrino Observatory

T2K Tokai to Kamioka

VLVNT Very Large-Volume Neutrino Telescope

WMAP Wilkinson Microwave Anisotropy Probe